UNIVERSITY OF BIRMINGHAM

PICO- AND FEMTO-SECOND OPTICAL PULSE PROPAGATION IN SEMICONDUCTOR OPTICAL AMPLIFIERS: ANALYSIS, OPTIMIZATION AND QUANTUM TRANSMISSION LINE MODELLING

BY

MINGJUN XIA

A thesis submitted to
the University of Birmingham
for the degree of
DOCTOR OF PHILOSOPHY

DEPARTMENT OF ELECTRONIC, ELECTRICAL AND SYSTEM ENGINEERING
SCHOOL OF ENGINEERING
UNIVERSITY OF BIRMINGHAM
August 2016

UNIVERSITY OF
BIRMINGHAM

University of Birmingham Research Archive

e-theses repository

This unpublished thesis/dissertation is copyright of the author and/or third parties. The intellectual property rights of the author or third parties in respect of this work are as defined by The Copyright Designs and Patents Act 1988 or as modified by any successor legislation.

Any use made of information contained in this thesis/dissertation must be in accordance with that legislation and must be properly acknowledged. Further distribution or reproduction in any format is prohibited without the permission of the copyright holder.

Abstract

This thesis has theoretically and experimentally investigated the ultrashort optical pulse propagation in semiconductor optical amplifiers (SOAs), which is an important topic in the optical fiber communication and optical signal processing. Some new work has been done:

Firstly, effects of carrier heating on the ultrashort optical pulse propagation in quantum well SOAs are first studied taking into account the holes' non-parabolic density of states; for bulk SOAs, an accurate and simple analytical method to study carrier heating effects is presented based on Fermi-Dirac integrals approximation.

Secondly, this thesis reports a novel bias current optimization method for ultrashort optical pulse distortionless amplification in SOAs based on the newly proposed bias current relation function. Detailed theoretical and experimental work is done to analyze the relation between the optimized bias current and the parameters of the input ultrashort pulse train.

Finally, a novel modelling technique-quantum transmission line modelling (Q-TLM) method is proposed by combining quantum statistic description and photon-electron dynamic interaction process description. Q-TLM is used to establish models for quantum well and quantum dot structures and analyze the dynamic performance of ultrashort optical pulse propagation in SOAs. The Q-TLM technique provides an effective method to study semiconductor optical devices.

To my beloved parents

Acknowledgements

First and Foremost, I would like to express my sincere gratitude to my PhD supervisor, Dr. Hooshang Ghafouri-Shiraz, for his continuous kindness, encouragement and advice that enable me to achieve all my goals in my research to the best of my standard. He is a great teacher with insight and knowledge.

I hope to give my deep thanks to the time that I spent at the University of Birmingham. It is really a happy time to study in the department of Electronic, Electrical and System Engineering. Sometimes strive alone with passion and sometimes play together with freedom.

I have special thanks to Dr. Anthony Kelly for supporting my research work at the University of Glasgow. Thanks to my colleagues, M. S. Rabbani from University of Birmingham and Dr. Lianping Hou, Dr. Ding Ying from University of Glasgow for their constructive discussions and assistance. I would like to thank the colleagues who have contributed to the field of semiconductor optical lasers and amplifiers etc., which are the fundamentals for the further creation.

Finally, I am deeply grateful for the unconditional attention, encouragement and love from my parents and my grandma throughout the years; I also hope to thank my girlfriend Miao Ma for studying in the UK with me and for her patience, selfless and love. My profound love goes to them.

Birmingham, UK. August, 2016

Table of Contents

Chapter 1 Introduction....1

1.1 Evolution of semiconductor optical amplifiers....1

1.2 Ultrashort optical pulse amplification....2

1.3 Motivation of thesis work....3

1.3.1 Nonlinear effects on ultrashort optical pulse propagation in SOAs....3

1.3.2 Modelling of ultrashort optical pulse propagation in SOAs....6

1.4 Outline of thesis....7

Chapter 2 Electronic and optical properties of semiconductor optical amplifiers. 11

2.1 Introduction....11

2.2 Electronic band structure of semiconductor optical amplifiers....12

2.2.1 Band structure of quantum wells....12

2.2.2 Finite difference method for solving the Schrodinger Equation....16

2.3 Stimulated and spontaneous emissions in semiconductor optical amplifiers....17

2.3.1 Concepts of stimulated and spontaneous emissions in semiconductors....18

2. 3.2 Optical properties in spontaneous and stimulated emissions....18

2. 4 Calculation of the electronic and optical properties of QW-SOAs....23

2.4.1 Band structure calculation....23

2.4.2 Strain effects on the band structure....25

2.4.3 Analysis of QW-SOAs' optical properties....29

2.5 Conclusions....33

Chapter 3 Effects of carrier heating on optical pulse propagation in semiconductor optical amplifiers....34

3.1 Introduction....34

3.2 Modelling optical pulse propagation in SOAs based on the travelling wave rate equations....35

3.2.1 Traveling wave rate equations....35

3.2.2 Gaussian pulse amplification....36

3.3 Effects of carrier heating on the picosecond pulse amplification in quantum well semiconductor optical amplifiers....38

3.3.1 Theory of carrier heating effects in quantum well semiconductor optical amplifiers.38

3.3.2 Effects of carrier heating on the gain and spontaneous emission spectra of quantum

wells.. 41

3.3.3 Analysis of carrier heating effects on the picosecond pulse amplification in quantum well semiconductor optical amplifiers…………………….……………………………......43

3.4 Effects of carrier heating on picosecond pulse amplification in bulk amplifiers..………..47

3.4.1 Theory of carrier heating effects in bulk SOAs.. 48

3.4.2 Gain model of bulk SOAs.. 52

3.4.3 Analysis of carrier heating effects on the picosecond pulse amplification in bulk SOAs.. 53

3.5 Conclusions.. 63

Chapter 4 Theoretical investigation on optimization of semiconductor optical amplifier bias current for distortionless amplification of ultrashort pulses.............64

4.1 Introduction.. 64

4.2 Effects of different bias currents on the SOA gain recovery and pulse amplification....... 65

4.3 Evolution of optical pulse amplification along the amplifier cavity.................................68

4.4 Analysis of the optical amplfier bias current for distortionless pulse amplification.......... 69

4.4.1 Bias current as a function of distance...69

4.4.2 Optimization of the optical amplifier bias current... 72

4.5 Distortionless amplification of pulse trains...76

4.6 Conclusions.. 79

Chapter 5 Experimental investigation on optimization of semiconductor optical amplifier bias current for high speed pulse train amplification...............................80

5.1 Introduction.. 80

5.2 Experimental Investigations.. 81

5.3 Optimization of the SOA bias current..83

5.3.1 Characteristics of the SOA used in the experiment...84

5.3.2 Optimization of the SOA bias current.. 87

5.4 Relationship between SOA optimized bias current and input pulse duration, power and repetition rate...89

5.4.1 Relationship between the optimum SOA bias current and the input pulse duration...90

5.4.2 Relationship between the optimum SOA bias current and the input pulse power...... 93

5.4.3 Relationship between the optimum SOA bias current and the repetition rate of the input pulse train...95

5.5 Effects of assist light injection and temperature on SOA optimum bias current.............. 97

5.5.1 Effects of assist light injection on the SOA optimum bias current............................ 98
5.5.2 Relationship between the SOA optimum bias current and its temperature................99
5.6 Conclusions.. 100

Chapter 6 Transmission line modelling method..101

6.1 Introduction.. 101
6.2 Transmission line matrix (TLM) method...102
6.2.1 Analysis of TEM wave propagation using TLM method..102
6.2.2 Representation of lossy and lossless boundary.. 105
6.2.3 Numerical simulation for TEM waves... 106
6.4 TLM for high-frequency circuits...110
6.4.1 TLM link and stub lines... 111
6.4.2 Scattering and connecting processes in TLM..112
6.4.3 TLM for parallel RLC filter.. 113
6.5 Transmission line laser model (TLLM).. 115
6.5.1 Review of TLLM... 115
6.5.2 Disadvantages of TLLM.. 118
6.6 Conclusions.. 119

Chapter 7 Quantum transmission line modelling method......................................120

7.1 Introduction.. 120
7.2 TLM method for photon emission...121
7.3 Applications of quantum transmission line modelling method.......................................124
7.3.1 Modelling of quantum well structures..124
7.3.2 Gain model of quantum well devices..129
7.3.3 Spontaneous emission model of quantum well devices based on Q-TLM............... 135
7.4 Theoretical model of the quantum dot structure based on Q-TLM.................................138
7.5 Conclusions.. 145

Chapter 8 Application of quantum transmission line modelling to semiconductor optical amplifiers and lasers..146

8.1 Introduction.. 146
8.2 Q-TLM method for quantum well amplifiers...147
8.2.1 Model for quanum well semiconductor optical amplifiers (QW-SOAs).................. 147
8.2.2 Carrier density distribution model...148
8.2.3 Modelling of picosecond pulse propagation in QW-SOAs......................................149

8.3 Q-TLM method for quantum dot amplifiers.......... 155
8.3.1 Model for quanum dot semiconductor optical amplifiers (QD-SOAs).......... 155
8.3.2 Carrier density distribution model.......... 155
8.3.3 Modelling of femtosecond pulse propagation in quantum dot amplifiers.......... 156
8.4 Q-TLM model of quantum well lasers.......... 160
8.4.1 Description of the model.......... 160
8.4.2 Carrier transport effects in the Q-TLM laser model.......... 162
8.4.3 Analysis of quantum well lasers based on the Q-TLM method.......... 163
8.5 Conclusions.......... 171

Chapter 9 Analysis of femtosecond pulse propagation in QW-SOAs based on quantum transmission line modelling method.......... 172

9.1 Introduction.......... 172
9.2 Wavelength-dependent femtosecond pulse amplification in tapered QW-SOAs.......... 174
9.2.1 The Q-TLM model for tapered QW-SOAs.......... 174
9.2.2 Analysis of femtosecond pulse amplification in straight, exponential and linear tapered QW-SOAs.......... 177
9.3 Effects of strain on the dynamic spectrum of femtosecond pulse amplification in QW-SOAs.......... 190
9.3.1 Strain effects on the gain and spontaneous emission spectra.......... 191
9.3.2 Dynamic spectral analysis in the femtosecond pulse amplification.......... 194
9.4 Conclusions.......... 197

Chapter 10 Conclusions and Future Work.......... 199

10.1 Conclusion and Contributions.......... 199
10.2 Future work.......... 204

References.......... 206

Publication in Journals

The work in Chapter 2 and Chapter 3 of the thesis has appeared in the publications as follows:

1. **Mingjun Xia** and H. Ghafouri-Shiraz, “Analysis of carrier heating effects in quantum well semiconductor optical amplifiers considering holes’ non-parabolic density of states,” *J. Optical and Quantum Electronics*, vol. 47, no.7, pp.1847-1858, Oct. 2014.

2. **Mingjun Xia** and H. Ghafouri-Shiraz, “Theoretical analysis of carrier heating effect in semiconductor optical amplifiers,” *J. Optical and Quantum Electronics*, vol. 47, no.7, pp.2141-2153, Dec. 2014.

The work in Chapter 4 and Chapter 5 of the thesis has appeared in the following publications:

3. **Mingjun Xia** and H. Ghafouri-Shiraz, “Pump current optimization for pulse distortionless amplification in quantum well amplifiers,” *IEEE J. Lightw. Technol.*, vol. 33, no. 18, pp. 3907-3913, Sept. 2015.

4. **Mingjun Xia**, H. Ghafouri-Shiraz, Lianping Hou and A. E. Kelly, “Experimental study of SOA bias current optimization for high-speed pulse train amplification,” *OSA Journal of Applied Optics*, under review.

The work of Chapters 6-9 in the thesis has appeared in the publications as follows:

5. **Mingjun Xia** and H. Ghafouri-Shiraz, “Quantum transmission line modelling method and its application to quantum dot amplifiers,” *IEEE J. Quantum Electron.*, vol. 52, no. 5, pp. 5100107, May 2016.

6. **Mingjun Xia** and H. Ghafouri-Shiraz, “A new optical gain model for quantum wells based on quantum well transmission line modelling method,” *IEEE J. Quantum Electron.*, vol. 51, no. 3, pp. 2500108, Mar. 2015.

7. **Mingjun Xia** and H. Ghafouri-Shiraz, “A novel transmission line model of quantum well semiconductor optical amplifiers,” *J. Optical and Quantum Electronics*, vol. 48, no. 52, pp. 51-64, Jan. 2016.

8. **Mingjun Xia** and H. Ghafouri-Shiraz, “Transmission line model for strained quantum well lasers including carrier transport and carrier heating effects,” *OSA Journal of Applied Optics*, vol. 55, no. 7, pp.1518-1524, Feb. 2016.

9. **Mingjun Xia** and H. Ghafouri-Shiraz, “Wavelength-dependent femtosecond pulse amplification in wide band tapered-waveguide quantum well semiconductor optical amplifiers,” *OSA Journal of Applied Optics*, vol. 55, no. 3, pp.10524-10531, Dec. 2015.

10. **Mingjun Xia** and H. Ghafouri-Shiraz, “Analysis of strain effects on the dynamic spectra of a quantum well semiconductor optical amplifier using quantum well transmission line modelling method,” *J. Opt. Communications.*, vol. 364 pp. 60-66, Apr. 2016.

11. **Mingjun Xia** and H. Ghafouri-Shiraz, “Effects of spontaneous emission excited state lifetime on the output performance of quantum well lasers,” *J. Optical and Quantum Electronics*, under review.

Publication in Conference

The following conference paper are the related work of Chapter 7 in this thesis.

1. **Mingjun Xia** and H. Ghafouri-Shiraz, “High-performance quantum well amplifiers for the WDM system,” *the 36th IEEE Sarnoff Symposium*, New Jersey, pp. 62-65, Sept. 2015.

List of Figures

Fig. 1.1 (a) schematic diagram of bulk SOAs and quantum well SOAs (b) Electron density of states $\rho(E)$ for the bulk SOAs (dashed line) and quantum well SOAs (solid line)........................5

Fig. 2.1 Schematic diagram of stimulated and spontaneous emission processes, E_1 and E_2 are the energies of excited state and ground state..18

Fig. 2.2 Energy band structure of a compressively strained QW-SOA (a) conduction band structure (b) valence band structure..25

Fig. 2.3 Schematic diagram of conduction and valence bands energy distributions under (a) compressive strain, (b) no strain and (c) tensile stain..26

Fig. 2.4 Electron effective mass of $In_{1-x}Ga_xAs$ the blue and the green line are the mass in the growth direction and the in-plane mass, the red line shows the electron effective mass without considering the direction..27

Fig. 2.5 Conduction band structures of three strained $In_{1-x}Ga_xAs$ - $InGaAsP$ quantum wells.......27

Fig. 2.6 First three valence bands (HH band, HL band and SO band) of three strained $In_{1-x}Ga_xAs$ - $InGaAsP$ quantum wells (a) $x=0.40$ (b) $x=0.47$ (c) $x=0.59$ 29

Fig.2.7 Momentum matrix element of $In_{1-x}Ga_xAs$ - $InGaAsP$ QW-SOAs..................................29

Fig. 2.8 Modal gain spectrum of a compressively strained QW-SOA..................................30

Fig. 2.9 The $qL_z r_{sp}(\hbar\omega)$ spectra in a compressively strained QW-SOA..................................31

Fig. 2.10 The differential gain spectra of a compressively strained QW-SOAs..............................31

Fig. 2.11 Linewidth enhancement factor of a compressively strained QW-SOAs..........................32

Fig. 3.1 Division of the amplifier cavity into m small sections to analyse the optical pulse propagation in SOAs using the step transition method..37

Fig. 3.2 Modal gain spectra of TE mode in a compressively strained QW-SOA at different temperatures..42

Fig.3.3 The spontaneous emission spectra of a compressively strained QW-SOA at different temperatures…………………………………………………………...........……………...…...43

Fig. 3.4 QW-SOAs picosecond pulse amplification (input peak value $10mw$) with and without carrier heating effects………………………………………………………………………......45

Fig.3.5 QW-SOAs picosecond pulse amplification (input peak value $100mw$) with and without carrier heating effects……………………………………………………...…………...……46

Fig.3.6 Average carrier temperature of the amplifier cavity in the picosecond pulse amplification process with the input peaks $10mw$ and $100mw$ ……………………………………………......47

Fig. 3.7 Variations of the average material gain coefficient with the propagation time within the cavity during the pulse amplification process in a bulk SOA…………......…………………...…56

Fig. 3.8 Variations of the average carrier density with the propagation time within the cavity during the pulse amplification process in a bulk SOA…………………………………………...…56

Fig. 3.9 Variations of material gain coefficient and carrier temperature near the exit facet of the amplifier cavity……………………………………………………………………….…….57

Fig.3.10 Picosecond pulse amplification in SOA with and without carrier heating effects ($Peak = 10mw$)…………………………………………………………………………….…58

Fig.3.11 Picosecond pulse amplification in SOA with and without carrier heating effects ($Peak = 100mw$)……………………………………………………………….……………...59

Fig.3.12 Variation of the carrier temperature near the exit facet of the amplifier cavity during the pulse amplification for the two different input signals 59

Fig.3.13 Variation of the carrier temperature near the exit facet of the amplifier cavity during the pulse amplification with different pump currents……………………………………......……...60

Fig. 3.14 The amplified 80Gbit/s picosecond pulse train output both in the presence (blue) and absence (green) of the carrier heating effect (red)……………………..................……………..61

Fig. 3.15 Variations of modal gain of the amplifier near the exit facet when a Gaussian pulse train at 80Gbit/s is applied to the amplifier input both in the presence (blue) and absence (green) of the carrier heating effect……………………………................………………………….…...……62

Fig. 4.1 The pump input temporal waveform of the unchirped Gaussian optical pulse……....…66

Fig. 4.2 Gain recovery of the SOA at two different bias currents……………………...…...…67

Fig. 4.3 Picosecond pulse amplification at different bias currents……………………...…...…68

Fig. 4.4 Evolution of an unchirped Gaussian input pulse inside the strained $In_{0.64}Ga_{0.36}As$ - $InGaAsP$ quantum well semiconductor optical amplifier's cavity...…………….........………....69

Fig. 4.5 Variations of the bias current with maximum distance Z_m …………………….....……..71

Fig. 4.6 Curve fitting results of the amplifier bias current with maximum distance Z_m ……..…...72

Fig. 4.7 The amplified distortionless output pulse obtained at the optimum bias current..……..…73

Fig. 4.8 Variations of γ in the vicinity of optimum bias current $I_m = 29.86mA$ ………..................74

Fig. 4.9 The optimized bias current I_m versus peak power P_{in} ………………...………………......76

Fig. 4.10 Gain recovery of the QW-SOA……………………………….………………………...…77

Fig. 4.11 The $14Gb/s$ amplified output pulse train at proposed optimized bias current.……........78

Fig. 4.12 The $28Gb/s$ amplified output pulse train at proposed optimized bias current…........…79

Fig. 5.1 Experimental system used to measure high-speed pulse train amplification in a SOA (a) Block diagram (b) Experimental setup……………………………..........................……....83

Fig. 5.2 Auto-correlation response during $320ps$ time interval...……...84

Fig. 5.3 SOA characteristics curves (a) output power (b) voltage of the amplifier active region.....86

Fig. 5.4 SOA spontaneous emission spectrum at the bias current $120mA$ (a) forward (b) backward……………………………………………………………………...……....……….87

Fig. 5.5 Variations of the duration of SOA amplified output pulse at different bias currents for input pulse duration of $1.37 ps$ ……………………………………..........................……..……..88

Fig. 5.6 Variations of the SOA gain at different bias currents for input pulse duration of

$1.37\,ps$ ………………………………………...……..……88

Fig. 5.7 Variation of the pulse duration of the SOA input pulse train with the pump current of EDFA-1…………………...…90

Fig. 5.8 Schematic diagram of the input pulse train with fixed power and different pulse durations……………………………..…91

Fig. 5.9 Pulse duration of amplified output pulse train vs SOA bias currents at different SOA input pulse durations (a) $1.60\,ps$ (b) $1.89\,ps$ (c) $2.39\,ps$ (d) $2.79\,ps$ ……….................................…...92

Fig. 5.10 Variations of the SOA optimum bias and gain at the different SOA input pulse durations……………………………………………………………………………..................……93

Fig. 5.11 Variation of SOA input pulse train duration at different optical attenuation values…………………………………………………………………………….........................94

Fig. 5.12 Variations of the optimum SOA bias currents and gain at the different attenuation levels……………………………………………………...95

Fig. 5.13 Variations of the SOA optimum bias current and gain with the applied input pulse train repetition rate…………………………...…96

Fig. 5.14 Schematic diagram of the experimental system for high-speed pulse train amplification with the assist light injection…………………………………………….............................97

Fig. 5.15 SOA gain recovery at different amplifier bias currents……………………........……...…97

Fig. 5.16 Variations of the SOA optimum bias currents with different pulse train repetition rates both in the presence and absence of the assist light……………………...............................…98

Fig. 5.17 Variations of SOA optimum bias currents with its temperatures……….....................…100

Fig. 6.1 Cartesian mesh of transmission lines used in discretized Huygen's wave model……...103

Fig. 6.2 (a) Incident impulse at the node n (b) Reflection impulse at the node n (c) the reflected impulse becomes the incident impulse at the adjacent node………......................................…103

Fig. 6.3 Schematic diagram of transmission matrix boundaries (blue and black dashed lines represent the mesh and boundaries, respectively)………………........................………………105

Fig. 6.4 Equivalent lumped-element model of a 2-dimensional TLM network (a) TLM network, (b) its equivalent LEM………...…107

Fig. 6.5 Transmission rectangular mesh used for simulation of TEM wave impedance…………109

Fig. 6.6 Gain curve model in TLLM…………………………………………………..…....…116

Fig.7.1 Q-TLM photon emission model (a) RLC circuit model (b) transmission line model with voltage input and (c) transmission line model with the electric filed input……………….….…..122

Fig. 7.2 The proposed QW-TLM unit of a quantum well device………..…………………...…...125

Fig. 7.3 Voltage propagation process in the stub filter…………………………………........…126

Fig. 7.4 Thevenin equivalent circuit of the stub filter……………………………….........……127

Fig. 7.5 Gain spectra of the strained $In_{0.64}Ga_{0.36}AS / InGaAs$ quantum well both in the presence and absence of spin-orbit split-off band electron transition……………....……………………...130

Fig. 7.6 Gain model of quantum well devices based on QW-TLM………………..………..…131

Fig. 7.7 Normalized gain spectra of a compressively strained $In_{0.64}Ga_{0.36}AS / InGaAs$ quantum well device (i) analytical (green) and QW-TLM (blue) methods…………………………………134

Fig. 7.8 Spontaneous emission model of a quantum well device based on QW-TLM…………...136

Fig. 7.9 Computation of the normalized spontaneous emission spectra of a compressively strained $In_{0.64}Ga_{0.36}AS / InGaAs$ quantum well SOA using (i) analytical (blue) and (ii) QW-TLM (green) methods………...…...138

Fig. 7.10 QD-TLM unit structure…………………………………………………..………..139

Fig. 7.11 Structure of one section of QD-TLM model (a) forward and (b) backward directions...140

Fig. 7.12 The stimulated emission module…………………...........................……………141

Fig.7.13 Spontaneous emission model of a quantum dot device……......................................…...143

Fig. 7.14 Quantum dot normalized (a) gain and (b) ASE spectra computed by both Q-TLM and analytical methods at carrier density $8.3\times10^{14} cm^{-3}$ ………………………………............……144

Fig. 8.1 The Q-TLM model for the QW-SOA……………….........................……………....147

Fig. 8.2 Gaussian pulse input (a) temporal waveform (b) power spectral density……………..…...151

Fig. 8.3 Amplified output waveform of a Gaussian input pulse with the peak power of $0.1mw$ (a) temporal waveform (b) power spectral density……………………...............……………………….152

Fig. 8.4 Amplified outputs of a Gaussian pulse with the peak power value $1mw$ (a) temporal waveform (b) power spectral density……………………………………………………………......154

Fig. 8.5 Scheme diagram of QD amplifiers. The quantum dot amplifier consists of a six-layer quantum dot active region and two cladding layers. The materials for the quantum dots, wells and the material for the quantum dot is $InGa$ while the materials for the wells and barriers are $InGaAs$ and $GaAs$, respectively…………………………………………........................…..…156

Fig. 8.6 Temporal evolution of an input femtosecond pulse along the amplifier cavity obtained by the proposed Q-TLM method…………………………....……………………………………159

Fig. 8.7 Spectra evolution of an input femtosecond pulse along the amplifier cavity obtained by the Q-TLM method…………………………………………………………………………...........159

Fig. 8.8 Carrier density distribution along the amplifier cavity when the peak power of the input femtosecond pulse is $1mW$ ……………………………………………………...…………..…160

Fig. 8.9 The proposed Q-TLM model for quantum well laser……………………............…...161

Fig. 8.10 Electric field flow for a laser facet model…………………………………...……....161

Fig. 8.11 Power-current characteristics of a $340\mu m$ long quantum well laser……………........165

Fig. 8.12 Turning-on transients of strained QW lasers without (blue) and with (green) carrier transport effect………………………………………………………………………………….…...166

Fig. 8.13 Output power spectral density at the steady state both in the presence (green) and absence (blue) of the carrier transport……………......……………………………………………...…..167

Fig. 8.14 Output power spectral density in the presence of the carrier transport. at the oscillation process (blue, around $37.9ps$) and the steady state (green , i.e. $t > 100ps$)…………………….…..168

Fig. 8.15 Turning-off transients of QW lasers both in the presence (green) and absence of the transport effect…………………………………………………....................…………....…169

Fig. 8.16 Impulse bias current……………………………………………………………………170

Fig. 8.17 Effect of impulse bias current on the laser output spectra…………………………….170

Fig. 9.1 Schematic diagram of the active regions of different tapered QW-SOAs (a) rectangular (b) exponential (c) linear...……………………………………………..173

Fig. 9.2 The proposed Q-TLM model for a tapered waveguide QW-SOA……….......................175

Fig. 9.3 Temporal waveforms of the amplified output pulse in the Con, ET and LT QWAs…....179

Fig.9.4 Power spectral density of the amplified output pulse in the conventional, exponential and linear tapered QWAs………………………………………...……………………….....……180

Fig.9.5 Amplification of femtosecond pulse propagation along the QWA cavity (a) conventional (b) exponential taper and (c) linear taper……………….............................………………………...181

Fig. 9.6 Power spectral density evolution of a femtosecond pulse propagation along the QWA cavity (a) conventional (b) exponential taper and (c) linear taper……………………………......182

Fig.9.7 Temporal outputs of the amplified femtosecond pulse in the tapered QW amplifiers with and without taking into account the effects of lateral carrier density.………………...…...….…185

Fig.9.8 Output power spectral density waveforms of two simultaneously amplified femtosecond pulses in the three different structures with the three different peak power values of the input pulses (a) 0.5mW, (b) 2mW and (c) 8mW…………………………………......……………………...187

Fig. 9.9 Temporal waveform of the input pulse train……………………………………………188

Fig. 9.10 Temporal output waveforms of the amplified femtosecond pulse train in the QWA (a) conventional (b) exponential taper and (c) linear taper……………………………....………..190

Fig. 9.11 Normalized gain spectra of QW amplifiers for three strain cases at carrier density of $8\times10^{24}m^{-3}$ obtained by the scattering module in the Q-TLM model……………….................192

Fig. 9.12 Normalized spontaneous emission spectra of QW amplifiers for three strain cases at the carrier density of $8\times10^{24}m^{-3}$ obtained by the spontaneous emission source in the Q-TLM model…………………………………………………………………………...................…....193

Fig. 9.13 Normalized gain spectra of the compressively strained(CS) QW amplifier at three different carrier densities obtained by the scattering module in the QW-TLM model…………...193

Fig. 9.14 Evolution of the amplified pulse spectra waveforms along 4 different positions of a compressively strained QW amplifier cavity………………………………………………........194

Fig. 9.15 Variations of carrier densities in a compressively strained QW amplifier at different distances along the amplifier cavity……………………………………….........................…195

Fig. 9.16 Output spectra of the amplified femtosecond pulse (a) CS, (b) US and (c) TS……......196

List of Tables

Tab. 2.1 Material parameters of quantum well……………………………………………………24

Tab. 3.1 Modelling parameters of QW-SOAs…………………………………………………….44

Tab. 3.2 SOA parameters for studying carrier heating effects……………...…………………..54

Tab. 4.1 Data for the coefficient calculation……………………………………………………70

Tab. 4.2 Coefficient values and fitting effect…………………………………………………...72

Tab. 4.3 Optimized bias currents and amplifier gains at different input peak powers………….74

Tab. 6.1 Numerical calculation of the intrinsic impedance Z ………………………………...110

Tab. 7.1 Parameters used in calculation of gain spectral of strained $In_{0.64}Ga_{0.36}AS / InGaAs$ quantum well device…………………..134

Tab. 8.1 Parameters used in the analysis of pulse amplification..........................…………...149

Tab. 8.2 Parameters used in the analysis of femtosecond pulse amplification in QD-SOAs….157

Tab. 8.3 Simulation parameters for quantum well lasers…………………………………...163

Tab. 8.4 Four stages in the ToT with and without carrier transport effect.......................……166

Tab. 8.5 Output spectral parameters with and without bias current spike…………………….170

Tab. 9.1 Simulation parameters for three kinds of QW-SOAs ……………………………….177

Tab 9.2 Characteristic parameters of dynamic spectra………………………………………...183

Tab. 9.3 Output peak powers for different waveguides and input powers…………………….187

Tab. 9.4 Parameters used in the analysis of strain effects……………………………………..191

List of Abbreviations

AE	Analytical expression
ASE	Amplified spontaneous emission
CHE	Carrier heating effect
CS	Compressively strained
CTE	Carrier transport effect
CUT	Compressively strained, unstrained and tensile strained
CW	Continuous wave
DCA	Digital communication analyzer
EDFA	Erbium-doped fiber amplifier
EFRC	Electric field reflection coefficient from the cavity to cavity
EFTC	Electric field transmission coefficient from cavity to air
ET	Exponential tapered
ETW	Exponential tapered waveguide
LTW	Linear tapered waveguide
FFT	Fast Fourier Transform
FWHM	Full width at half maximum
HH	Heavy hole
IBC	Impulse bias current
LEM	Lumped-element model
LH	Light hole
LT	Linear tapered

MBE	Molecular beam epitaxy
MOCVD	Metal organic chemical vapor deposition
OSA	Optical spectrum analyzer
QD	Quantum dot
QD-SOA	Quantum dot semiconductor optical amplifier
QD-TLM	Quantum dot transmission line modelling
Q-TLM	Quantum transmission line modelling method
QW	Quantum well
QWA	Quantum well amplifier
QW-TLM	Quantum well transmission line modelling
QW-SOA	Quantum well semiconductor optical amplifier
RF	Radio frequency
RLC	Resister, inductor and capacitor
SCH	Separate confinement heterostructure
SE	Stimulated emission
SLSR	Side lobe suppression ratios
SO	Spin-orbit spilt-off
SOA	Semiconductor optical amplifier
TE	Transverse electric
TEM	Transverse electromagnetic
TL	Transmission line
TLM	Transmission line matrix
TLLM	Transmission line laser modelling
TM	Transverse magnetic

TOT	Turning-on transients
TS	Tensile strained
TW	Tapered-waveguide
US	Unstrained

Chapter 1

Introduction

1.1 Evolution of Semiconductor Optical Amplifiers

Semiconductor optical amplifiers (SOAs) stem from the investigations of semiconductor optical lasers. After semiconductor injection lasers were demonstrated in 1962 [1-2], scientists began to pay attention to the similar structure-semiconductor optical amplifiers. The initial SOAs was made of $GaAs/AlGaAs$ material and had to work at low temperature near the $830nm$ wavelength window [3-4]. The employment of double heterojunction semiconductor structures enabled SOAs to work at room temperature [5-6]. In the 1980s, InP - $InGaAsP$ material was employed to fabricate SOAs in order to extend their operation wavelength to $1300nm$ and $1500nm$ windows [7] where optical fibre loss is very low at these operating wavelength windows. Prior to 1989, SOA structures were based on the anti-reflection coated laser diodes which have asymmetrical waveguide structures leading to strong polarization sensitive gain [8]. In 1989, SOAs began to be designed as a semiconductor device with symmetrical waveguide structure to reduce polarization sensitivity [9]. As the fabrication technique, especially the molecular beam epitaxy (MBE) and metal organic chemical vapor deposition (MOCVD), rapidly develops [10-11], SOAs attract more attention in the optical fibre communications and all-optical signal processing. Recently, development of SOAs is on going with particular interests in (i)

high-performance amplification which includes high gain, low loss and low noise for different applications in optical fibre communication system and (ii) photonic integrated circuits with special functions, such as switching and wavelength conversion [9].

1.2 Ultrashort Optical Pulse Amplification

Ultrashort (picosecond and femtosecond) optical pulse amplification has close relation with the research fields of optical fibre communication, ultrafast optics and quantum computing [12-14]. The generation of ultrashort optical pulses has opened the door of ultrafast optical technique. In 1961, a pulse with the duration of around $10ns$ was produced by means of a Kerr-cell shutter [15], which results in the initial development of pulse lasers. In 1966, the duration of the pulse obtained by a passive mode locking laser arrived in the picosecond timescale [16]. The first femtosecond pulse was obtained by Shank and Ippen in 1974 [17] while these femtosecond pulse generation systems are complicated and unstable. The era of femtosecond pulse came with the application of additive pulse mode locking [18] and Kerr-lens mode locking [19]. Although the duration of pulse has become very short, one drawback of the ultrashort pulse source is that their output power is low, which limits the application of ultrashort pulse laser in the medical detection, fibre optical communications and physical process analysis [20-22]. Therefore, we need to choose suitable means to boost the output power of ultrashort pulse laser. One way is to adopt erbium doped fibre amplifier (EDFA), which was invented in 1985 [9]. The invention of EDFA brought a revolution in optical communications as it made possible the optically transparent networks and thereby overcome the 'electronic bottleneck'. EDFAs become attractive for the reason that they can amplify the light signal with high gain, low insertion loss, low noise figure and negligible nonlinearities [23]. However, fibre-based amplifiers

also have their own disadvantages, such as large size, difficult to be integrated and external laser for pumping [9]. Semiconductor optical amplifiers are another choice for the amplification of ultrashort optical pulse. Compared with EDFAs, SOAs have the advantages of small size, direct current pump, cost-effective and easy to be integrated [24-26]. As the fabrication technology rapidly develops, SOAs become a promising candidate for optical signal processing, silicon photonic integration circuits and these functions can't be realized by EDFA. Recently, ultrashort optical pulse amplification has become of significant importance in the applications based on ultrafast optics, such as high harmonic generation, femto-chemistry, ultrafast nonlinear spectroscopy, coherent quantum control, laser surgery and optical frequency comb [27-32]. The timescale over which the pulses interact with matter is very short allows us to control atomic or molecular systems independently from processes such as heat, phase transitions and relaxation processes. Besides, the amplified ultrashort pulse can concentrate large amounts of photons in a short timescale, which give access to ultra-intense electric fields. With all the applications comes the need for understanding, analysing and controlling the ultrashort optical pulse propagation in semiconductor optical amplifiers.

1.3 Motivation of Thesis Work

1.3.1 Nonlinear Effects on Ultrashort Optical Pulse Propagation in SOAs

The above mentioned advantages of SOAs have attracted researchers' attention. However, the propagation of ultrashort optical pulse signal in SOAs suffers from distortion due to the gain saturation mechanism. Moreover, the nonlinear effect induced by carrier heating imposes a further constrain on the gain dynamics [33-35]. The nonlinear gain in semiconductor optical amplifiers (SOAs) was studied for various applications [36-39]. The

basic mechanisms responsible for carrier heating effects are carrier injection, non-radiative recombination, free carrier absorption, stimulated emission and spontaneous emission [40]. Carrier heating effects maintain electrons and holes at a different temperature with the lattice. Temperature changes lead to the different Fermi-Dirac distributions in the conduction and valence bands. This causes gain suppression in the optical pulse amplification. Accurate calculation of this effect enables us to better analyse the gain dynamics during the optical pulse amplification process. J.M. Dailey et al. [41-42] experimentally illustrated the impact of carrier heating on the dynamic recovery process of SOAs. Their experimental results show that the carrier heating not only induces the suppression of material gain but also can accelerate the carrier dynamic recovery. However, in these reported studies the effects that carrier heating has on the performance of amplifiers have not been theoretically described in details. In bulk SOAs, the distribution of energy band structure is continuous while in quantum well semiconductor optical amplifiers (QW-SOAs), the distribution of energy band structure is discontinuous and due to the strong coupling among heavy hole (HH) bands, and light hole (LH) bands as well as spin-orbit split-off bands, the valence band structure is non-parabolic. These determine that the theoretical descriptions of carrier heating effects in bulk and quantum well SOAs are different. The Fermi-Dirac approximation cannot be adopted to analyse carrier heating effects in QW-SOAs. Figure 1.1 shows the schematic diagram of bulk and quantum well SOAs and the corresponding electron density of states in the two structures.

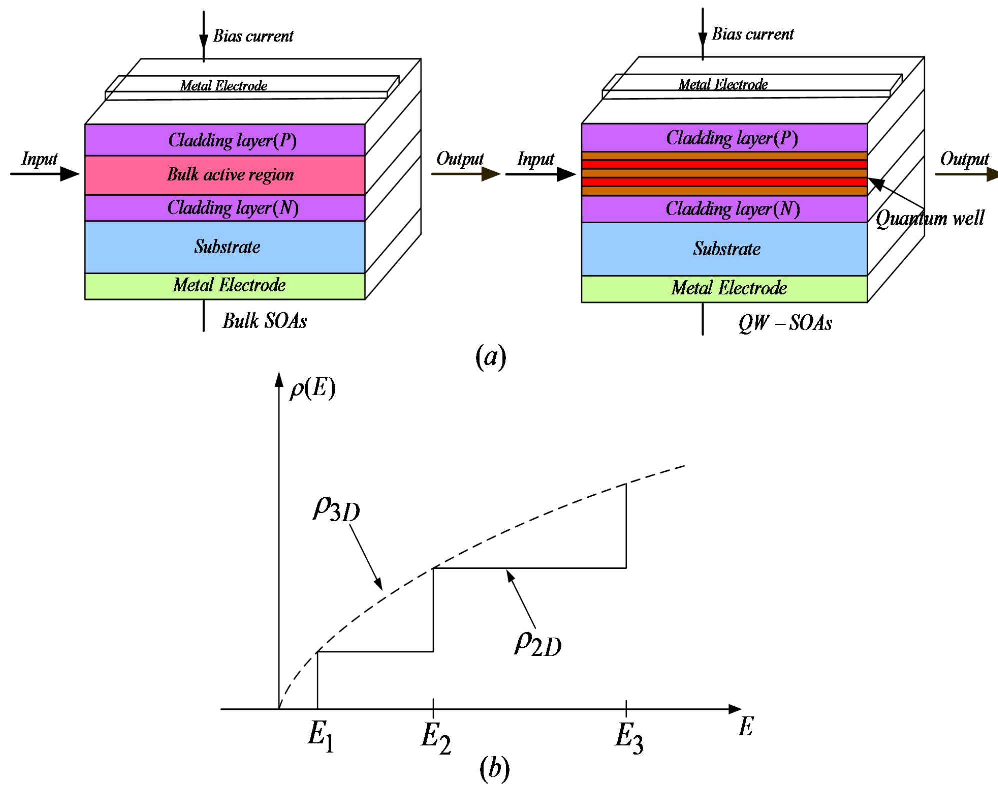

Fig. 1.1 (a) Schematic diagram of bulk SOAs and quantum well SOAs (b) electron density of states $\rho(E)$ for the bulk SOAs (dashed line) and quantum well SOAs (solid line) [9].

Semiconductor optical amplifiers suffer from the gain saturation, which leads to distortion when ultrashort optical pulse is amplified. Distortions of pulse amplification induced by the gain saturation in SOAs were theoretically and experimentally analysed [35, 43-45]. Some methods have been proposed to improve the gain dynamics, including optimizing the structure of SOAs [46-47], injecting the assist light [48] and doping the barrier region in QWs [49]. These measures can effectively accelerate the gain recovery of SOAs rather than totally remove the distortion of amplified output pulse. When a peak temporal shift exists in an amplified pulse the time interval between two peaks of the adjacent amplified pulses varies. This variation needs to be eliminated in order for the amplifier to handle the synchronous clock signal in the optical signal processing and optical fibre communication system [37, 50-52]. It is expected that an optical amplifier amplifies the input pulse with

high gain while producing no peak temporal shift. Experimental results have shown either distortionless pulse amplification or temporal pulse distortion which depends on the amplifier's construction and operating conditions. The bias current is one important factor that determines the amplifier gain and influences the distortion of amplified pulse. The bias current needs to be adjusted for distortionless pulse amplification in SOAs. This is because if the bias current is too high, the amplified output pulse suffers from distortion and if it is too low the amplifier gain reduces, which limits the amplification ability of the SOA. Therefore it is necessary to understand the relationship between the bias current and the amplified output pulse distortion in order to realize high gain distortionless pulse amplification in SOAs.

It is also important to realize the free-distortion amplification when SOA is adopted to merge the multi-channel high-speed pulse trains [53]. For the generation of high repetition rate pulse trains, merging the pulse trains from the multiple channels each of which is amplified by SOA has become a promising method. However, the inconsistency in the amplified output pulse trains of the multiple channels, especially the difference in the pulse duration affects the performance of high repetition rate pulse source. The pulse amplification in semiconductor optical amplifiers has been theoretically analysed using the rate equations [54] and the systematical analytical method [55]. However, these theoretical analyses have made assumptions to obtain the analytic solutions or to aid the numerical computation, which has restricted the accuracy of the simulation results. There are no detailed experiments to investigate the SOA optimized bias current for the high-speed ultrashort pulse train amplification.

1.3.2 Modelling of Ultrashort Optical Pulse Propagation in SOAs

Accurate models are required to predict and analyse the propagation of ultrashort optical pulse in semiconductor optical amplifiers. A complete model with the ability to analyse the dynamic spectra under modulation is essential to study semiconductor optical amplifiers. To date, many models have been reported in literature for analysing the performance of SOAs [56-59]. In these models, either the amplifier's gain is considered to be frequency independent or the input signal is fixed at a certain frequency. However, the optical signal that applies to the input of an amplifier has a large bandwidth and also the spectrum of the amplified optical signal during the propagation are changing dynamically which clearly indicates that the existing models are difficult to accurately study the dynamic spectrum of amplified signal in amplifiers.

Transmission line matrix (TLM) method is first successfully applied to analyse the characteristics of microwave circuits [60]. In ref [61], A. J. Lowery established the bulk laser model based on TLM, which adopted the response of one stub filter to represent the whole gain spectrum of the bulk laser diode. Since then, the laser transmission line modelling method was used to simulate both lasers and laser amplifiers [62-63]. Compared with other modelling methods, the merits of using TLM to model semiconductor optical devices are that TLM can provide continuous spectrum and easily simulate the integrated system which saves the computation time [64-66]. However, the reported models based on TLM only used the spectral response of one RLC stub filter to approximate the whole gain spectrum of lasers or amplifiers and ignore the dynamic photon-electron interaction. These determine that TLM can't accurately analyse and describe the optical processes in semiconductor optical devices.

1.4 Outline of Thesis

The organisation of the thesis is as follows:

Chapter 2 introduces the fundamental physics of semiconductor optical amplifiers. The electronic and optical properties of semiconductor optical amplifiers are analysed. The band structure and the electron wave function are calculated by solving the Schrodinger equation using the finite difference method. The stimulated and spontaneous emission processes in semiconductor optical amplifiers are physically described. The optical properties, such as the gain spectrum, spontaneous spectrum and the refractive index etc. are studied.

Chapter 3 is dedicated to study effects of carrier heating in bulk and quantum well semiconductor optical amplifiers. A new analytical method for carrier heating effects in bulk SOAs is proposed by combining the Fermi-Dirac integral of 3/2 order and 1/2 order while for the quantum well SOAs, the numerical method for calculating the carrier heating effects is proposed, which considers the strong coupling among the HH band, LH band and SO band. Effects of carrier heating on the picosecond pulse amplification in bulk and quantum well SOAs are investigated based on the proposed theoretical methods.

Chapter 4 proposes a new bias current optimization method for distortionless ultrashort pulse amplification. A new function which relates the amplifier bias current with the maximum distance along the amplifier cavity where the amplified pulse is ditortionless is reported in order to optimize the SOA bias current and achieve ditortionless pulse amplification at high gain. The relation between the optimized bias current and the parameters of the input pulse train are investigated. Furthermore, in Chapter 5, the optimized bias current for ultrashort pulse amplification is experimentally investigated in details. As the SOA bias current decreases from the high level (more than the saturated level) to the low level, the pulse duration of the amplified output pulse is measured and analysed. In order to realize high gain and low distortion amplification of the high-speed

input pulse train, the SOA optimized bias current is defined based on the changes of the pulse duration of the amplified output pulse with the SOA bias currents. The relation between the SOA optimized bias current and the parameters of the SOA input pulse train are also experimentally studied. The effects of assisted light injection and different temperatures on the SOA optimized bias current are also discussed.

The transmission line matrix method, based on which the TEM wave propagation in the bounded and unbounded space is reviewed in Chapter 6. The wave impedance in a rectangular waveguide is obtained based on transmission line matrix method and the calculation results are compared with the results obtained by the analytical expression. Also, the microwave circuit techniques for modelling the semiconductor lasers are introduced and the previous transmission line modelling method for modelling the laser diode is reviewed. The disadvantages of transmission line laser modelling method are also discussed.

Chapter 7 proposes a new modelling technique hereby referred to as quantum transmission line modelling method (Q-TLM), which is obtained by combining the quantum statistic and photon-electron interaction process descriptions. Detailed studies are done to show how to use the new modelling method to establish gain and spontaneous emission models for quantum well and quantum dot structures. The simulation results obtained by quantum transmission line modelling method are compared with those obtained by the analytical model.

In Chapter 8, Q-TLM is adopted to establish theoretical models for quantum well/dot amplifiers and lasers and the newly proposed model is used to analyse performances of quantum well amplifiers and lasers in both time and frequency domains. Furthermore, picosecond and femtosecond pulse amplifications are analysed in quantum well and dot

amplifiers, respectively. Chapter 9 reports the Q-TLM-based investigations of wavelength-dependent femtosecond pulse propagation in conventional straight waveguide, exponentially tapered waveguide and linearly tapered waveguide quantum well amplifiers and the effects of strain on the femtosecond pulse amplification in quantum well semiconductor optical amplifiers.

Finally, the thesis is concluded in Chapter 10. The important results and contributions are given as well as relevant future research topics are proposed.

Chapter 2

Electronic and Optical Properties of Semiconductor Optical Amplifiers

2.1 Introduction

The understanding of the basic electronic and optical properties of semiconductor optical amplifiers is significantly important to analyse optical signal propagation in semiconductor optical amplifiers. As the introduction of quantum theory in 1900 when Planck first proposed that the energy of electromagnetic waves is quantized [67], the description of light-matter interaction in semiconductors has been an intriguing subject. The general mechanism for explaining the light-matter interaction includes stimulated emission, spontaneous emission and absorption, all of which are based on the analysis of the electronic band structure of semiconductors. Band structure including the conduction and valence bands describe the energy range of an electron within the solid. Knowledge of the discontinuities of the conduction and valence bands is essential to further investigate the optical properties of semiconductor optical amplifiers.

Considering that most work in this thesis has focused on the optical signal propagation in QW-SOAs, in this chapter, the electronic properties of quantum wells, including band structure and electron wave functions are numerically calculated by solving the

Hamiltonian Schrodinger equations. Based on the calculation of band structure, the optical properties of QW-SOAs, such as matrix element, stimulated emission spectrum, spontaneous emission spectrum, differential gain and linewidth enhancement factor are analysed. The optical properties of semiconductor optical amplifiers are necessary to be obtained in order to be able to describe the optical signal propagation in semiconductor optical amplifiers. Moreover, these parameters can be used to evaluate the performance of semiconductor optical amplifiers.

The introduction of strain could be a powerful tool to modify band structures of semiconductors in a predicable way [68]. The existing theoretical and experimental works have confirmed the strained quantum well semiconductor optical amplifiers have more superior characteristics as compared with the unstrained SOAs [68-69]. Strain can effectively tune the gain and spontaneous emission spectrum of SOAs by modifying the conduction and valence bands. The strain effects on the band structure of SOAs are analysed in this chapter.

2.2 Electronic Band Structure of Semiconductor Optical Amplifiers

2.2.1 Band Structure of Quantum Wells

For the III-V direct bandgap semiconductors, the strained conduction band can be characterized by the following parabolic band model [70]:

$$H^c(k) = (\frac{\hbar^2}{2})(\frac{k_t^2}{m_{e,t}} + \frac{k_z^2}{m_{e,z}}) + V_c(z) + a_c Tr(\bar{\varepsilon}) \quad (2.1)$$

where, $\hbar$ is the Plank constant divided by 2π , $k_t^2 = k_x^2 + k_y^2$ is in-plane wave vector (k_x *and* k_y are wave vectors in the transverse plane), k_z is the wave vector in the growth direction, $V_c(z)$ is the potential energy of the unstrained conduction band edge, a_c is the

hydrostatic deformation potential for the conduction band, and $Tr(\bar{\varepsilon}) = \varepsilon_{xx} + \varepsilon_{yy} + \varepsilon_{zz}$ is the fractional volume change ($\varepsilon_{xx}, \varepsilon_{yy}$ *and* ε_{zz} are defined below), $m_{e,t}$ and $m_{e,z}$ are the electron effective masses perpendicular and parallel to the growth direction. For the strained lattice case where a strained-layer semiconductor grows on the substrate z-axis, the strain is described as [71]:

$$\varepsilon_{xx} = \varepsilon_{yy} = \frac{a_0 - a}{a} \tag{2.2}$$

$$\varepsilon_{zz} = -\frac{2C_{12}}{C_{11}}\varepsilon_{xx} \tag{2.3}$$

$$\varepsilon_{xy} = \varepsilon_{yz} = \varepsilon_{zx=0} \tag{2.4}$$

where, a_0 and a are the lattice constants of the substrate and the epitaxial material, C_{11} and C_{12} are the stiffness constants. The conduction band structure $E_n^c(k_t)$ is obtained by solving the following Schrodinger equation [70]:

$$H^c \phi_n(z;k_t) = E_n^c(k_t)\phi_n(z;k_t) \tag{2.5}$$

where, H^c is the Hamiltonian for the conduction band, $\phi_n(z;k_t)$ is the envelope function of the *nth* conduction subband and $E_n^c(k_t)$ is the conduction band energy dispersion. The solution of Eq. (2.5) at $k_t = 0$ can be obtained using the finite difference method [70]. Assuming the parabolic distribution, we can obtain the whole conduction band structure using the following expression [70]:

$$E_n^c(k_t) = E_n^c(k_t = 0) + \frac{\hbar^2 k_t^2}{2m_{e,t}} \tag{2.6}$$

$$\phi_n(z;k_t) = \phi_n(z;k_t = 0) \tag{2.7}$$

The band structure of the valence band can be determined by solving the following equation [70]:

$$\sum_{j=HH,LH,SO} H^{\sigma}_{3\times3,ij}(k_z = -i\frac{\partial}{\partial z})g^{\sigma}_{m,j}(z;k_t) = E^{\upsilon}_{\sigma,m}(k_t)g^{\sigma}_{m,i}(z;k_t) \quad (2.8)$$

where, $H^{\sigma}_{3\times3,ij}$ is the Hamiltonian in the valence band, $g^{\sigma}_{m,j}$ is the mth hole envelope function and $E^{v}_{\sigma,m}$ is the mth valence subband energy dispersion. The Hamiltonian in the valence band is obtained by transforming the 6×6 Hamiltonian into the block-diagonalized expression [72]:

$$H^{v}(k) = \begin{bmatrix} H^{U}_{3\times3}(k) & 0 \\ 0 & H^{L}_{3\times3}(k) \end{bmatrix} \quad (2.9)$$

$$H^{\sigma}_{3\times3} = -\begin{bmatrix} P+Q-V_h(z) & R_k \mp iS_k & \sqrt{2}R_k \pm \frac{i}{\sqrt{2}}S_k \\ R_k \pm iS_k & P-Q-V_h(z) & \sqrt{2}Q \pm i\sqrt{\frac{3}{2}}S_k \\ \sqrt{2}R_k \mp \frac{i}{\sqrt{2}}S_k & \sqrt{2}Q \mp i\sqrt{\frac{3}{2}}S_k & P+\Delta(z)-V_h(z) \end{bmatrix} \quad (2.10)$$

where,

$$P = P_k + P_\varepsilon, \qquad Q = Q_k + Q_\varepsilon \quad (2.11)$$

$$P_k = (\frac{\hbar^2}{2m_0})\gamma_1(k_t^2 + k_z^2), \quad Q_k = (\frac{\hbar^2}{2m_0})\gamma_2(k_t^2 - 2k_z^2) \quad (2.12)$$

$$R_k = (\frac{\hbar^2}{2m_0})\sqrt{3}(\frac{\gamma_2+\gamma_3}{2})k_t^2, \quad S_k = (\frac{\hbar^2}{2m_0})2\sqrt{3}\gamma_3 k_t k_z \quad (2.13)$$

$$P_\varepsilon = -a_v(\varepsilon_{xx} + \varepsilon_{yy} + \varepsilon_{zz}), \quad Q_\varepsilon = -\frac{b}{2}(\varepsilon_{xx} + \varepsilon_{yy} - 2\varepsilon_{zz}) \quad (2.14)$$

where, m_0 is the electron mass in the free space, $V_h(z)$ is the unstrained valence band edge, γ_1, γ_2 and γ_3 are the Luttinger parameters, a_v is the hydrostatic stress deformation potential in the valence band, b is the shear deformation potential, $\Delta(z)$ is the spin-orbit splitting energy, σ represents the upper 'U' and the lower 'L', respectively. In here the unstrained valence band edge '$V_h(z)$' in the well is taken as the reference energy and hence

the unstrained conduction band edge $V_c(z) = V_h(z) + E_g$, where E_g is the bandgap energy in the well. The band edge in the barrier can be determined by the model-solid theory based on the first principle [73]. The energy distribution in the valence band can also be obtained using the finite difference method. In Eqs. (2.5) and (2.8), the envelope function is normalized as:

$$\int \left|\phi_n(z;k_t)\right|^2 dz = 1 \tag{2.15}$$

$$\sum_{j=HH,LH,SO} \int \left|g_{m,j}^{\sigma}(z;k_t)\right|^2 dz = 1 \tag{2.16}$$

In the following analysis, the well and barrier materials are, respectively, $In_{1-x}Ga_xAs$ and $In_{1-x}Ga_xAs_yP_{1-y}$ where x and y are Ga and As molar fractions, respectively. The barrier material bandgap wavelength is $\lambda = 1.15\mu m$ as it is lattice-matched to the InP substrate. The quantum well is grown on a 001-oriented substrate. The well width is chosen so that the peak of the TE and TM gain spectrum lies near the 1550nm. For the above well and barrier materials the energy bandgaps are [74]:

$$E_{gw} = 1.424x + 0.536(1-x) - 0.5317x(1-x) \tag{2.17}$$

$$E_{gb} = 1.35 - 0.775y + 0.149y^2 \tag{2.18}$$

The relationship between the molar fractions x and y when the barrier material is lattice-matched to the InP substrate is given by [74]:

$$x = \frac{0.1894y}{0.4184 - 0.013y} \tag{2.19}$$

In Eq. (2.1), the electron effective masses both in perpendicular ($m_{e,t}$) and parallel ($m_{e,z}$) to the growth directions can be expressed, respectively, as [71]:

$$1/m_{e,t} = (1+D^{'})/m_0 + \frac{P^2}{3}\left(\frac{3}{E_A + P_\varepsilon^c - E_{HH}} + \frac{(\alpha - \sqrt{2}\beta)^2}{E_A + P_\varepsilon^c - E_{LH}} + \frac{(\beta + \sqrt{2}\alpha)^2}{E_A + P_\varepsilon^c - E_{SO}}\right) \quad (2.20)$$

$$1/m_{e,z} = (1+D^{'})/m_0 + \frac{2P^2}{3}\left(\frac{(\sqrt{2}\alpha - \beta)^2}{E_A + P_\varepsilon^c - E_{LH}} + \frac{(\sqrt{2}\beta + \alpha)^2}{E_A + P_\varepsilon^c - E_{SO}}\right) \quad (2.21)$$

where, $D^{'}$ is a second-order perturbation factor [71], P^2 is the momentum matrix element, α and β are the coefficients representing the degree of mixing between the two states $\left|\frac{3}{2},\pm\frac{1}{2}\right\rangle$ and $\left|\frac{1}{2},\pm\frac{1}{2}\right\rangle$, E_A is the bandgap of the semiconductor A .The expressions for E_{HH}, E_{LH} and E_{SO} in Eqs.(2.20) and (2.21) are given as [71]:

$$E_{HH} = -P_\varepsilon - Q_\varepsilon \quad (2.22)$$

$$E_{LH} = -P_\varepsilon + \frac{1}{2}(Q_\varepsilon - \Delta + \sqrt{\Delta^2 + 2\Delta Q_\varepsilon + 9Q_\varepsilon^2}) \quad (2.23)$$

$$E_{SO} = -P_\varepsilon + \frac{1}{2}(Q_\varepsilon - \Delta - \sqrt{\Delta^2 + 2\Delta Q_\varepsilon + 9Q_\varepsilon^2}) \quad (2.24)$$

where Δ is the spin-orbit splitting energy.

2.2.2 Finite Difference Method for Solving the Schrodinger Equation

The finite difference method was widely used in the solving the nonlinear equations of active optical waveguides and optical fibers. The Schrodinger equations for the conduction and valence bands were solved using the finite difference method. All the differential operators in Eqs.2.1and 2.8 are written as $A(z)\partial^2/\partial z^2$ or $B(z)\partial/\partial z^2$, where, z is the position vector, A and B represents the position-dependent inverse effective mass parameters. The Hermitian properties of the Hamiltonian can be obtained using the following different equations [70]:

$$A(z)\frac{\partial^2 g}{\alpha z^2}\Big|_{z=z_i} \rightarrow \frac{\partial}{\partial z}\left(A(z)\frac{\partial g}{\partial z}\right)\Big|_{z=z_i}$$

$$= \frac{A(z_{i+1}) + A(z_i)}{2(\Delta z)^2} g(z_{i+1}) - \frac{A(z_{i-1}) + 2A(z_i) + A(z_{i+1})}{2(\Delta z)^2} g(z_i)$$

$$+ \frac{A(z_i) + A(z_{i-1})}{2(\Delta z)^2} g(z_{i-1}) \quad (2.26)$$

$$B(z)\frac{\partial g}{\alpha z}\Big|_{z=z_i} \rightarrow \frac{1}{2}\left(B(z)\frac{\partial g}{\partial z} + \frac{\partial (Bg)}{\partial z}\right)\Big|_{z=z_i}$$

$$= \frac{B(z_{i+1}) + B(z_i)}{4\Delta z} g(z_{i+1}) - \frac{B(z_i) + B(z_{i-1})}{4\Delta z} g(z_{i-1}) \quad (2.27)$$

When the finite difference method is used to solve the conduction and valence energy bands, the Hamiltonian expressions for each one should be written as a function of the wave vector k_z so that it can then be replaced by the differential operators. The orders of differential operators are equal to the index number of k_z, so the Hamiltonian in Eq. 2.8 should be expressed as:

$$H_k^v = -\begin{bmatrix} P_k + Q_k & -iS_k & \frac{i}{\sqrt{2}}S_k \\ iS_k & P_k - Q_k & \sqrt{2}Q_k + i\sqrt{\frac{3}{2}}S_k \\ -\frac{i}{\sqrt{2}}S_k & \sqrt{2}Q_k - i\sqrt{\frac{3}{2}}S_k & P_k \end{bmatrix} - \begin{bmatrix} 0 & R_k & \sqrt{2}R_k \\ R_k & 0 & 0 \\ \sqrt{2}R_k & 0 & 0 \end{bmatrix}$$

$$-\begin{bmatrix} -V_h(z) + P_\varepsilon + Q_\varepsilon & 0 & 0 \\ 0 & -V_h(z) + P_\varepsilon - Q_\varepsilon & \sqrt{2}Q_\varepsilon \\ 0 & \sqrt{2}Q_\varepsilon & -V_h(z) + P_\varepsilon + \Delta(z) \end{bmatrix} \quad (2.28)$$

2.3 Stimulated and Spontaneous Emissions in Semiconductor Optical Amplifiers

2.3.1 Concepts of Stimulated and Spontaneous Emissions in Semiconductors

The understandings of stimulated and spontaneous emission processes are important to analyze the optical signal amplification and noise in the active semiconductor optical devices. Stimulated emission describes the process in which an excited atomic electron in the higher energy state stimulated by an incoming photon with the specific frequency transfer to the lower energy state, resulting in that a new photon is created having the identical phase, polarization, frequency and travelling direction with the incident photon. Spontaneous emission describes the process by which an excited state transfers to a lower energy state, resulting in generation of a photon having random phase, polarization, frequency and travelling direction. Fig. 2.1 shows the schematic diagram of stimulated and spontaneous emission process.

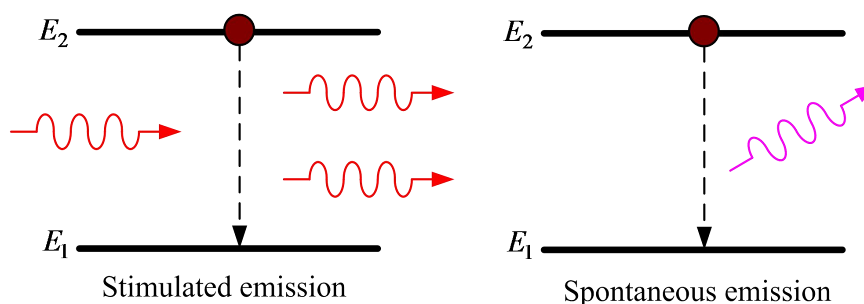

Fig. 2.1 Schematic diagram of stimulated and spontaneous emission processes, E_1 and E_2 are the energies of excited state and ground state.

2. 3.2 Optical Properties in Spontaneous and Stimulated Emissions

2.3.2.1 Gain and Spontaneous Emission Rate

The material gain in the active region of a QW-SOA can be derived from the Fermi's golden rule [74-75] as:

$$g(\omega)=\frac{q^2\pi}{n_r c\varepsilon_0 m_0^2\omega L_z}\sum_{\eta=\uparrow,\downarrow}\sum_{\sigma=U,L}\sum_{n,m}\int\left|\hat{e}\cdot M_{nm}^{\sigma\eta}\right|^2$$

$$\times\frac{(f_n^c(k_t)-f_{\sigma m}^v(k_t))(\gamma/\pi)}{(E_{\sigma,nm}^{cv}(k_t)-\hbar\omega)^2+\gamma^2}\frac{k_t dk_t}{2\pi} \tag{2.29}$$

where,

$$f_n^c(k_t)=1/(1+\exp(\frac{E_n^c(k_t)-E_{fc}}{K_B T})) \tag{2.30}$$

$$f_{\sigma m}^v(k_t)=1/(1+\exp(\frac{E_{\sigma,m}^{\upsilon}(k_t)-E_{fv}}{K_B T})) \tag{2.31}$$

$$E_{\sigma,nm}^{cv}(k_t)=E_n^c(k_t)-E_{\sigma,m}^v(k_t) \tag{2.32}$$

In the above equations q is the magnitude of the electron charge, n_r is the ground refractive index, c is the speed of light in free space, ε_0 and γ are the permittivity in free space and the half linewidth of the Lorentzian function, respectively, ω is the optical angular frequency, K_B is Boltzmann constant, T is the carrier temperature, $\hat{e}$ is the polarization vector of the optical electric field, $M_{nm}^{\sigma\eta}$ is the momentum matrix element, E_{fc} and E_{fv} are the quasi-Fermi levels in the conduction and valence bands. For both TE and TM modes, the momentum matrix elements are given by [74]:

$$\left|M_{TE}\right|^2=\left|\hat{x}\cdot M_{nm}^{\eta\sigma}(k_t)\right|^2=\left|\hat{y}\cdot M_{nm}^{\eta\sigma}(k_t)\right|^2$$

$$=\frac{M_b^2}{4}\{\left|\left\langle g_{m,lh}^{\sigma}+\sqrt{2}g_{m,so}^{\sigma}\middle|\phi_n\right\rangle\right|^2+3\left|\left\langle g_{m,hh}^{\sigma}\middle|\phi_n\right\rangle\right|^2\} \tag{2.33}$$

$$\left|M_{TM}\right|^2=\left|\hat{z}\cdot M_{nm}^{\eta\sigma}(k_t)\right|^2=M_b^2\{\left|\left\langle g_{m,lh}^{\sigma}-\frac{1}{\sqrt{2}}g_{m,so}^{\sigma}\middle|\phi_n\right\rangle\right|^2\} \tag{2.34}$$

where,

$$M_b^2 = \frac{m_0 E_p}{6} \tag{2.35}$$

is the momentum matrix element for the bulk material and E_P is an energy parameter.

The spontaneous emission spectrum $r_{sp}(\hbar\omega)$ is given by [74, 76]:

$$r_{sp}(\hbar\omega) = \frac{q^2 n_r \omega}{\pi\hbar c^3 \varepsilon_0 m_0^2 L_z} \sum_{\eta=\uparrow,\downarrow} \sum_{\sigma=U,L} \sum_{n,m} \int \left| M_{sp}(k_t) \right|^2$$

$$\times \frac{f_n^c(k_t)(1 - f_{\sigma m}^v(k_t))(\gamma/\pi)}{(E_{\sigma,nm}^{cv}(k_t) - \hbar\omega)^2 + \gamma^2} \frac{k_t dt}{2\pi} \tag{2.36}$$

where, the momentum matrix element of the spontaneous emission $\left| M_{sp} \right|^2$ is related to the TE and TM polarization components, which can be expressed as [72]:

$$\left| M_{sp} \right|^2 = \frac{1}{3}(2\left| M_{TE} \right|^2 + \left| M_{TM} \right|^2) \tag{2.37}$$

The spontaneous emission rate is obtained by integrating the spontaneous emission spectrum over the whole optical energy by:

$$R_{sp} = \int r_{sp}(\hbar\omega) d(\hbar\omega) \tag{2.38}$$

2.3.2.2 Determination of the Quasi-Fermi Levels

The Quasi-Fermi levels describe the population of electrons in the conduction and the valence bands. Some external forces, such as external voltage or exposure to the light can lead to the displacement of equilibrium of populations of electrons in the conduction and valence bands. If the disturbance is not too quick or too great, the conduction and valence bands arrive in a state of quasi thermal equilibrium, which corresponds to a quasi-Fermi level in the conduction or valance band. Since the relaxing time of electrons within the conduction or valence band is much less than the relaxing time of electrons across the band gap, the internal relaxing time of electrons is ignored except that the ultrafast processes

need to be analysed. The quasi-Fermi level is dependent on the carrier density and the carrier temperature. The electron density in the conduction band N_c can be expressed as [77]:

$$N_c = \int \frac{\rho^{2D}(E) f_c(E) dE}{V}$$

$$= \int_{E_1^c}^{\infty} \frac{m_e^*}{\pi\hbar^2 L_z} f_c(E) dE + \int_{E_2^c}^{\infty} \frac{m_e^*}{\pi\hbar^2 L_z} f_c(E) dE + \cdots + \int_{E_n^c}^{\infty} \frac{m_e^*}{\pi\hbar^2 L_z} f_c(E) dE \qquad (2.39)$$

where, $f_c(E)$ is the quasi-Fermi distribution function for the conduction band, L_z is the width of quantum well, m_e^* is the effective mass of electron, E_n^c is the energy of the *nth* subband in the conduction band.

The quasi-Fermi level in the valence band is difficult to calculate. This is because the coupling between the heavy hole, light hole and spin-orbit spilt-off band results in the non-parabolic distribution of the valence band. For a certain sub-band in the valence band, the density state is not constant. In this case, the quasi-Fermi level for the holes in the valence band can be determined from the following equation:

$$N_p = \sum_{j=HH,LH,SO} P_j \qquad (2.40)$$

$$P_j = \sum_m \frac{2}{V} \iint f_m^v(k_x, k_y) \frac{dk_x}{2\pi / l_x} \frac{dk_y}{2\pi / l_y} = \frac{1}{\pi L_z} \sum_m \int_0^{\infty} f_m^v(k_t) k_t dk_t \qquad (2.41)$$

where, $f_v^m(E)$ is the quasi-Fermi distribution function for the valence band, V is the crystal volume. The dichotomy method [78] is used to calculate the quasi-fermi levels in the conduction and valence bands.

Based on Eqs. (2.39) and (2.41), it has been found both carrier density and temperature influence the quasi-Fermi levels of electrons and holes. The higher carrier density leads to the larger quasi-Fermi level, which indicates that the carrier occupation level is high.

Also, the higher carrier temperature results in the lower quasi-Fermi level. This is because the carrier temperature describes the carrier average energy in the system. Assuming the initial carrier density is constant, as the carrier temperature increases, more carriers are distributed in the higher-energy band and hence the corresponding carrier occupation level in the lower energy band decreases.

2.3.2.3 Differential Gain and Linewidth Enhancement Factor

The high-speed performance of a semiconductor optical amplifier depends on the amplifier differential gain and spectra linewidth enhancement factor. The differential gain is defined as the derivative of material gain with respect to the carrier density and can be expressed as [76]:

$$\frac{\partial g(N)}{\partial N} = \frac{q^2 \pi}{n_r c \varepsilon_0 m_0^2 \omega L_z} \sum_{\eta=\uparrow,\downarrow} \sum_{\sigma=U,L} \sum_{n,m} \int \left| \hat{e} \cdot M_{nm}^{\sigma\eta} \right|^2$$

$$\times \frac{\gamma k_t}{2\pi^2 k_B T((E_{\sigma,nm}^{cv}(k_t) - \hbar\omega)^2 + \gamma^2)}$$

$$\times (f_n^c(k_t)(1 - f_n^c(k_t)) \frac{\partial E_{fc}(N)}{\partial N} - f_{\sigma m}^v(k_t) \times (1 - f_{\sigma m}^v(k_t)) \frac{\partial E_{fv}(N)}{\partial N}) dk_t \tag{2.42}$$

The refractive index change is $\Delta n_r = \Delta\varepsilon_1 / (2 n_r \varepsilon_0)$, where, ε_1 is the permittivity of active region. The change of the real part of the permittivity $\Delta\varepsilon_1 / \varepsilon_0$ is given as [74]:

$$\frac{\Delta\varepsilon_1}{\varepsilon_0} = \frac{2q^2\hbar^2}{\varepsilon_0 m_0^2 L_z} \sum_{\eta=\uparrow,\downarrow} \sum_{\sigma=U,L} \sum_{n,m} \int \left| \hat{e} \cdot M_{nm}^{\sigma\eta} \right|^2$$

$$\times \frac{(E_{\sigma,nm}^{cv}(k_t) - \hbar\omega)}{E_{\sigma,nm}^{cv}(k_t)(E_{\sigma,nm}^{cv}(k_t) + \hbar\omega)^2}$$

$$\times \frac{(f_n^c(k_t) - f_{\sigma m}^v(k_t))}{(E_{\sigma,nm}^{cv}(k_t) - \hbar\omega)^2 + \gamma^2} \frac{k_t dk_t}{2\pi} \tag{2.43}$$

The linewidth enhancement factor is defined as the ratio of derivatives of refractive index and material gain with respect to the carrier density, that is [79]:

$$\alpha = -\frac{4\pi}{\lambda_0} \frac{\partial \Delta n_r / \partial N}{\partial g / \partial N} \tag{2.44}$$

where, λ_0 is the central wavelength of SOAs.

2.4 Calculation of the Electronic and Optical Properties of QW-SOAs

In the following calculations, a compressively strained $InGaAs/InGaAsP$ QW-SOA with its lattice matched to InP substrate is analysed. The barrier band-gap wavelength is $\lambda = 1.15\mu m$ and the well and barrier widths are $4.5nm$ and $10nm$, respectively. The material parameters of QW-SOAs are listed in Tab. 2.1.

2.4.1 Band Structure Calculation

Figure 2.2 (a) and (b) show the energy band structures of both conduction and valence bands of the above mentioned compressively strained ($x = 0.36$) QW-SOA. Fig. 2.2 (a) shows that the energy in the conduction band varies parabolically with the wave vector k_t while Fig. 1(b) clearly shows that the band structure in valance band is non-parabolic due to the strain-dependent coupling among heavy holes bands, light holes bands and spin-orbit bands. Since the energy band structure is discontinuous and the valence band structure is non-parabolic for QW-SOAs, the Fermi-Dirac approximation cannot be employed to calculate the effects of carrier heating in QW-SOAs, which will be further discussed in Chapter 3.

Tab. 2.1 Material parameters of quantum well [74]

Parameters	Symbol	*InP*	*InAs*	*GaP*	*GaAs*
Lattice constant (A)	d	5.8688	6.0684	5.4512	5.6533
Band gap energy (eV)	E_g	1.344	0.354	2.78	1.424
Stiffness constants ($10^{11}\,dyn/cm^2$)	C_{11}	10.220	8.329	14.120	11.880
	C_{12}	5.760	4.526	6.253	5.380
Luttinger Parameters	γ_1	4.95	20.4	4.05	6.85
	γ_2	1.65	8.3	0.49	2.1
	γ_3	2.35	9.1	1.25	2.9
Bir-Pikus deformation potentials (eV)	a_c	-5.04	-5.08	-7.41	-7.17
	a_v	-1.27	-1.00	-1.70	-1.16
Shear deformation potential (eV)	b	-1.7	-1.8	-1.7	-1.8
Spin-orbit splitting energy (eV)	Δ	0.11	0.38	0.08	0.34

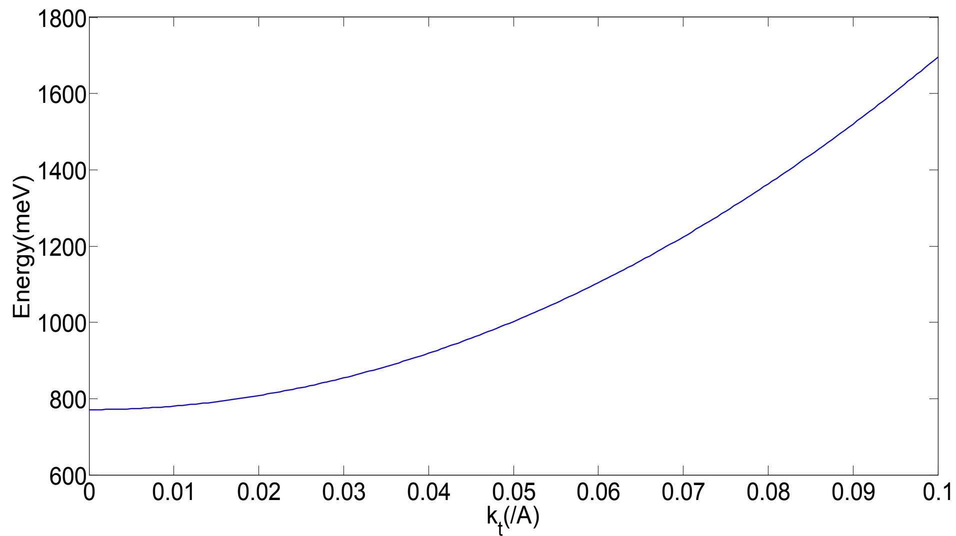

(a)

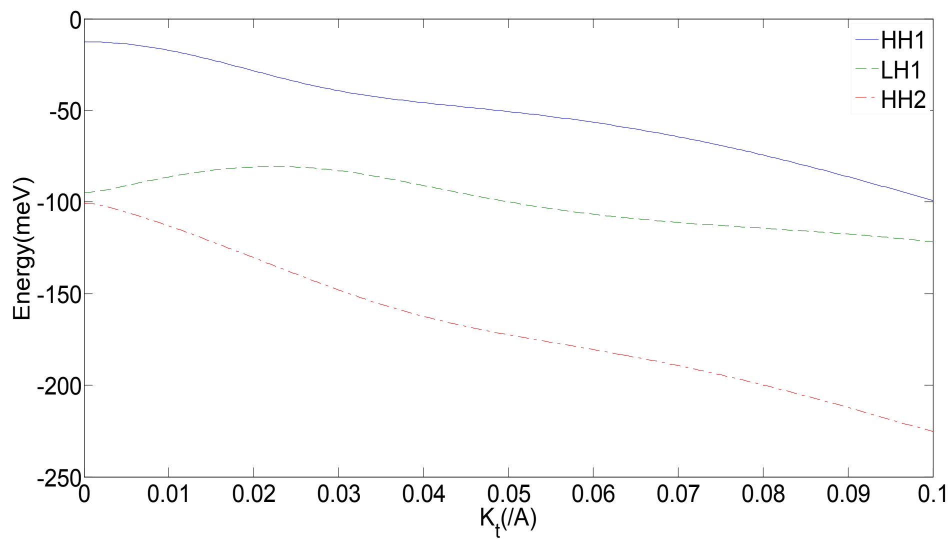

(b)

Fig. 2.2 Energy band structure of a compressively strained QW-SOA (a) conduction band structure (b) valence band structure.

2.4.2 Strain Effects on the Band Structure

The presence of uniaxial stress or elastic strain due to the lattice mismatch leads to the reduced cubic symmetry of standard semiconductors. This provides a powerful tool to adjust the intrinsic properties of semiconductors, such as the energy gap, the deformation potentials and the other band-structure parameters. It has been confirmed that the introduction of compressive strain can effectively improve the output performance of semiconductor amplifiers [80]. Fig. 2.3 shows the schematic diagram of the distribution of conduction and valence band structures under the compressive strain, no strain and tensile strain. It can be observed that the different band structure distributions of heavy and light holes under different strained cases are due to the difference of the effective mass of electrons in the heavy and light hole bands.

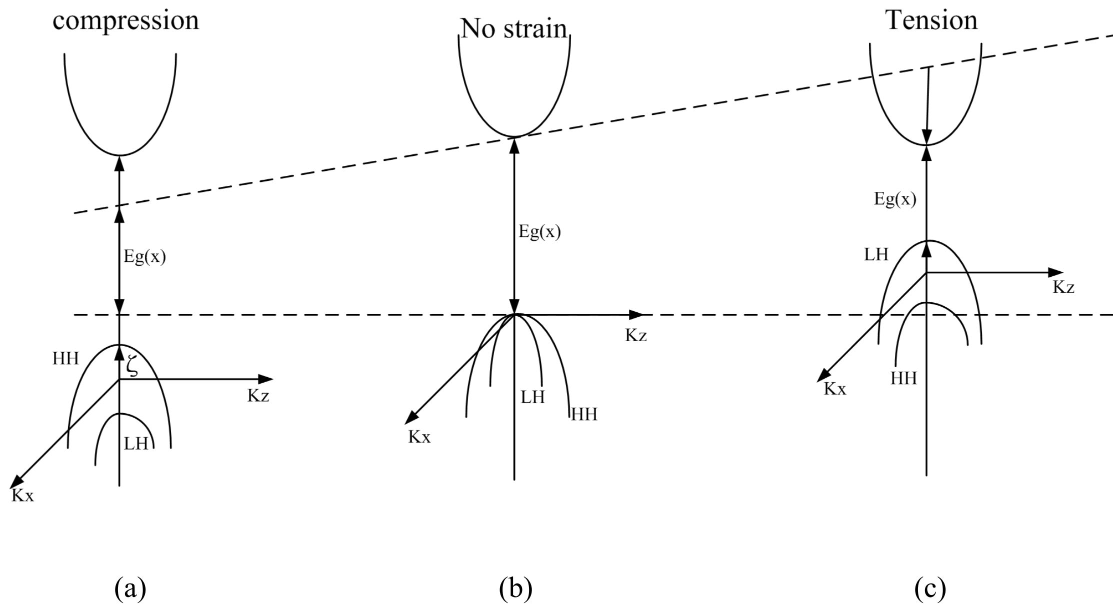

Fig. 2.3 Schematic diagram of conduction and valence bands energy distributions under (a) compressive strain, (b) no strain and (c) tensile stain.

Figure 2.4 shows the effective mass of electrons in the perpendicular and parallel to the growth direction calculated based on Eqs. (2.20) and (2.21). From this figure, we can conclude that the electron effective mass varies with the strain (i.e different values of x) of quantum wells. The electron effective masses perpendicular to the direction under the compressively strained case ($x < 0.47$) is lighter than that under the tensile strained case.

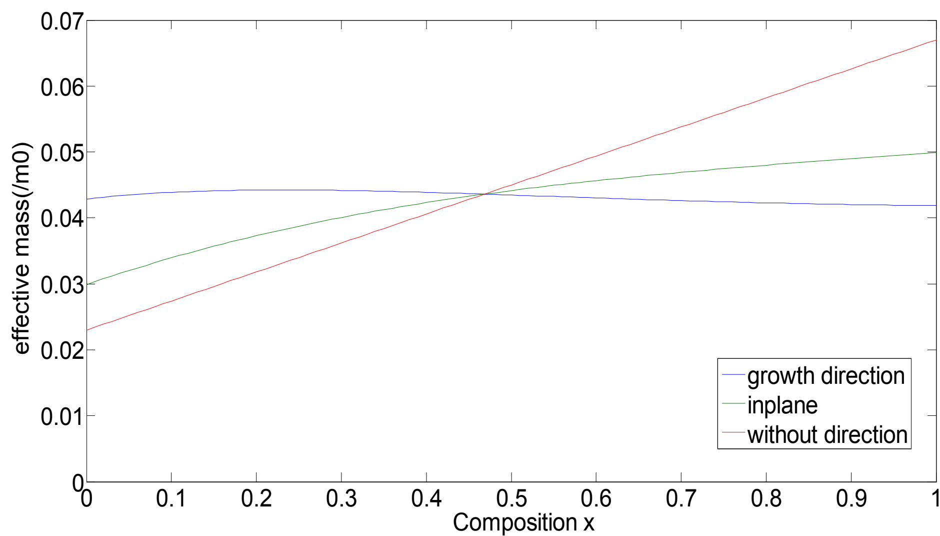

Fig. 2.4 Electron effective mass of $In_{1-x}Ga_xAs$ the blue and green lines are masses in the growth and in-plane directions. The red line is the electron effective mass without considering the direction.

Figure 2.5 shows the conduction band of quantum well under compressively strained ($x = 0.40$), unstrained ($x = 0.47$) and tensile strained ($x = 0.59$) cases and the valence band structures of quantum well in the above three strained cases are shown in Fig. 2.6. In all simulation results parameters listed in Tab. 2.1 are used. From Fig. 2.5, we can observe that the value of the conduction band at the Γ point (the states near the zone center of the ground state) is the lowest in the compressively strained quantum well while it is the largest in the tensile strained case. Figure 2.6 shows that the difference between the first two valence subband energies (i.e.HH1 and LH1) in the compressively strained quantum well is larger as compared with that in tensile strained quantum well. Besides, in the tensile strained quantum well, the light hole (LH) band is the first subband, which is because the effective mass at the zone center is negative due to the coupling between the heavy hole band and light hole band.

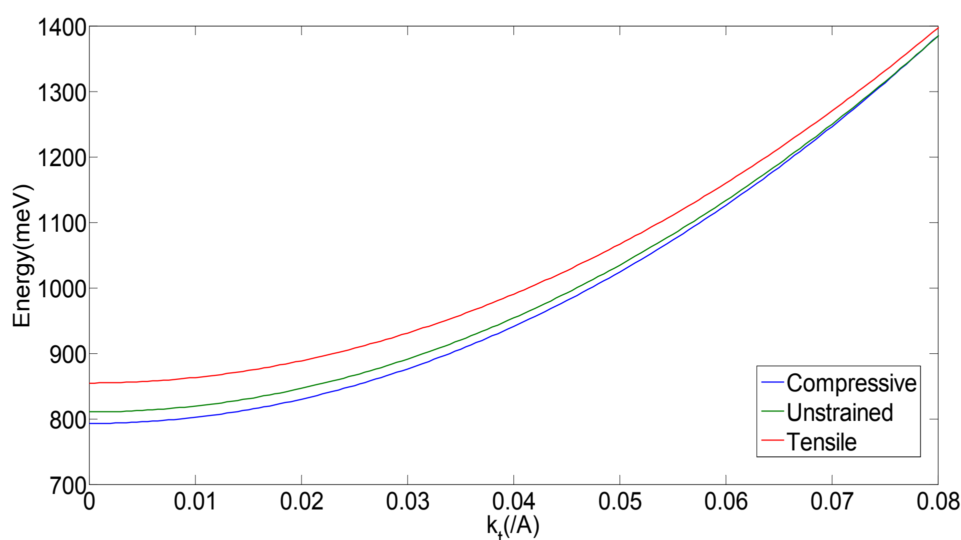

Fig. 2.5 Conduction band structures of three strained $In_{1-x}Ga_xAs$ - $InGaAsP$ quantum wells.

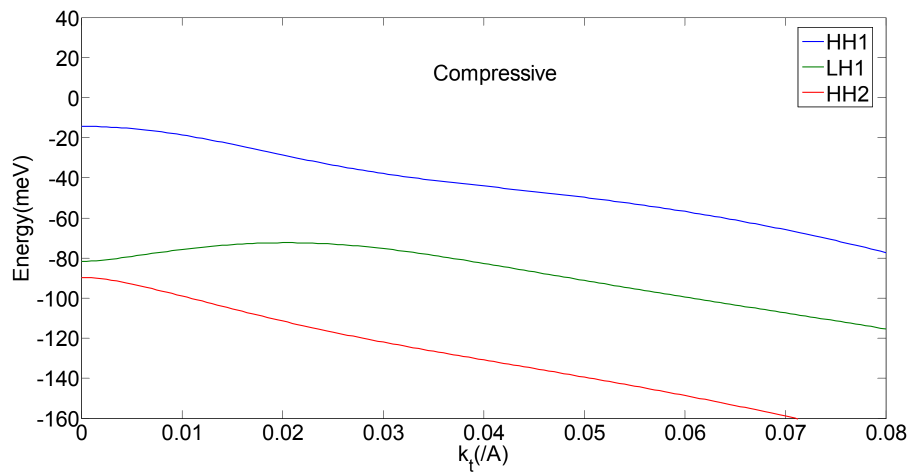

(a)

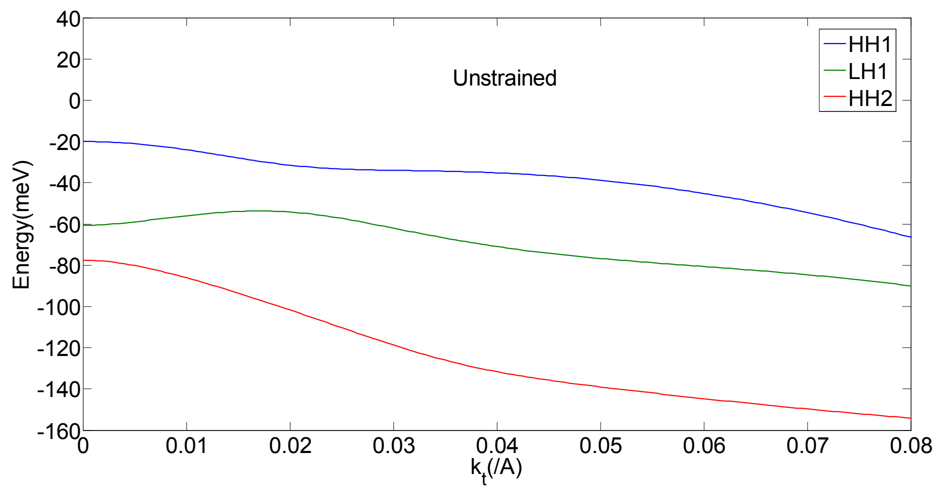

(b)

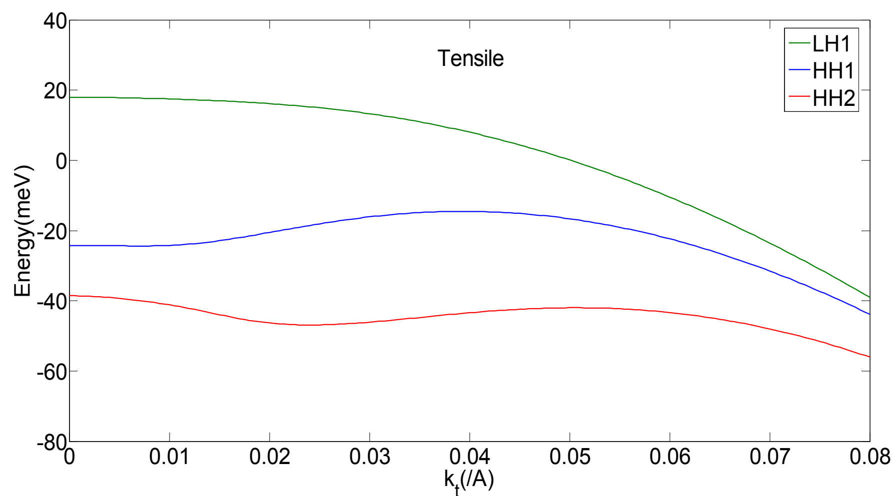

(c)

Fig. 2.6 First three valence bands (HH band, HL band and SO band) of three strained $In_{1-x}Ga_xAs$ - $InGaAsP$ quantum wells (a) $x = 0.40$ (b) $x = 0.47$ (c) $x = 0.59$.

2.4.3 Analysis of QW-SOAs' Optical Properties

In this section the optical properties of a compressively strained $In_{1-x}Ga_xAs / InGaAsP$ QW-SOA (with $x = 0.40$) are simulated based on the formula that were discussed in the previous section and the material parameters listed in Tab. 2.1.

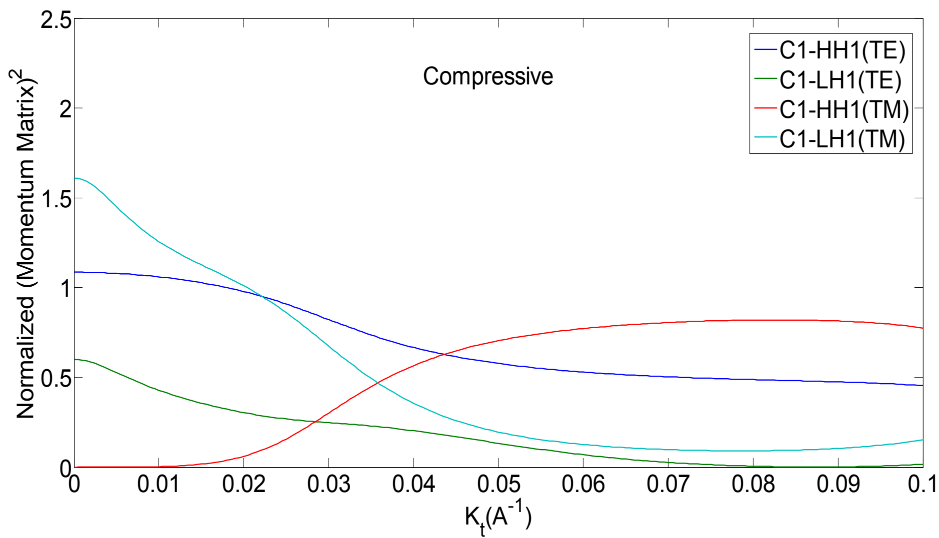

Fig.2.7 Momentum matrix element of $In_{1-x}Ga_xAs$ - $InGaAsP$ QW-SOAs.

Figure 2.7 shows the optical momentum matrix elements for both TE and TM modes of the HH1 and LH1 bands in a compressively strained QW-SOA. In a semiconductor, to satisfy the Fermi-Dirac distribution most electrons occupy the Γ point ($k_t = 0$). Hence in the following analysis for the optical momentum matrix we use its value at $k_t = 0$ (i.e. the Γ point). The momentum matrix values for TE mode HH1 and LH1 bands are 1.05 and 0.59, respectively, whereas these values for TM mode are 0 and 1.62 , respectively. The latter results clearly show that in TM mode case, the electron transition between the conduction band and the light hole band contributes more to the optical gain.

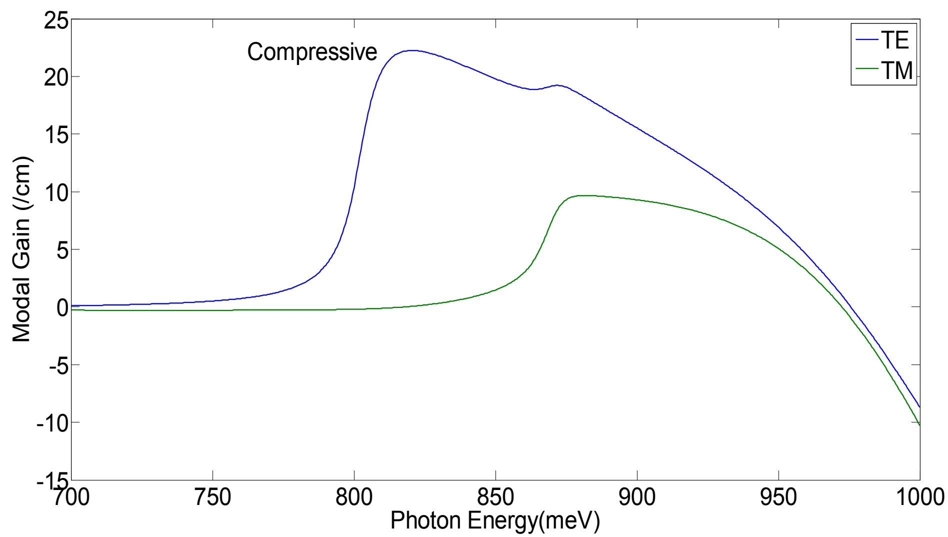

Fig. 2.8 Modal gain spectrum of a compressively strained QW-SOA.

Figure 2.8 shows the model gain spectrum of a compressively strained QW-SOA. It was found that in this case the peak wavelengths of modal gain spectra for the TE and TM modes are $1532nm$ and $1402nm$, respectively. Also, the peak values of the modal gain spectra for TE and TM modes are $22.50/cm$ and $9.67/cm$, respectively. The presence of two peaks in the TE mode gain spectra is due to the electron transition from the conduction band to the heavy hole band and also the electron transition from the conduction band to the light hole band. The TM gain spectrum only has one peak. This is because in the compressively strained case, the value of the optical momentum matrix element contributed by the electron transition from the conduction band to the heavy hole band is 0. The modal gain spectra of TE and TM modes are important optical parameters to determine the QW-SOAs' characteristics.

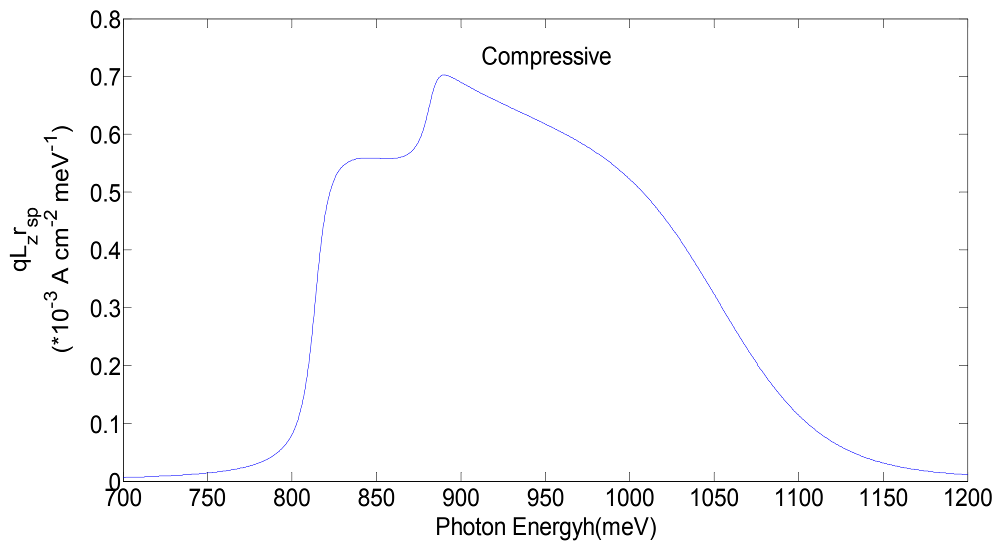

Fig. 2.9 The $qL_z r_{sp}(\hbar\omega)$ spectra in a compressively strained QW-SOA.

In QW-SOAs, there are unwanted effects caused by the spontaneous emission. The optical field created by the spontaneous emission decreases the carrier density in the active region and hence suppresses the optical gain further. Moreover, the optical field generated by the spontaneous emission usually has a much larger spectral bandwidth, which leads to the broadening of the amplified output signal. Fig.2.9 shows the spontaneous emission spectra in a compressively strained QW-SOA with the 3-dB bandwidth of 330nm.

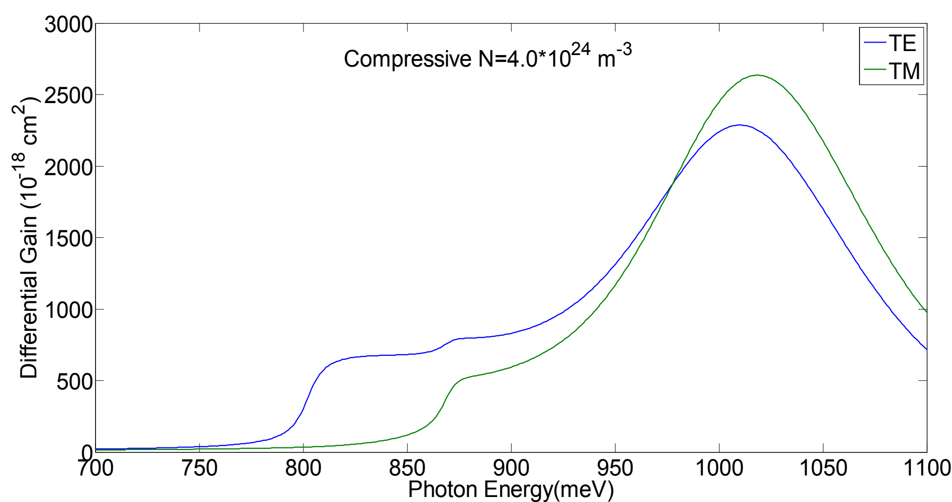

Fig. 2.10 The differential gain spectra of a compressively strained QW-SOA.

The differential gain is defined as the optical gain differential to the incremental carrier density. It can be used to evaluate the high speed performance of QW-SOAs and has an important influence on the amplifier gain dynamics. Fig. 2.10 shows the differential gain spectra of TE and TM mode at the carrier density $N = 4.0 \times 10^{24} / m^3$. The results show that as the photon energy increases (or the corresponding wavelength decreases), the differential gain initially increases and then decreases. Comparison of Figs. 2.8 and 2.10 shows that the peaks of the differential gain spectra appear at the wavelengths at which the values of the gain spectra fall sharply.

Another important high-speed parameter in QW-SOAs is the linewidth enhancement factor. The amplifier linewidth is defined as the optical spectra full width at half maximum. The linewidth in a QW-SOA is dependent on the semiconductor refractive index and the carrier density. Fig. 2.11 shows the linewidth enhancement factor of a compressively strained QW-SOA at the carrier density $N = 4.0 \times 10^{24} / m^3$. Comparison of Figs.2.10 and Fig. 2.11 clearly indicates that the linewidth enhancement factor is inversely proportional to the differential gain.

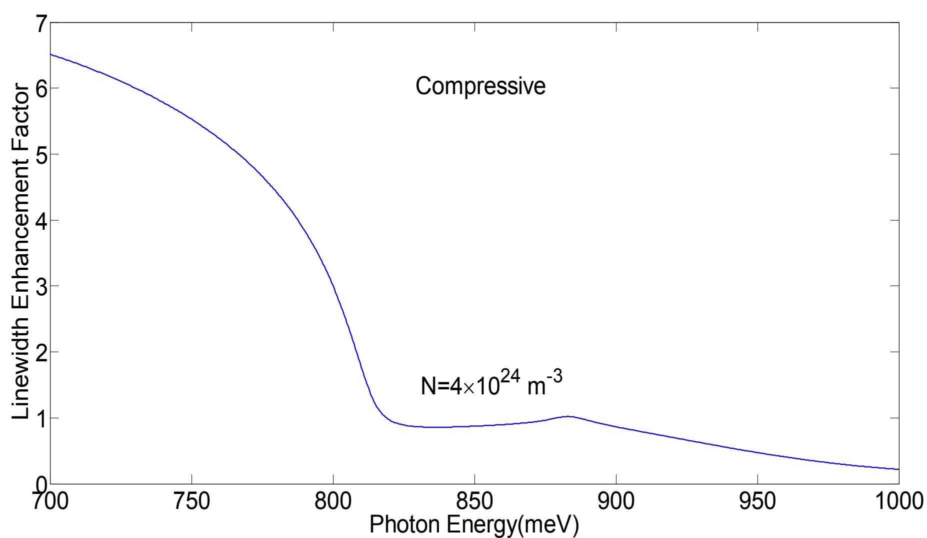

Fig. 2.11 Linewidth enhancement factor of a compressively strained QW-SOA.

2.5 Conclusions

In this chapter optical properties of semiconductor optical amplifiers are discussed, which are important in understanding of optical signal propagation in SOAs. The electronic band structure in semiconductor optical amplifier which can be obtained by solving the Schrodinger equations is presented. The stimulated and spontaneous emission processes in semiconductor optical amplifiers are described and some important parameters related to the optical processes of semiconductor optical amplifiers are defined and analyzed. Also, parameters related to both electronic and optical properties of a compressively strained QW-SOA are obtained and discussed.

Chapter 3

Effects of Carrier Heating on Optical Pulse Propagation in Semiconductor Optical Amplifiers

3.1 Introduction

A drawback for the conventional pulse laser system is the low energy output [81-82]. Compacted semiconductor optical amplifiers provide a practical tool to enhance the output power of the pulse laser system. Semiconductor-based pulse amplification has many advantages such as cost-effectiveness, optimal compactness, direct current pump and broad gain bandwidth [83-84]. However, carrier heating effects influence the optical pulse amplification in SOAs. Hence, it is important to establish a complete model to analyze the effect of carrier heating on the optical pulse propagation in SOAs. Carrier heating effect causes holes and electrons temperatures to exceed that of the lattice and this leads to reduction of the amplifier modal gain. Moreover, the effects of carrier heating intensify the nonlinear gain, which affects the modulation bandwidth and even leads to the cross talk between multiplexed signals [85-89]. Accurate theoretical description of carrier heating effects in semiconductor optical amplifiers enables us to better analyze the amplified output pulse. As the energy band in a quantum well structure is discontinuous, the theoretical description of carrier heating effects in quantum well SOAs becomes more

complicated as compared with the bulk SOAs. Hence, it is necessary to establish a more robust model which also includes the carrier heating effect so that we can analyse optical pulse amplification in both quantum well and bulk SOAs more accurately.

In this chapter, the conventional travelling wave rate equations for modelling the optical signal propagation in SOAs are introduced and the modelling for the Gaussian pulse amplification in SOAs is discussed. Based on the theoretical analysis presented in Chapter 2, a more accurate model is introduced which takes into account effects of (i) hole's non-parabolic density of states, (ii) carrier heating, (iii) spontaneous emission spectrum and (iv) picosecond pulse propagation in QW-SOAs. Besides, for the analysis of bulk SOAs, the Fermi-Dirac integration approximation is used to describe the carrier temperature dynamics and the influences of carrier heating on the picosecond pulse propagation.

3.2 Modelling Optical Pulse Propagation in SOAs Based on the Travelling Wave Rate Equations

3.2.1 Traveling Wave Rate Equations

The traveling-wave rate equations are used to describe the dynamic variations of photon and carrier densities. In the following, the traveling wave rate equations are employed to model the optical pulse propagation in a SOA. It should be noted that as the spontaneous and stimulated emissions spectra's wavelength ranges are different, two traveling wave rate equations are employed to describe the propagation of optical signals generated by spontaneous and stimulated emissions.

The rate equation for photo densities can be expressed as:

$$\left(\frac{\partial}{\partial t} \pm \upsilon_g \frac{\partial}{\partial z}\right) S_{v_i}^{\pm} = \upsilon_g S_{v_i}^{\pm} \left(\Gamma g(N, v_i) - \alpha_0\right) \tag{3.1}$$

where, t is the propagation time, z is the propagation distance along the amplifier cavity, υ_g is the group velocity, ν_i is the frequency of the optical input signal, $S^+_{\nu_i}$ and $S^-_{\nu i}$ are the forward and backward propagating signals photon densities at the frequency ν_i, α_0 is the waveguide loss, Γ is the optical confinement factor, $g(N,\nu_i)$ is the material gain (see Eq. 2.29 in Chapter 2), which is dependent on the carrier density N and the optical signal wavelength. The travelling wave rate equation for the photons generated by spontaneous emission can be given as:

$$(\frac{\partial}{\partial t} \pm \upsilon_g \frac{\partial}{\partial z})E^{\pm}_{\nu_j} = \upsilon_g E^{\pm}_{\nu_j}(\Gamma g(N,\nu_j) - \alpha_0) + R_{sp}(\nu_j, N) \qquad (3.2)$$

where, ν_j is the frequency of photons generated by the spontaneous emission, $E^+_{\nu_j}$ and $E^-_{\nu_j}$ are the forward and backward photon densities due to the amplified spontaneous emission (ASE) of the amplifier, $R_{sp}(\nu_j, N)$ is the spontaneous emission rate (see Eq. 2.38 in Chapter 2).

The carrier density rate equation is:

$$\frac{dN}{dt} = \frac{I}{qV} - \Gamma \upsilon_g \sum_{\nu_i} g(N,\nu_i)(S^+_{\nu_i} + S^-_{\nu_i})$$

$$- \Gamma \upsilon_g \sum_{\nu_j} g(N,\nu_j)(E^+_{\nu_j} + E^-_{\nu_j}) - AN - BN^2 - CN^3 \qquad (3.3)$$

where, I is the injected current, q is the electron charge, V is the active area volume, A, B, and C are linear, Bi-molecular and Auger recombination coefficients, respectively.

3.2.2 Gaussian Pulse Amplification

The expression for the amplifier input unchirped Gaussian pulse signal power $P(t)$ can be expressed as:

$$P(t) = P_{in}\, e^{-\frac{(t-t_0)^2}{2c^2}} \tag{3.4}$$

where, P_{in} is the peak power, t_0 is the time at which $P(t_0) = P_{in}$ and c is the standard deviation. The full width at half maximum (FWHM) of the Gaussian pulse t_f is given as:

$$t_f = 2.35482\, c \tag{3.5}$$

In Eqs.(3.1) and (3.2) photon densities are used to represent the input signal so the associated photon density ‘ S ’ for this input Gaussian pulse is:

$$S = \frac{P(t)}{v_g D W h v_i} \tag{3.6}$$

where, h is the Plank constant, D and W are the thickness and width of the active region of the amplifier. The input power $P(t)$ is converted into photon density S at the input facet of the amplifier (i.e. at $t = 0$ and $z = 0$). In the simulation, the step transition method [90] is adopted and thus the amplifier cavity is divided into m small sections as shown in Fig. 3.1):

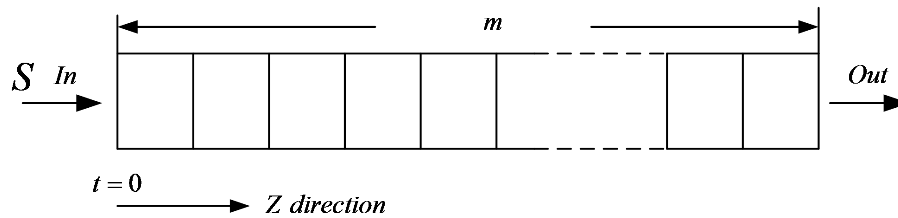

Fig. 3.1 Division of the amplifier cavity into m small sections to analyse the optical pulse propagation in SOAs using the step transition method.

3.3 Effects of Carrier Heating on the Picosecond Pulse Amplification in Quantum Well Semiconductor Optical Amplifiers

Because of non-parabolic distribution of valence band structure caused by the strong coupling between the HH, LH and spin-orbit spilt-off (SO) bands in quantum wells, the parabolic-approximation method which is commonly used for analysis of carrier heating effect in bulk SOAs can't be applied to quantum well semiconductor optical amplifiers. In this section the carrier heating effects in quantum well semiconductor optical amplifiers are analyzed based on a new method where the in-plane wave functions are used to express the energy densities in both conduction and valence bands. The gain and spontaneous emission spectra of quantum well semiconductor optical amplifiers at the different temperature are analysed and effects of carrier heating on the picosecond pulse amplification in quantum well semiconductor optical amplifier are studied.

3.3.1 Theory of Carrier Heating Effects in Quantum Well Semiconductor Optical Amplifiers

The temperature dynamics in QW-SOAs can be expressed by the following expression [42, 91]:

$$\frac{dT}{dt}=\frac{1}{\partial U/\partial T}\left(\frac{dU}{dt}-\frac{\partial U}{\partial N}\frac{dN}{dt}\right)-\frac{T-T_0}{\tau} \tag{3.7}$$

where, T is the carrier temperature, U is the total plasma energy density, τ is the temperature recovery time and T_0 is the lattice temperature. The expression for the rate of change of energy due to the spontaneous emission, stimulated emission, free carrier and inter-valence band absorptions is given by [76, 91]:

$$\frac{dU}{dt} = -\upsilon_g \sum_i (h\nu_i - E_g(N)) g(N,\nu_i)(S_{\nu_i}^+ + S_{\nu_i}^-)$$
$$+\upsilon_g \alpha_{FC} N \sum_i h\nu_i (S_{\nu_i}^+ + S_{\nu_i}^-)$$
$$-\upsilon_g \sum_j (h\nu_j - E_g(N)) g(N,\nu_j)(E_{\nu_j}^+ + E_{\nu_j}^-)$$
$$+\upsilon_g \alpha_{FC} N \sum_j h\nu_j (E_{\nu_j}^+ + E_{\nu_j}^-) \tag{3.8}$$

where, $E_g(N)$ is the bandgap energy, α_{FC} is the free carrier absorption coefficient. In the above equation the photon densities $S_{\nu_i}^{\pm}$ and $E_{\nu_j}^{\pm}$ are forward (+) and backward (-) signal and spontaneous emission photon densities that can be obtained by solving the photon density rate equation (i.e. Eq.(3.1)) and the travelling wave rate equation for the photons generated by spontaneous emission (i.e.Eq.(3.2)). Furthermore, the carrier dynamics dN/dt in Eq. 3.7 can be obtained by using the carrier density rate equation (i.e. Eq. (3.3)).

One key point in obtaining the carrier temperature changes caused by carrier heating effects is to calculate the derivatives of the energy density with respect to both temperature (dU/dT) and carrier density (dU/dN). The density of states is not a constant for a certain sub-band due to the non-parabolic distribution of energy band structure in a two-dimension system. This is due to the coupling effects between HH, LH and SO bands as well as the strain effects in the valence band. This leads to the computation complexity for the carrier heating effects in QW-SOAs. Thus, a new numerical calculation method is proposed to analyze the carrier heating effects in quantum well amplifiers. The electron density in the conduction band can be calculated by using the following equation [74]:

$$N = \frac{2}{V} \sum_{n} \sum_{k_x} \sum_{k_y} f(E) \qquad (3.9)$$

where, k_x and k_y are the wave vector in the x and y directions. $f(E)$ is the Fermi-Dirac distribution. n represents the nth sub-band, where in Eq.(3.9) all the occupied sub-bands are considered. The summation over k_x and k_y can be converted into integration:

$$\frac{2}{V} \sum_{k_x} \sum_{k_y} = \frac{2}{V} \int \frac{dk_x}{2\pi / L_x} \int \frac{dk_y}{2\pi / L_y} = \frac{2}{L_z} \int \frac{dk_x dk_y}{(2\pi)^2} \qquad (3.10)$$

Equation (3.10) in the polar coordinate can be expressed as:

$$\frac{2}{V} \sum_{k_x} \sum_{k_y} = \frac{2}{L_z} \int \frac{2\pi k_t dk_t}{(2\pi)^2} \qquad (3.11)$$

where, $dk_x dk_y = d\phi_k k_t dk_t$ with $k_t = \sqrt{k_x^2 + k_y^2}$ [74].

By substituting Eq. (3.11) into Eq. (3.9), the electron density in the conduction band becomes:

$$N = \sum_{n} \frac{1}{\pi L_z} \int_0^{+\infty} f(E_n(k_t)) k_t dk_t \qquad (3.12)$$

In the valence band, the density of states is considered as the summation of the density of states in HH, LH and SO bands, which is given as:

$$P = \frac{2}{V} \sum_{m} \sum_{HH,LH,SO} \sum_{k_x} \sum_{k_y} f(E) \qquad (3.13)$$

In the above equation summations over k_x and k_y can be converted into a single integration with respect to k_t [74]. Then, the holes' density in the valence band can be expressed as:

$$P = \sum_{m} \sum_{HH,LH,SO} \frac{1}{\pi L_z} \int_0^{+\infty} f(E_m(k_t)) k_t dk_t \qquad (3.14)$$

In Eqs. (3.12) and (3.14), $E_n(k_t)$ and $E_m(k_t)$ denote the *nth* sub-band energy in the conduction band and the *mth* HH LH and SO sub-bands energies in the valence band. Based on Eqs. (3.12) to (3.14), the energy density in quantum well can be expressed as:

$$U = U_C + U_V \tag{3.15}$$

$$U_C = \sum_n \frac{1}{\pi L_z} \int_0^{+\infty} \frac{E_n^c(k_t) - E_c}{1 + \exp((E_n^c(k_t) - E_{fc}) / K_B T)} k_t dk_t \tag{3.16}$$

$$U_V = \sum_m \sum_{HH,LH,SO} \frac{1}{\pi L_z} \int_0^{+\infty} \frac{E_v - E_m^v(k_t)}{1 + \exp((E_{fv} - E_m^v(k_t)) / K_B T)} k_t dk_t \tag{3.17}$$

where, K_B is the Boltzmann constant, L_z is the well width, E_{fc} and E_{fv} are the Fermi levels in the conduction band and in the valence band, E_c and E_v are the conduction band edge and the valence band edge. Since the energy band structures in the conduction and valence bands of QW-SOAs are functions of the in-plane wave vector k_t, the integrals in Eqs. (3.16) and (3.17) can be replaced by the numerical summation at the different wave vectors. It should be noted that the energy density U given in Eq.(3-15) is a function of Fermi level and hence it is functions of both carrier density (N) and temperature (T) as the Fermi level depends on both N and T . Hence, both partial differential equations $\frac{\partial U}{\partial T}$ and $\frac{\partial U}{\partial N}$ can be computed numerically by finding the rate of change of energy density with respect to N and T .

3.3.2 Effects of Carrier Heating on the Gain and Spontaneous Emission Spectra of Quantum Wells

Figure 3.2 shows variations of TE mode modal gain spectra of a compressively strained QW-SOA at different temperatures when carrier density is $8.0 \times 10^{24} m^{-3}$. The peak value of the modal gain is near $1550nm$ which is the wavelength window used in long haul optical

fibre communication systems as the optical fibre loss is minimum. The results show that the peak wavelength of the modal gain spectra decreases as the temperature increases. This is because, Fermi-levels in the conduction and valence bands are temperature dependent and hence, when temperature increases, Fermi-level in the conduction band decreases, while that in the valence band increases. These changes in Fermi-levels lead to the reduction of carrier densities which causes the modal gain spectra shifts to the shorter wavelength at higher temperature. The peak wavelengths of the modal gain spectra are, respectively, $1544.61nm\ (T = 300K)$, $1544.50nm\ (T = 350K)$ and $1544.28nm\ (T = 400K)$. This indicates that a small blue shift occurs in the modal gain peak wavelength as temperature increases.

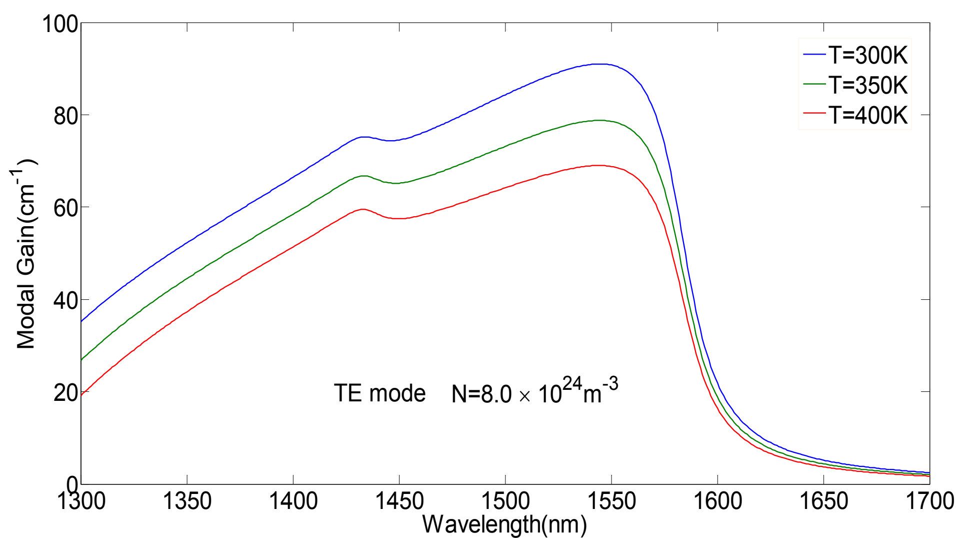

Fig. 3.2 Modal gain spectra of TE mode in a compressively-strained QW-SOA at different temperatures.

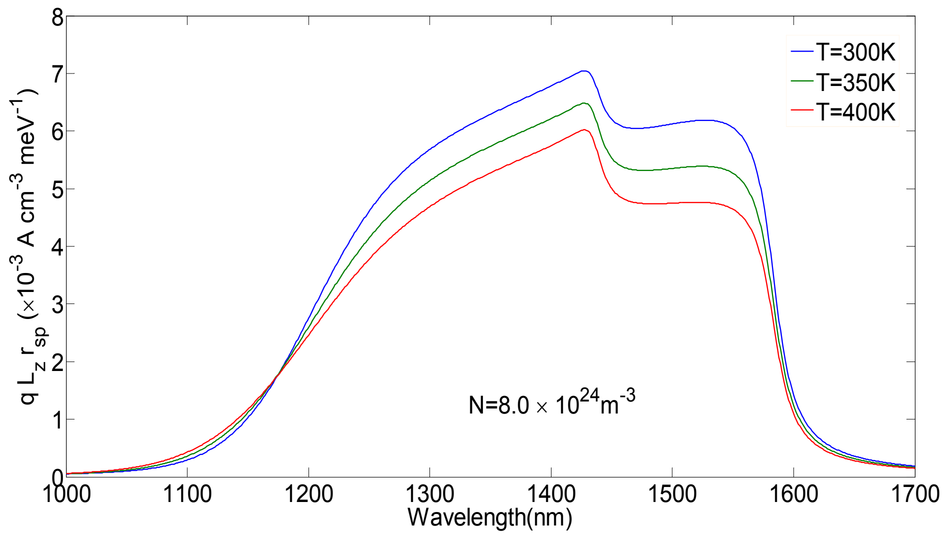

Fig.3.3 The spontaneous emission spectra of a compressively-strained QW-SOA at different temperatures.

The spontaneous emission spectra ($qL_z r_{sp}$) for the carrier density $N = 8.0\times10^{24} m^{-3}$ is also shown in Fig. 3.3. The results show that the spontaneous emission spectra values decrease with temperature while the spectra 3-dB bandwidths increase with temperature. This is because of having different density of states distributions due to changes in quasi-Fermi level with temperature.

3.3.3 Analysis of Carrier Heating Effects on the Picosecond Pulse Amplification in Quantum Well Semiconductor Optical Amplifiers

The influences of carrier heating on the picosecond pulse amplification in QW-SOAs are analysed based on the numerical method discussed in the previous sections. In the simulation the travelling rate equations (3.1), (3.2) and the boundary conditions in Ref. [57] are used to analyze the optical pulse propagation. The amplifier cavity is divided into 200 sections and parameters listed in Tab. 3.1 are used. An ideal $10mW$ peak power Gaussian

pulse cantered at $6ps$ with FWHM of $4ps$ at the wavelength $1550nm$ is applied to the input of the amplifier.

Figure 3.4 shows the pulse amplification responses of the above Gaussian input pulse both with and without considering the carrier heating effects. The time origin in x-axis means the signal begins to exit the amplifier. The figure shows that the carrier heating effects have reduced the output signal peak power from $2.62W$ to $1.03W$ and increased its FWHM from $2ps$ to $2.40ps$. This is because of material gain reduction due to the carrier heating effects as explained in Fig. 3.2. Moreover, less amplification occurs in the leading edge and around the peak region. On the other hand, when the trail edge of the pulse signal arrives, a small number of carriers are depleted so that the gain coefficient remains high. However, when the carrier heating effects are not considered the amplification in the leading edge depletes more carrier density due to the higher gain. The gain coefficient decreases sharply after the leading edge amplification. Therefore, the output signal FWHM is narrower than the input signal.

Tab. 3.1 Modelling parameters of QW-SOAs [45]

Symbol	Description	Value
n	Background refractive index	3.67
α_{FC}	Free carrier absorption	$0.5\times10^{-21}m^2$
A	Linear recombination	$2\times10^8 s^{-1}$
B	Bi-molecular recombination	$6\times10^{-16}m^3s^{-1}$
C	Auger recombination	$8\times10^{-41}m^6s^{-1}$
τ	Intraband scatting time	$1ps$
α_0	Waveguide loss	$1000m^{-1}$
Γ	Confinement factor	0.025

N_0	Transparent carrier density	1.2×10^{24}
I	Input current	$300mA$
W	SOA width	$1\mu m$
D	SOA thickness	$24.5nm$
L	SOA length	$750\mu m$

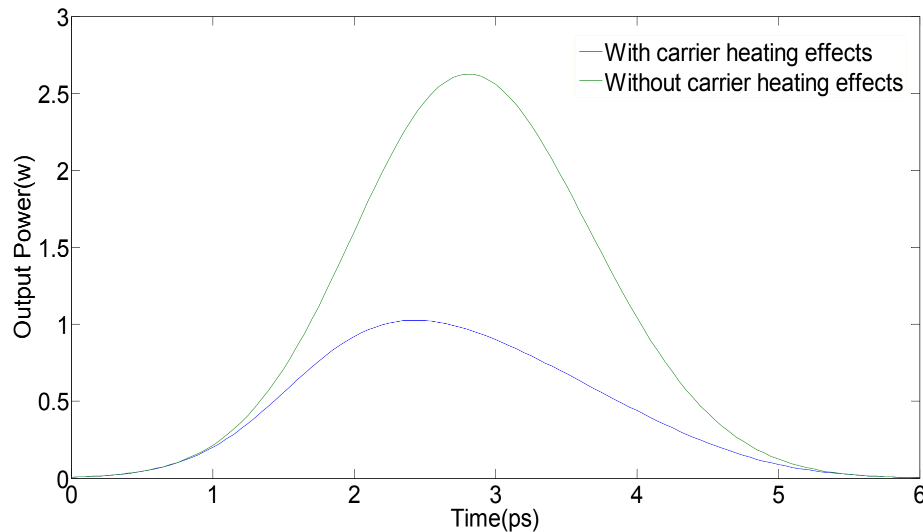

Fig. 3.4 QW-SOAs picosecond pulse amplification (input peak value $10mw$) with and without carrier heating effects.

Figure 3.5 shows similar results for the input Gaussian signal with peak power $100mW$. In this case the output signal peak value has decreased from $9.23W$ to $1.87W$ and its FWHM value has increased from $1.9ps$ to $2.8ps$ due to carrier heating effects. Comparison of Figs. 3.4 and 3.5 indicates that when carrier heating effect is considered the amplified output pulse broadens as the input pulse power increases, which is agreeable with the experimental results reported in Ref. [86]. The reported experimental results in Ref. [86] has shown that carrier heating effects lead to a increase of pulse duration of amplified output pulse.

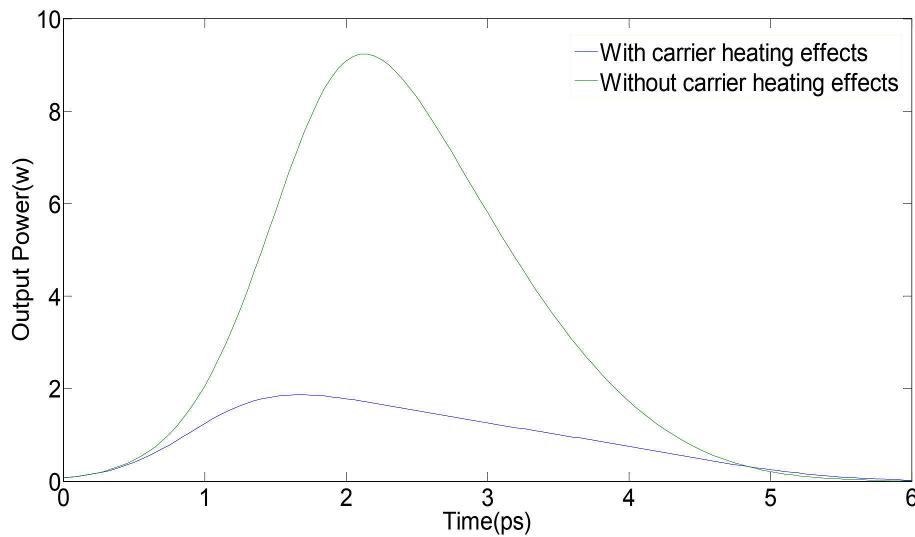

Fig.3.5 QW-SOAs picosecond pulse amplification (input peak value $100mw$) with and without carrier heating effects.

Figure 3.6 shows the average carrier temperature of the amplifier cavity during the pulse propagation. The initial lattice temperature is 300K and the time on the x-axis means the optical signal begins to enter the amplifier. The results indicate that the carrier temperature hardly changes when $t < 4ps$ this is because the propagation and amplification of the input pulse needs time. When $t > 4ps$, due to the large electromagnetic field (stimulated emission) and the free carrier absorption in the amplification cavity, the rates of energy and carrier density changes are high. In the two cases, the highest temperatures are $350.9K$ and $441.1K$, respectively. When the input peak value is $100mw$, the carrier temperature arrives at the peak point earlier. This is because a smaller amplification has saturated the amplifier when the input power is higher.

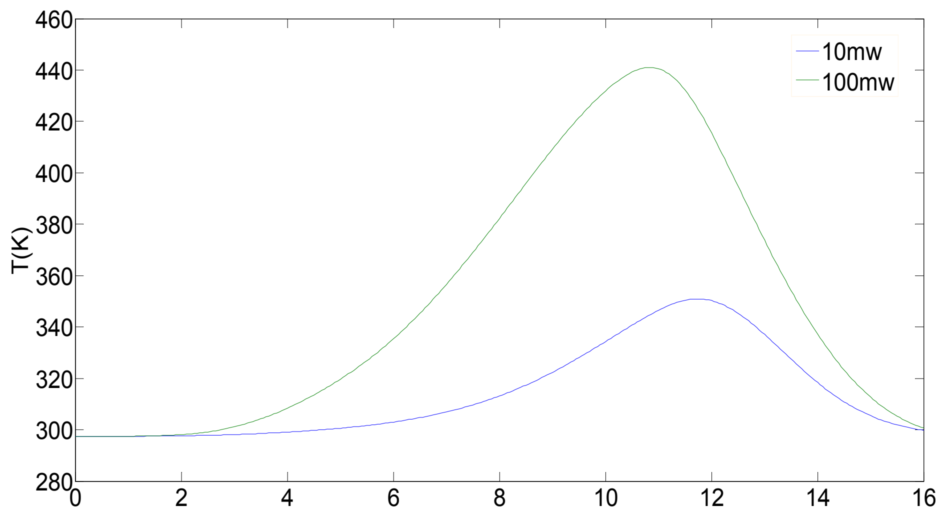

Fig.3.6 Average carrier temperature of the amplifier cavity in the picosecond pulse amplification process with the input peak powers of $10mw$ and $100mw$

3.4 Effects of Carrier Heating on Picosecond Pulse Amplification in Bulk Amplifiers

In the above section we discussed the carrier heating effects in quantum well semiconductor optical amplifiers together with its influences on the optical pulse amplification. In the following, the effects of carrier heating on picosecond pulse amplification in bulk semiconductor optical amplifiers are studied using a new analytical method. The carrier temperature is used to describe the influences of carrier heating in SOAs. Since the band structure of the bulk SOAs is parabolic, global approximations of Fermi-Dirac integrals of 3/2 order and 1/2 order are applied to calculate the carrier temperature changes caused by the carrier heating effects. In the following section the carrier heating effects on the picosecond pulse amplification in the bulk semiconductor optical amplifier are analysed.

3.4.1 Theory of Carrier Heating Effects in Bulk SOAs

The temperature dynamics in both quantum well and bulk semiconductor optical amplifiers can be expressed using the temperature dynamic rate equation (i.e. Eq. 3.7). In the temperature dynamic rate equation, the expression for the energy changes with time can be described using Eq. 3.8. As mentioned in the above section, the important point for calculating the temperature dynamics induced by carrier heating effects is to calculate the two partial differential items $\frac{\partial U}{\partial T}$ and $\frac{\partial U}{\partial N}$.

The energy density U in bulk SOAs can be expressed as [91]:

$$U = \frac{2}{\sqrt{\pi}} KT(N_c F_{3/2}^c + N_v F_{3/2}^v) \tag{3.18}$$

where, K is the Boltzmann constant, N_c and N_v are the effective densities of states in the conduction and valence bands, respectively which can be expressed as [92]:

$$N_c = 2(\frac{2\pi m_e^* KT}{h^2})^{3/2} \tag{3.19}$$

$$N_v = 2(\frac{2\pi\, m_v^* KT}{h^2})^{3/2} \tag{3.20}$$

where,

$$m_v^* = (m_{hh}^{3/2} + m_{lh}^{3/2})^{2/3} \tag{3.21}$$

m_e^* is the effective mass of electron in the conduction band, m_{hh} and m_{lh} are effective masses of heavy and light holes in the valence band, respectively. In Eq. (3.18), $F_{3/2}^c$ and $F_{3/2}^v$ are the Fermi-Dirac integral of 3/2 order for the conduction and valence bands, respectively. They can be expressed as [92]:

$$F_{3/2}^c = \int_0^{+\infty} \frac{x_c^{3/2}}{\exp(x_c - \varepsilon_c) + 1} dx_c \tag{3.22}$$

$$F^{v}_{3/2} = \int_0^{+\infty} \frac{x_v^{3/2}}{\exp(x_v - \varepsilon_v) + 1} dx_v \quad (3.23)$$

$$\varepsilon_c = (E_{Fc} - E_c) / KT \quad (3.24)$$

$$\varepsilon_v = (E_v - E_{Fv}) / KT \quad (3.25)$$

where, x_c and x_v are the energy variables for the conduction and valence bands, where, E_{Fc} is the quasi-Fermi levels in the conduction band and E_{Fv} is the quasi-Fermi level in the valence band, E_c and E_v are the conduction and valance bands edges, respectively. The two partial differentials $\partial U / \partial T$ and $\partial U / \partial N$ are given as:

$$\frac{\partial U}{\partial T} = \frac{2}{\sqrt{\pi}} K (N_c F^{c}_{3/2} + N_v F^{v}_{3/2})$$

$$+ \frac{2}{\sqrt{\pi}} KT \left(\frac{\partial (N_c F^{c}_{3/2})}{\partial T} + \frac{\partial (N_v F^{v}_{3/2})}{\partial T} \right) \quad (3.26)$$

$$\frac{\partial U}{\partial N} = \frac{2}{\sqrt{\pi}} KT \left(N_c \frac{\partial (F^{c}_{3/2})}{\partial N} + N_v \frac{\partial (F^{v}_{3/2})}{\partial N} \right) \quad (3.27)$$

It is difficult to calculate $\partial U / \partial T$ and $\partial U / \partial N$ without using any approximation due to the complexity of Fermi Dirac integral and the dependency of the quasi-Fermi levels on both temperature and carrier density which have been indicated in Eqs. (3.18) to (3.27). The partial differential terms on the right hand sides of Eqs. (3.26) and (3.27) can be expressed as:

$$\frac{\partial (N_c F^{c}_{3/2})}{\partial T} = \frac{\partial N_c}{\partial T} F^{c}_{3/2} + N_c \frac{\partial F^{c}_{3/2}}{\partial \varepsilon_c} \frac{\partial \varepsilon_c}{\partial T} \quad (3.28)$$

$$\frac{\partial (N_v F^{v}_{3/2})}{\partial T} = \frac{\partial N_v}{\partial T} F^{v}_{3/2} + N_v \frac{\partial F^{v}_{3/2}}{\partial \varepsilon_v} \frac{\partial \varepsilon_v}{\partial T} \quad (3.29)$$

$$N_c \frac{\partial (F^{c}_{3/2})}{\partial N} = N_c \frac{\partial (F^{c}_{3/2})}{\partial \varepsilon_c} \frac{\partial \varepsilon_c}{\partial N} \quad (3.30)$$

$$N_v \frac{\partial (F_{3/2}^v)}{\partial N} = N_v \frac{\partial (F_{3/2}^v)}{\partial \varepsilon_v} \frac{\partial \varepsilon_v}{\partial N} \tag{3.31}$$

As the effective densities of states N_c and N_v as well as the Fermi-Dirac integral of 3/2 order $F_{3/2}^c$ and $F_{3/2}^v$ are functions of temperature, Eqs. (3.28) and (3.29) are obtained by applying the product derivative rule to functions $N_c F_{3/2}^c$ and $N_v F_{3/2}^v$ given in Eqs. (3.19) to (3.25). The relationship between the Fermi-Dirac integrals of 3/2 and 1/2 orders [93] is used to eliminate the 1st derivates of $F_{3/2}^c$ and $F_{3/2}^v$ in Eqs (3.28) to (3.31), which is given as:

$$\frac{dF_{3/2}(\varepsilon)}{d\varepsilon} = \frac{3}{2} F_{1/2}(\varepsilon) \tag{3.32}$$

Substituting Eqs. (3.24), (3.25) and (3.32) into Eq. (3.28) to (3.31), the four partial differential items become:

$$\frac{\partial (N_c F_{3/2}^c)}{\partial T} = \frac{\partial N_c}{\partial T} F_{3/2}^c + \frac{3}{2} N_c F_{1/2}^c \times \left(\frac{KT \frac{(\partial E_{Fc})}{\partial T} - K(E_{Fc} - E_c)}{(KT)^2} \right) \tag{3.33}$$

$$\frac{\partial (N_v F_{3/2}^v)}{\partial T} = \frac{\partial N_v}{\partial T} F_{3/2}^v + \frac{3}{2} N_v F_{1/2}^v \times \left(\frac{-KT \frac{(\partial E_{Fv})}{\partial T} - K(E_v - E_{Fv})}{(KT)^2} \right) \tag{3.34}$$

$$N_c \frac{\partial (F_{3/2}^c)}{\partial N} = \frac{3}{2} N_c F_{1/2}^c (KT)^{-1} \frac{\partial E_{Fc}}{\partial N} \tag{3.35}$$

$$N_v \frac{\partial (F_{3/2}^v)}{\partial N} = -\frac{3}{2} N_v F_{1/2}^v (KT)^{-1} \frac{\partial E_{Fv}}{\partial N} \tag{3.36}$$

The differential terms of Fermi-Dirac integral have been eliminated from Eqs. (3.33) to (3.36), which simplifies the calculations $\frac{\partial U}{\partial T}$ and $\frac{\partial U}{\partial N}$. Also, the derivates of quasi-Fermi levels in the conduction and valence bands with respect to temperature and carrier density can be obtained through the numerical calculation of the following approximated formula [94]:

$$E_{Fc} = (\ln u_c + \frac{u_c}{[64 + 0.05524\, u_c(64 + u_c^{1/2})]^{1/4}})KT \tag{3.37}$$

$$E_{Fv} = -(\ln u_v + \frac{u_v}{[64 + 0.05524\, u_v(64 + u_v^{1/2})]^{1/4}})KT \tag{3.38}$$

where

$$u_c = \frac{N}{N_c} \quad \text{and} \quad u_v = \frac{N}{N_v} \tag{3.39}$$

The Fermi-Dirac integral 3/2 order is approximated as:

$$F_{3/2}(\varepsilon) = [\frac{\frac{5}{2} \times 2^{5/2}}{(2.64 + \varepsilon + (|\varepsilon - 2.64|^{9/4} + 14.9)^{4/9})^{5/2}} + \frac{e^{-\varepsilon}}{\Gamma(5/2)}]^{-1} \tag{3.40}$$

where, ε is valid for all the values ranging from $-\infty$ to $+\infty$ (with a relative error below 0.7%) [93]. The Fermi-Dirac integral of 1/2 order can be approximated as [95]:

$$F_{1/2}(\varepsilon) \approx \frac{1}{2}\sqrt{\pi}[\frac{3}{4}\sqrt{\pi}a^{-3/8}(\varepsilon) + \exp(-\varepsilon)]^{-1} \tag{3.41}$$

$$a(\varepsilon) = \varepsilon^4 + 33.6\varepsilon\{1 - 0.68\exp[-0.17(\varepsilon + 1)^2]\} + 50 \tag{3.42}$$

where, ε is valid for all the values ranging from $-\infty$ to $+\infty$. Substituting the global approximations for Fermi-Dirac integrals of 3/2 and 1/2 orders (i.e. Eqs.(3.40) to (3.42)) into Eqs. (3.33) to (3.36), the two differential items $\frac{\partial U}{\partial T}$ and $\frac{\partial U}{\partial N}$ can be calculated and hence, the change of the carrier temperature due to carrier heating effects can be obtained through Eq. (3.7).

The above mentioned method provides an effective analytical method for calculation of carrier heating effects in bulk SOAs. It should be noted that the method can’t be used for quantum well SOAs due to the discontinuous distribution of the energy density and the coupling effects among the valence bands in quantum well SOAs. Besides, based on the

valid range of ε_c and ε_v, which are determined by the quasi-Fermi level and the band edge, a simpler non-global approximation for Fermi-Dirac integral of 1/2 order [92] can be obtained to calculate the carrier heating effects in bulk SOAs.

3.4.2 Gain Model of Bulk SOAs

The active region of the modelled bulk SOA is $In_{1-x}Ga_xAs_yP_{1-y}$ lattice matched to InP where x and y are the corresponding molar fractions of Ga and As, respectively. The optical gain of the active region is a function of the frequency and carrier density. The material gain coefficient $g(\omega, N)$ can be expressed as [57]:

$$g(\omega, N) = \frac{c^2}{2\hbar^{1/2} n_r^2 \tau_s(N)\omega^2}\left(\frac{2m_e^* m_{hh}}{\hbar(m_e^* + m_{hh})}\right)^{3/2}$$

$$\times\sqrt{\hbar\omega - E_g(N)}\,(f_c(\omega) - f_v(\omega)) \quad (3.43)$$

where, ω is the optical angular frequency, c is the speed of light in free space, $\hbar$ is the Plank constant h divided by 2π, n_r is the refractive index of the active region material, $\tau_s(N)$ is the radiative carrier recombination lifetime, $E_g(N)$ is the bandgap energy, $f_c(\omega)$ and $f_v(\omega)$ are the Fermi-Dirac distribution functions in the conduction and valence bands, respectively, which can be expressed as [57]:

$$f_c(\omega, N) = 1/(1 + \exp(\frac{E_a - E_{Fc}}{KT})) \quad (3.44)$$

$$f_v(\omega, N) = 1/(1 + \exp(\frac{E_b - E_{Fv}}{KT})) \quad (3.45)$$

where

$$E_a = (\hbar\omega - Eg(N))\frac{m_{hh}}{m_e^* + m_{hh}} \quad (3.46)$$

$$E_b = -(\hbar\omega - Eg(N))\frac{m_e^*}{m_e^* + m_{hh}} \tag{3.47}$$

The quasi-Fermi levels in the conduction and valence bands (E_{Fc} and E_{Fv}) are obtained based on Eqs.(3.37) and (3.38). The bandgap energy $E_g(N)$ can be expressed as [96]:

$$E_g(N) = E_{g0} - qK_g N^{1/3} \tag{3.48}$$

where, K_g is the coefficient of the bandgap shrinkage. Since the lattice of $In_{1-x}Ga_x As_y P_{1-y}$ is matched to InP, the initial bandgap energy E_{g0} is given by [97]:

$$E_{g0} = q(1.35 - 0.775y + 0.149y^2) \tag{3.49}$$

In Eq. (3.43), the carrier recombination lifetime $\tau_s(N)$ is given as:

$$\tau_s(N) = 1/(A + BN + CN^2) \tag{3.50}$$

Equations (3.43) to (3.50) model the gain of bulk SOAs, which is used to calculate the optical signal propagation in bulk SOA cavity through the travelling wave rate equations (i.e. Eqs. 3.1 and 3.2).

3.4.3 Analysis of Carrier Heating Effects on the Picosecond Pulse Amplification in Bulk SOAs

In the following, the influences of carrier heating on the picosecond pulse amplification in a bulk SOA is studied based on the analysis explained in sections 3.4.1 and 3.4.2. The photon and carrier densities are obtained by solving the travelling wave rate equations using the step-transition method [89]. The amplifier cavity is divided into 200 sections. The input signal is an unchirped Gaussian pulse centered at $3ps$ with FWHM $2ps$ and central wavelength $1550nm$. Other simulation parameters are given in Tab.3.2.

Tab. 3.2 SOA parameters for studying carrier heating effects [56]

Symbol	Description	Value
n	Background refractive index	3.22
y	Molar fraction of As in the active region	0.905
α_{FC}	Free carrier absorption cross-section	$0.5\times10^{-21}m^2$
A	Linear recombination	$1\times10^{7}s^{-1}$
B	Bi-molecular recombination	$5.6\times10^{-16}m^3s^{-1}$
C	Auger recombination	$3\times10^{-41}m^6s^{-1}$
K_g	Bandgap shrinkage coefficient	$0.9\times10^{-10}m$
τ	Electron phonon interaction time	$1ps$
α_0	Waveguide loss	$12000m^{-1}$
Γ	Confinement factor	0.45
N_0	Transparent carrier density	$1.0\times10^{24}m^{-3}$
I	Input current	$100mA$
W	SOA width	$1\mu m$
D	SOA thickness	$0.4\mu m$
L	SOA length	$750\mu m$
m_e^*	Effective mass of electron in the CB	$4.07\times10^{-32}kg$
m_{hh}	Effective mass of heavy hole in the VB	$4.19\times10^{-31}kg$
m_{lh}	Effective mass of light hole in the VB	$5.01\times10^{-32}kg$

3.4.3.1 Single Pulse Amplification

A Gaussian pulse having peak power of $10mW$ is applied to the bulk amplifier. Figure 3.7 shows variations of average gain coefficient with propagation time within the amplifier cavity. The blue and green curves are the gain coefficient variations in the presence and absence of carrier heating effect. Also shown in Fig.3.8 is the variation of the average carrier density within the amplifier. As Fig. 3.7 shows, for propagation time less than $2.15ps$ the gain coefficient without carrier heating effects is larger than that with carrier heating effects. This is because the increase of carrier temperature causes the conduction band quasi-Fermi level to decrease and that of the valance band to increase which results in suppression of the amplifier gain. Also, above $2.15ps$, the gain coefficient without carrier heating effects is smaller than that with carrier heating effects. This can be explained as follow: in case of without carrier heating effect, initially the input signal receives larger amplification, which causes significant reduction in the carrier density. Thus, after $2.15ps$, the gain coefficient without carrier heating effect becomes smaller as compared to that with carrier heating effect due to the low carrier density level (also shown clearly in Fig.3.8). As shown in Fig. 3.8 when the carrier heating effect is considered, the average carrier density level in the amplifier cavity is higher.

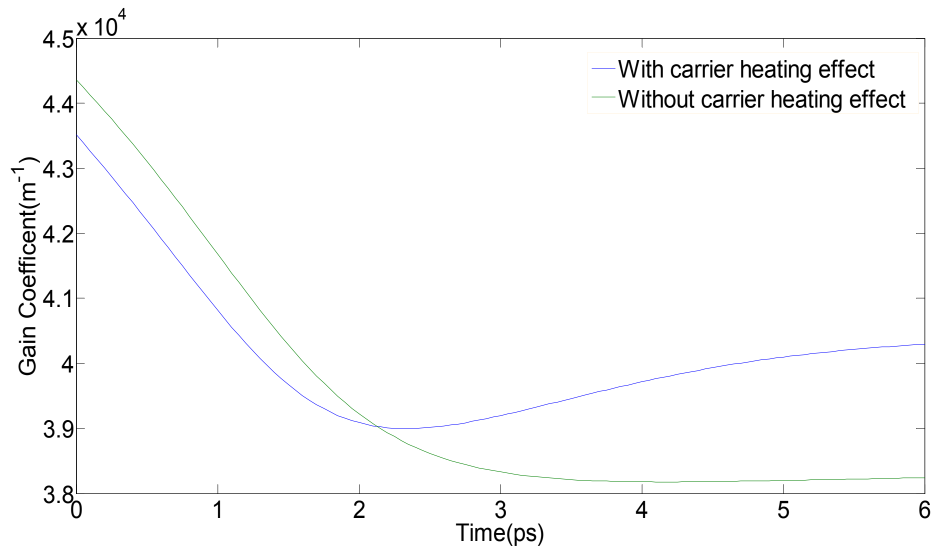

Fig. 3.7 Variations of the average material gain coefficient with the propagation time within the cavity during the pulse amplification process in a bulk SOA.

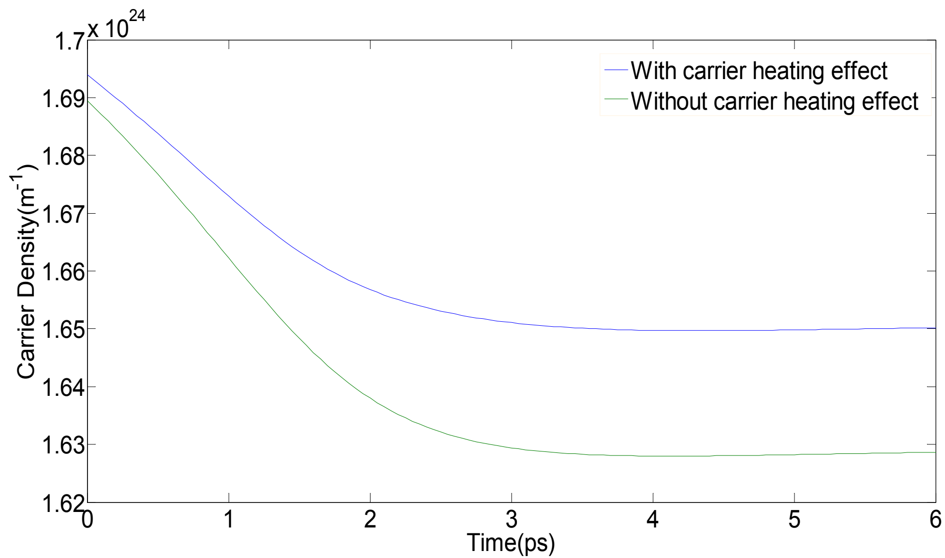

Fig. 3.8 Variations of the average carrier density with the propagation time within the cavity during the pulse amplification process in a bulk SOA.

Figure 3.9 shows the variations of the gain coefficient (solid blue curve) and the carrier temperature (dashed red curve) near the exit facet of the amplifier cavity during the pulse amplification process. The analysis indicates that the carrier temperature initially increases

due to carrier heating effect and reaches the peak $\Delta T = 19.20K$ at $t = 2.45 ps$ and then decreases. This is because initially the carrier density level is high so the pulse amplifies and then after that carrier density decreases due to gain saturation which results in reduction of electromagnetic fields within the amplifier and thus the energy density in the amplifier cavity decreases. Also, the gain coefficient decreases due to the (i) increase in the carrier temperature and (ii) decrease in carrier density during the pulse amplification process. Fig. 3.9 shows that the maximum carrier temperature occurs at $t = 2.45 ps$ whereas at this temperature the gain coefficient does not reach to its minimum value. This is because when $t > 2.45 ps$, the gain suppression induced by the decrease of carrier density (shown in Fig. 3.8) is more than the gain increase due to the decrease of carrier temperature.

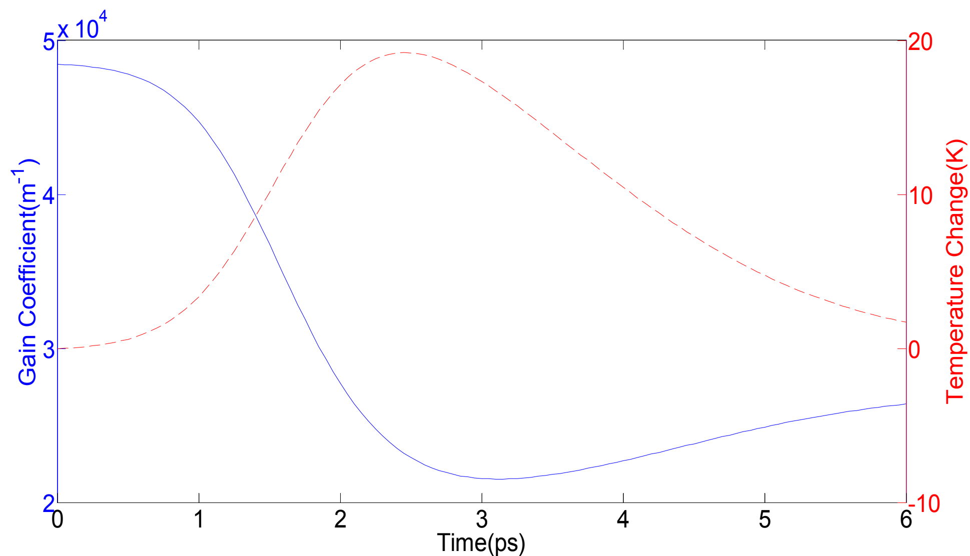

Fig. 3.9 Variations of material gain coefficient and carrier temperature near the exit facet of the amplifier cavity.

The amplified output power responses of two ideal Gaussian pulses centered at $3 ps$ with the same FWHM of $2 ps$ but different peak power values of $10 mw$ and $100 mw$ are shown in Figs.

3.10 and 3.11, respectively. The results show that in each case the carrier heating effect (CHE) reduces the peak value (P_m) of the output power, broaden the amplified pulse ($\Delta\tau_1$) and produces peak temporal shift (τ_1) as compared to both the applied input pulse and the amplified output pulse obtained without considering CHE. When the input pulse power is $10mw$ (Fig.3.10): P_m, $\Delta\tau_1$ and τ_1 are, respectively, $1.63mw$, $1.8ps$ and $1.2ps$ when CHE is present and $2.34mw$, $1.75ps$ and $1.05ps$ when it is not present. Similarly, when the peak power value of the input signal is $100mw$, P_m, $\Delta\tau$ and τ are, respectively, $2.40w$, $2.25ps$ and $2ps$ when CHE is present and $3.78w$, $2ps$ and $1.85ps$ when it is not present. Comparison of Figs. 3.10 and 3.11 shows that when the peak power value of the input signal is high, carrier heating effect causes a more pronounced distortion of the amplified output signal (i.e. larger pulse broadening and temporal peak shift).

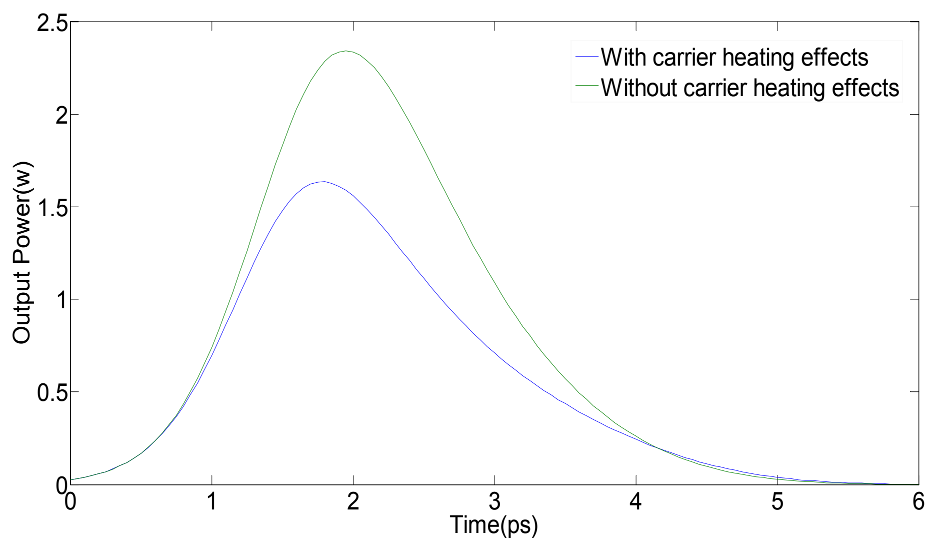

Fig.3.10 Picosecond pulse amplification in SOA with and without carrier heating effects ($Peak = 10mw$).

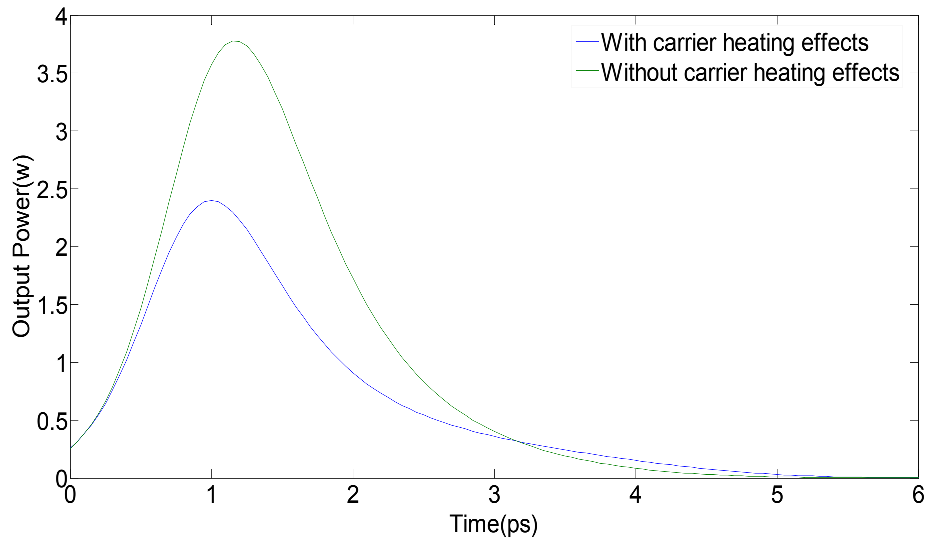

Fig.3.11 Picosecond pulse amplification in SOA with and without carrier heating effects ($Peak = 100mw$).

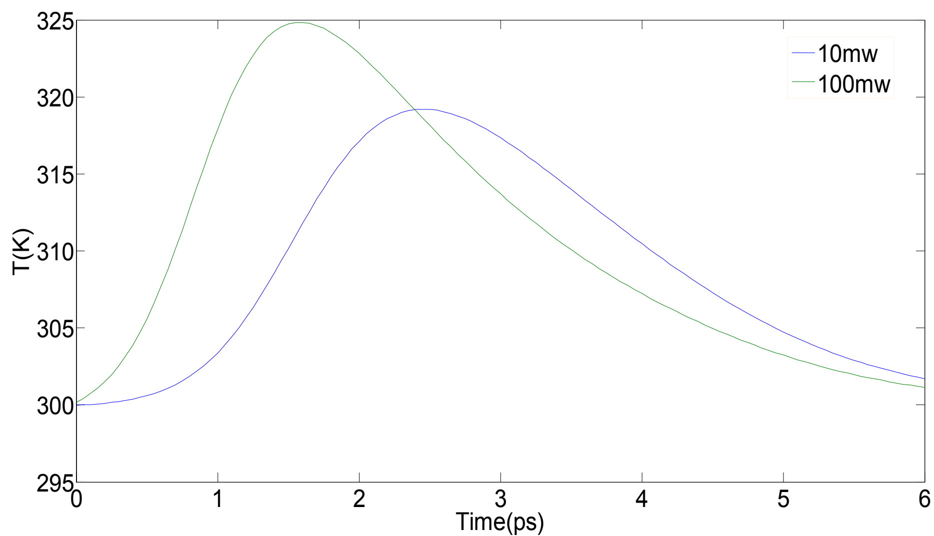

Fig.3.12 Variations of the carrier temperature near the exit facet of the amplifier cavity during the pulse amplification for the two different input signals.

Figure 3.12 shows the variations of carrier temperature near the exit facet of the amplifier cavity when the input signals peak power values are $10mw$ and $100mw$. The results show that for a given input pulse power, the carrier temperature has a maximum value which are $319.20K$ and $324.83K$ when the applied input pulse powers are $10mw$ and $100mw$,

respectively. This is because when the peak power value of the input signal is $100mw$, the electromagnetic fields (stimulated emission) and free carrier absorption in the amplifier cavity are larger, which result in higher values for both energy and carrier densities rates. When the applied input pulse peak power is $100mw$, the peak of the carrier temperature occurs earlier because when the applied input pulse power is high the amplifier earlier saturates.

Figure 3.13 shows variations of carrier temperature near the exit facet of the amplifier cavity for two different pump currents of $100mA$ and $120mA$. The peak power of the input signal in both cases is $10mw$. As the figure shows the peak carrier temperature values are $319.20K$ and $340.35K$ for the pump currents of $100mA$ and $120mA$, respectively. As the pump current increases, the temperature increases due to carrier heating effect. This is because as the pump current increases the carrier density increases too which enhances the carrier heating effect.

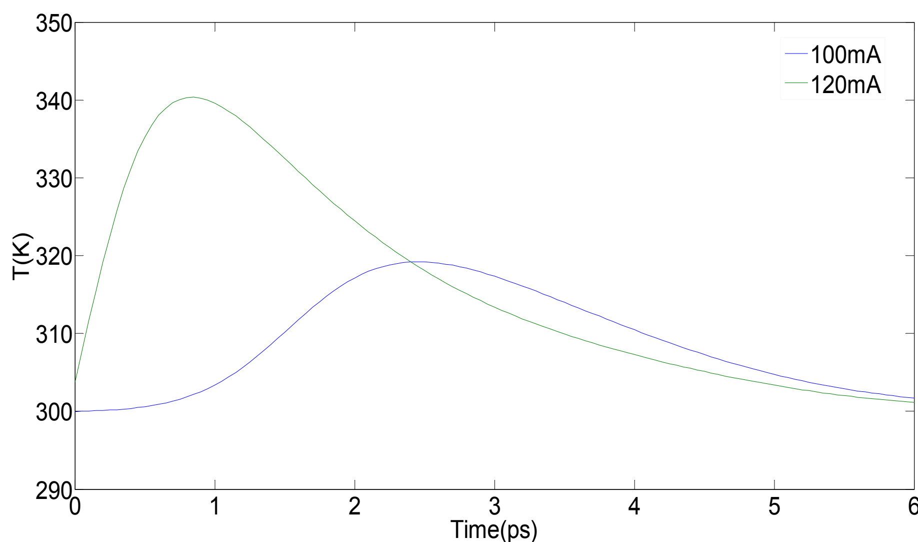

Fig.3.13 Variations of the carrier temperature near the exit facet of the amplifier cavity during the pulse amplification with different pump currents.

3.4.3.2 High Speed Pulse Train Amplification in Bulk SOA

The carrier heating effect on the high-speed pulse amplification in bulk SOA are analyzed in the following. An ideal Gaussian pulse sequence (train) with $2ps$ FWHM and $1mw$ peak power at $80Gbit/s$ is applied to the input of the amplifier.

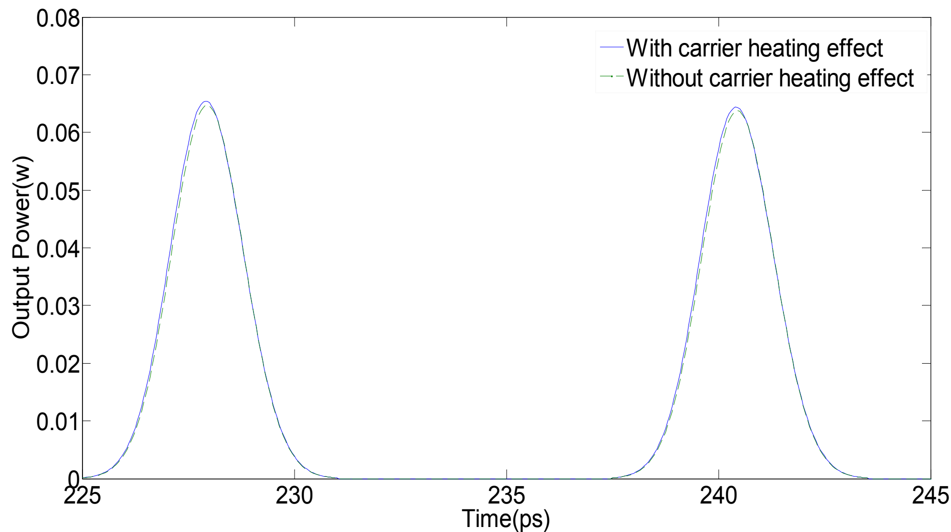

Fig. 3.14 The amplified 80Gbit/s picosecond pulse train output both in the presence (blue) and absence (green) of the carrier heating effect (red).

Figure 3.14 shows the temporal response of the amplified output pulse waveform from $225ps$ to $245ps$ when the input pulse train is applied. The result shows that the peak power value of the amplified output pulse train is slightly larger when the carrier heating effect is considered. This is because, the gain coefficient of SOA is function of both carrier density and carrier temperature. In the low-speed pulse sequence amplification, the time interval between two adjacent pulses is large enough for carrier density to recover to its normal level. Hence, the effect of carrier heating is mainly to increase the carrier temperature which results in the amplifier gain suppression. However, when the speed of the pulse train is high, the time interval between two adjacent pulses is much smaller than the carrier recovery time. In this case, in the initial stage of amplification carrier heating effect increase the carrier temperature which results in amplifier gain suppression followed

by an increase in the carrier density and hence the amplifier gain increases which surpasses the gain suppression.

The variations of the modal gain G_m ($G_m = \Gamma G_0$ with G_0 being the material gain coefficient and Γ is the amplifier confinement factor) near the exit facet of amplifier cavity both in the presence and absence of the carrier heating effect from $225ps$ to $245ps$ (i.e. the same duration as that in Fig.14) are shown in Fig. 3.15. The result shows that in the presence of carrier heating effect there exist two gain recovery processes namely a fast gain recovery process of $2.7ps$ and a slow gain recovery process. When the input rate is 80Gbit/s, the time interval between the two consecutive pulses is $12.5ps$, which is smaller than the gain recovery time of $272ps$ **.** The fast recovery process imposed by carrier heating effect forces the gain value to reach to its high level quickly as explained earlier in Fig. 3.14.

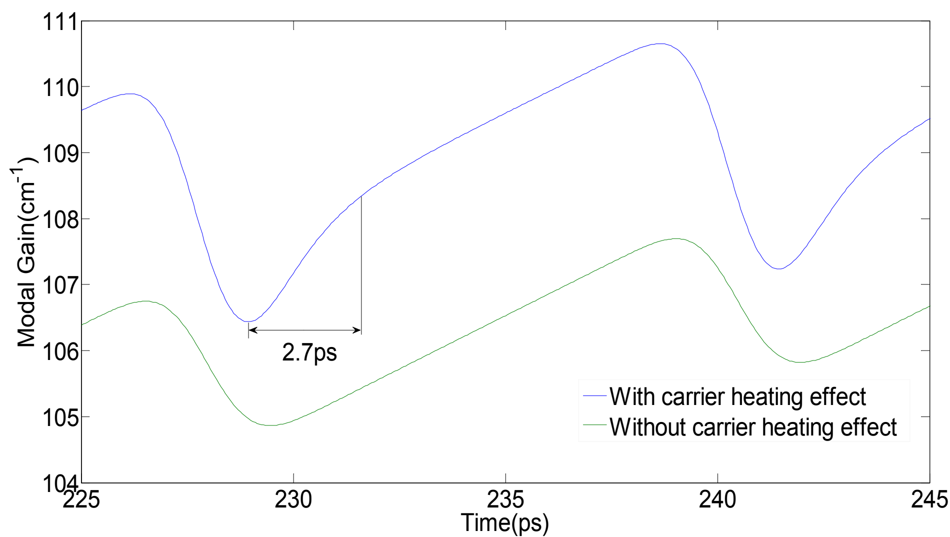

Fig. 3.15 Variations of modal gain of the amplifier near the exit facet when a Gaussian pulse train at 80Gbit/s is applied to the amplifier input both in the presence (blue) and absence (green) of the carrier heating effect.

3.5 Conclusions

In this chapter, we have discussed the carrier heating effect on optical pulse propagation in semiconductor optical amplifiers. The conventional travelling wave rate equations are employed to model the Gaussian optical pulse signal amplification in SOAs by using the step transition method. Detailed theoretical work is done to describe the effect of carrier heating in both quantum well and bulk semiconductor optical amplifiers based on the temperature dynamics rate equation. Considering different energy band distributions in quantum well and bulk amplifiers, two different methods were introduced for the analysis of carrier heating effect in quantum well and bulk optical amplifiers. For the quantum well amplifiers, the numerical method is proposed to analyse the carrier heating which takes into account the strong coupling among the HH, LH and SO bands. As for bulk SOAs, a new analytical method is proposed to investigate the carrier heating effect. This can be done by combining the Fermi-Dirac integrals of 3/2 order and 1/2 order. Effects of carrier heating on the picosecond pulse amplification in bulk and quantum well SOAs have also been investigated based on the proposed theoretical methods. Variations of carrier temperature, carrier density and gain coefficient in the amplifier cavity during the pulse propagation process are analysed. Also, the carrier heating effect on the amplification of input pulses having different peak power values are discussed and compared.

Chapter 4

Theoretical Investigation on Optimization of Semiconductor Optical Amplifier Bias Current for Distortionless Amplification of Ultrashort Pulses

4.1 Introduction

In many applications including high-speed optical fiber transmission and optical signal processing, amplification of ultrashort optical pulses is important [98-100]. Semiconductor optical amplifiers (SOA) are good candidates for amplification of ultrashort pulses because of their large amplification bandwidth [101-103]. However, due to the amplifier gain saturation caused by the slow carrier density recovery, the amplified ultrashort optical pulse suffers from distortion [44]. It has been shown theoretically and experimentally that both the amplifier structure and bias current play important roles in minimization or removal of the amplified pulse distortion [104-105]. In fact, when a SOA bias current is large, the amplified output pulse suffers from distortion due to the amplifier high gain coefficient. On the other hand, when its bias current is small, the amplifier gain is low which limits the amplification ability. Thus, we need to choose a suitable bias current for SOAs to realize the distortionless amplification of high-speed ultrashort optical pulses at high gain. In this chapter, an effective method which optimizes the SOA bias current for distortionless pulse amplification is reported.

Recently reported studies have revealed how the amplified spontaneous emission [106] and the assist light injection [48] influence the distortion of amplified output pulse. However, elimination of the amplified output pulse distortion in certain types of SOAs has not been reported. This is especially an important issue when amplification of the optical clock signal is required in the optical communications and networks. It was reported in Fig.4(a) of ref. [106] that when the bias current increases below $100mA$, the distortion of the amplified pulse is increases too. The reduction of amplified pulse distortion has been reported in Ref.[48] with the help of assist light injection at the bias current of $160mA$. In both cases although the amplified pulse distortion has reduced but not totally eliminated and no suggestion to do so is reported in the literature.

In this chapter, an effective method which optimizes the amplifier bias current in order to achieve distortionless amplification is reported. Analysis of temporal waveforms of the amplified pulse along the amplifier cavity have revealed that the maximum distance along the amplifier cavity where the amplified pulse has no temporal shift is a function of the amplifier bias current. This function can be used to optimize the bias current of a given amplifier having known length to avoid the distortion caused by the gain saturation during amplification of ultrashort Gaussian pulses. A new formula which relates the optimized bias current and the peak value of the input power is derived and also variations of the bias current with the input pulse duration is analyzed. The suitability of the proposed formula for amplifications of both single pulse and high-speed pulse train are also discussed.

4.2 Effects of Different Bias Currents on the SOA Gain Recovery and Pulse Amplification

In this section, effects of varying the amplifier bias current on gain recovery and pulse

amplification are analyzed. The pump-probe technique [48] is adopted to simulate the gain recovery of the amplifier. The pump signal is a Gaussian pulse train at $80 Gbit/s$ and each pulse is centered at $3ps$ with $10mW$ peak power and $2ps$ pulse width. The temporal waveform of the input pump signal is shown in Fig. 4.1.

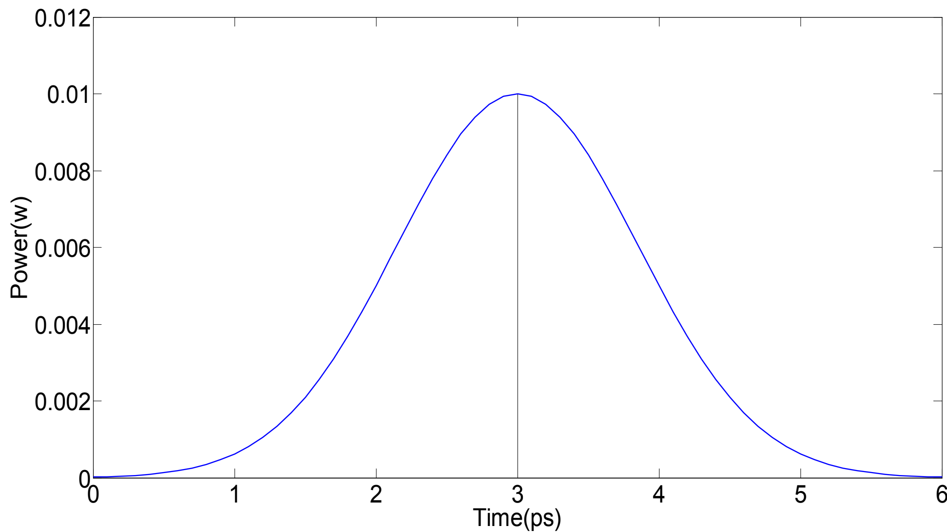

Fig. 4.1 The pump input temporal waveform of the unchirped Gaussian optical pulse.

The probe signal is assumed to be a CW optical signal with the input power $1mW$. The wavelengths of the pump and probe pulses are $1555nm$ and $1550nm$, respectively. Figure 4.2 shows variations of the normalized probe gain with the delay time 107] at the SOA bias currents of $I_1 = 80mA$ and $I_2 = 40mA$, respectively. This graph is referred to as the amplifier gain recovery response.

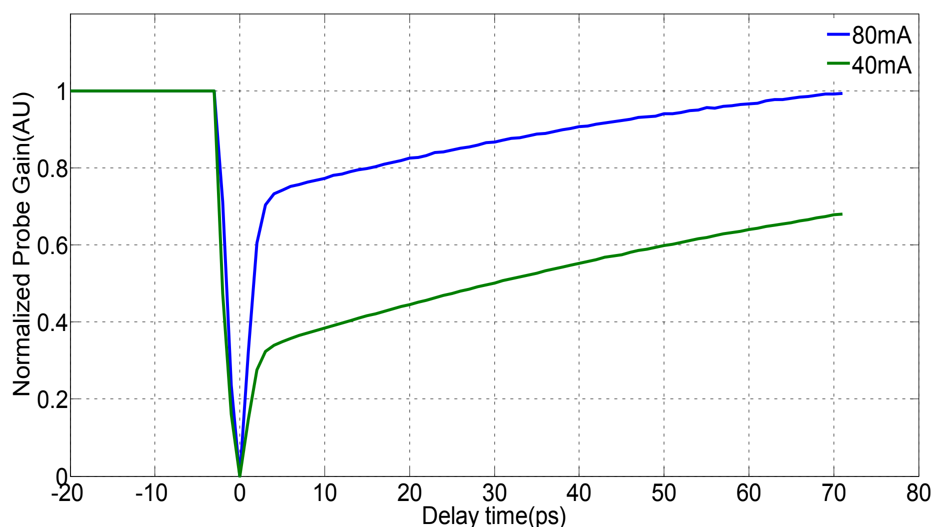

Fig.4.2 Gain recovery of the SOA at two different bias currents.

Results in Fig. 4.2 reveals that when the delay time is $70ps$, the value of the normalized probe gain at the bias current of $80mA$ reaches to unity (i.e. probe gain value before the pump signal is injected). However, the probe normalized gain is about 0.64 for the same delay time of $70ps$ when the bias current is $40mA$. This implies by increasing the amplifier bias current, its gain recovery speeds up. A Gaussian pulse similar to that of the pump pulse with different peak power ($5mW$) is applied to the input of the amplifier. Figure 4.3 shows the amplifier output temporal responses at different bias currents. Results reveal that the amplified output pulse distortion and FWHM bandwidth have increased with the bias current and also, the time at which the output pulse is maximum is shifted. Hence, an increase in the bias current reduces the gain recovery time but increases the amplified output pulse distortion. In the following a new bias current optimization method is introduces to obtain distortionless amplification at high gain which provides a useful approach to be used in practice for producing high-gain, high-speed distortionless semiconductor optical amplifier output.

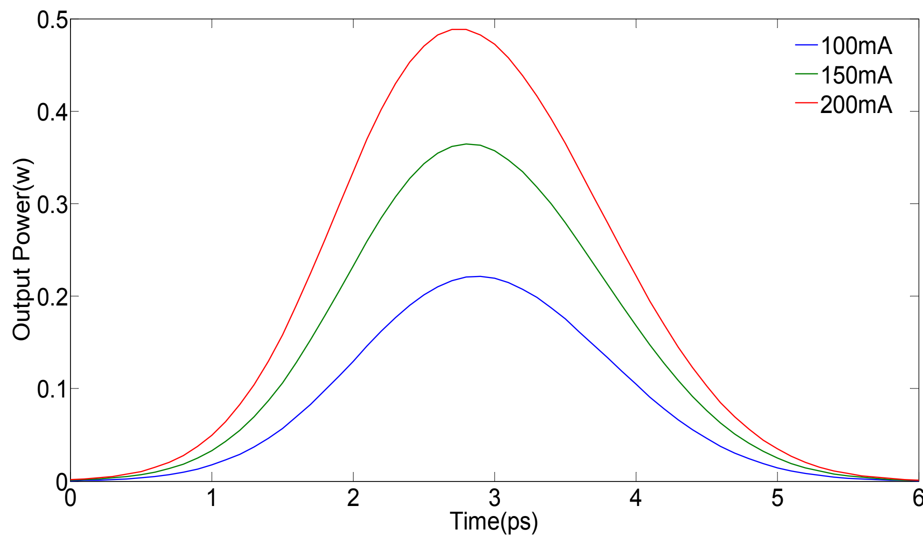

Fig. 4.3 Picosecond pulse amplification at different bias currents.

4.3 Evolution of Optical Pulse Amplification along the Amplifier Cavity

This same Gaussian pulse as the above pump pulse (shown in Fig. 4.1) is applied to the input of a $750\mu m$ long strained $In_{0.64}Ga_{0.36}As$ - $InGaAsP$ quantum well amplifier with both well and barrier widths of are $4.5nm$ and $10nm$, respectively. The barrier has a bandgap wavelength $\lambda_g = 1.15\mu m$, which is lattice-matched to the InP substrate. Also, the width and thickness of the amplifier active region are $1\mu m$ and $24.5nm$, respectively. The other parameters used in the simulation are provided in Tab. 3.2 of Chapter 3. In here the input pulse power is comparable with the amplifier saturation power, which means we should expect to see a temporal peak shift in the amplified output waveform. Figure 4.4 shows the evolution of the input pulse shape at different distances along the amplifier cavity when the applied amplifier bias current is $300mA$. As results in Fig. 4.4 show, the amplified pulse becomes asymmetric as the distance increases from $270\mu m$ to $750\mu m$ which is due to the amplifier gain saturation. The reason for this peak temporal shift in the amplified output

pulse is because of asymmetric amplification of the optical pulse that is, in the amplification process the pulse leading edge amplifies more than that of the tailing edge. The peak temporal shift value increases with the propagation distance along the amplifier cavity and is highest at the amplifier exit. In general, there exists a maximum distance z_m along the amplifier cavity where the amplified pulse waveform has no temporal shift (i.e. in this case both the input and output peaks are centered at $3ps$). In this example $Z_m = 300\mu m$ when the amplifier bias current is $300mA$.

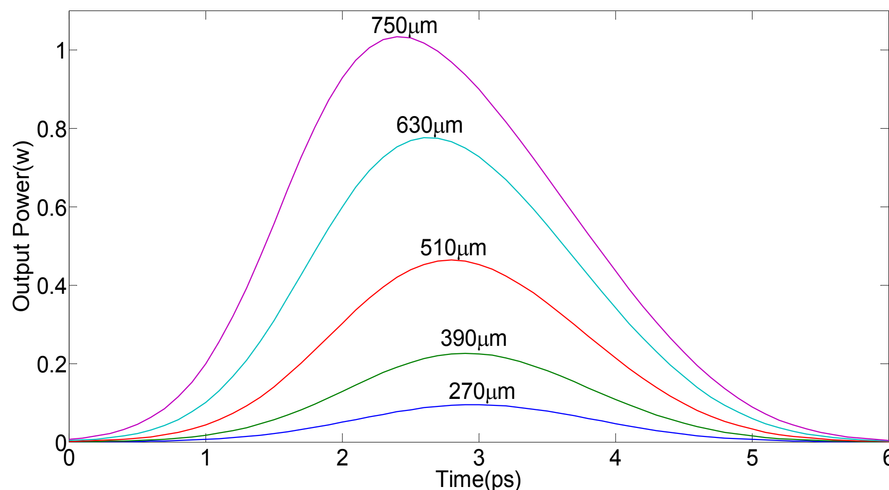

Fig. 4.4 Evolution of an unchirped Gaussian input pulse inside the strained $In_{0.64}Ga_{0.36}As$ - $InGaAsP$ quantum well semiconductor optical amplifier's cavity.

4.4 Analysis of the Optical Amplifier Bias Current for Distortionless Pulse Amplification

4.4.1 Bias Current as a Function of Distance

The bias current determines the initial carrier density along the amplifier cavity before the optical signal amplification and the carrier density distribution determines the maximum distance, z_m , along the amplifier cavity where the amplified pulse waveform has no

temporal shift. The relationship between the amplifier bias current I and the maximum distance can be expressed as:

$$I = a e^{b Z_m} + c e^{d Z_m} \quad (0 < Z_m \le L, \quad b \le 0, \quad d \le 0) \tag{4.1}$$

where, L is the amplifier cavity length and parameters a, b, c and d are functions of the applied input pulse and the amplifier parameters. To obtain these parameter we need to find first the relationship between the amplifier bias current I and the corresponding maximum distances Z_m numerically. This can be achieved by analyzing the optical pulse propagation within the amplifier cavity using the travelling wave rate equations which were discussed in Chapter 3. Then by using an appropriate curve fitting technique we can obtain a, b, c and d parameters. Tab.4.1 shows values of both bias currents (I) and their associated maximum distances Z_m for 11 different amplifier bias currents ranging from $50mA$ to $300mA$. Fig. 4.5 (dotted curve) also shows variation of I with Z_m.

Tab. 4.1 Data for the coefficient calculation

Group	Bias current I (mA)	Maximum distance Z_m (μm)
1	50	592.5
2	75	485.1
3	100	427.5
4	125	392.1
5	150	367.5
6	175	350.6
7	200	337.5
8	225	325.1

9	250	315
10	275	307.1
11	300	300

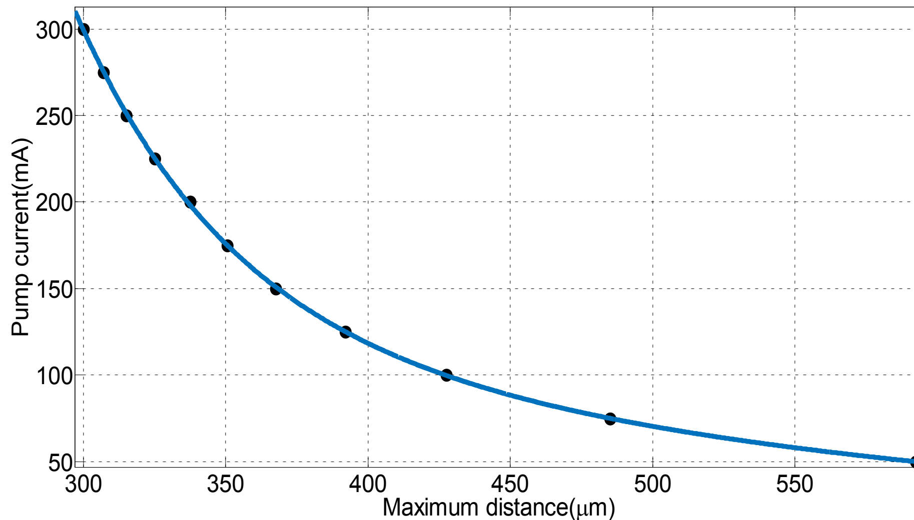

Fig. 4.5 Variations of the bias current with maximum distance Z_m.

The solid curve shown in Fig.4.5 is the fitted curve (i.e. $I = f(Z_m)$) obtained by using MatLAB curve fitting tool kit. Fig. 4.5 clearly indicates there is a very good agreement between $I = f(Z_m)$ given in Eq. (4.1) and the simulation data provided in Tab. 4.1. It should be noted that Eq.(4.1) is not only very accurate but also minimizes the computation time as we do not need to run the simulation for each bias current. Tab. 4.2 shows values of 4 parameters used in Eq.(4.1). The fitting effect is evaluated by the statistic parameter $R - square$, which describes how close the data is to be fitted regression line. The fitting result $R - square = 0.9999$ indicates that Eq. 4.1 can accurately describe the data in Tab. 4.1.

Tab. 4.2 Coefficient values and fitting effect

Coefficients	Value	Fitting effect
a	4.422×10^{4}	
b	-0.01845	$\begin{pmatrix} Goodnees\ of\ fit \\ R-square=0.9999 \end{pmatrix}$
c	324.5	
d	-0.003183	

The influence of presence and absence of the $2nd$ term in Eq.(4.1) on the accuracy of the result is investigated as shown in Fig.4.6 where the dotted, blue and green curves are, respectively, data given in Tab. 4.1, Eq.(4.1) and Eq.(4.2) given by:

$$I_1 = a \times e^{bZ_m} \tag{4.2}$$

Comparison of Eqs.(4.1) and (4.2) results with the dotted ones clearly indicates that Eq.(4.1) gives a more accurate result.

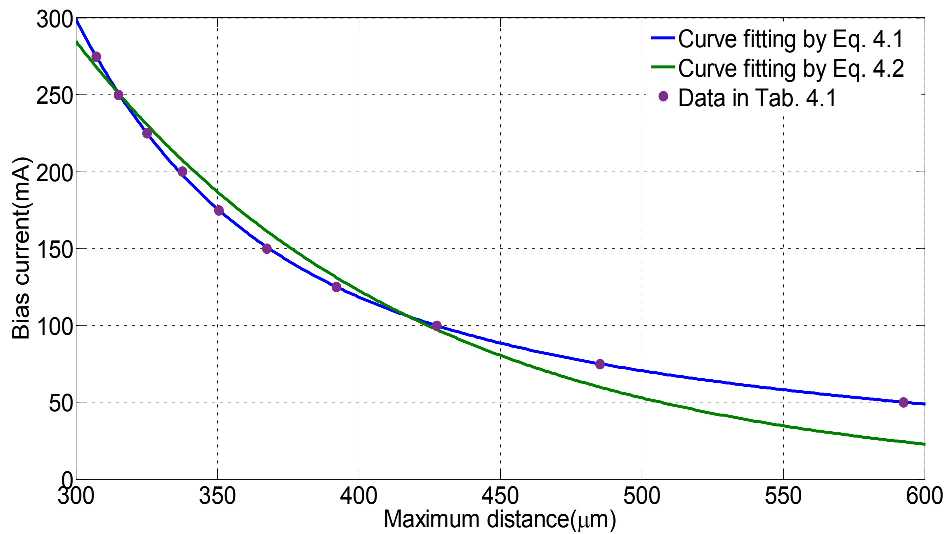

Fig. 4.6 Curve fitting results of the amplifier bias current with maximum distance Z_m .

4.4.2 Optimization of the optical Amplifier Bias Current

Equation (4.1) describes the relationship between the SOA bias current I and the maximum

distance Z_m . By substituting $Z_m = L$ (where L is the amplifier cavity length) into this equation, the maximum bias current I_m which gives distortionless pulse amplification can be obtained as:

$$I_m = ae^{bL} + ce^{dL} \tag{4.3}$$

Based on the coefficient values listed in Tab. 4.2 and $L = 750\mu m$, from the above equation $I_m = 29.86mA$. In order to verify the validity of the proposed method, this value of I_m is taken as the bias current of the amplifier. Fig. 4.7 shows the amplified output pulse for the amplifier input pulse shown in Fig.(4.1). As the result clearly shows the amplified output pulse like the input pulse is centred at $3ps$ which confirms the amplified output pulse is distortionless.

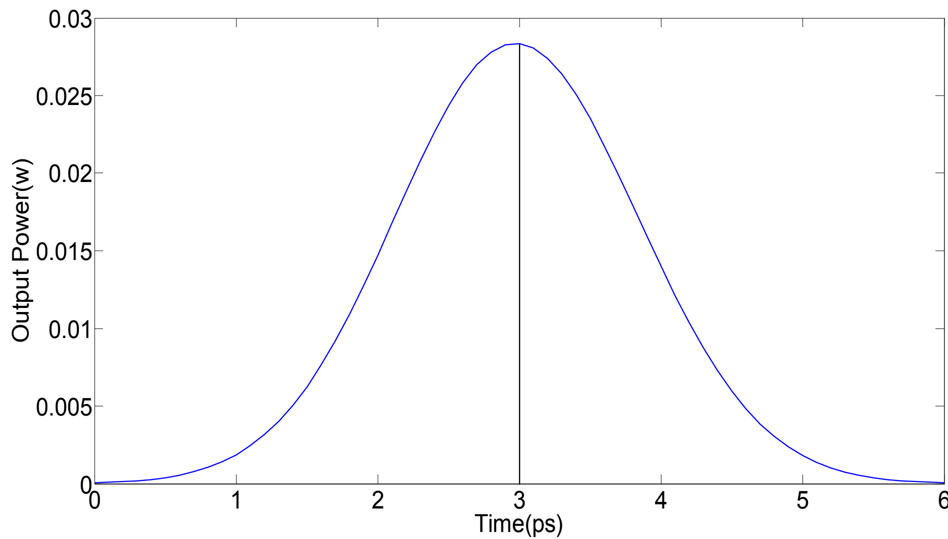

Fig. 4.7 The amplified distortionless output pulse obtained at the optimum bias current.

Let us define the peak temporal shift sensitivity parameter γ as:

$$\gamma = \frac{|t_p - t_0|}{t_0} \times 100\% \tag{4.4}$$

where, t_0 and t_p are the input and amplified output pulse peak times, respectively.

Figure 4.8 shows variations of γ with the bias current I in the vicinity of the optimized bias current $I_m = 29.86mA$. The results show that no temporal shift in the amplified output pulse waveform when the bias current changes from $28.5mA$ to $I_m = 29.86mA$. However, when the bias current changes from $I_m = 29.86mA$ to $I_m = 31mA$, γ increases by less than 2.2%. The above result confirms the strength of the proposed method in optimizing the amplifier bias current to produce distortionless amplified output waveform with minimal sensitivity.

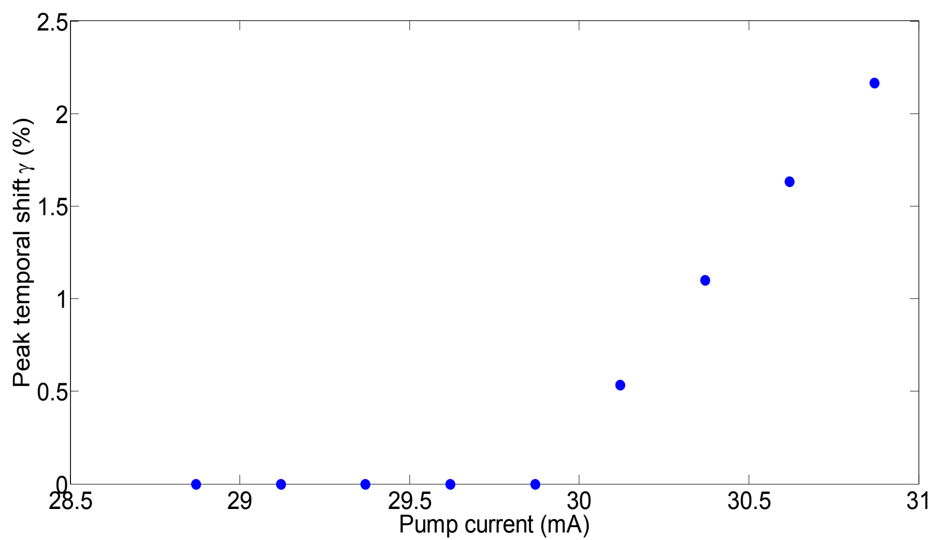

Fig. 4.8 Variations of γ in the vicinity of optimum bias current $I_m = 29.86mA$

The proposed optimization method has also been used to find a relationship between the optimized bias current and the amplifier gain for different input peak powers ranging from $1mW$ to $10mW$. In Tab. 4.3 values of the optimized bias current and amplifier gain are shown at different input peak powers.

Tab. **4.3** Optimized bias currents and amplifier gains at different input peak powers

Peak Power (mw)	Optimized bias current(mA)	Gain(dB)
1	123.61	18.74

2	94.65	16.71
3	75.82	14.94
4	63.97	13.47
5	54.73	12.04
6	47.47	10.64
7	41.69	9.28
8	37.50	8.11
9	32.54	6.48
10	29.86	4.53

The data provided in Tab. 4.3 is used to obtain a relationship between the optimized bias current I_m and the input peak pulse power P_{in}. The dotted points in Fig.4.9 shows variations of I_m with P_{in}. Also shown in Fig.4.9 is the solid curve of the best fit which can be expressed as:

$$I_m = 82.92 \times e^{-0.6372\,P_{in}} + 89.13 \times e^{-0.111\,P_{in}} \tag{4.5}$$

The $R - square$ value of the fitting is 0.9999, which indicates how well Eq. (4.5) is fitted with the data (dotted points) in Fig.4.9.

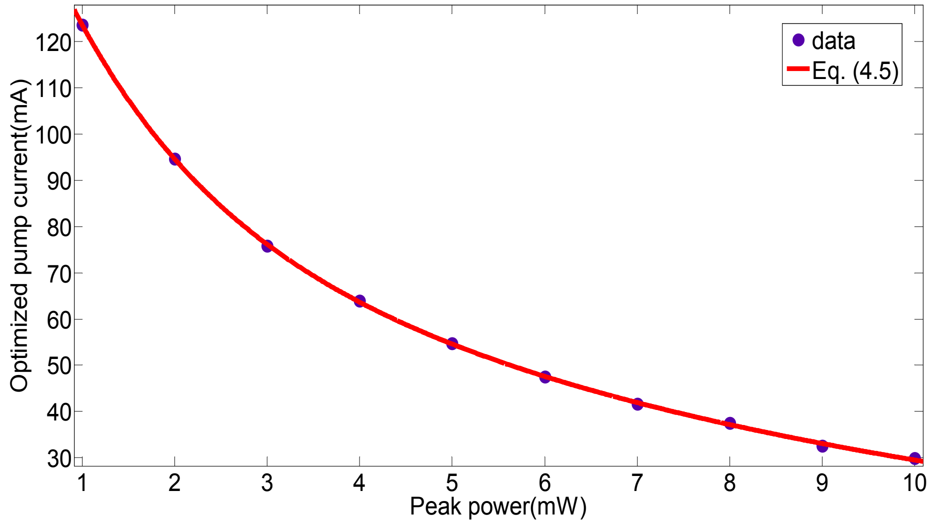

Fig. 4.9 The optimized bias current I_m versus peak power P_{in} .

4.5 Distortionless Amplification of Pulse Trains

In order to confirm that the proposed bias current optimization method can also be applied to pulse trains, we have used the pump-probe technique described in [107] to investigate the gain recovery response of a quantum well semiconductor optical amplifier (QW-SOA). In doing so, a pump pulse centred at $3ps$ with pulse width of $2ps$ and peak pulse power of $5mW$ was applied to the amplifier input. Then after a time delay $\Delta\tau$ a probe pulse similar to the pump pulse but with peak power of $1mW$ is applied to the amplifier input. It should be noted that amplification gain of the probe signal depends on $\Delta\tau$ which is the time interval between applying the probe and pump signals to amplifier. From Tab. 4.3, the optimized bias current is $54.73mA$. The amplifier normalized probe gain $\overline{G}$ is defined as [107]:

$$\overline{G} = \frac{G - G_{SAT}}{G_F - G_{SAT}} \tag{4.6}$$

where, G is the gain of amplified probe signal, G_F is the gain at full recovery and G_{SAT} is the amplifier saturation gain. Fig. 4.10 shows variations of $\overline{G}$ with the delay time which is also known as the gain recovery response of the amplifier. The negative delay time indicates that the probe pulse arrives before the pump pulse.

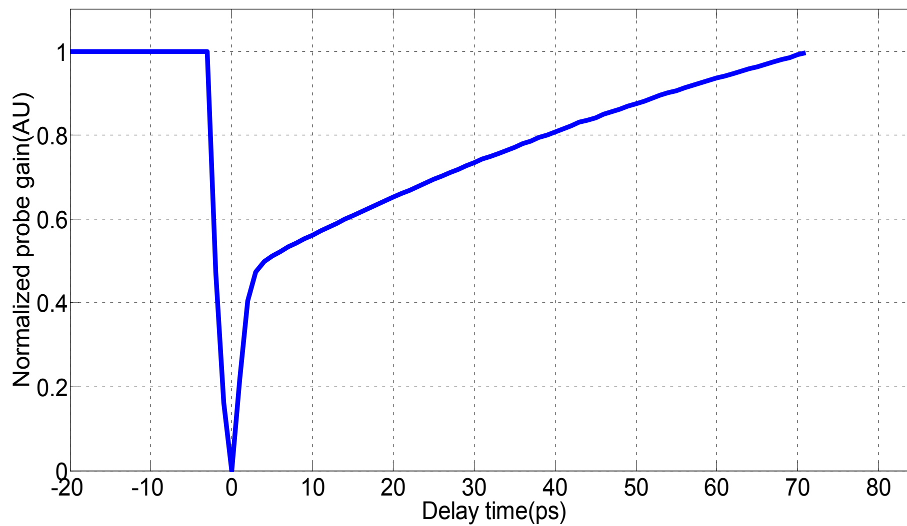

Fig. 4.10 Gain recovery of the QW-SOA.

Figure 4.10 shows that the amplifier normalized gain response has the following two recovery processes namely fast recovery process (around $3ps$) caused by carrier heating and slow recovery process which is due to slow increase in the carrier density. The results show that amplifier gain recovery time (i.e. the time at which the amplifier gain reaches to 90% of its maximum value) is $53ps$. A $14Gb/s$ pulse train, with each pulse having the same waveform and peak power as the above mentioned pump pulse, is applied to the amplifier input which is biased at the optimised current of $54.73mA$. To verify the effectiveness of the bias current optimisation we consider the following two cases; (i) the time interval between two adjacent pulses in the pulse train waveform τ_1 is more than the amplifier gain recovery time τ_{gr} ($\tau_1 > \tau_{gr}$) and (ii) $\tau_1 < \tau_{gr}$. For the above case (i)

Fig. 4.11 shows the amplified output pulse train waveform. In this figure the exit time is the time at which the amplified output pulse begins to exit from the amplifier output facet and pulse temporal time refers to the time description of the amplified pulse envelope waveform. The results clearly show that the amplified output train waveform is distortionless and the peak value of each pulse remains centered at $3ps$ and also all amplified pulses have the same peak power.

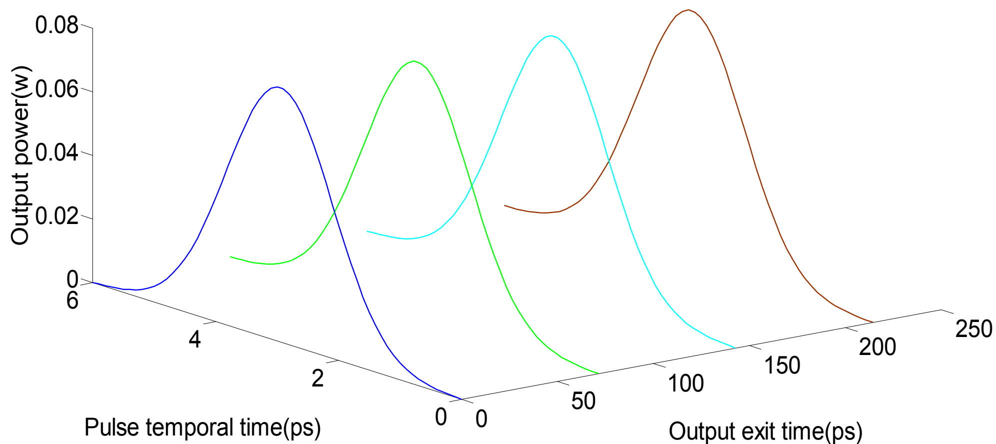

Fig. 4.11 The $14Gb/s$ amplified output pulse train at proposed optimized bias current.

We have also investigated (ii) where $\tau_1 < \tau_{gr}$. Figure 4.12 shows the amplified output pulse train waveform for a $28Gb/s$ pulse train having the same parameters as those of $14Gb/s$ pulse train. In this case also, the amplified output waveform is distortionless and each pulse peak is centered at $3ps$ however, the slow recovery has led to a gradual reduction in the magnitude of each amplified output pulse. Based on results shown in Figs. 4.11 and 4.12, it can be concluded that the above proposed bias current optimization method which results in distortionless output waveform can also be applied in high- speed pulse trains transmission.

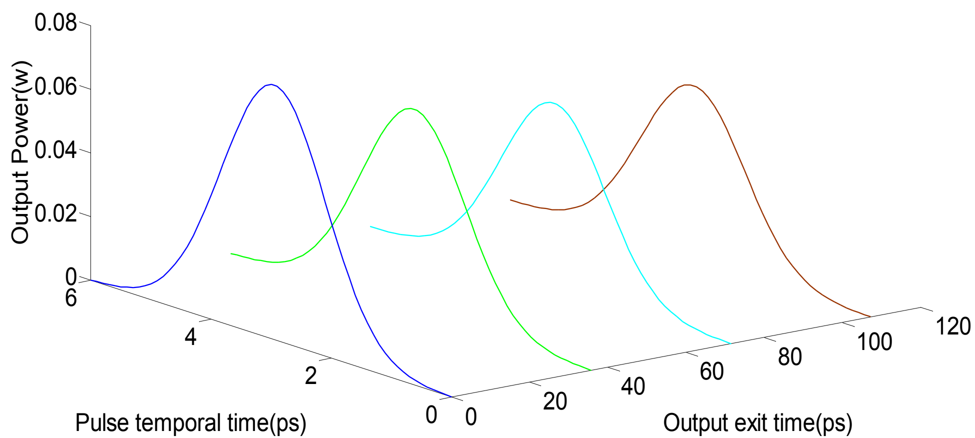

Fig. 4.12 The $28 Gb/s$ amplified output pulse train at proposed optimized bias current.

4.6 Conclusions

In this chapter semiconductor optical amplifier (SOA) bias current optimization method is introduced in order to obtain distortionless amplification at high speed transmission. To this end a new expression is introduced which relates the amplifier bias current with the maximum distance along the amplifier cavity for distortionless amplification. This expression can be used (for a given amplifier length) to obtain the optimum amplifier bias current. Moreover, a formula which gives the relationship between the optimized bias current and the input pulse peak power is derived. We have also shown that in high-speed pulse train amplification, the proposed bias current optimisation method can also be used to produce distortionless output waveform. In practical application of semiconductor optical amplifier, this proposed optimization method can applied to find a suitable bias current to realize distortionless amplification.

Chapter 5

Experimental Investigation on Optimization of Semiconductor Optical Amplifier Bias Current for High Speed Pulse Train Amplification

5.1 Introduction

Ultrafast optical pulse amplification has been under intensive investigations due to its potential application in the optical communication, optical signal processing and optical measurement [109-111]. Semiconductor Optical Amplifiers (SOAs) are excellent candidates for optical pulse amplification due to their small size, large bandwidth and simple direct current pumping. SOAs can be monolithically integrated with semiconductor optical lasers to boost up their output power for high-speed ultrashort pulse transmission [53]. Moreover, SOAs have potential to generate high-speed pulse train by merging multi-channel pulses [9]. However, gain saturation mechanism in a SOA which is due to slow recovery of carrier density leads to the distortion of amplified output pulse and hence degrade the transmission performance of high-speed ultrashort pulse. In Chapter 4 we have proposed theoretically a new SOA bias current optimization method for distortionless pulse amplification and found a formula which relates the amplifier bias current and the maximum distance along the amplifier cavity which results in distortionless output (i.e. no

temporal peak shift). Experimentally in high-speed ultrashort pulse transmission it is not easy to measure the amplified pulse temporal peak shift [30, 107]. A feasible method to minimize the distortion of the amplified output pulse train is to minimize pulse broadening of the amplified output pulse. In this chapter details of our experimental investigation on optimization of the amplifier bias current for high-speed ultrashort pulse train amplification are explained. Variations of the amplified pulse duration with the amplifier bias current are explored and based on this study we have defined the amplifier optimized bias current for high gain and low distortion pulse amplification. Relationships between the optimized bias current and the input pulse power, repetition rate and duration are experimentally investigated. Also, effects of the amplifier temperature and an assisted light injection on the amplifier optimized bias current are studied.

5.2 Experimental Investigations

Figure 5.1(a) shows the schematic diagram of the experimental setup for the high-speed pulse train amplification. The pulse train at the wavelength of $1550nm$ is generated by the active mode-locked fibre laser (hereby referred to as PriTel), which is stimulated by the RF generator. The generated pulse train is coupled into a distortion free erbium doped fibre amplifier (referred to as EDFA-1). The output power of EDFA-1 can be adjusted by controlling its pump bias current and the pulse compressor is used to adjust the pulse durations of the EDFA-1 output which is then used as SOA input signal. The optical attenuator is employed to control the input power of SOA. The SOA input pulse train's repetition rate, power and duration can be controlled by the pulse compressor, optical attenuator and EDFA1, respectively. The optical spectrum analyser (OSA) and RF analyser are used to monitor the output of the pulse laser in the frequency domain. The digital

communication analyser (DCA) is used to measure the temporal waveform of the pulse laser output. The SOA used in this experiment is provided by the Compound Semiconductor Technologies. The SOA operating temperature and wavelength are $20^{\circ}C$ and $1554nm$, respectively. In order to find the optimum value of the SOA bias current we have decreased its bias current from $200mA$ (which was more than the amplifier saturation bias current) to $30mA$ in $5mA$ steps. The SOA output pulse train is amplified by another distortion free erbium doped fibre amplifier (EDFA2) to improve the measurement accuracy of the auto-correlator (Femto-chrome). The corresponding actual experimental setup is shown in Fig. 5.1 (b).

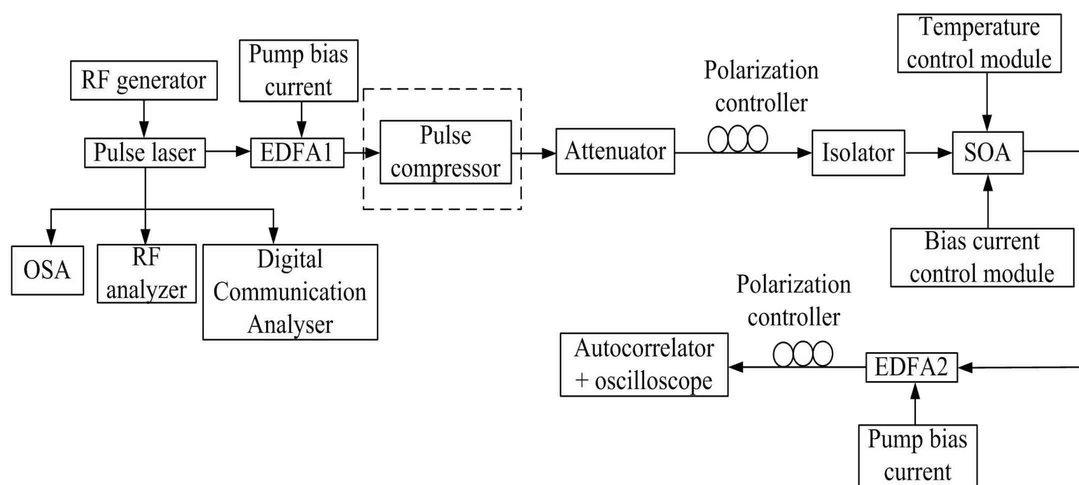

(a)

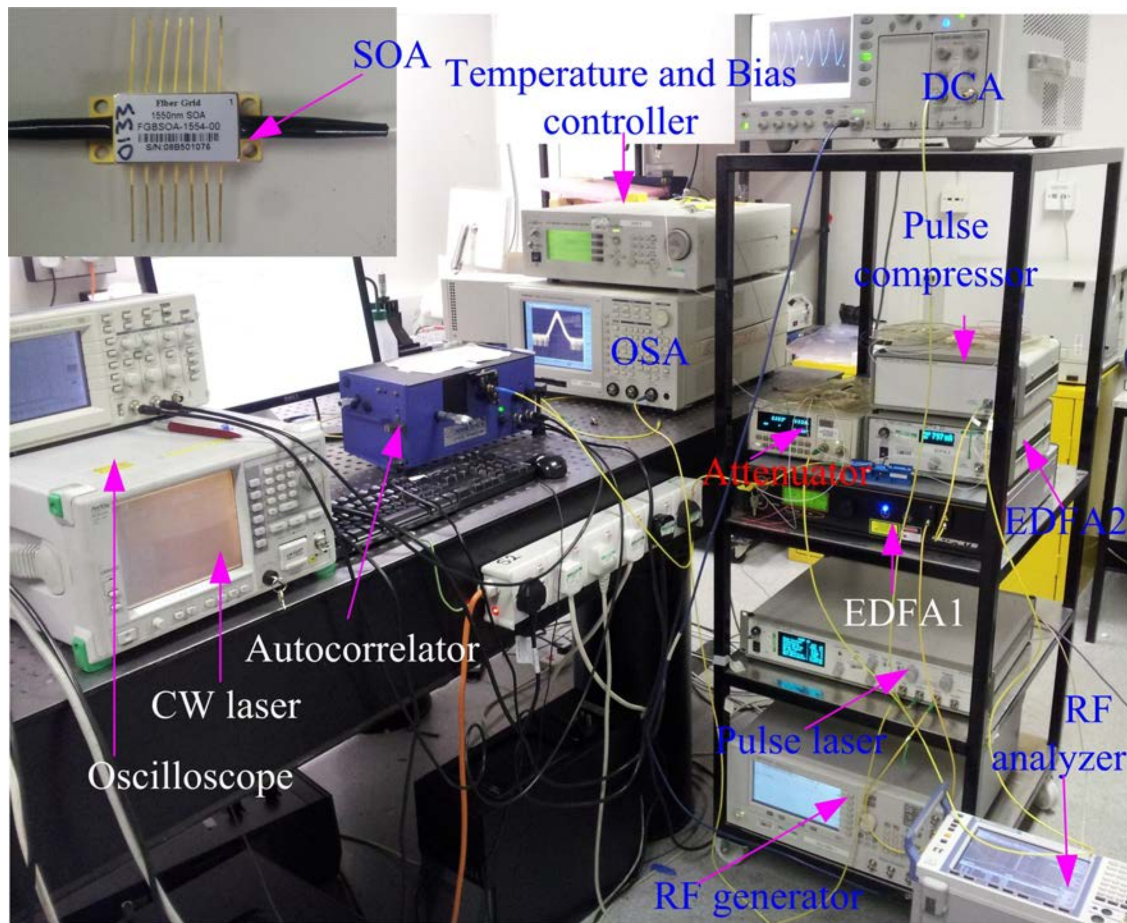

(b)

Fig. 5.1 Experimental system used to measure high-speed pulse train amplification in a SOA (a) Block diagram (b) Experimental setup.

5.3 Optimization of the SOA Bias Current

In order to find experimentally the optimum value of the SOA bias current, we have measured variations of the pulse duration of the amplified output pulse train with SOA bias currents using the setup shown in Fig.5.1 (b). The input of EDFA-1 as shown in Fig.5.1(a), is a $10GHz$ pulse train at the wavelength $1550nm$ which is generated by PriTel and its amplified output pulse train duration and power can be changed by the pulse compressor and optical attenuator, respectively. This output is then injected into the SOA input. The

function of distortionless EDFA-2 is to increase the output power of the SOA which can effectively improve the accuracy of the autocorrelation measurement obtained by the auto-correlator and oscillator. Fig. 5.2 shows the measured amplified output pulse autocorrelation results. As the results show there are two pulses in the auto-correlator response during the fixed $320ps$ measurement time interval. It should be noted that number of the pulses per a given fixed time interval is determined by the repetition rate of the pulse train. It was found that the pulse train generated by pulse laser (see Fig.5.1(a)) can be closely approximated to the Gaussian pulse, which has a better fitting result as compared with other pulse shapes. Thus, based on the autocorrelation response we can find the best Gaussian fitted response from which we can obtain the pulse duration of each pulse in the train. We have found that by dividing the duration of each pulse in the auto-correlation response by $\sqrt{2}$ the actual pulse duration can be obtained.

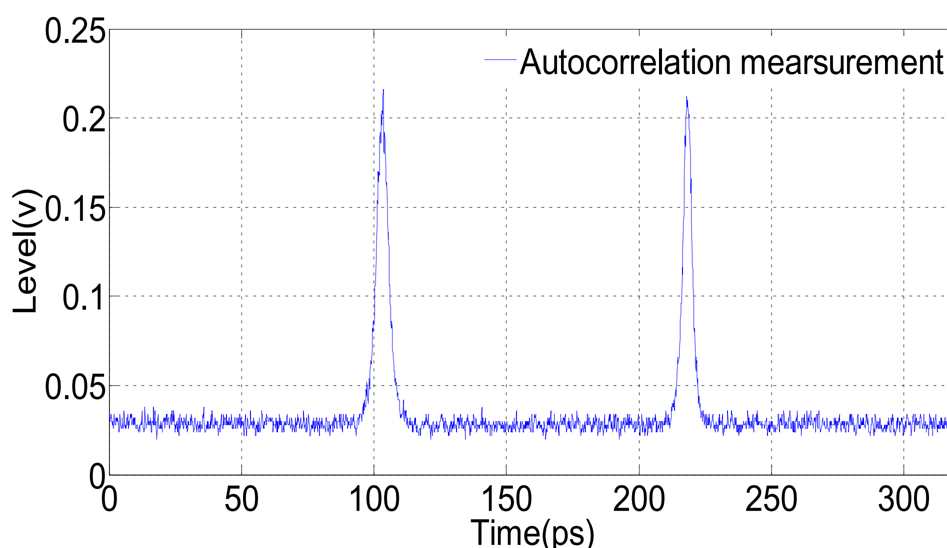

Fig. 5.2 Auto-correlation response during $320ps$ time interval.

5.3.1 Characteristics of the SOA Used in the Experiment

Prior to the exploration experiments, SOA characteristic curves are measured to make sure that SOA has a normal working status. Fig. 5.3 (a) shows the variations of the forward and

backward output powers with respect to the SOA bias currents without applying any external optical signal at its input. It was found that as the SOA bias current increases from $30mA$ to $200mA$, the forward and backward output power first increases rapidly and then slowly due to the SOA gain saturation. As results in Fig.5.3 (a) show the difference between the forward and backward output power at different bias current is very small, which the SOA is in a good operating condition. Figure 5.3 (b) shows the corresponding amplifier active region voltage (DC) variations with the injected bias currents. The voltage value is measured by the bias current control module (i.e. Temperature (T) and bias controllers in Fig. 5.1b).

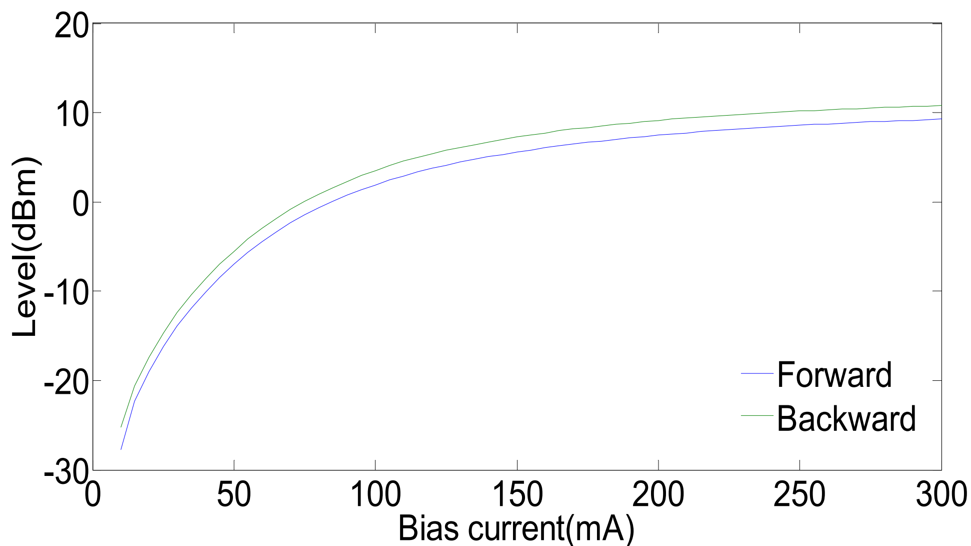

(a)

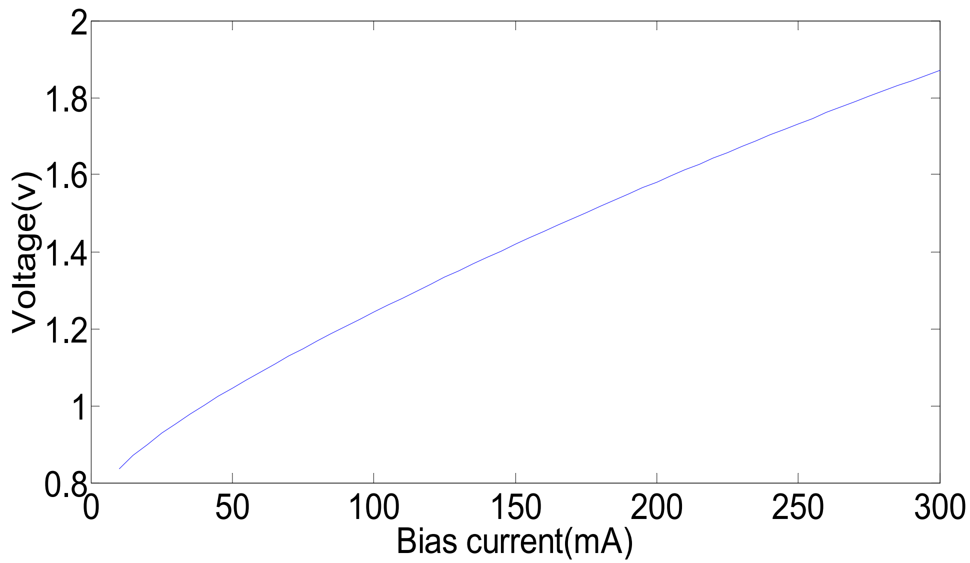

(b)

Fig. 5.3 SOA characteristics curves (a) output power (b) voltage of the amplifier active region

Figure 5.4 (a) and (b) show the forward and backward spontaneous emission spectra, respectively, at the bias current $120mA$ when no signal is applied to the SOA input. It was found that the magnitude of the SOA spontaneous emission spectrum at the bias current $120mA$ is around $-37dBm$. There exists an apparent spike in the forward spontaneous emission spectrum due to the reflection from the optical fibre facet.

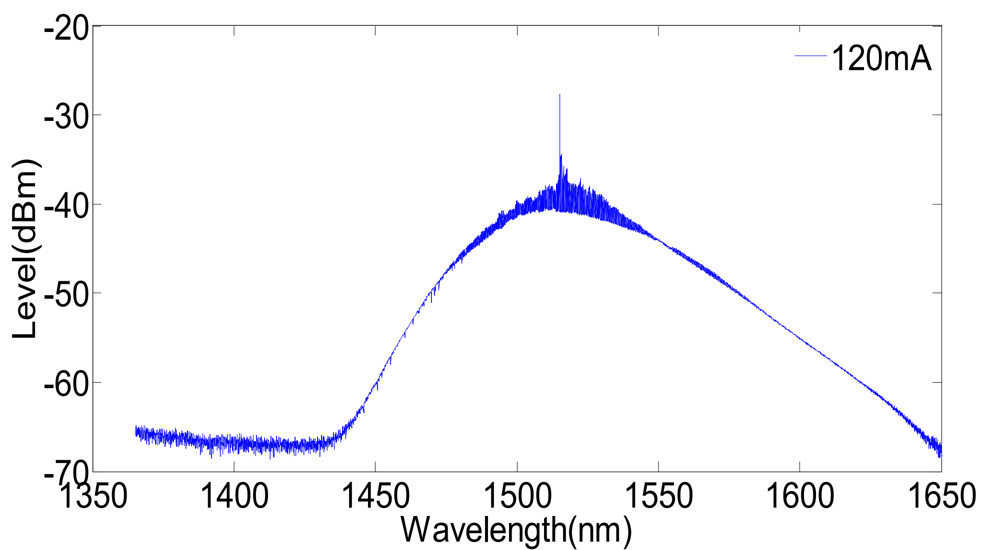

(a)

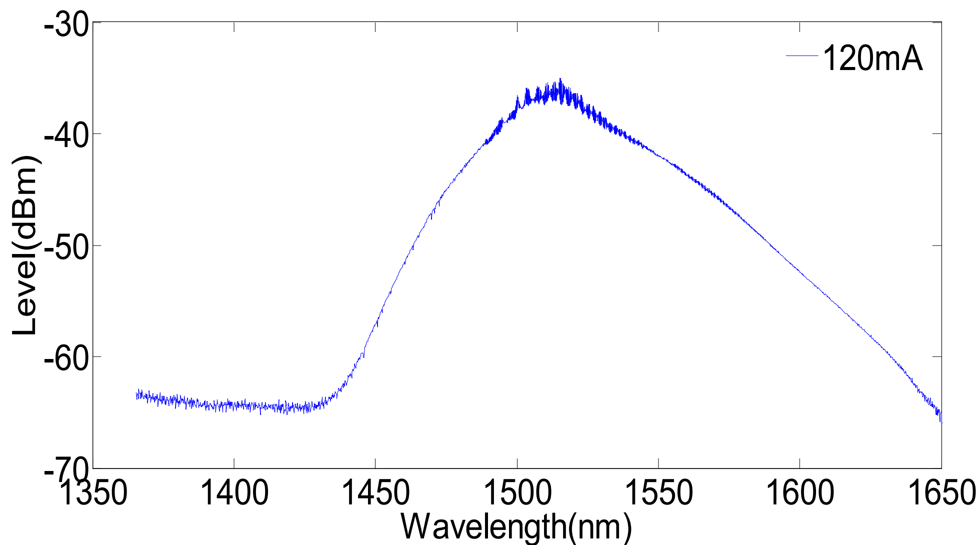

(b)

Fig. 5.4 SOA spontaneous emission spectra at the bias current $120mA$ (a) forward (b) backward

5.3.2 Optimization of the SOA Bias Current

An input pulse train with duration of $1.37\,ps$ and $10GHz$ repetition rate which is generated by the pulse laser at 1550nm wavelength is applied to the input of the SOA. Fig. 5.5 shows variations of the SOA output pulse duration with the bias currents when the pulse duration of the SOA input pulse is $1.37\,ps$ .The SOA input pulse train is centered at $1550nm$ wavelength with a repetition rate of $10GHz$. From Fig. 5.5, it can be observed that as the SOA bias current I increases from $30mA$ to $120mA$, the pulse duration of the SOA amplified output pulse increases quickly however, when the bias current further increased from $120m$ to about $185mA$ the output pulse duration increases very slowly. The figure clearly shows that at all bias currents the output pulse duration is larger than that of the input pulse. The minimum pulse duration of the amplified output pulse is $1.43\,ps$ which is obtained when the amplifier bias current is $30mA$. The variations of the SOA gain at different bias currents when the input pulse duration is $1.37\,ps$ are shown in Fig.

5.6. It was found that as the bias current increases from $30mA$ to $200mA$, the SOA gain increases from $2.17dB$ to $21.14dB$. Here, the SOA gain is obtained by measuring the peak power difference between the SOA input and output pulse spectra.

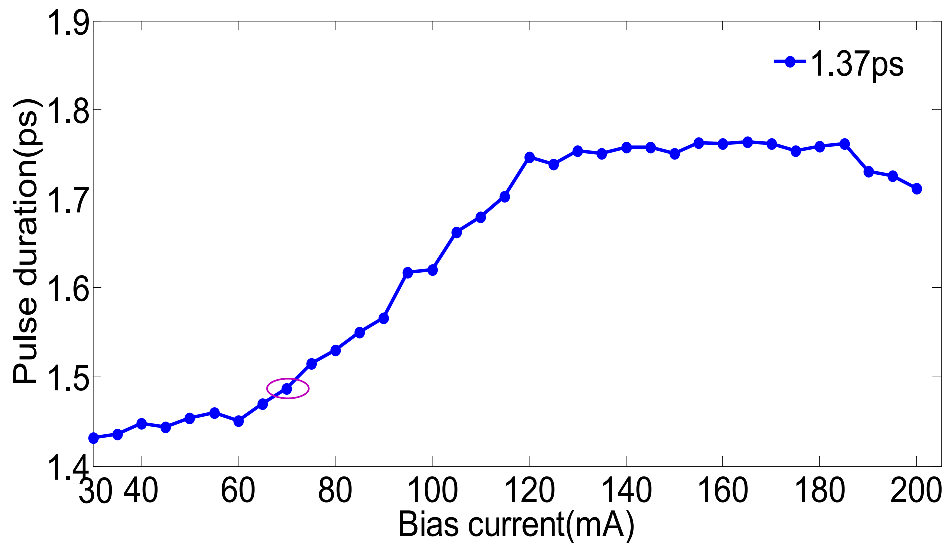

Fig. 5.5 Variations of the duration of SOA amplified output pulse at different bias currents for input pulse duration of $1.37\ ps$.

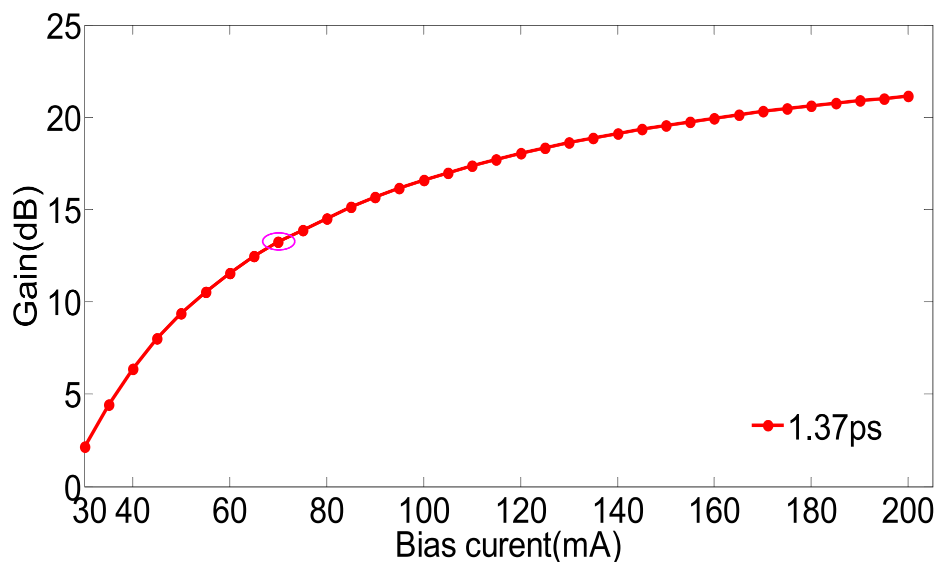

Fig. 5.6 Variations of the SOA gain at different bias currents for input pulse duration of $1.37\ ps$.

The above analysis shows that the pulse duration of the amplified output pulse is apparently broadened due to the gain saturation when the SOA bias current is high. In

order to reduce the pulse duration broadening, the SOA bias current needs to be decreased from a high level to a low level. However, the low bias current restricts the SOA unsaturated gain (see Fig. 5.6). Thus, a suitable SOA bias current needs to be chosen for realizing the pulse train amplification with low distortion and high gain. In the following, the SOA optimized bias current is defined. In order to find the optimized bias current I_{opt} , we first increase the amplifier bias current to the saturated status ($200mA$) and then decrease it until the pulse duration of the amplified output pulse satisfies the following condition:

$$\tau \leq \beta\tau_{in} \tag{5.1}$$

where, τ is the duration of the amplified output pulse, τ_{in} is that of the input pulse and β is the SOA bias current optimization coefficient. The optimized bias current I_{opt} can be expressed as:

$$I_{opt} = \max(I), where, I\ safisfies\ \tau \leq \beta\tau_{in} \tag{5.2}$$

In the following experimental analysis, we set the SOA bias current optimization coefficient β equal to 1.1. When $\beta = 1.1$ and $\tau_{in} = 1.37\,ps$ then $\beta\tau_{in} = 1.507$. Based on Eqs.(5.1) and (5.2), we can obtain the SOA optimum bias current which is $70mA$. At this bias current the amplifier gain is $13.25dB$. This point is marked in both Figs. 5.5 and 5.6.

5.4 Relationship between the SOA Optimized Bias Current and Input Pulse Duration, Power and Repetition Rate

The above analysis has shown that how we can in practice optimize the SOA bias current in order to have high gain and minimum pulse duration broadening at the amplifier output. In the following section, we have studied experimentally relationships between the

optimized bias current and input pulse train parameters (i.e. pulse duration, power and repetition rate).

5.4.1 Relationship between the Optimum SOA Bias Current and the Input Pulse Duration

The input to SOA is a $10GHz$ pulse train at $1550nm$ wavelength and its pulse duration can be controlled by the pump current of EDFA-1 as shown in the experimental system of Fig.5.1(a). Figure 5.7 shows the variation of the duration of the SOA input pulse τ_{in} with the pump current of EDFA-1. It was found that τ_{in} decreases from $4.95\,ps$ to $1.37\,ps$ with the EDFA-1 pump current increasing from $700mA$ to $1100mA$. The power of the SOA input pulse train is fixed at $-18.4dBm$ by controlling the optical attenuator. Fig. 5.8 shows the schematic diagram of the temporal waveform of the input pulses with different pulse durations at the same input power.

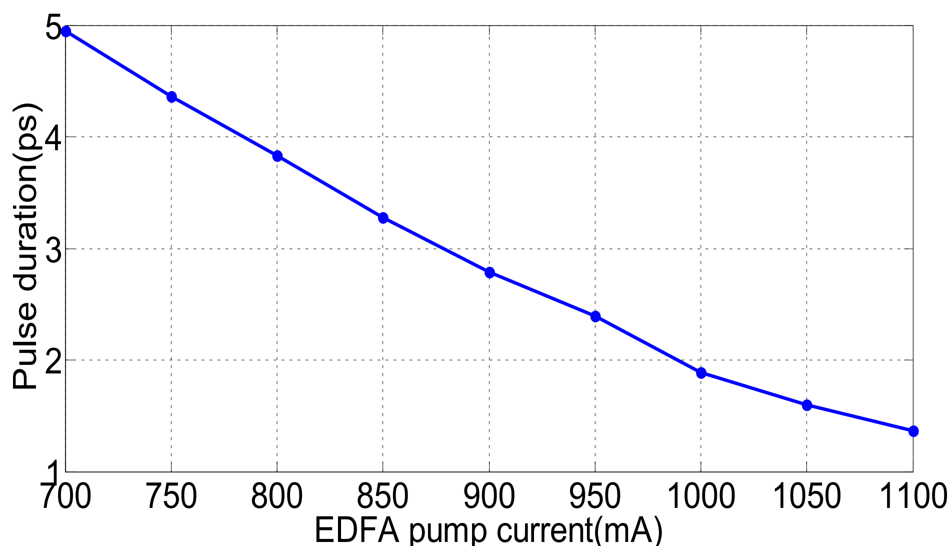

Fig. 5.7 Variation of the pulse duration of the SOA input pulse train with the pump current of EDFA-1.

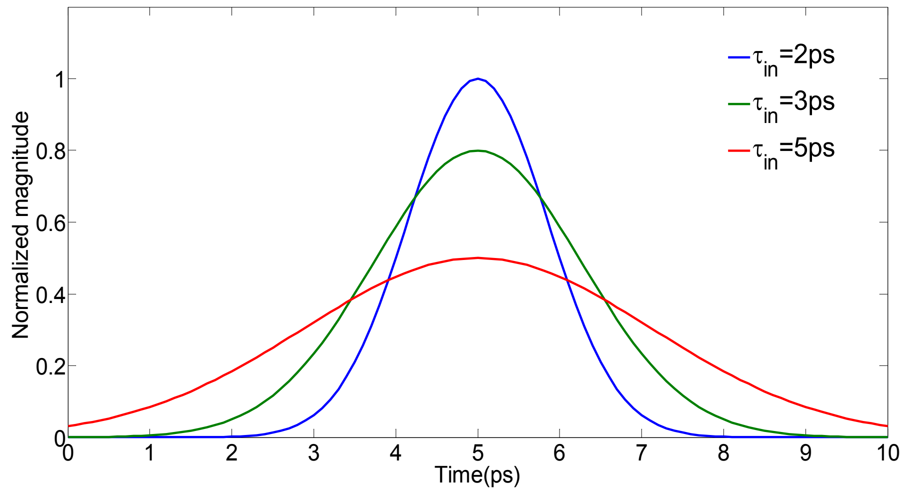

Fig. 5.8 Schematic diagram of the input pulse train with fixed power and different pulse durations.

In the following, the experimental system shown in Fig. 5.1a is adopted to explore the relationship between the SOA optimum bias current and its input pulse duration τ_{in} . Fig. 5.9 (a)-(d) shows the variations of the pulse duration of the SOA amplified output pulse train τ_{out} with the bias currents when τ_{in} are $1.60\,ps$, $1.89\,ps$, $2.39\,ps$ and $2.79\,ps$, respectively. It is found that at certain τ_{in} , as the SOA bias current increases from $30mA$ to $200mA$, the variation process of τ_{out} can be divided into the fast increase stage and the slow increase stage. As τ_{in} increases from $1.60\,ps$ to $2.79\,ps$, the bias current threshold between the two stages increases from $130mA$ to $155mA$ and the difference between the maximum value of τ_{out} and the minimum value of τ_{out} decreases from $0.647\,ps$ to $0.404\,ps$, which indicates that the pulse train with the narrower pulse duration is more easily broadened in the SOA amplification process. Based on Eq. 5.2, the optimum bias current has been obtained and labelled in Fig. 5.9 (a)-(d).

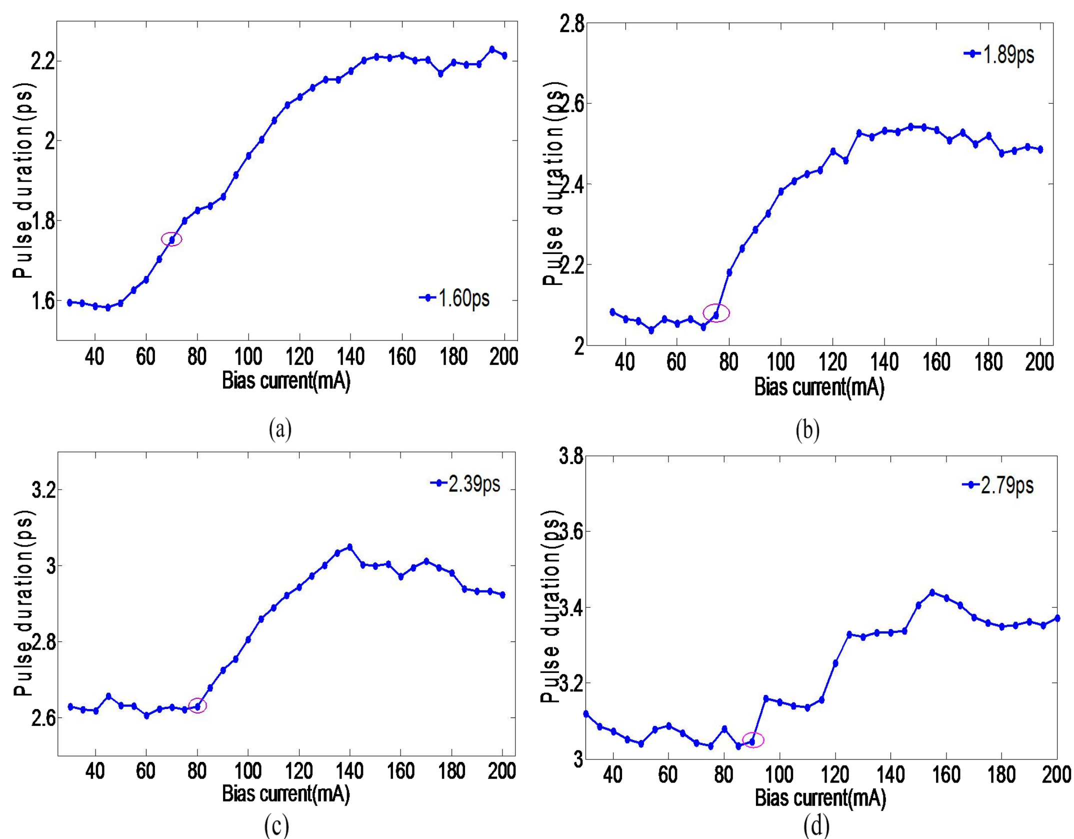

Fig. 5.9 Pulse duration of amplified output pulse train vs SOA bias currents at different SOA input pulse durations (a) 1.60 *ps* (b) 1.89 *ps* (c) 2.39 *ps* (d) 2.79 *ps*

The relationship between the SOA input pulse duration τ_{in} and the SOA optimum bias current is shown in Fig. 5.10 (blue line). Also, the red line curve in Fig.5.10 shows the SOA gain at the optimum bias current. It was found that both the SOA optimum bias current and gain increase as τ_{in} increases which indicates that for the same input power, the pulse train with the larger pulse duration can be amplified with less distortion at a higher gain. This is because for the same input power, the pulse with a larger duration has a lower peak power (shown in Fig. 5.8), which depletes fewer carrier densities during the pulse amplification process. Hence, at the same bias current the input pulse with a larger duration is more difficult to suffer from distortion.

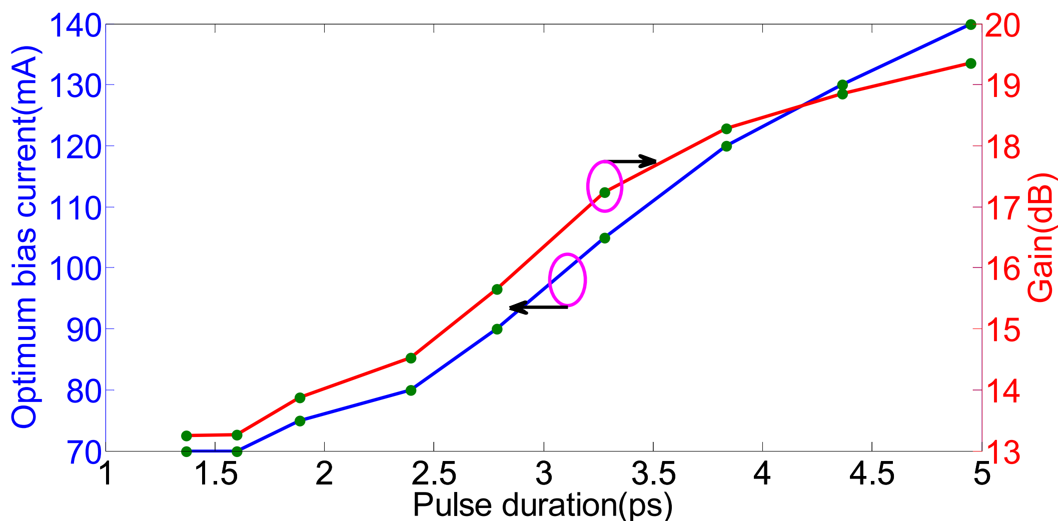

(b)

Fig. 5.10 Variations of the SOA optimum bias and gain at the different SOA input pulse durations.

5.4.2 Relationship between the Optimum SOA Bias Current and the Input Pulse Power

The power of the SOA input pulse train is an important parameter that influences the SOA gain dynamics. In the following, the relationship between the SOA optimum bias current and input pulse train power is investigated. The pulse train with the repetition rate $10GHz$ at the central wavelength $1550nm$ was generated by the pulse laser (Fig.5.1(a)). The pulse compressor is removed from the experimental system shown in Fig. 5.1a and the output of EDFA-1 is directly connected to the attenuator. Here, the attenuator is used to vary the applied SOA input pulse train power. The analysis of Fig. 5.10 has shown that the duration of the SOA input pulse τ_{in} has a big influence on the SOA optimum bias current. Thus, we first explore the influences induced by the attenuation of optical pulse on τ_{in}. Figure 5.11 shows the variation of τ_{in} at the different attenuation values. It was found that as the values of the attenuator increases from $0dB$ to $10dB$, the maximum and minimum values of τ_{in} are $3.247\ ps$ and $3.118\ ps$, respectively, (i.e. $\Delta\tau_{in} = 0.129 ps$). Based on Fig.5.10, this small

variation ($\Delta\tau_{in}$) has very little influence on the SOA optimum bias current. Fig. 5.11 confirms that variation of τ_{in} caused by attenuation of optical pulse has negligible effect on the SOA optimum bias current.

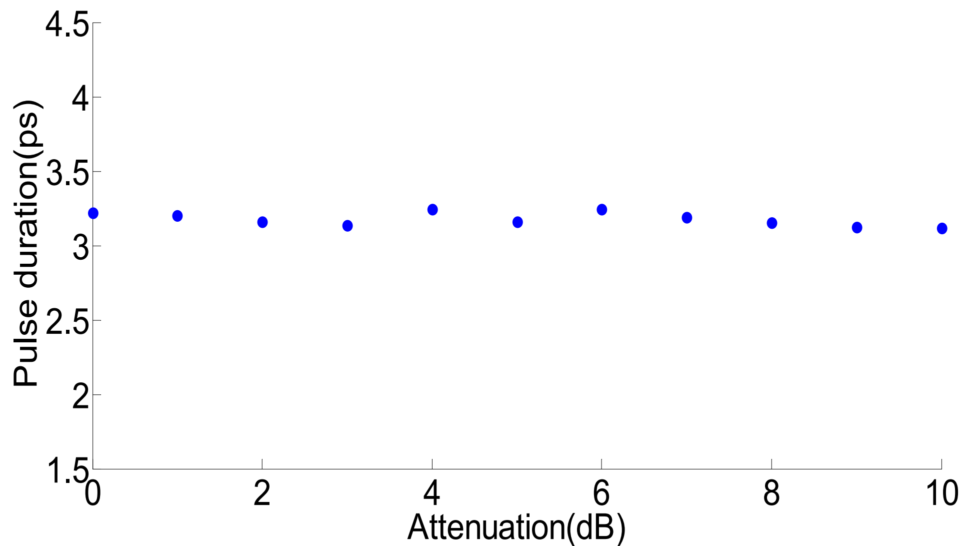

Fig. 5.11 Variation of SOA input pulse train duration at different optical attenuation values.

Figure 5.12 shows the variation of the SOA optimum bias current with the optical attenuator (blue line) and the SOA gain at the corresponding optimum bias current (red line). It was found that as the value of the attenuator increases, which means that the power of the SOA input pulse train reduces, both the optimum bias current and the corresponding SOA gain increases. This is because when the power of the SOA input pulse train is high, the amplification of the leading edge of the input pulse depletes more carriers, which results in lower carrier density level in the amplifier cavity; the SOA gain decreases when the pulse tailing edge arrives. The inconsistent amplification between the leading edge and the tailing edge of the input pulse induces large distortion of the amplified output pulse. Thus in this case that the input pulse train has a higher power (the attenuation value is low), the optimum bias current and the associated SOA gain are lower. The experimental result shown in Fig. 5.12 is in agreement with the theoretical calculation result shown in Fig. 4.9

of Chapter 4. Both of the theoretical and experimental results have shown that as the power of the SOA input pulse increases, the optimum bias current decreases. The experimental result of Fig. 5.12 confirms the validity of the newly proposed SOA bias current optimization method discussed in Chapter 4.

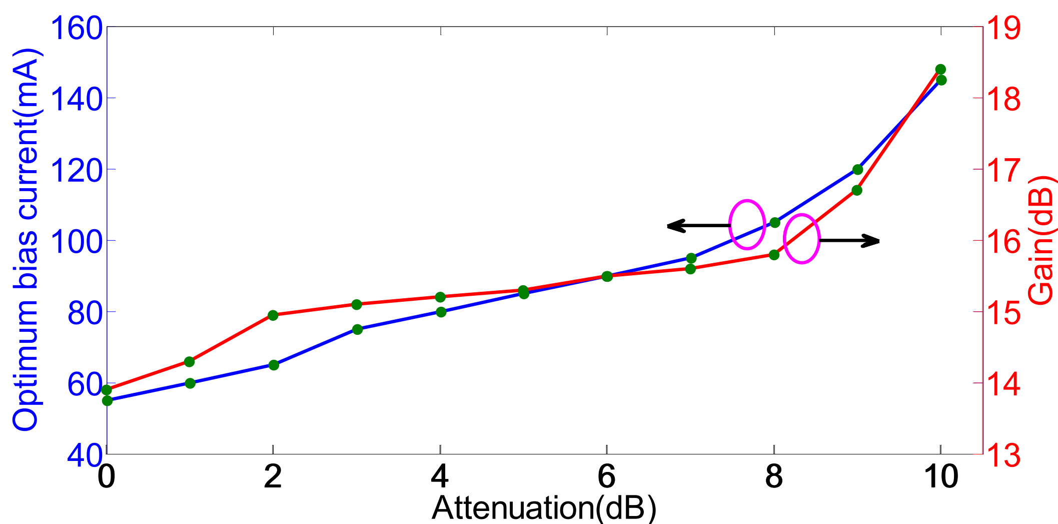

Fig. 5.12 Variations of the optimum SOA bias currents and gain at the different attenuation levels.

5.4.3 Relationship between the Optimum SOA Bias Current and the Repetition Rate of the Input Pulse Train

In the following the experimental system shown in Fig. 5.1a is used to explore the relationship between the SOA optimum bias current and the repetition rate of the applied input pulse train. The pulse laser generates the input pulse train with central wavelength of is $1550nm$ and repetition rates which changes from $10GHz$ to $20GHz$. The input pulse train power is fixed at $-14dBm$ by controlling the attenuator. Fig. 5.13 shows variations of the SOA optimum bias current and its associated gain with the input pulse train repetition rate. The results reveal that both SOA optimum bias current and gain increase with the input pulse repetition rate. This is because, at higher input pulse train repetition rate, the time interval between two adjacent pulses becomes shorter and this does not provide enough

time for the SOA carrier density to fully recover which results in having less carrier density level in the SOA cavity. This implies SOA needs more optimum bias current in order to accelerate the carrier recovery speed for distortionless amplification of the applied input pulse train.

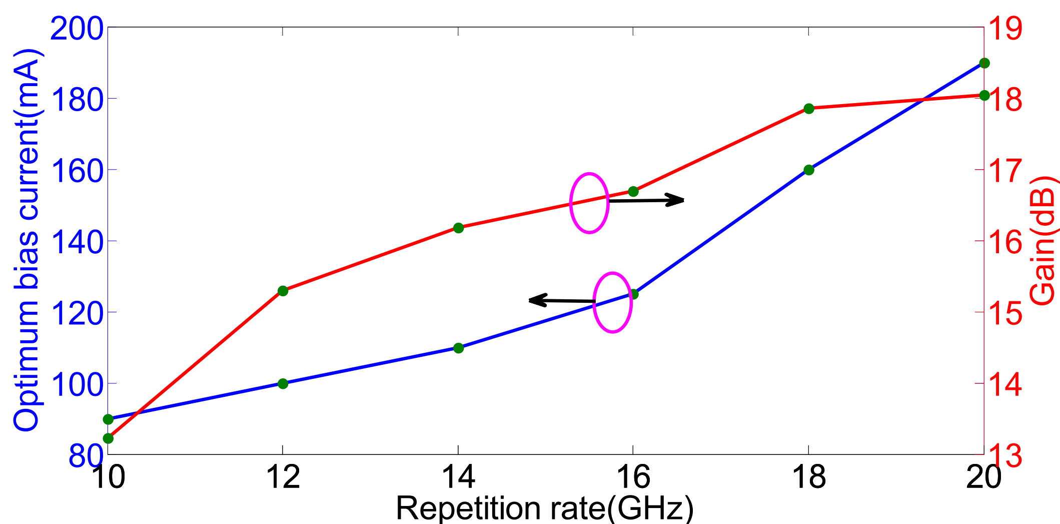

Fig. 5.13 Variations of the SOA optimum bias current and gain with the applied input pulse train repetition rate.

In the following, the pump-probe experiments are performed to analyse the relationship between the SOA bias current and its carrier density recovery speed. The schematic diagram for the experimental system is shown in Fig. 5.14. The forward signal is a pulse train with power, pulse duration and repetition rate of $10dBm$, $3.2ps$ and $10GHz$, respectively, which is generated by the pulse laser. The backward probe signal is a continuous wave optical signal with the power $0dBm$, which is obtained by the CW laser. The wavelengths for the pump and probe signals are $1550nm$ and $1555nm$, respectively. The temporal waveform of SOA amplified output pulse is measured by the digital communication analyser DCA2 in Fig.5.14. Figure 5.15 shows the SOA gain recovery process at three different bias currents of $100mA$, $120mA$ and $150mA$. It was found that as the SOA bias current increases, the average output power in a pulse period ($100ps$)

increases too, which implies the amplifier obtains a higher carrier density level due to a faster carrier density recovery.

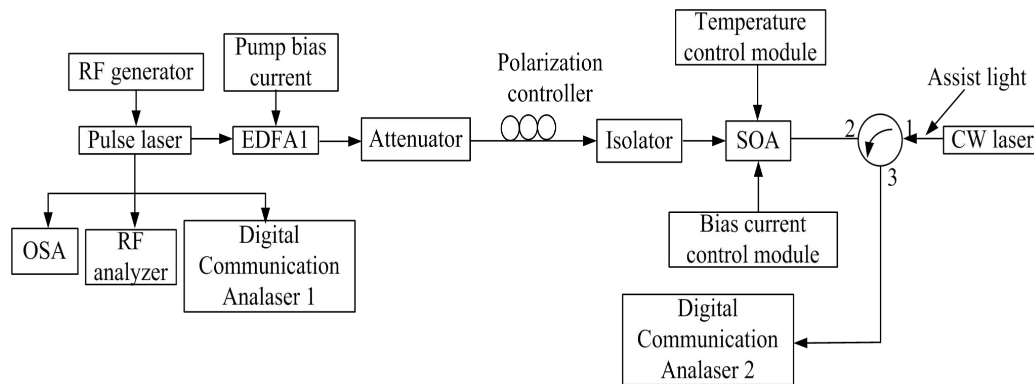

Fig. 5.14 Schematic diagram of the experimental system for high-speed pulse train amplification with the assist light injection.

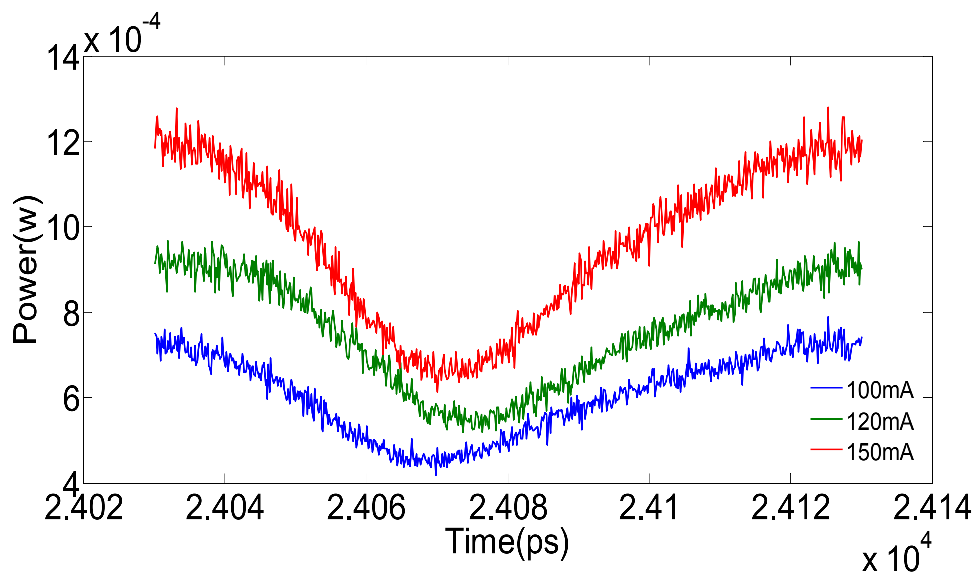

Fig. 5.15 SOA gain recovery at different amplifier bias currents.

5.5 Effects of Assist Light Injection and Temperature on SOA Optimum Bias Current

5.5.1 Effects of Assist Light Injection on the SOA Optimum Bias Current

Assist light injection can speed up the carrier recovery in the amplifier cavity and reduces the distortion of SOA amplified output pulse [48]. In this section, the experimental system shown in Fig. 5.14 is used to investigate the effect of assist light injection on variations of the amplifier optimum bias current with the input pulse train repetition rates. The digital communication analyser (DCA-2) in Fig. 5.14 is replaced by the autocorrelator for measuring the pulse duration of the amplified output pulse. The CW laser generates the assist light (continuous wave) with the central wavelength and power of $1535nm$ and $2dBm$, respectively, which counter-propagates into the SOA through the optical circulator. The pulse laser generates pulse train at $1550nm$ wavelength, which is forward injected into the SOA. Figure 5.16 shows the variations of SOA optimum bias current with input pulse train repetition rate both in the presence and absence of the assist light. Results reveal that the assist light injection increases the SOA optimum bias current at all repetition rates. This is because the amplification of injected assist light results in further depletion of the carrier density and hence which means SOA gain saturation occurs at a higher bias current.

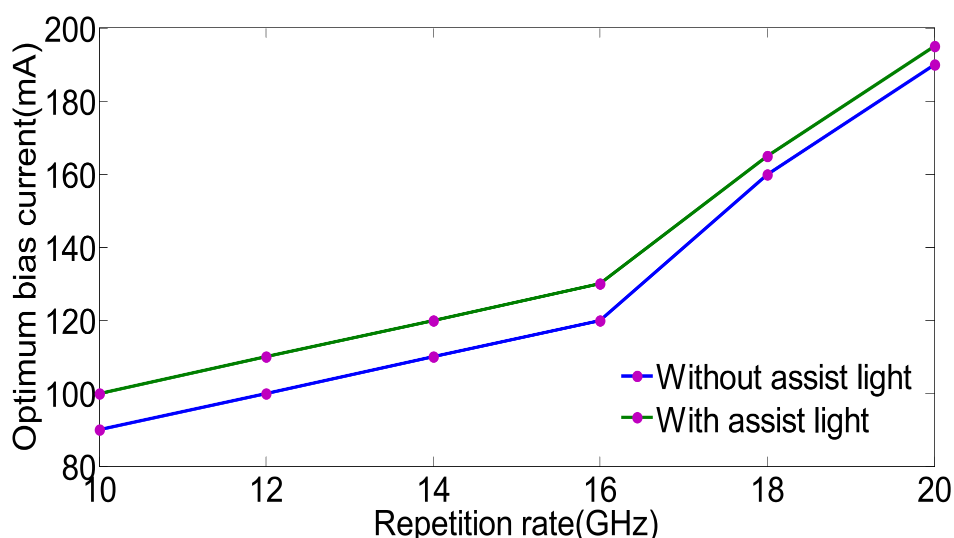

Fig. 5.16 Variations of the SOA optimum bias currents with different pulse train repetition rates

both in the presence and absence of the assist light.

5.5.2 Relationship between the SOA Optimum Bias Current and its Temperature

The experimental system in Fig. 5.1a is used to investigate the relationship between the amplifier optimum bias current (I_{opt}) and its temperature. Fig. 5.16 shows variations of I_{opt} with temperature (T) ranging from $5^{\circ}C$ to $40^{\circ}C$. Results show that as the temperature increases initially from when $5^{\circ}C$ to $20^{\circ}C$ the SOA I_{opt} decreases and reaches to its minimum value of $75mA$ at the temperature of $20^{\circ}C$ and any further increase in temperature increases the amplifier I_{opt} . This is because the working temperature of $20^{\circ}C$ is very close to the lattice temperature of the SOA active region which implies when the bias current associated to this temperature (i.e. $75mA$) is applied to SOA, its conduction band Quasi Fermi-level is higher than that at other temperatures while its valence band Quasi Fermi-level is lower. This results in a higher SOA gain; the amplification of the leading edge of the SOA input pulse depletes more carrier density which leads to the lower carrier density level in the amplifier cavity when the tailing edge of the SOA input pulse arrives. This clearly indicates that at the temperature $20^{\circ}C$, the amplified pulse train suffers from distortion at lower amplifier bias current.

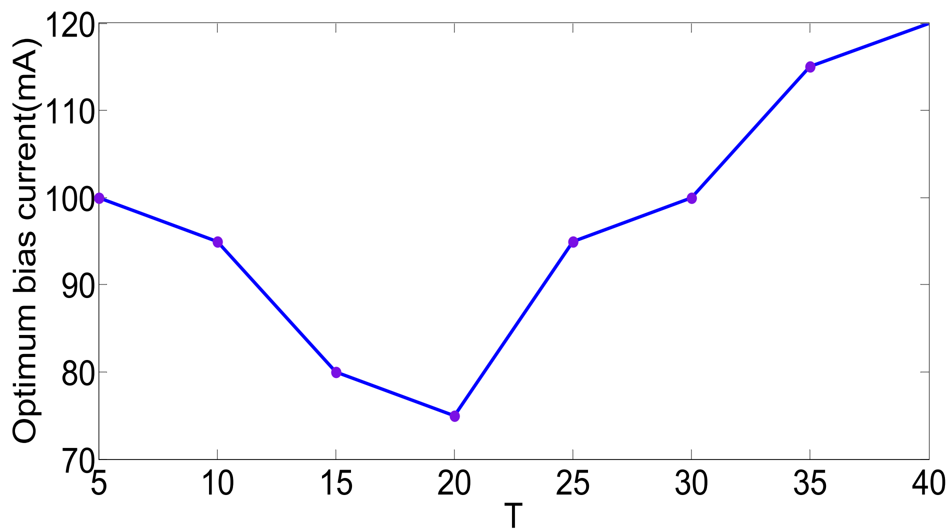

Fig. 5.16 Variations of SOA optimum bias currents with its temperatures.

5.6 Conclusions

In this chapter, various experimental results were demonstrated and explained to show how the bias current of a SOA can be optimized so that high gain and very low distortion amplification can be achieved when a high-speed optical pulse train enters the amplifier input. We have explored the variations of the amplified pulse duration with the amplifier bias current and based on this investigation the amplifier optimized bias current for high gain and low distortion pulse amplification is defined. Experiments are done to investigate the relationships between the amplifier optimum bias current and input pulse train duration, power and repetition rate. Also, effects of the amplifier working temperature and assist light injection on the amplifier optimum bias current are studied.

Chapter 6

Transmission Line Modelling Method

6.1 Introduction

During the first half of the 20th century, the similarity between the behavior of electromagnetic field as well as voltage and current was used to analytically solve high-frequency electromagnetic field problems [112-114]. The presence of modern computers equipped with powerful numerical software enabled scientists to predict behavior of electromagnetic waves at very high frequencies. In 1971, Johns and Beurle presented a new numerical method based on Huygen's model of wave propagation [60] to solve the 2-dimentional scattering problem. In their numerical method transmission line matrix (TLM) was introduced for the first time to analyse high frequency electromagnetic wave propagation by using computer simulation [60]. Since then, TLM was successfully applied in microwave [115-116] by including features such as variable mesh size, simple nodes and applying to more materials. In 1987, A. J. Lowery has applied the transmission line modelling method to the laser diode (transmission line laser modelling method) by adding a gain model [61] which was a simple 2nd-order band pass filter to approximate the entire gain spectrum of the laser diode.

In this chapter, the transmission line matrix method is reviewed and used to simulate the transverse electromagnetic (TEM) wave propagation in both bounded and unbounded space. The wave impedance in a rectangular waveguide is calculated based on TLM and compared with the result obtained by the analytical expression. The microwave circuit technique which can be used to model semiconductor lasers is introduced. Also, the disadvantages of the conventional transmission line laser modelling (TLLM) method are discussed.

6.2 Transmission Line Matrix (TLM) Method

6.2.1 Analysis of TEM Wave Propagation Using TLM Method

According to Huygen's principle, a wavefront consists of a number of secondary radiators, each of which can be taken as a new excitation source [117]. The envelope of wavelets forms a new wavefront which gives rise to new generation of spherical wavelets. The Huygen's principle can give an accurate description of wave propagation and scattering. In order to investigate the Huygens' principle numerically, a Cartesian matrix of nodes separated by the mesh is established. In a mesh matrix, every node can be taken as a radiator. Each node has four transmission lines (i.e. lines 1 to 4) which are in clockwise order around the node (see Fig.6.1(a)). Both space and time are discretized and represented by basic elementary units, Δl and Δt . The relationship between the space and time can be expressed as:

$$\Delta t = \Delta l / c \tag{6.1}$$

where, Δt is the time interval for an electromagnetic pulse to travel from one node to the adjacent node, Δl is the length of each transmission line between two successive nodes and c is the light velocity in the free space.

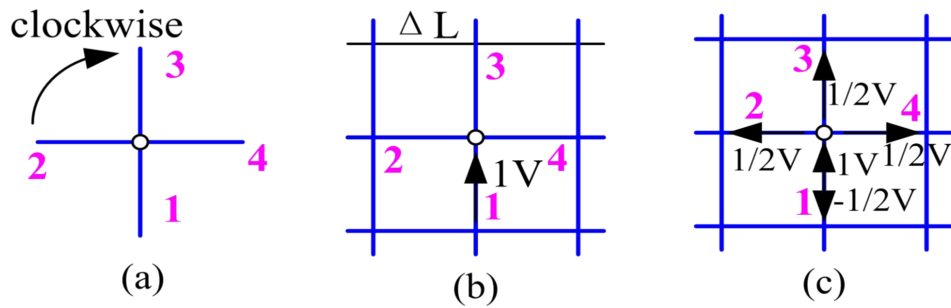

Fig. 6.1 Cartesian mesh of transmission lines used in discretized Huygen's wave model.

At time t, a delta function impulse with the magnitude $1V$ is applied at one of the nodes along the positive x-axis direction (Fig.6.1(b)). According to Huygen's principle, in an isotropic material at time $t+\Delta t$ each radiated pulse will carry one fourth of the incident energy and hence, the corresponding electric filed magnitude (voltage) is $1/2V$ at time $t+\Delta t$. The reflection coefficient must be negative to satisfy the requirement of electromagnetic field continuity at the node and the coefficient of the reflected impulse is -1/2 [60]. Thus, the incident impulse with the magnitude $1V$ at the time t (Fig. 6.1(b)) results in a reflected impulse of $-1/2V$ in the transmission line 1 and three transmitted impulses of $1/2V$ in the transmission lines 2, 3 and 4 at the time $t+\Delta t$ (Fig. 6.1(c)).

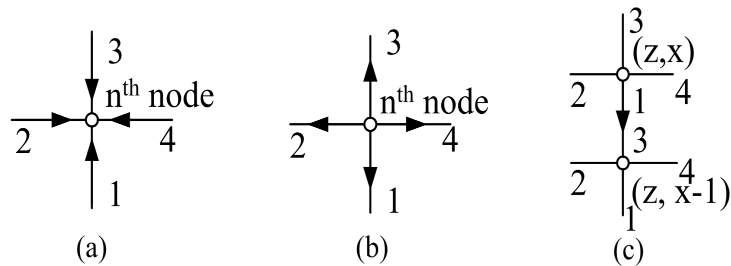

Fig. 6.2 (a) Incident impulse at the node n (b) Reflection impulse at the node n (c) the reflected impulse becomes the incident impulse at the adjacent node.

In a 2-dimentioanal mesh matrix each node is connected to four transmission lines 1 to 4 as shown in Fig.6.1(a). Also, there are eight transmission statuses at each node, these include four incident and four reflection impulses on transmission lines 1 to 4 as shown in

Figs.6.2(a) and (b), respectively. Let us consider the nth node, at time $t = k\Delta t$, the incident impulse voltages on transmission lines 1 to 4 are ${}_k v_1^i$, ${}_k v_2^i$, ${}_k v_3^i$ and ${}_k v_4^i$, respectively. Also, the reflected impulse voltages on the transmission lines 1 to 4 at time $t = k\Delta t$ are ${}_k v_1^r$, ${}_k v_2^r$, ${}_k v_3^r$ and ${}_k v_4^r$, respectively. The reflected voltage along the transmission line 1 (i.e. TL-1) of the nth node at time $(k+1)\Delta t$ can be expressed as [60]:

$$ {}_{k+1}v_1^r = \frac{1}{2}({}_k v_2^i + {}_k v_3^i + {}_k v_4^i - {}_k v_1^i) \tag{6.2} $$

When the impulse voltage is reflected from a node at the position (z, x), it automatically becomes an incident impulse on the adjacent node (z, x-1), i.e.

$$ {}_{k+1}v_1^r(z,x) = {}_{k+1}v_3^i(z,x-1) \tag{6.3} $$

In general, the reflected voltage impulse along the nth transmission line of any node at time $(k+1)\Delta t$ is:

$$ {}_{k+1}v_n^r = \frac{1}{2}[\sum_{m=1}^{4} {}_k v_m^i] - {}_k v_n \tag{6.4} $$

The reflected impulses emerging at the nth node become automatically an incident impulse at the adjacent nodes, that is:

$$ \begin{aligned} {}_{k+1}v_1^i(z,x) &= {}_{k+1}v_3^r(z,x-1) \\ {}_{k+1}v_2^i(z,x) &= {}_{k+1}v_4^r(z-1,x) \\ {}_{k+1}v_3^i(z,x) &= {}_{k+1}v_3^r(z,x+1) \\ {}_{k+1}v_4^i(z,x) &= {}_{k+1}v_2^r(z+1,x) \end{aligned} \tag{6.5} $$

Consequently, if at a given time (i.e. $t = k\Delta t$), magnitudes, positions, and directions of all impulses are known, the corresponding values at time $(k+1)\Delta t$ can be obtained from Eqs. (6.4) and (6.5). The impulse response of each node in the network can be found by initially fixing the voltages at time $t = 0$ and examining the output impulse voltage at the

successive time intervals of $\Delta l / c$.

6.2.2 Representation of Lossy and Lossless Boundary

Both open and short circuits are used to represent the electric and magnetic walls at the appropriate position in the matrix mesh [60]. They must be placed halfway between two nodes in order to ensure synchronism. An incident impulse at the nth node propagates along the line to the boundary, where it is reflected. After time interval Δt, the impulse reflected from the boundary arrives at the same node either in the same direction (the boundary parallel to the propagation direction of the input electromagnetic wave, i. e. boundary A and B in Fig. 6.3) or in the opposite direction (the boundary perpendicular to the propagation direction of the input electromagnetic wave, i. e. Boundary C in Fig. 6.3) [60]. The reflection coefficient can be used to represent the loss in the boundary. The propagation of a plane TEM wave can be represented in a rectangular matrix mesh as shown in following Fig. 6.3:

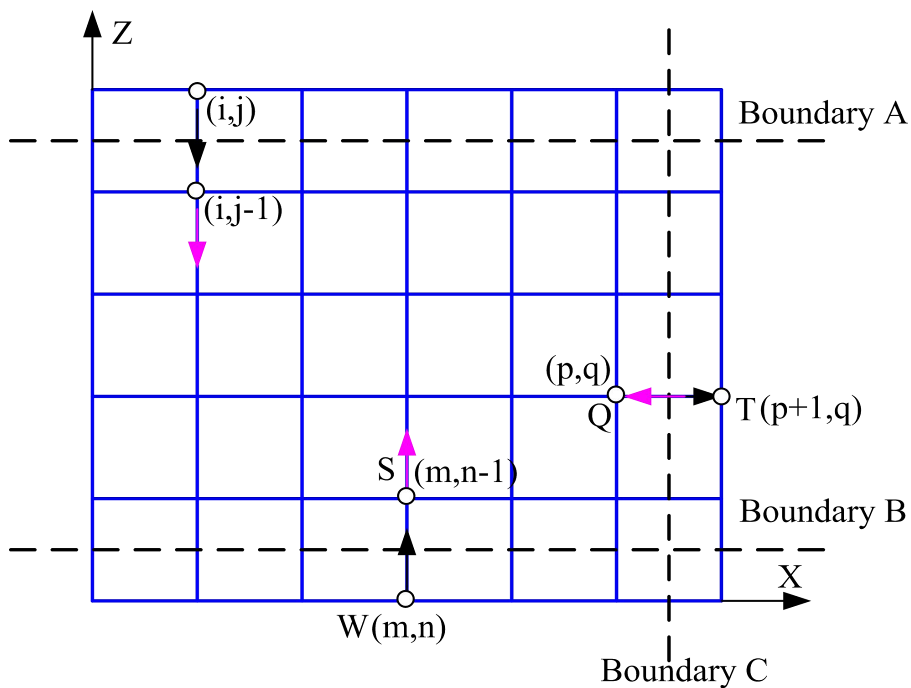

Fig. 6.3 Schematic diagram of transmission matrix boundaries (blue and black dashed lines

represent the mesh and boundaries, respectively).

Because the node located at (i, j) is very close but outside of boundary A, the following relationship is defined between the reflected voltages of the nodes inside (i.e. located at (i, j-1)), see Fig.6.3 [60]:

$$ {}_k v_1^r(i,j) = {}_k v_1^r(i,j-1) \tag{6.6} $$

Similarly at node (m, n) we have:

$$ {}_k v_3^r(m,n) = {}_k v_3^r(m,n-1) \tag{6.7} $$

When an impulse propagates from node Q (black arrow) towards node T as shown in Fig.6.3 its reflected impulse has the same magnitude but in opposite direction (pink arrow):

$$ {}_k v_4^i(p,q) = {}_k v_2^r(p+1,q) = -{}_k v_4^r(p,q) \tag{6.8} $$

On the other hand, in case of a lossy boundary we need to consider the reflection coefficient, ρ , in each boundary branch that is:

$$ {}_k v_4^i(p,q) = {}_k v_2^r(p+1,q) = \rho\left\{ {}_k v_4^r(p,q) \right\} \tag{6.9} $$

where,

$$ \rho = \frac{R-1}{R+1} \tag{6.10} $$

and R is the required resistive load.

6.2.3 Numerical Simulation of TEM Waves

A two-dimensional TLM network can be approximated by the lumped-element model (LEM) shown in Fig. 6.4 [60].

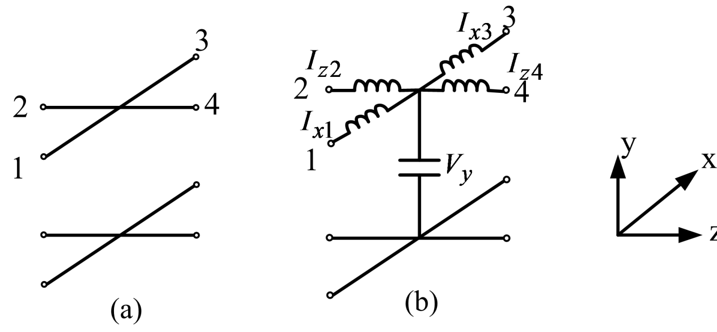

Fig. 6.4 Equivalent lumped-element model of a 2-dimensional TLM network (a) TLM network, (b) its equivalent LEM.

The relationship between voltages and currents in the equivalent circuit and TEM electromagnetic field components H_z, H_x and E_y can be expressed as [60]:

$$E_y = V_y \tag{6.11}$$

$$-H_z \equiv (I_{x3} - I_{x1}) \tag{6.12}$$

$$-H_x \equiv (I_{z2} - I_{z4}) \tag{6.13}$$

$$\mu \equiv L \qquad \varepsilon \equiv 2C \tag{6.14}$$

where in the above equations μ and ε are, respectively, the transmission line permeability and dielectrics constant, L and C are the TL inductance and capacitance per unit length, respectively, V_y is the voltage of the capacitor in the TLM network, I_{x1}, I_{z2}, I_{x3} and I_{z4} are the currents in the transmission lines 1 to 4, respectively (see Fig.6.4(b)). In a conventional transmission line matrix, we have $\mu_r = \varepsilon_r = 1$ and the velocity of light ,c, is given by:

$$c = 1/\sqrt{\varepsilon_0 \mu_0} = 1/\sqrt{LC} \tag{6.15}$$

Equations (6.11) to (6.15) can be used to find electromagnetic fields E_y and H_x at node W (see Fig.6.3), in terms of the node voltage and net current entering the node in z-direction, that is:

$$ {}_kE_y(m,n) = \frac{1}{2}\left\{ {}_kv_1^i(m,n) + {}_kv_2^i(m,n) + {}_kv_3^i(m,n) + {}_kv_4^i(m,n) \right\} \quad (6.16) $$

$$ -{}_kH_x(m,n) = {}_kv_2^i(m,n) - {}_kv_4^i(m,n) \quad (6.17) $$

and the boundary condition for TEM wave requires to have:

$$ {}_kH_z(m,n) = {}_kv_1^i(m,n) - {}_kv_3^i(m,n) = 0 \quad (6.18) $$

On the other hand, We can also find a series of discrete delta function for E_y and H_x which correspond to the time interval Δt by using Eqs.(6-4) to (6-5). These delta functions are used to obtain the output waveform. In the following simulation, the input is assumed to be a sinusoidal wave. The impulses obtained by sampling this sinusoidal signal arrive at node W (shown in Fig. 6.3) and then propagate towards the other nodes of the transmission line network (i.e. mesh) according to Eqs. (6.4) to (6.5). Then the output response can be obtained by taking the Fourier transform of all impulses arriving at the output node Q as shown in Fig.6.3. Since the output impulse response consists of a series of delta functions, the output Fourier integral becomes in the form of summation. The real and imaginary parts of the output spectra are [60]:

$$ \mathrm{Re}(F(\Delta l/\lambda)) = \sum_{k=1}^{N} {}_kI \cos(\frac{2\pi k\Delta l}{\lambda}) $$
$$ \mathrm{Im}(F(\Delta l/\lambda)) = \sum_{k=1}^{N} {}_kI \sin(\frac{2\pi k\Delta l}{\lambda}) \quad (6.19) $$

where $F(\Delta l/\lambda)$ is the frequency response, ${}_kI$ is the value of output voltage response at time $t = k\Delta l/c$ and N is the total number of time intervals. Numerical simulation for TEM waves are operated on a 25×11 rectangular matrix as shown in Fig. 6.5. In here, the propagation range for TEM wave in the x directions are fixed at lines $x = 2$ and $x = 10$ to have boundaries along the lines $x = 1.5$ and $x = 10.5$. The initial impulse excitation is on all points along the line $z = 4$ and the electromagnetic field along the line at all subsequent

time intervals is set to zero. Also, the propagation of TEM wave along the z direction is terminated at $z = 24$ which sets the boundary C along the line $z = 24.5$. The output is taken at node located at ($z = 14, x = 6$), see Fig. 6.5. The magnitudes of electromagnetic fields $|E_y|$ and $|H_x|$ can be obtained from Eqs. (6.4) and (6.5).

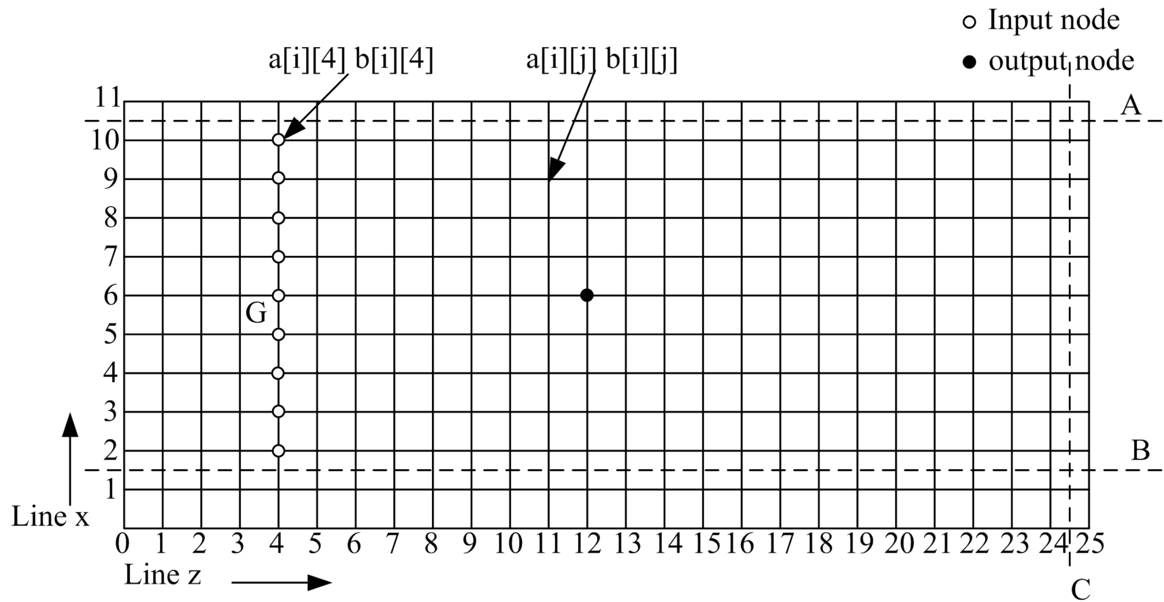

Fig. 6.5 Transmission rectangular mesh used for simulation of TEM wave impedance.

There are eight impulses at each given node. Four of them are input impulses which are stored in a two-dimensional array hereby referred to as “a” and four reflected impulses which are stored in another two-dimensional array referred to as “b”. In each iteration step, we can first obtain values of the reflected impulses at all non-boundary and boundary nodes and then values of the input impulses are calculated based on Eq. (6.5), i.e. array ‘a’. The magnitude of the intrinsic impedance $|z|$ of the network matrix is calculated after performing 200 iterations of transmission line matrix based on Eqs. (6.4) and (6.5). For low frequencies, the intrinsic impedance of the network matrix is $1/\sqrt{2}$ times the intrinsic impedance of free space, which can be obtained by velocity characteristics [60]. Assuming the resistive load R is $1/\sqrt{2}$ and substituting into Eq. (6.10), we can obtain the reflection

coefficient. According to the wave theory, the accurate value of the intrinsic impedance should be 0.7071. Tab. 6.1 shows the simulation results of the impedance Z using TLM method for different $\Delta l/\lambda$. The table shows that as $\Delta l/\lambda$ increases, the impedance Z value becomes very close to its theoretical value.

Tab. 6.1 Numerical calculation of the intrinsic impedance Z

$\Delta l/\lambda$	Abs(Z)
0.002	0.7025
0.004	0.7053
0.006	0.7062
0.008	0.7057
0.010	0.7073
0.012	0.7068
0.014	0.7066
0.016	0.7075
0.018	0.7067
0.020	0.7074

6.4 TLM for High-frequency Circuits

The transmission line matrix method that was explained in the above section was originally developed to model passive microwave cavities [118-119]. A lot of work has been carried out to analyze microwave waveguide structures using one-dimensional (1-D), 2D and 3-D TLM [60, 120]. Although microwave and optical frequencies are different however, some ideas that have been used in microwave were also applied in optics. For example, the idea of locking a microwave oscillator by an external electric signal has been applied to optical devices. That is, a semiconductor laser diode can be locked by injecting an external optical

signal to its bias circuitry [121]. Hence, the similarity between microwave and optical engineering indicates that it is possible to apply the microwave circuit modelling technique to model optical devices. One-dimensional TLM method has been used to model optical devices [61]. Hence, in the following sections1-D TLM will be reviewed.

6.4.1 TLM Link and Stub Lines

6.4.1.1 TLM Link Lines

The TLM is a time- and space-discrete model of wave propagation simulated by voltage impulse propagation along the transmission lines. The propagation medium is represented by transmission lines. TLM consists two elements namely sub- and link- lines. A lumped series inductor with inductance*, L,* can be represented by an equivalent transmission-line having the following inductance [66]:

$$L = L_d \Delta l \tag{6.20}$$

where, L_d is the inductance per unit length of the transmission line and Δl is the length of the transmission line. The characteristic impedance of the transmission line is given as [66]:

$$Z_l = \sqrt{\frac{L_d}{C_d}} \tag{6.21}$$

where， C_d is the capacitance per unit length of the transmission line. The propagation velocity v_p for a lossless transmission line can be expressed by:

$$v_p = \frac{1}{\sqrt{L_d C_d}} = \frac{\Delta l}{\Delta t} \tag{6.22}$$

where, Δt is the step time interval. The characteristic impedance of the transmission line can be obtained by substituting Eqs. (6.20) and (6.22) into Eq.(6.23). That is:

$$Z_l = \frac{L}{\Delta t} \tag{6.23}$$

Also, the characteristic impedance (Z_c) of the link transmission line can be expressed as [66]:

$$Z_c = \frac{\Delta t}{C} \tag{6.24}$$

6.4.1.2 TLM Stub Lines

In the above section, the lumped reactive elements were described by the link lines. The lumped inductor L can also be represented by an equivalent short-circuit transmission line stub with the characteristic impedance of [120]:

$$Z_l = \frac{2L}{\Delta t} \tag{6.25}$$

and the associated parasitic capacitance can be expressed as:

$$C_e = \frac{(\Delta t)^2}{4L} \tag{6.26}$$

Similarly, the lumped capacitor and the associated parasitic inductance can be represented by open-circuit stubs with the characteristic impedance [120]:

$$Z_c = \frac{\Delta t}{2C} \tag{6.27}$$

$$L_e = \frac{(\Delta t)^2}{4C} \tag{6.28}$$

The open and short transmission line stubs each with length $\Delta l / 2$ are used to represent the capacitor and inductor, respectively. The length of the stub transmission line is half of the length of the link line so that the impulse round-trip time along the stub line is the same as the impulse propagation time along the link line.

6.4.2 Scattering and Connecting Processes in TLM

Connecting and scattering are two main processes in the TLM algorithm which are described by matrices. The scattering matrix expresses the relationship between the incident and reflected voltage pulses of a given node at time $k\Delta t$ while the connecting matrix describes the process that the reflected pulses at the time $k\Delta t$ continue to propagate along the transmission line and become the new incident pulses at the adjacent scattering node at time $(k+1)\Delta t$. The two processes in the TLM algorithm can be expressed as [66]:

$$ {}_kV^r = S_k V^i \tag{6.29} $$

$$ {}_{k+1}V^i = C_k V^r \tag{6.30} $$

where, V^i and V^r are the incident and reflected voltages matrices and both S_k and C_k are the scattering and connecting matrices, respectively. The subscripts k and $k+1$ denote the kth *and* $(k+1)^{th}$ time iterations. The dimensions of the two matrixes are determined by the sub-network of the TLM. A detailed work example is provided in Ref. [66].

6.4.3 TLM for Parallel RLC Filter

The input impedance for a lossless transmission line can be written as [122]:

$$ Z_{in} = \frac{Z_0(Z_l + jZ_0\tan(\beta l))}{Z_0 + jZ_l\tan(\beta l)} \tag{6.31} $$

where, Z_0 is the characteristics impedance of the transmission line, Z_l is the load impedance, l is the length of the transmission line and the propagation constant of semiconductor materials β_r is:

$$ \beta_r = \frac{2\pi f_0 n_r}{c_0} \tag{6.32} $$

where, n_r is the effective refractive index, c_0 is the speed of the light in free-space and f_0 is the input signal frequency. In order to satisfy the synchronization criterion, the length of stub line should be such that it takes ΔT for the forward and backward propagations along the line, that is:

$$l = \frac{\Delta T c_0}{2 n_r} \tag{6.33}$$

The input impedance of an open-circuit transmission line ($Z_L = \infty$) is adopted to describe the capacitive stub line in TLM, which can be derived based on Eqs. (6.32-6.34):

$$Z_{inc} = Z_C / j \tan(\pi \Delta T f_0) \tag{6.34}$$

Also, the input impedance of a short-circuit transmission line ($Z_L = 0$) is used to describe inductive stub line in TLM. That is:

$$Z_{inL} = j Z_L \tan(\pi \Delta T f_0) \tag{6.35}$$

The relationship between the resonant frequency and stub impedances in a parallel inductive-capacitive circuit is [66]:

$$\sqrt{Z_C / Z_L} = \tan(\pi \Delta T f_0) \tag{6.36}$$

The Q-factor in a parallel RLC filter when the resistor $R = 1\Omega$ can be expressed as [61]:

$$Q = \sqrt{\frac{C}{L}} \tag{6.37}$$

Based on Eqs. (6.3.9), (6.27) and (6.29), the Q-factor of the TLM stub filter can be expressed as:

$$Q = 1 / \sqrt{Z_C Z_L} \tag{6.38}$$

Then, the admittance of the stub filter can be obtained based on Eq. (6.38) and Eq. (6.40) as:

$$Y_L = Q\tan(\pi \Delta T f_0) \tag{6.39}$$

$$Y_C = Q / \tan(\pi \Delta T f_0) \tag{6.40}$$

6.5 Transmission Line Laser Model (TLLM)

6.5.1 Review of TLLM

Transmission line laser model (TLLM) was first applied to laser diodes by including a 2nd order RLC gain model to the TLM [61]. The TLLM describes the optical wave propagation using a sampled optical filed rather than an energy densities, which allows continuous spectra to be obtained by the Fourier transform [123]. TLLM discretizes the physical space into sections; the spatial discretization is limited in one dimension when the optical waveguide is small enough to allow a fundamental transverse mode to propagate. The adjacent sections are connected by dispersionless transmission lines. An optical signal travels along the transmission line in both forward and backward directions. The scattering node lies in the center of each section, in which the fundamental optical processes can be described by the stub transmission lines.

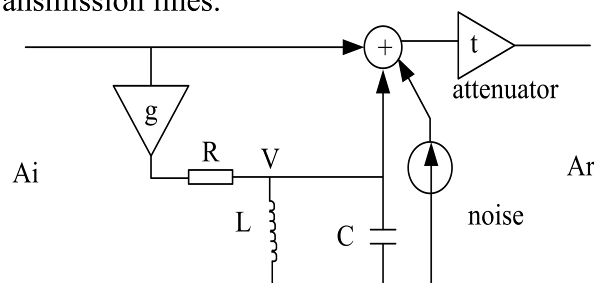

Fig. 6.6 Gain curve model in TLLM.

Figure 6.6 shows the basic structure of the TLLM. In this lumped circuit, the stimulated emission was represented by a filter and an adder. The frequency response of the RLC filter is used to approximate the gain spectrum. The spontaneous emission R_{sp} is

represented by adding a random current source and the attenuator represents the transmission loss in the optical waveguide. In Fig.6.6 Ai and Ar are the input and output voltages of the lumped circuit, respectively.

Equation (6.41) can be used to determine the mean square value of the current source shown in Fig. 6.6 that is [66]:

$$I_{sp}^{2} = \beta R_{sp} \Delta L / (Z_p v_g) \tag{6.41}$$

where, β is the spontaneous emission coefficient, ΔL is the length of each section, Z_p is the transverse wave impedance and v_g is the group velocity. Here, the attenuation coefficient, α , is assumed to be a constant. The stimulated emission, spontaneous emission and attenuation processes can be combined into a single scattering matrix for each section of the divided laser cavity. The matrix operates on the forwards and backwards travelling incident waves to produce a set of reflected waves. Then, they propagate along the transmission lines ready to become new incident waves for the adjacent scattering nodes after one iteration time step. The scattering matrix is given as [66]:

$$\begin{bmatrix} A^r \\ A_c^r \\ A_l^r \\ B^r \\ B_c^r \\ B_l^r \end{bmatrix} = \frac{1}{y} \begin{bmatrix} t(g+y) & 2tY_c & 2tY_l & 0 & 0 & 0 \\ g & 2Y_c - y & 2Y_l & 0 & 0 & 0 \\ g & 2Y_c & 2Y_l - y & 0 & 0 & 0 \\ 0 & 0 & 0 & t(g+y) & 2tY_c & 2tY_l \\ 0 & 0 & 0 & g & 2Y_c - y & 2Y_l \\ 0 & 0 & 0 & g & 2Y_c & 2Y_l - y \end{bmatrix} \begin{bmatrix} A^i \\ A_c^i \\ A_l^i \\ B^i \\ B_c^i \\ B_l^i \end{bmatrix} + \begin{bmatrix} I_s Z_p t/2 \\ 0 \\ 0 \\ I_s Z_p t/2 \\ 0 \\ 0 \end{bmatrix} \tag{6.42}$$

where,

$$y = 1 + Y_c + Y_l \tag{6.43}$$

$$t = \exp(-\alpha \Delta L / 2) \tag{6.44}$$

The linking equations are

$$A_{k+1}^{i}(n) = A_{k}^{r}(n-1) \tag{6.45}$$

$$B_{k+1}^{i}(n) = B_{k}^{r}(n+1) \tag{6.46}$$

The stimulated emission gain $g(N)$ of a single section as a function of carrier density N in each section can be expressed as [66]:

$$g(N) = G_0 \ln\left(\frac{AN + BN^2 + CN^3}{AN_0 + BN_0{}^2 + CN_0{}^3}\right) \tag{6.47}$$

where, N_0 is the transparent carrier density, G_0 is the gain coefficient. A, B and C are the linear recombination, Bi-molecular recombination and Auger recombination, respectively. The optical reflection of the cavity facets can be represented by a reflection coefficient. The right-travelling waves are reflected to become left-travelling waves and vice versa. The expressions are [66]:

$$_{K+1}B^{i} = \sqrt{R_K}\, A^{r} \tag{6.48}$$

$$_{K+1}A^{i} = \sqrt{R_K}\, B^{r} \tag{6.49}$$

where B^i and A^r are the incident right-travelling wave and reflected left- travelling wave at the right facet, A^i and B^r are the incident left-travelling wave and reflected right-travelling wave at the left facet and R_K is the facet reflectivity coefficient. The carrier density in each section is calculated by the following rate equation (i.e. Eq.(6.50). The average carrier density in each section is substituted into the gain equation (6.47) and the spontaneous emission rate (Eq.6.41) of the modelled laser.

$$\frac{dN}{dt} = \frac{J}{Dq} - \frac{N}{\tau_s} - \frac{c}{n_r}\Gamma g S \tag{6.50}$$

where, N is the carrier density in each section, J is the injected current density, D is the thickness of the active region, q is the electron charge, τ_s is the carrier recommendation

lifetime, c is the light speed in free space, Γ is the optical confinement factor, g is the gain coefficient, S is the photon density in each section, n_r is the effective refractive index.

6.5.2 Disadvantages of TLLM

Transmission line matrix was first introduced to analyze the characteristics of microwave circuits. It has been confirmed that TLM can easily model the integrated system, provide the continuous spectrum and save a lot of computation time [61]. The existing TLLM model which is used for laser diode modelling was introduced by adding a RLC filter and a gain model to the one dimensional TLM. However, this approach has created the following shortcomings for TLLM:

- The modern quantum physics have confirmed that light has both wave and particle properties. The particle properties are significantly important in the description of light-matter interaction. The TLLM ignores the description of the dynamic interaction between light and matter.
- TLLM adopts the response of only one RLC filter to represent the whole gain spectra of the laser diode whereas in practice the laser diode gain spectra is different so the spectral shape approximation obtained by TLLM is not accurate which implies TLLM lacks the necessary theoretical basis.
- In TLLM pulse voltage is used to represent optical field which does not provide a clear description of the optical field propagation and the interaction between the optical signal and the gain medium [65].

6.6 Conclusions

The chapter reviews the basic theory of transmission line modelling method, including the description of wave propagation in the transmission line meshes, the lossy and lossless boundary conditions and the calculation of the TEM wave impedance based on TLM. The foundations of applying the one-dimension TLM to model the high-frequency circuits are reviewed and the existing transmission line modelling method for modelling the laser diode is discussed. Although transmission line laser modelling (TLLM) was used to provide the explanation of the behavior of laser diodes, the disadvantages of TLLM limit its application in modelling semiconductor optical devices.

Chapter 7

Quantum Transmission Line Modelling Method

7.1 Introduction

In Chapter 6, we discussed the basic transmission line modelling method, which was originally used to describe the wave propagation and scattering in microwave areas [61,121]. In 1987, transmission line matrix method was employed to model the bulk material laser diode [62]. However, as discussed in Chapter 6, the existing studies of transmission line laser model (TLLM) adopted the response of only one filter to approximate the whole gain spectrum of laser diodes. This ignores the light's interaction with matter which clearly indicates TLLM cannot provide an accurate model of laser diodes. On the other hand, the transmission line modelling (TLM) method as compared with other available methods can provide a continuous spectrum, save a lot of computation time and easily simulate the integrated system [66-67, 124]. In this chapter, a new and accurate modelling method for semiconductor optical devices is introduced which is based on TLM but considers the dynamic process of light-matter interaction. This new idea is based on our discovery that the photon emission process in the two-level system between the higher energy state and lower energy state can be represented and described by a resonant RLC stub filter at the resonance.

In this chapter, a new theoretical modelling method for photon emission is presented by combining the time-dependent perturbation theory and the transmission line modelling

method. We refer to this new modelling technique as 'quantum transmission line modelling method (Q-TLM), which can be considered as the first basic theory which applies TLM to model the semiconductor optical devices. A detailed study is performed to explain how this new method can be applied to quantum well and quantum dot structures, both of which are promising waveguide structures for semiconductor optical amplifiers.

7.2 TLM Method for Photon Emission

In the following the TLM method for photon emission is introduced. Based on the time-dependent perturbation theory [125], the net photon emission rate R (i.e. the net downward transition rate from the higher energy state B to the lower energy state A) in a crystal per unit volume can be written as [126]:

$$R = \frac{2}{V}\sum_{k}\frac{2\pi}{\hbar}\left|H'_{BA}\right|^{2}\delta(E_B - E_A - \hbar\omega)(F_B - F_A) \quad (7.1)$$

where, $\hbar$ is the Plank constant h divided by 2π , V is the crystal volume, E_B and E_A are the energies of higher state B and lower state A, respectively, F_A and F_B are the corresponding Fermi-Dirac distribution functions for states A and B, H'_{BA} is the matrix element given by [126-127]:

$$H'_{BA} = \int \psi_A^*(r)H'(r)\psi_B(r)d^3r \quad (7.2)$$

where, $H'(r)$ is a small time-dependent perturbation of the Hamiltonian, r is the position vector, ψ_A and ψ_B are the electron wave functions at states A and B, respectively, which are solutions to the time-dependent Schrödinger equation.

Based on Heisenberg's uncertainty principle [128], the finite lifetime of an excited state causes uncertainty in the energy of electron transition, which results in a finite Lorentzian

linewidth in frequency. Considering the linewidth broadening during the photon emission process, the delta function in Eq. (7.1) is replaced by the Lorentzian function with the linewidth γ. Hence, the analytical expression for the net photon emission rate can be expressed as [126]:

$$R = \frac{2}{V}\sum_{k}\frac{2\pi}{\hbar}\left|H'_{BA}\right|^{2}(F_B - F_A)\frac{\gamma\hbar/2\pi}{(E_B - E_A - \hbar\omega)^2 + (\gamma\hbar/2)^2} \tag{7.3}$$

where ω is the optical angular frequency. In this Q-TLM model, the linewidth broadening in the photon generation process is described by the response of a 2nd order resonant RLC stub filter which consists of a unity resistor, a capacitor and an inductor as shown in Fig. 7.1a.

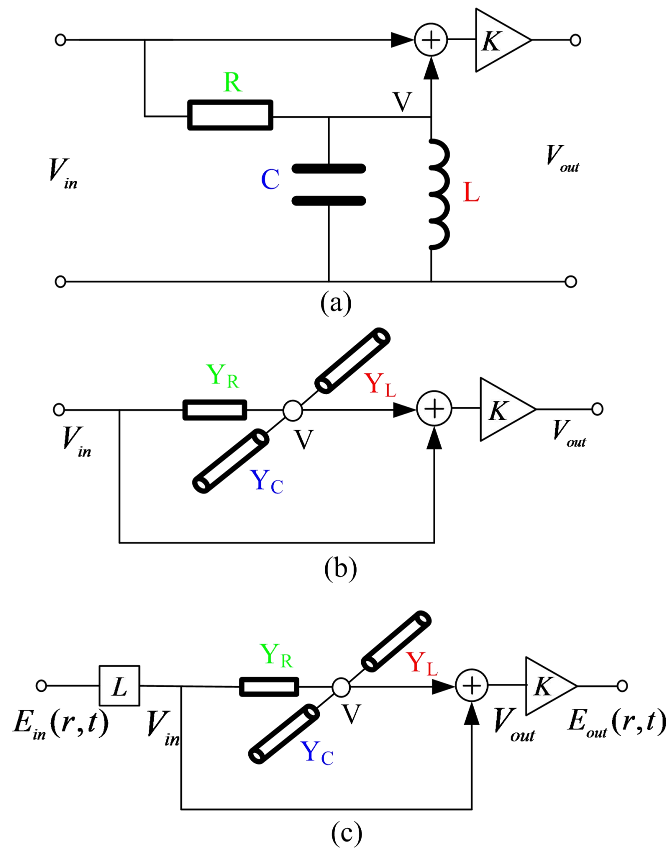

Fig.7.1 Q-TLM photon emission model (a) RLC circuit model (b) transmission line model with voltage input and (c) transmission line model with the electric filed input.

Based on the transmission line modelling technique at high frequencies, capacitors and inductors are modelled as open-circuit and short-circuit transmission line stubs [67] which are shown in Fig. 7.1b. The resonant frequency f_p of a two-level RLC system is determined by the frequency of the generated photon, which can be expressed as:

$$f_p = (E_A - E_B)/h \tag{7.4}$$

Based on Eq. (7.3), the frequency response, $H(\omega)$, of a two-level system which consists of both higher and lower energy states during the photon emission process is given by:

$$H(\omega) = \frac{1}{\pi\hbar} \frac{\gamma/2}{(\omega - 2\pi f_p)^2 + (\gamma/2)^2} \tag{7.5}$$

On the other hand, the frequency response of the RLC resonant circuit shown in Fig.7.1 can be expressed as:

$$H_1(\omega) = \frac{\omega_0}{2Q} \frac{\omega_0/2Q}{(\omega - \omega_0)^2 + (\omega_0/2Q)^2} \tag{7.6}$$

where, Q is the Q-factor of the RLC system, $\omega_0 = 2\pi f_P$ is the resonant angular frequency. By comparing Eqs.(7.5) and (7.6) we can describe the photon emission based on the RLC system as:

$$Q = \frac{2\pi f_P}{\gamma} \tag{7.7}$$

$$H(\omega) = GH_1(\omega) \tag{7.8}$$

$$G = 2/\pi\gamma\hbar \tag{7.9}$$

where, in Eq. (7.9), G is the coefficient for equating the magnitude of $H(\omega)$ and $H_1(\omega)$. Furthermore, the characteristic admittances of the capacitor and inductor in the RLC system can be expressed as [67]:

$$Y_L = Q\tan(\pi\Delta T f_P) = \frac{2\pi f_P}{\gamma}\tan(\pi\Delta T f_P) \tag{7.10}$$

$$Y_C = Q/\tan(\pi\Delta T f_P) = 2\pi f_P /[\gamma \tan(\pi\Delta T f_P)] \tag{7.11}$$

$$\Delta T = \frac{Ln_r}{c} \tag{7.12}$$

where, L is the length of the link transmission line ($L/2$ is the length of each stub transmission line which represents either a capacitor or an inductor), n_r is the refractive index, c is the speed of light in free space.

In the above analysis, the linewidth broadening in the photon emission process has been described by the two-level RLC system. However, according to Eq. 7.3, the probability that electrons transit upward and downward has not been considered. Thus, a weight coefficient K is defined as shown in Fig.7.1 to describe the electron transition rate between states A and B. From Eqs. (7.3)-(7.9) the weight coefficient K (per unit distance) can be expressed as:

$$K = G_0 \frac{2}{V} \sum_k \frac{2\pi}{\hbar} \left| H'_{BA} \right|^2 (F_B - F_A) \tag{7.13}$$

In Fig. 7.1(c), the input voltage V_{in} of the RLC circuit can be expressed in terms of the electric field $E_{in}(r,t)$ along the transmission line link as $V_{in} = E_{in}(r,t)L$.

7.3 Applications of Quantum Transmission Line Modelling Method

7.3.1 Modelling of Quantum Well Structures

In the following, the Q-TLM method which was introduced earlier in this chapter is used to establish a new model which can be used to analyse performance of a quantum well structure. Hereby, we refer to this proposed method as, quantum well transmission line modelling (QW-TLM). Fig. 7.2 represents one QW-TLM unit of a quantum well structure. It consists of three parallel Q-TLM sub-units. The 1st, 2nd and 3rd Q-TLM sub-units

represent photons' emissions during the electrons' transitions from the conduction band to the (i) heavy hole band (HH), (ii) light hole band (LH) and (iii) the spin-orbit split-off band (SO) at a certain wave vector, respectively. Also parallel QW-TLM units are employed to model the photons' emissions during the electrons' transitions from the conduction band to the valence band in the wave vector space. Axial approximation [72] is applied to simplify the electron transition process in the wave vector space. Hence, each QW-TLM unit (see Fig.7.2) includes three resonant stub filters and their corresponding weight coefficients A_1, B_1 and C_1. Equation 7.3 can be used to obtain the weight coefficient for each sub-unit by applying the associated wave vector's momentum matrix, Fermi-Dirac distribution and energy band.

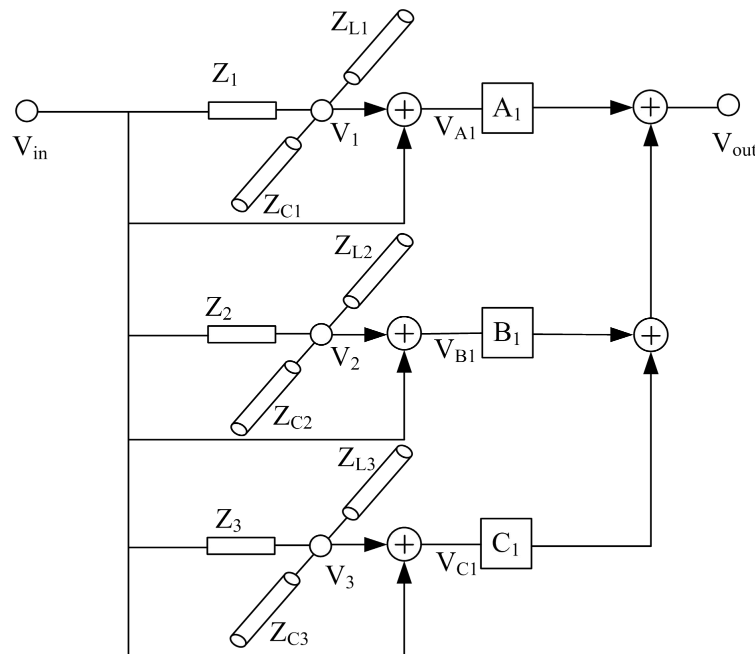

Fig. 7.2 The proposed QW-TLM unit of a quantum well device.

In the above QW-TLM unit, stub filters shown in the $1st$, $2nd$ and $3rd$ branches are used to describe the photon emissions generated by the electron transitions from the conduction band to the heavy hole, light hole and spin-orbit split-off bands at a specific

wave vector, respectively. For simplicity we assume the resistor value in each branch of the QW-TLM unit is unity (i.e. $Z_1 = Z_2 = Z_3 = 1\Omega$). Figure 7.3 describes the voltage propagation process in each stub filter. The input transmission line with the length Δl is used to represent the resistor while the open and short stub transmission lines each with length $\Delta l / 2$ are used to model the capacitor and inductor, respectively. At the time interval, the input voltage V_{in} propagates along the input transmission line and arrives at the scattering node S and the reflected voltages of the capacitor V_C^r and inductor V_L^r propagate towards the stubs ends and return to the scattering node (i.e. V_C^i and V_L^i in Fig.7.3)

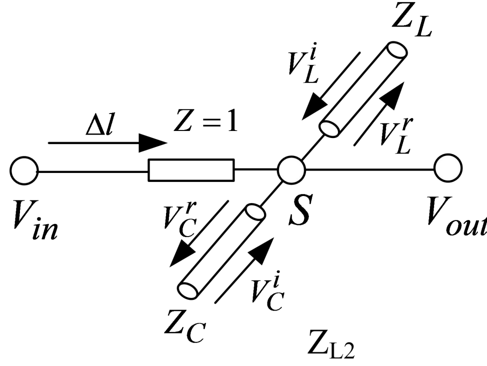

Fig. 7.3 Voltage propagation process in the stub filter.

Based on the TLM theory, the Thevenin equivalent circuit of the stub filter is shown in Fig.7.4. The input currents i_1, i_2 and i_3 of the node's 1st , 2nd and 3rd branches and the node voltage V can be expressed as:

$$i_1 = V_{in} Y_R = V_{in} \tag{7.14}$$

$$i_2 = 2V_C^i Y_C \tag{7.15}$$

$$i_3 = 2V_L^i Y_L \tag{7.16}$$

$$V = \frac{1}{Y}(i_1 + i_2 + i_3) = \frac{1}{Y}(V_{in} + 2Y_c V_C^i + 2Y_L V_L^i) \tag{7.17}$$

where,

$$Y = 1 + Y_C + Y_L \tag{7.18}$$

Y_C and Y_L in Eq.(7.18) are capacitance and inductance admittances, respectively.

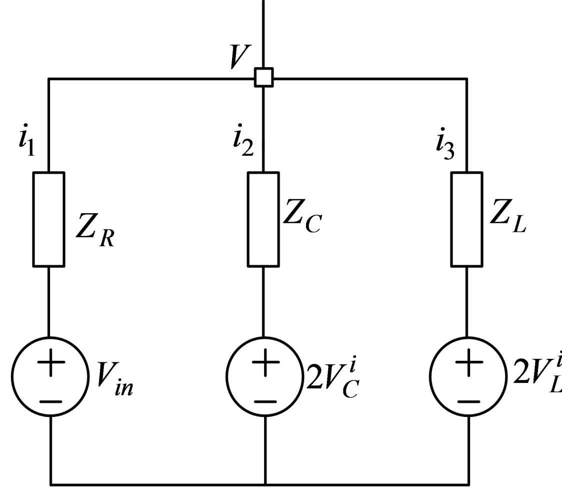

Fig. 7.4 Thevenin equivalent circuit of the stub filter.

Based on the above analysis, the node voltages V_1, V_2 and V_3 of each stub filter in the QW-TLM unit shown in Fig.7.2 can be expressed as:

$$V_1 = \frac{1}{Y_1}(V_{in} + 2Y_{C1}V_{C1}^i + 2Y_{L1}V_{L1}^i) \tag{7.19}$$

$$V_2 = \frac{1}{Y_2}(V_{in} + 2Y_{C2}V_{C2}^i + 2Y_{L2}V_{L2}^i) \tag{7.20}$$

$$V_3 = \frac{1}{Y3}(V_{in} + 2Y_{C3}V_{C3}^i + 2Y_{L3}V_{L3}^i) \tag{7.21}$$

where,

$$Y_p = 1 + Y_{Cp} + Y_{Lp}, p = 1,2,3 \tag{7.22}$$

$$Y_{Cp} = \frac{1}{Z_{Cp}} = Q / \tan(\pi \Delta T f_p), p = 1,2,3 \tag{7.23}$$

$$Y_{Lp} = \frac{1}{Z_{Lp}} = Q \tan(\pi \Delta T f_p), p = 1,2,3 \tag{7.24}$$

In the above equations, V_{in} is the input voltage, (V_{C1}^i, V_{C2}^i, V_{C3}^i) and ($V_{L1}^i, V_{L2}^i, V_{L3}^i$) are

the incident voltages of the capacitive and inductive stub lines, respectively, Y_{Cp} and Y_{Lp} are the characteristic admittances of the capacitive and inductive stub lines and f_p is the central frequency of the pth stub filter. The output voltage of each stub filter is:

$$V_{A1} = V_{in} + V_1 \tag{7.25}$$

$$V_{B1} = V_{in} + V_2 \tag{7.26}$$

$$V_{C1} = V_{in} + V_3 \tag{7.27}$$

and the output voltage of the whole QW-TLM unit is expressed as:

$$V_{out} = A_1 V_{A1} + B_1 V_{B1} + C_1 V_{C1} \tag{7.28}$$

Referring to Fig.7.3 voltages reflected into capacitor, V_{Cp}^{r}, and inductor, V_{Lp}^{r}, of each QW-TLM sub-unit can be expressed as:

$$V_{Cp}^{r} = V_p - V_{Cp}^{i}, p = 1,2,3 \tag{7.29}$$

$$V_{Lp}^{r} = V_p - V_{Lp}^{i}, p = 1,2,3 \tag{7.30}$$

The associated reflected voltages from the stubs' ends become new incident voltages (V_C^i and V_L^i) after one iteration [129-130], that is:

$$_{N+1}V_{CP}^{i} = {}_{N}V_{CP}^{r}\ , p = 1,2,3 \tag{7.31}$$

$$_{N+1}V_{LP}^{i} = -{}_{N}V_{LP}^{r}\ , p = 1,2,3 \tag{7.32}$$

where, K is the iteration number and N is the iteration number. According to Eq. (7.4) the frequency in each sub-unit filter of QW-TLM is a function of the wave vector k_t that can be expressed as[65]:

$$f_p(k_t) = (E_n^c(k_t) - E_{\sigma,m}^{\upsilon}(k_t))/h,\ \upsilon = HH, LH, SO \tag{7.33}$$

where, h is the Plank constant, $E_n^c(k_t)$ and $E_{\sigma,m}^{\upsilon}(k_t)$ are the energy band structure in the

conduction and valence bands, respectively. When the heavy hole energy band ($E^{\upsilon}_{\sigma,m}(k_t)$, $\upsilon = HH$) is substituted into Eq. (7.33), the central frequency of the first sub-unit filter ($f_1(k_t), p=1$) can be obtained. The band structures are obtained by solving the Schrodinger equations for the conduction and valence bands (see Eq. (2.5) and Eq. (2.8) in Chapter 2). Due to spin orbit interaction, the valence band is spilt into the HH, LH and SO bands. Thus, in one QW-TLM unit, three stub filters are used to describe the photon emissions from the different processes in which electrons transit from the conduction band to heavy hole band, light hole band and spin-orbit split-off band at the same wave vector. According to Eq. (7.7), the Q-factor of each sub-unit filter can be expressed as:

$$Q = 2\pi f_m / \gamma \tag{7.34}$$

where, f_m is the frequency of the generated photon, γ is the linewidth broadening factor during the photon emission process.

7.3.2 Gain Model of Quantum Well Devices

The gain of an active quantum well semiconductor optical device is dependent on the wavelength, carrier density and carrier temperature. As the gain spectrum of a quantum well structure is complex and asymmetric, TLLM method cannot be used to describe the complex processes in such devices. The following explains how to apply the QW-TLM units to model the gain of quantum well structures. In order to verify the validity of the QW-TLM method we compare the results obtained by the reported analytical expression [74] with those obtained by the proposed QW-TLM method. In the following analysis, the strained $In_{0.64}Ga_{0.36}As$ - $InGaAsP$ quantum well device is used and its material parameters used in the simulation are listed in Tab.2.1 of Chapter 2.

7.3.2.1 Gain Spectrum Computation of Strained $In_{0.64}Ga_{0.36}AS / InGaAs$

Quantum Well Device Using Analytical Method

Equations (2.28) to (2.31) in Chapter 2 are used to calculate the gain spectra of the strained $In_{0.64}Ga_{0.36}AS / InGaAs$ quantum well device both in considering and ignoring the contribution of the spin-orbit split-off band electron transition. Fig. 7.5 shows the simulation results for both cases. These results are also in good agreements with those reported in Ref. [70]. As Fig.7.5 clearly indicates, the effect of electron transition from conduction band to spin-orbit split-off band on the gain spectra of this quantum well device is negligibly small and hence, we can ignore the effect of this low energy band in gain calculation.

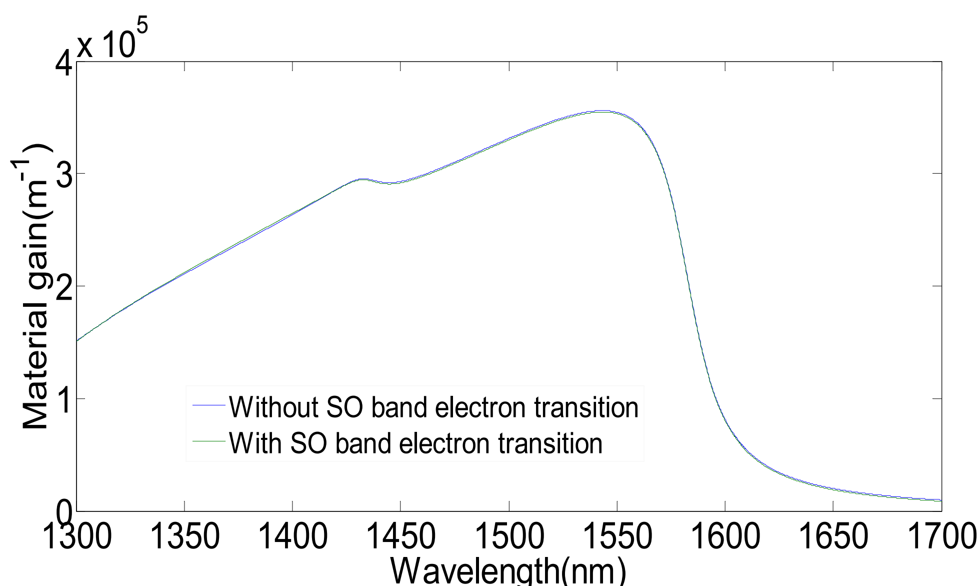

Fig. 7.5 Gain spectra of the strained $In_{0.64}Ga_{0.36}AS / InGaAs$ quantum well both in the presence and absence of spin-orbit split-off band electron transition.

7.3.2.2 Gain Spectrum Computation of Strained $In_{0.64}Ga_{0.36}AS / InGaAs$ Quantum Well Device Using QW-TLM Method

Figure 7.6 shows the gain model for quantum well devices based on the proposed QW-TLM method. The model consists of a number of parallel QW-TLM units and a

coefficient G_0 . Each unit has two weight coefficients A_i and B_i , where, i denotes the branch number. Because the effect of the electron transition from the conduction band to the spin-orbit split-off band is negligible we have not included the 3rd branch of the QW-TLM unit (see Fig.7.5) in this proposed gain model.

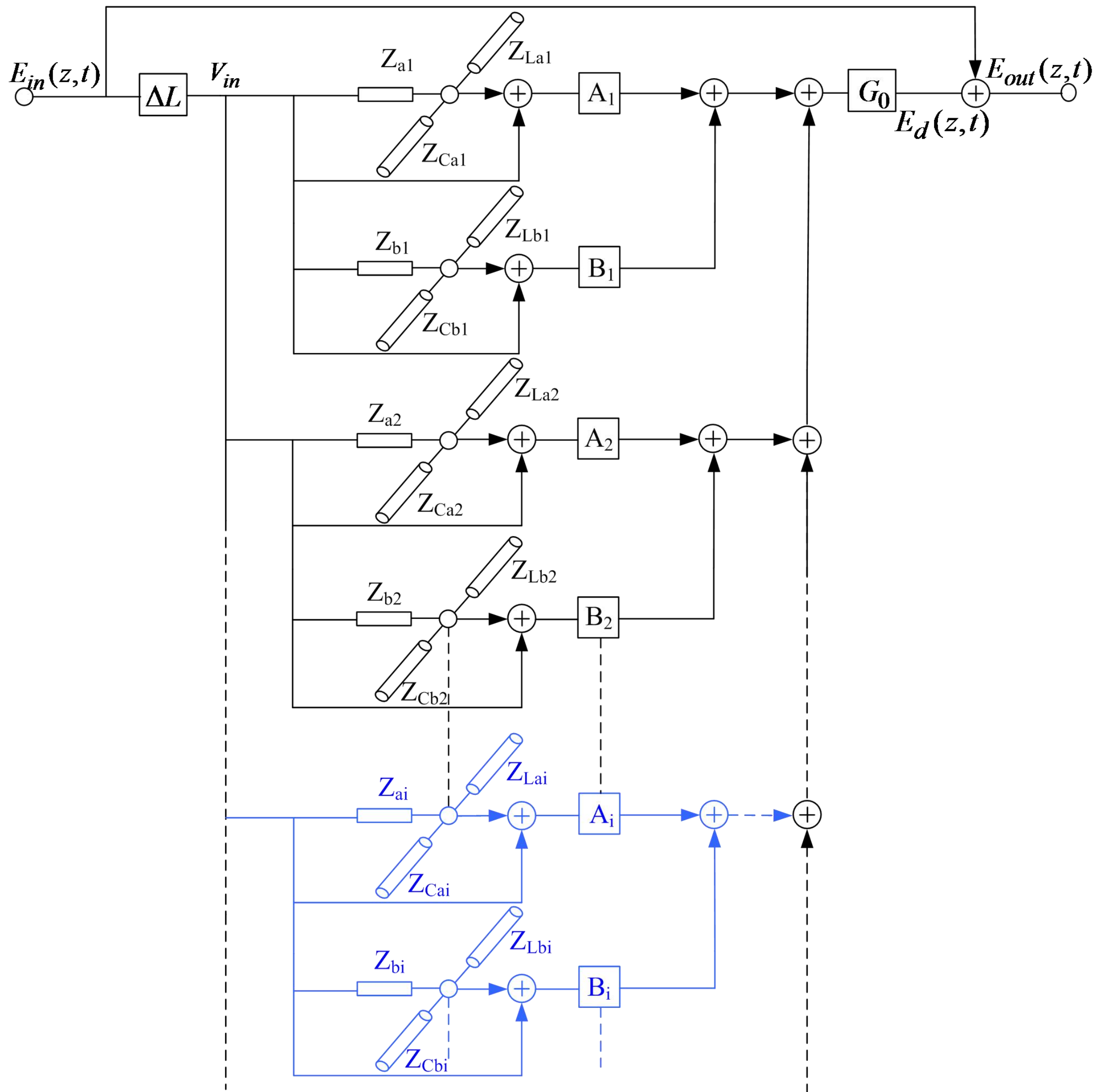

Fig. 7.6 Gain model of quantum well devices based on QW-TLM.

Referring to the ith QW-TLM unit in Fig.7.6, its 1st Q-TLM unit branch includes the impedances (Z_{ai} , Z_{Lai} and Z_{Cai}) and the coefficient A_i , which are used to model the photon emission during the electron transitions from the conduction band to the heavy hole

band while the Q-TLM unit in the 2nd branch, which consists of the impedances (Z_{bi} , Z_{Lbi} and Z_{Cbi}) and the coefficient B_i , represents the photon emission during the electron transition from the conduction band to the light hole band. The frequencies of the 1st and the 2nd branches of stub filters in the ith QW-TLM unit can be expressed as:

$$f_1(k_t(i)) = [E_n^c(k_t(i)) - E_{\sigma,m}^h(k_t(i))]/h \tag{7.35}$$

$$f_2(k_t(i)) = [E_n^c(k_t(i)) - E_{\sigma,m}^l(k_t(i))]/h \tag{7.36}$$

In the above equations $E_n^c(k_t(i))$ is the *nth* conduction band energy at the wave vector $k_t(i)$, $E_{\sigma,m}^h(k_t(i))$ and $E_{\sigma,m}^l(k_t(i))$ are the *mth* heavy-hole and light-hole band energies at the wave vector $k_t(i)$, respectively. The characteristic admittance values in the ith QW-TLM unit can be obtained by substituting $f_1(k_t(i))$ and $f_2(k_t(i))$ into Eq. (7.23) to (7.24).The time interval ΔT in Eqs. (7.23) and (7.24) can be expressed as:

$$\Delta T = 1/f_{sam} \tag{7.37}$$

where, f_{sam} is the sampling frequency which can be determined by the following expression:

$$f_{sam} \geq 2\max[f_1(k_t(i)), f_2(k_t(i))] \tag{7.38}$$

The weight coefficients A_i and B_i are given as:

$$A_i = \frac{1}{f_1(k_t(i))}\left|\hat{e}M_{nm}^{\sigma\eta}(k_t(i))\right|^2 \times [F_n^c(k_t(i)) - F_{\sigma m}^h(k_t(i))]k_t(i)dk_t \tag{7.39}$$

$$B_i = \frac{1}{f_2(k_t(i))}\left|\hat{e}M_{nm}^{\sigma\eta}(k_t(i))\right|^2 \times [F_n^c(k_t(i)) - F_{\sigma m}^l(k_t(i))]k_t(i)dk_t \tag{7.40}$$

where, $M_{nm}^{\eta\sigma}(k_t(i))$ is the momentum matrix element at the wave vector $k_t(i)$, dk_t is the wave vector interval used in the numerical calculation, $F_n^c(k_t(i))$ is the value of the Fermi-Dirac distribution function for the conduction band at the wave vector $k_t(i)$, the values

of the Fermi-Dirac distribution functions for the heavy hole, $F^{h}_{\sigma m}(k_t(i))$, and the light hole, $F^{l}_{\sigma m}(k_t(i))$, bands can be calculated from Eq. (2.31) in Chapter 2. The coefficient G_0 can be derived from the time-dependent perturbation theory, that is [65]:

$$G_0 = \frac{\Gamma q^2}{\pi n_r c \varepsilon_0 m_0^2 L_z h \gamma} \tag{7.41}$$

where, Γ is the optical confinement factor, q is the magnitude of the electron charge, n_r and ε_0 are the refractive index and the permittivity in free space, c is the speed of light in free space, m_0 is the electron effective mass in free space, L_z is the quantum well width. The output electric field of the gain model can be expressed as:

$$E_{out}(z,t) = E_{in}(z,t) + E_d(z,t) \tag{7.42}$$

where, $E_d(z,t)$ is obtained by adding all outputs of parallel Q-TLM units multiplied by the coefficient G_0.

In the following section, the gain spectra of the compressively strained $In_{0.64}Ga_{0.36}AS / InGaAs$ quantum well is simulated using the following two methods (i) the analytical expression derived from Fermi's golden rule (i.e. Eq.(2.29) in Chapter 2 and (ii) the proposed QW-TLM method. Both gain spectra are compared to verify the validity of the proposed QW-TLM method. The gain spectra of the proposed model can be obtained by applying FFT to the pulse sequence of the output node when a unit impulse is applied to the input node of the gain model shown in Fig.7.6. All parameters used in the gain spectrum calculation are given in Tab.7.1.

Tab. 7.1 Parameters used in calculation of gain spectral of strained $In_{0.64}Ga_{0.36}AS / InGaAs$ quantum well device.

Symbol	Parameter	Value
Q	Stub filter Q-factor	60.8
Q_s	Compensation stub filter Q-factor	5
N	Carrier density	$8.0\times10^{24}m^{-3}$
f_{sam}	Sampling frequency	$1.0\times10^{15}Hz$
b	Band number	3
γ	Linewidth of the Lorentzian function	$2\times10^{13}rad/s$
W_w	Well width	$4.5nm$
W_b	Barrier width	$10nm$
n_r	Background refractive index	3.67

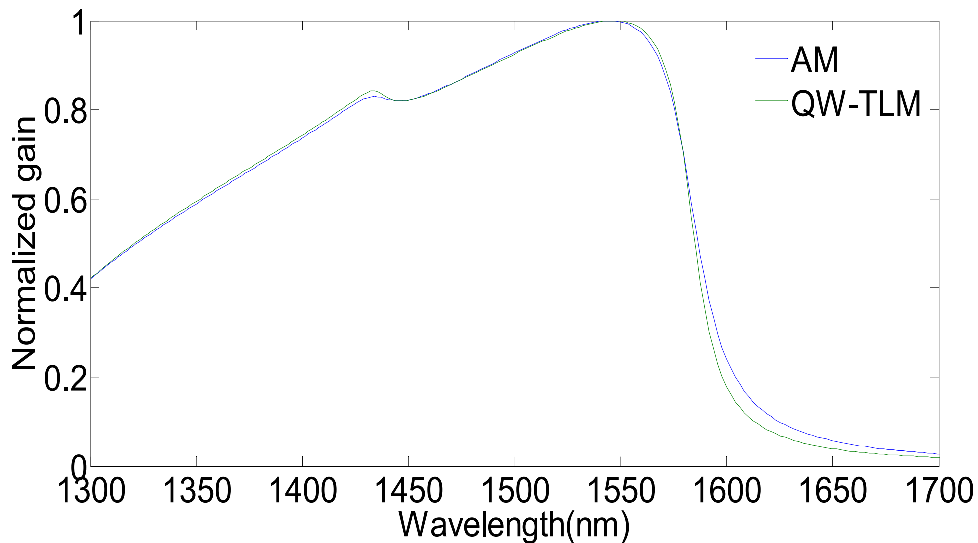

Fig. 7.7 Normalized gain spectra of a compressively strained $In_{0.64}Ga_{0.36}AS / InGaAs$ quantum well device (i) analytical (green) and QW-TLM (blue) methods.

Figure 7.7 shows the normalized gain spectra obtained using both the analytical and the proposed QW-TLM methods. As the results clearly indicate, the gain spectra obtained by the proposed model is in a very good agreement with that obtained by the analytical method (i.e. Eq. (2.29) of Chapter 2) within $1300\,nm$ and $1700\,nm$ wavelength band. In order to reduce the computation time we have assumed that the Q-factor in the proposed model is the same for all units and this assumption has caused a negligibly small difference between the two methods within $1585\,nm$ and $1670\,nm$ wavelength band.

7.3.3 Spontaneous Emission Model of Quantum Well Devices Based on Q-TLM

Since the amplified spontaneous emission (ASE) takes part in draining the carrier density and propagates together with the amplified optical signal, it is necessary to accurately describe this process for a complete model of quantum well device. In the following, the QW-TLM method shown in Fig.7.8 is introduced to model the spontaneous emission process. The model consists of a source S_{ASE} , parallel QW-TLM units and the coupling coefficient β .

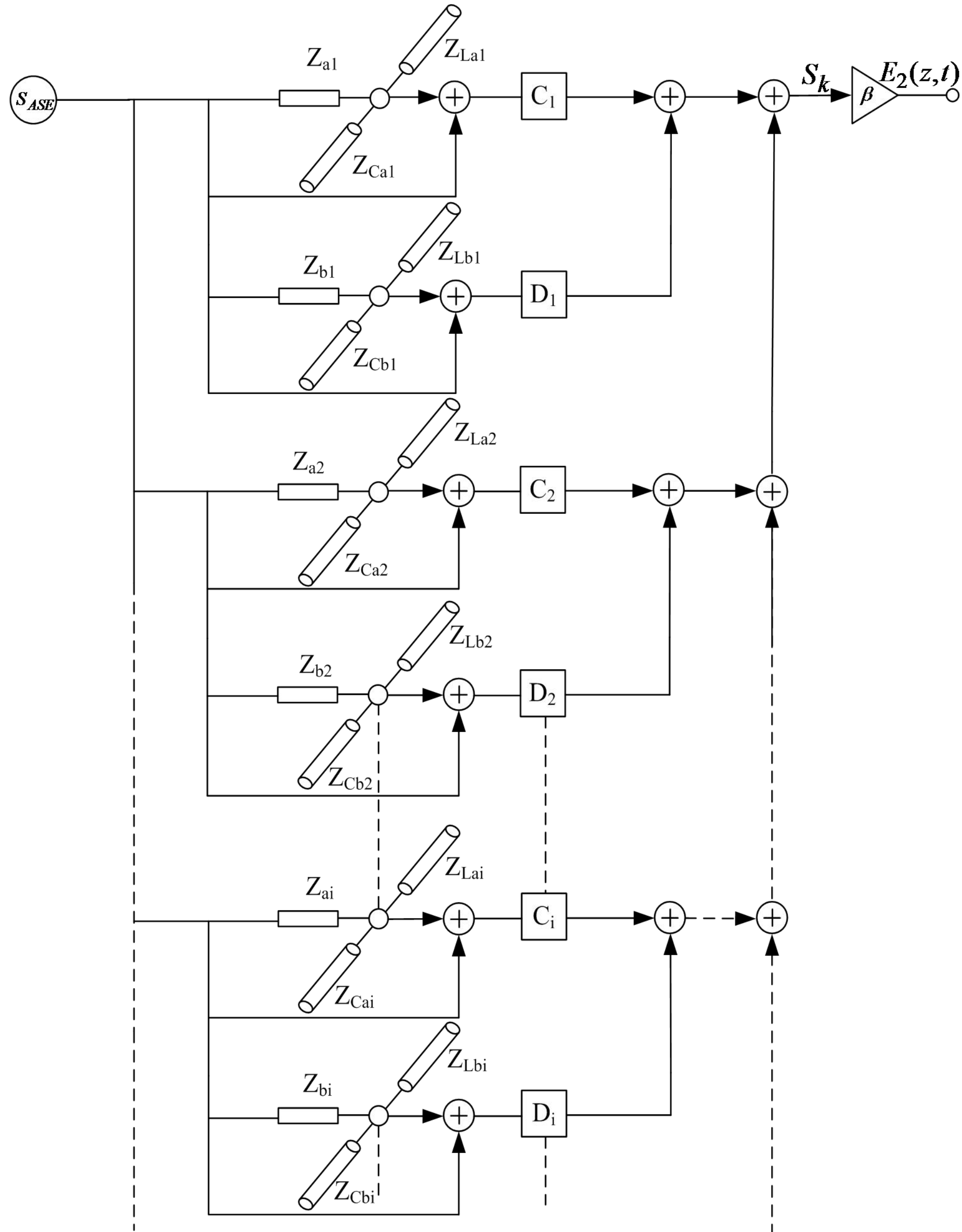

Fig. 7.8 Spontaneous emission model of a quantum well device based on QW-TLM.

The ASE source can be expressed as:

$$S_{ASE}(t) = \begin{cases} E_0 / q & for \quad t = nT_1, n = 0,1,2... \\ 0 & for \quad (n-1)T_1 < t < nT_1, n = 1,2... \end{cases} \tag{7.43}$$

where, E_0 is the energy of a photon, T_1 is the spontaneous emission lifetime of the exited state. The weight coefficients C_i and D_i can be obtained Eq. (7.13) as [65]:

$$C_i = S_0 f_1(k_t(i)) \left| M_{sp}(k_t(i)) \right|^2 \times F_n^c(k_t(i)) \times (1 - F_{\sigma m}^h(k_t(i))) k_t(i) dk_t \tag{7.44}$$

$$D_i = S_0 f_2(k_t(i)) \left| M_{sp}(k_t(i)) \right|^2 \times F_n^c(k_t(i)) \times (1 - F_{\sigma m}^l(k_t(i))) k_t(i) dk_t \tag{7.45}$$

where,

$$S_0 = \frac{4q^2 n_r^2 \Delta V}{\pi h c^4 \varepsilon_0 m_0^2 L_z} \tag{7.46}$$

In the above equations $M_{sp}(k_t(i))$ is the momentum matrix element of the spontaneous emission at the wave vector $k_t(i)$, ΔV is the volume of each section of the amplifier cavity. The impedances shown in Fig.7.8 can be obtained from Eqs. (7.10) and (7.11). The output electric filed $E_2(z,t)$ can be expressed as:

$$E_2(z,t) = \beta S_k \tag{7.47}$$

where, S_k is the sum of the outputs of the parallel QW-TLM units, β is the coupling coefficient representing the number of photons generated by spontaneous emission that are coupled into the gain model to be amplified.

Figure 7.9 shows the spontaneous emission spectra of the of strained $In_{0.64}Ga_{0.36}AS / InGaAs$ quantum well semiconductor optical amplifier (QW-SOA) obtained by both analytical (blue) and QW-TLM (green) methods. The figure clearly shows that there is good agreement between the analytical and QW-TLM methods within the spectra width ranging from $1300nm$ to $1700nm$. In the wavelength region ranging from $1585nm$ to $1670nm$ there is a negligibly small difference between the two methods due to the assumption used in gain spectra calculation which was mentioned earlier.

From the above analysis of the spontaneous emission spectrum and gain spectrum of QW-SOAs, we can conclude that QW-TLM model gives an accurate description of the wavelength-dependent of both spontaneous and stimulated emission processes.

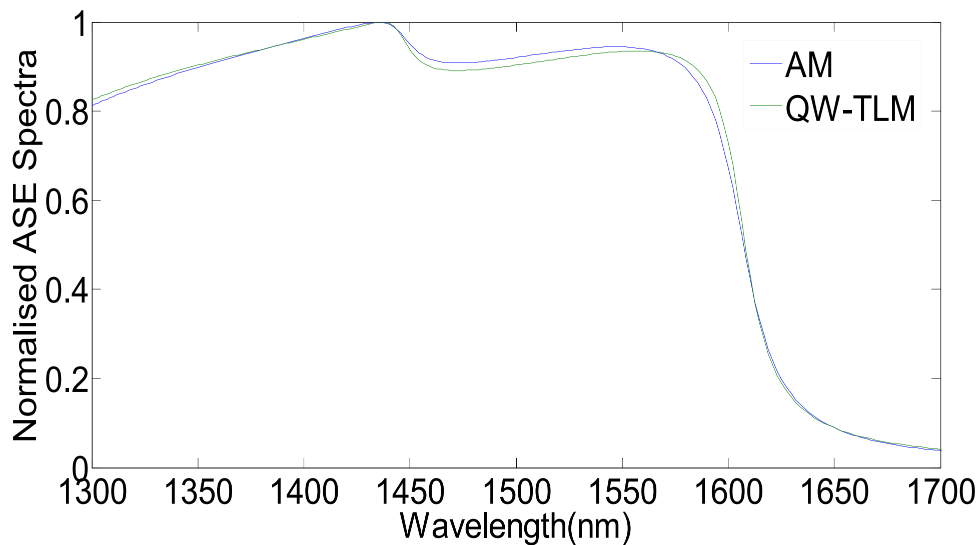

Fig. 7.9 Computation of the normalized spontaneous emission spectra of a compressively strained $In_{0.64}Ga_{0.36}AS$ / $InGaAs$ quantum well SOA using (i) analytical (blue) and (ii) QW-TLM (green) methods.

7.4 Theoretical Model of the Quantum Dot Structure based on Q-TLM

Quantum dots are very small particles (nano-scale) that exhibit different optical and electronic properties as compared with the larger particles. Such semiconductor materials tightly confine either electrons or electron holes. They have properties that are intermediate between those of bulk semiconductors and those of discrete molecules. The quantum confinement in a quantum dot structure is in all three dimensions. This makes its tunability higher than that of quantum well and bulk structures. Quantum dots can provide higher differential gain and spectral purity (i.e. no chirping) hence, they are promising structures for active semiconductor optical devices including semiconductor lasers and amplifiers [12, 14, 35].

In the following, the Q-TLM method is employed to establish a model for quantum dot structure. This model is referred to as quantum dot (QD) TLM. In this quantum dot TLM

model, the basic composition is quantum dot transmission line modelling (QD-TLM) unit, which is shown in Fig. 7.10. From Fig. 7.10, it can be observed that one QD-TLM unit consists of a stub filter and a corresponding weight coefficient. The stub filter consists of one unity resister, a capacitor and an inductor.

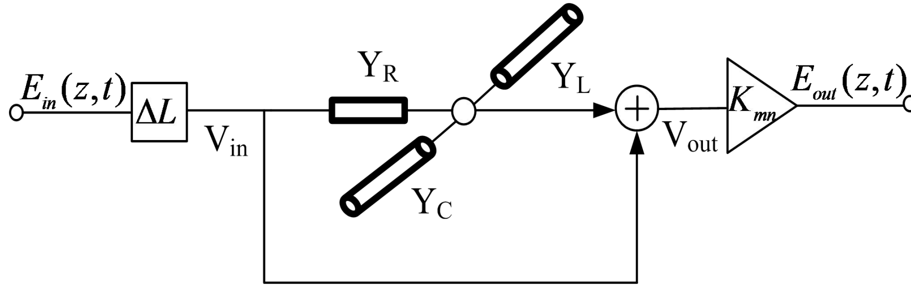

Fig. 7.10 QD-TLM unit structure.

Based on Eq. (7.4), the central frequency of the stub filter is:

$$f_{mn} = (E_m^c - E_n^v) / h \tag{7.48}$$

where, E_m^c and E_n^v are the discrete confined energy of quantum dot in the conduction and valence bands, which can be determined by solving the Schrödinger equation [126]. The subscripts m and n are used to label the electrons and holes. Based on Eqs. (7.10) and (7.11), the characteristic admittances for both capacitor and inductor can be expressed as:

$$Y_{Cmn} = \frac{Q}{\tan(\pi f_{mn} \Delta T)} \tag{7.49}$$

$$Y_{Lmn} = Q \tan(\pi f_{mn} \Delta T) \tag{7.50}$$

where, Q is the quality factor of the stub filter. In Fig. 7.10, the stub filter accounts for the broadening caused by the carrier scattering process while the weight coefficient accounts for the electron transition rates and the inhomogeneous broadening determined by the quantum size shape. The global quasi-Fermi levels of the conduction and valence bands can be determined by the carrier density in the quantum dots [126]. When Q-TLM is used

to model the quantum dot, its structure is divided into many small sections along the active region, the model for each section is shown in Fig. 7.11 (for both right (R) and left (L) propagation directions). This model consists of a transmission line with length ΔL, a transmission coefficient α, an amplified spontaneous emission module (ASE) and a stimulated emission module (SE).

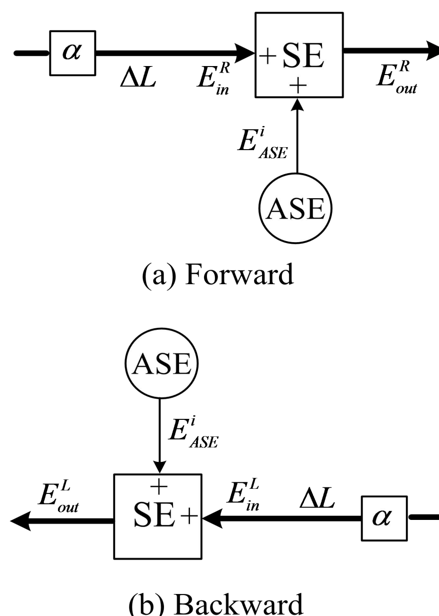

Fig. 7.11 Structure of one section of QD-TLM model (a) forward and (b) backward directions.

The electric field is sampled with a period ΔT. The adjacent sections are connected by transmission lines having length of $\Delta L = v\Delta T$ where v is the velocity of the electric field propagation. The transmission coefficient α is used to represent the waveguide loss. The spontaneous and stimulated emissions modules describe the photons spontaneous and stimulated emissions processes, respectively. The electric fields from the adjacent section (E_{in}) and that generated from the spontaneous emission module (E^{i}_{ASE}) are input into the stimulated emission (SE) module, where the electric fields stimulate the electron transition from the higher energy state to the lower energy state and consequently new photons having the same frequency are produced. Both the spontaneous and stimulated

emissions modules consist of QD-TLM units.

Fig. 7.12 shows the structure for the stimulated emission module. It consists of parallel QD-TLM units and the coefficient (G_0). Parallel QD-TLM units are employed to describe the electron transitions, which is stimulated by the incident electric field $E_1(z,t)$. The output electric field $E_2(z,t)$ consists of the original incident electric field and the newly generated electric field during the electron transitions. The length of each section (ΔL) can be chosen small enough so that we can assume the electric filed distribution within the small section is constant and then the input voltage V_{in} of this section in terms of the electric filed can be expressed as:

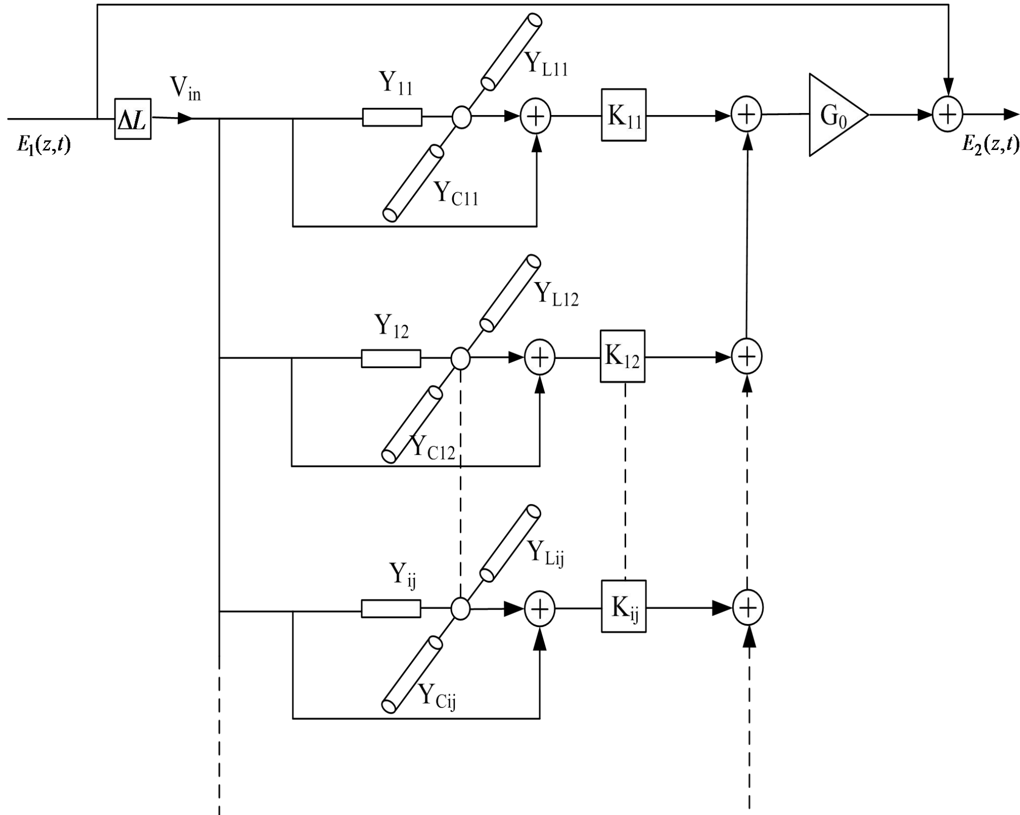

Fig. 7.12 The Stimulated emission module.

$$V_{in} = (E_{in}^R + E_{ASE}^i) \times \Delta L \tag{7.51}$$

Based on Eq. (7.13), the weight coefficient K_{mn} and the coefficient G_0 in Fig. 7.12 can be expressed as [65]:

$$K_{mn} = \frac{1}{f_{mn}} \int_{-\infty}^{\infty} \left| \langle \psi_c | \hat{e} \cdot P | \psi_v \rangle \right|^2 \times (f_c(E, E_m^c) - f_v(E, E_n^v)) \times e^{-(E - E_{mn}^{cv})^2 / 2\sigma^2} dE \tag{7.52}$$

$$G_0 = \frac{\sqrt{2\pi}\Gamma q^2 N_{dot}^{2D}}{\pi \sigma n_r c \varepsilon_0 m_0^2 L_Z \gamma_d h} \tag{7.53}$$

where,

$$E_{mn}^{cv} = E_m^c - E_n^v \tag{7.54}$$

$\left| \langle \psi_c | \hat{e} \cdot P | \psi_v \rangle \right|^2$ is the interband momentum matrix element of the stimulated emission. $f_c(E_m^c)$ and $f_v(E_n^v)$ are the Fermi-Dirac distribution functions for the conduction and valence bands, respectively, σ determines the FWHM of inhomogeneous broadening, q is the electron charge, Γ is the confinement factor, N_{dot}^{2D} is the number of quantum dots per unit area, n_r is the refractive index of the material, L_Z is the thickness of the layer containing the dots, γ_d is the full width at half maximum of the Lorentzian lineshape function that accounts for homogeneous broadening. The model for spontaneous emission process is shown in Fig. 7.13 which consists of parallel QD-TLM units, spontaneous emission coupling coefficient β and spontaneous emission source (S_{ASE}). The spontaneous emission module describes the process in which the electron in the excited state spontaneously transits to the lower energy state. The electron transition processes are described by the parallel QD-TLM units. The spontaneous emission source is given by:

$$S_{ASE}(t) = \begin{cases} E_0 / q & for \quad t = nT_0, n = 0,1,2... \\ 0 & for \quad (n-1)T_0 < t < nT_0, n = 1,2... \end{cases} \tag{7.55}$$

where, E_0 is the energy of a photon and T_0 is the excited lifetime in the spontaneous emission. Based on Eq. (7.13), the weight coefficient in each QD-TLM unit is given as [65]:

$$K'_{mn}=S_0 f_{mn}\int_{-\infty}^{\infty}\left|\langle\psi_c|\hat{e}\cdot M|\psi_v\rangle\right|^2\times(f_c(E,E_m^c)\times(1-f_v(E,E_n^v)))\times e^{-(E-E_{mn}^{cv})^2/2\sigma^2}dE \tag{7.56}$$

where

$$S_0=\frac{8\sqrt{2\pi}n_r^2q^3N_{dot}^{2D}\Delta V}{h^2\gamma_d\sigma\varepsilon_0 m_0^2c^4L_Z} \tag{7.57}$$

$\left|\langle\psi_c|\hat{e}\cdot M|\psi_v\rangle\right|^2$ is the interband momentum matrix element for the spontaneous emission, ΔV is the volume of each section of quantum dot structure.

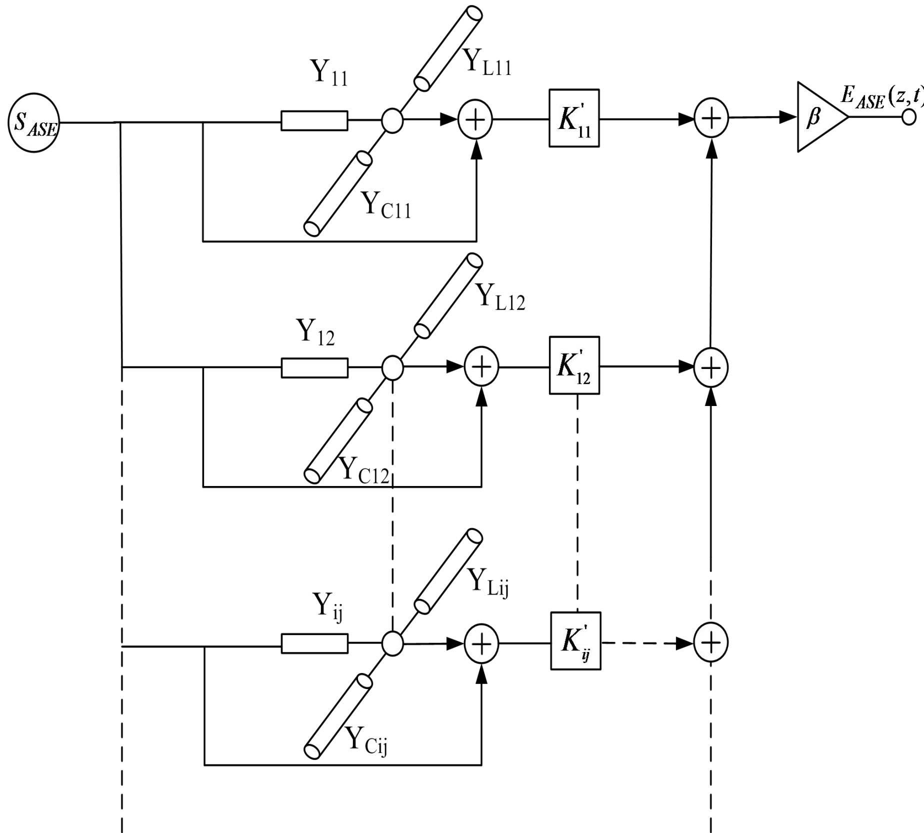

Fig. 7.13 Spontaneous emission model of a quantum dot device.

Figure 7.14 (a) and (b) show the gain and spontaneous emission spectra of the quantum dot structure at the injection carrier density of $8.3\times10^{14}cm^{-3}$ obtained by both Q-TLM and analytical methods [126] (AM). In the simulation, the $750\ \mu m$ long quantum dot structure is divided into 10000 sections. The Q factor and the sampling frequency ($1/\Delta T$) used in the

analysis are 22 and $10^{15}\,Hz$, respectively. The boundary condition provided in Ref. [72] is used and the other required simulation parameters of quantum dot are taken from Ref. [126]. The results shown in Fig.7.14 clearly confirmed that the proposed Q-TLM can accurately describe the gain and spontaneous emission spectra of the quantum dot structure.

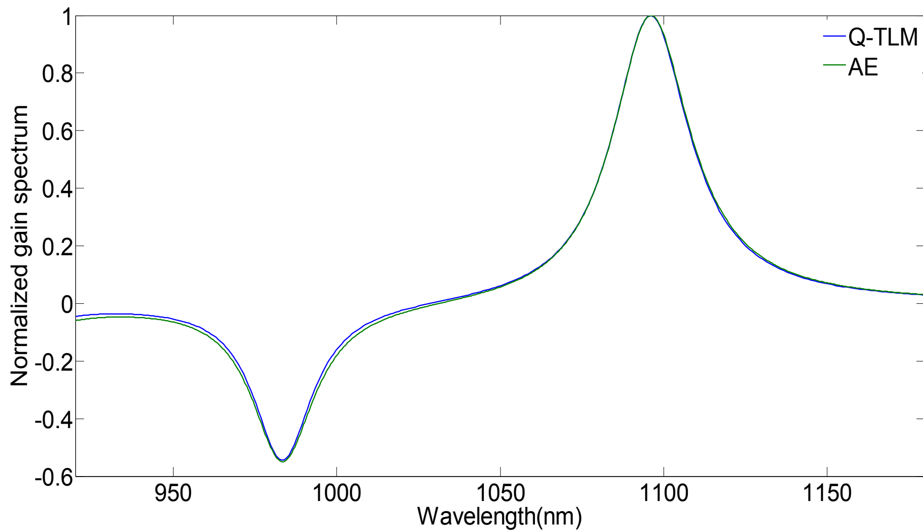

(a)

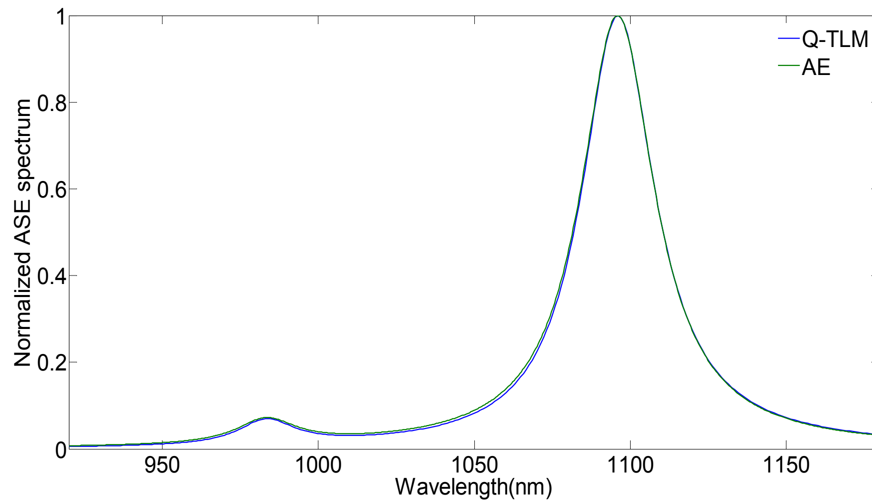

(b)

Fig. 7.14 Quantum dot normalized (a) gain and (b) ASE spectra computed by both Q-TLM and analytical methods at carrier density $8.3\times10^{14}\,cm^{-3}$.

7.5 Conclusions

In this Chapter, a new modelling method referred to as quantum well transmission line modelling (QW-TLM) was introduced for both quantum well and quantum dot structures. The model is based on photon emission which can be explained by both quantum statistic and photon-electron interaction process. Detailed studies are performed to show how to use the new modelling method to establish gain and spontaneous emission models for quantum well and quantum dot structures. The simulation results showed a very good agreement between the results obtained by this proposed new Q-TLM and the analytical methods. The Q-TLM technique provides an effective method to study the temporal and spectral behavior of semiconductor optical devices.The advantages of Q-TLM are that the modelling method can model accurately the temporal and spectral performance of semiconductor optical devices; it can be used to analyze the chip-based optical integrated system; the modelling method can also be adopted the predict the microscopic dynamics by analyzing the macroscopic performance of semiconductor optical devices. Furthermore, considering that the simulation of optical field propagation as well as the interaction between optical field with materials is in the time domain, the solution of large numbers of simultaneous equations is avoided in the Q-TLM method. There are no problems with the convergence and stability.

Chapter 8

Application of Quantum Transmission Line Modelling to Semiconductor Optical Amplifiers and Lasers

8.1 Introduction

Theoretical models for semiconductor lasers and amplifiers have been studied to facilitate their performance analysis and hence, aid in their designs [131-135]. Several approaches including the microscopic description to rate equations have been applied to model the nanostructured semiconductor optical devices. Many of these models have not considered the dynamic photon-electron interaction, which is significantly important to accurately describe the optical signal propagation in nanostructured semiconductor optical devices[65]. The method of studying the spectral properties of QW amplifier or laser by solving a set of rate equations [136] cannot provide the continuous spectrum and requires a lot of time to perform a simulation. The reported transmission line laser models [66, 137] were established to analyse performances of bulk lasers (i.e. non-quantum well lasers) [66, 137] however, in this model the symmetric frequency-dependent gain curve [61] are employed by introducing only one stub filter. This approximation clearly indicates that such a model which does not consider dynamic photon-electron interaction cannot accurately predict the spectral behavior of active semiconductor optical devices. In Chapter 7, a new modelling method referred to as quantum transmission line modelling (Q-TLM)

method was introduced to overcome this shortcoming.

In this chapter the Q-TLM is adopted to establish new theoretical models to analyse performance characteristics of quantum well lasers, quantum well amplifiers and quantum dot structures both in the time and frequency domains.

8.2 Q-TLM Method for Quantum Well Amplifiers

8.2.1 Model for Quantum Well Semiconductor Optical Amplifiers (QW-SOAs)

Let $E(x, y, z, t)$ denotes the electric field of the optical wave propagating within the optical amplifier. By averaging the optical intensity over the transverse plane of the amplifier we can express the magnitude of one dimensional electric field $E(z,t)$ as [62]:

$$|E(z,t)|^2 = \frac{1}{DW}\int_{-\infty}^{+\infty}\int_{-\infty}^{+\infty}|E(x,y,z,t)|^2 dxdy \tag{8.1}$$

where, D and W are the thickness and width of the amplifier active region, respectively. Figure 8.1 shows the structure of a QW-SOA model based on Q-TLM.

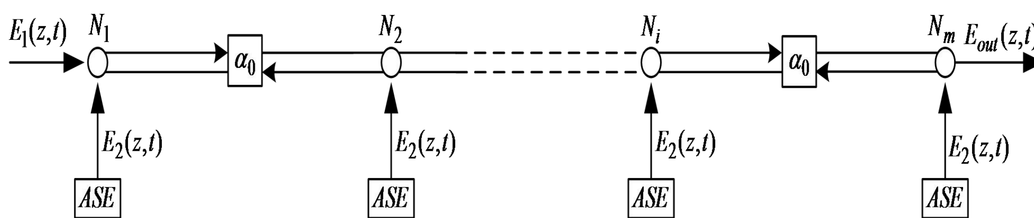

Fig. 8.1 The Q-TLM model for the QW-SOA.

In this model the amplifier active region length L is divided into m sections where each section consists of stimulated emission module N_m, spontaneous emission module ASE, transmission line and transmission coefficient α_0. The length of each transmission line between two adjacent scattering modules is ΔL. The spontaneous and stimulated emissions'

processes are described in their associated modules as shown in Fig.8.1. The electric fields produced by the input optical signal and the spontaneous emission module propagate along the transmission line and vary with both time and space. The input electric filed can be expressed as:

$$E_1(z,t) = I(t)\,e^{i(2\pi f t+\phi)} \tag{8.2}$$

where, $I(t)$, f and ϕ are, respectively, the envelope function, frequency and phase of the input electric field. A chirp is a signal in which the frequency varies with time.Ultrashort pulse propagation also exhibits chirp due to the interaction with the dispersion properties of materials. It should be noted that Q-TLM employs the time-dependent electric field to describe the optical signal propagation in the amplifier cavity rather than the photon density, and thus this modelling method can be used to investigate the chirp during ultrashort pulse propagation. The corresponding power $P(t)$ of the input signal can be expressed as:

$$P(t) = \frac{dW\,|E_1(z,t)|^2}{Z_p} \tag{8.3}$$

where $|E_1(z,t)|^2$ is the light intensity which can be obtained from Eq.(8.1) and Z_p is the transverse wave impedance [62] which is equal to the impedance value of the transmission line between the two sections. The transmission coefficient α_0 accounts for the waveguide loss during the optical signal propagation. The internal structures of the stimulated emission and spontaneous emission modules have been described in Chapter 7(Sections 7.3.2 and 7.3.3).

8.2.2 Carrier Density Distribution Model

The carrier density has significant influences on stimulated and spontaneous emissions'

processes. The quasi-Fermi levels for electrons and holes are determined by the carrier density. Also, carrier density variations cause a small change in the bandgap energy between the conduction and valence bands [57]. As mentioned earlier the active region in the QW-SOA model is divided into m sections. In each section, the rate of change of carrier density, dN / dt can be calculated by the following rate equation [76]:

$$\frac{dN}{dt} = \frac{I}{qV_{act}} - \frac{N}{\tau_s} - \frac{\Gamma}{qDW\Delta L}\frac{V_{in}}{Z_p} \tag{8.4}$$

where, I is the injected current, V_{act} is the volume of the active region, V_{in} is the input voltage of the stimulated emission module in each section, q is the electron charge, N is the carrier density and Γ is the optical confinement factor. The carrier recommendation lifetime τ_s is given by [138]:

$$\tau_s = \frac{1}{A + BN + CN^2} \tag{8.5}$$

where, A , B and C are the linear recombination constant, Bi-molecular recombination constant and Auger recombination constant, respectively.

8.2.3 Modelling of Picosecond Pulse Propagation in QW-SOAs

In this section the Q-TLM model for QW-SOAs which was introduced in the previous section (Fig.8.1) is employed to analyse the compressively strained $In_{0.67}Ga_{0.33}As / InGaASP$ amplifier output temporal and spectral responses when Gaussian input pulses with different peak powers are applied to its input. All parameters used in the simulation are listed in Tab.8.1. The Gaussian pulse amplification will suffer from transform limited. Transform limited pulses are pulses which are as short as its spectral bandwidth permits. In other words, the time-bandwidth product is as small as possible. For a Gaussian pulse, the minimum time-bandwidth product is 0.44 .

Tab. 8.1 Parameters used in the analysis of pulse amplification [129]

Symbol	Description	Value
n	Background refractive index	3.67
Q	Stub filter Q-factor	60.8
f_{sam}	Sampling frequency	$1.0\times10^{15}\,Hz$
A	Linear recombination	$2\times10^{8}\,s^{-1}$
B	Bi-molecular recombination	$6\times10^{-16}\,m^{3}s^{-1}$
C	Auger recombination	$8\times10^{-41}\,m^{6}s^{-1}$
γ	Linewidth broadening of photon emission	$2\times10^{13}\,rad/s$
α_0	Transmission coefficient	0.99755
β	Spontaneous emission coupling coefficient	10^{-8}
Γ	Confinement factor	0.025
N_0	Transparent carrier density	$1.2\times10^{24}\,m^{-3}$
W	QW-SOA width	$1\mu m$
D	QW-SOA thickness	$24.5nm$
L	QW-SOA length	$750\mu m$

Figures 8.2a and b show the temporal and power spectra density waveforms of the input signal, respectively. The input signal temporal waveform is a Gaussian pulse with a peak power of $0.1mw$, centered at $t_{pi}=3ps$, with FWHM pulse width of $2ps$. From the power spectral density of the input signal (Fig. 8.2b), it can be seen that the central frequency of the input signal is $193.484THz$ (i.e. corresponding to the wavelength of $\lambda=1.55\mu m$) and the $3dB$ bandwidth of $229.83GHz$.

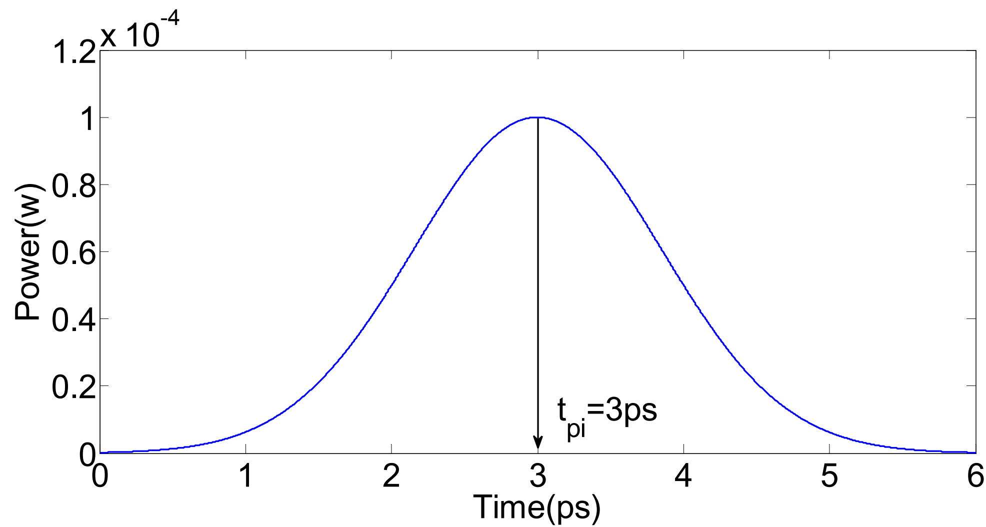

(a)

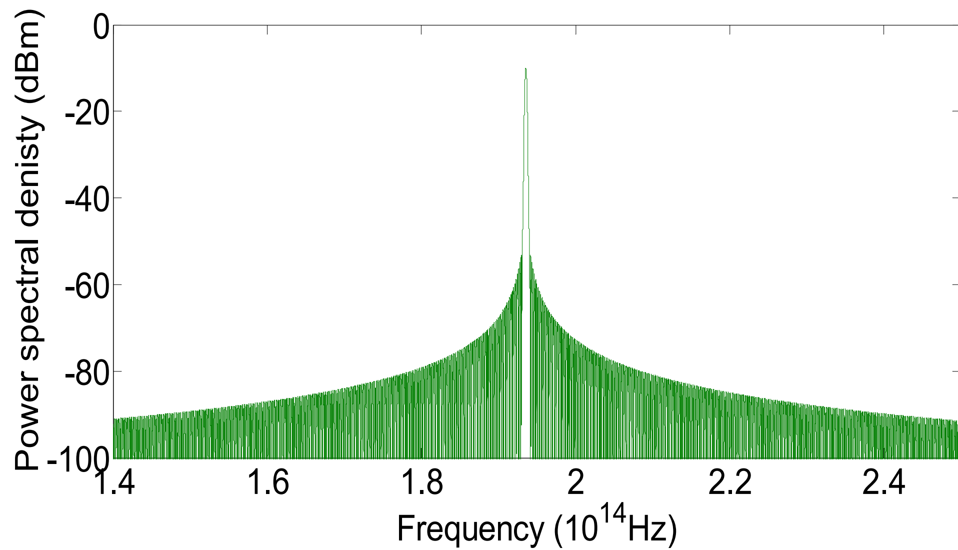

(b)

Fig. 8.2 Gaussian pulse input (a) temporal waveform (b) power spectral density.

The associated temporal and power spectra density waveforms of the amplified output for the above Gaussian input pulse are shown in Figs. 8.3a and 8.3b. Comparison of both input and output temporal responses which are shown in Figs. 8.2a and 8.3a reveals that the output peak time t_{po} (i.e. the time at which the output pulse power is maximum) is shifted from its input peak time of $t_{pi} = 3ps$ (i.e. the time at which the input pulse power

is maximum) to $t_{po} = 1.33\,ps$ (i.e. decreased by about 44%) and the FWHM of the amplified output waveform decreases from $2\,ps$ to $1.374\,ps$. The central frequencies of the input (Fig.8.2b) and the output (Fig.8.3b) spectra are $193.484\,THz$ and $193.539\,THz$, respectively, which implies the output spectrum exhibits a red shift of $8.464\,GHz$.(i.e. the output wavelength decreases). Their $3dB$ spectra bandwidths are $229.83\,GHz$ and $283.84\,GHz$ which shows the output power spectra are broaden which is due to the gain saturation caused by the carrier density reduction.

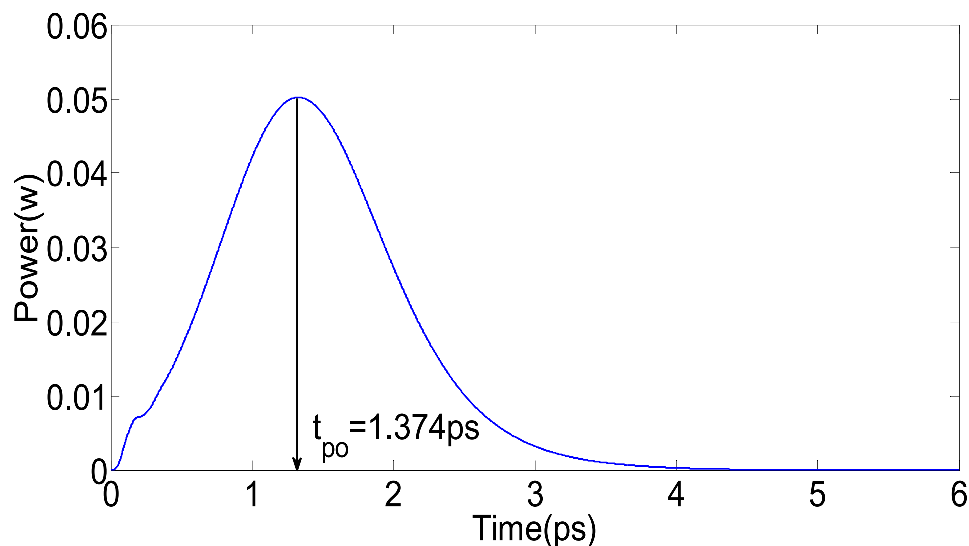

(a)

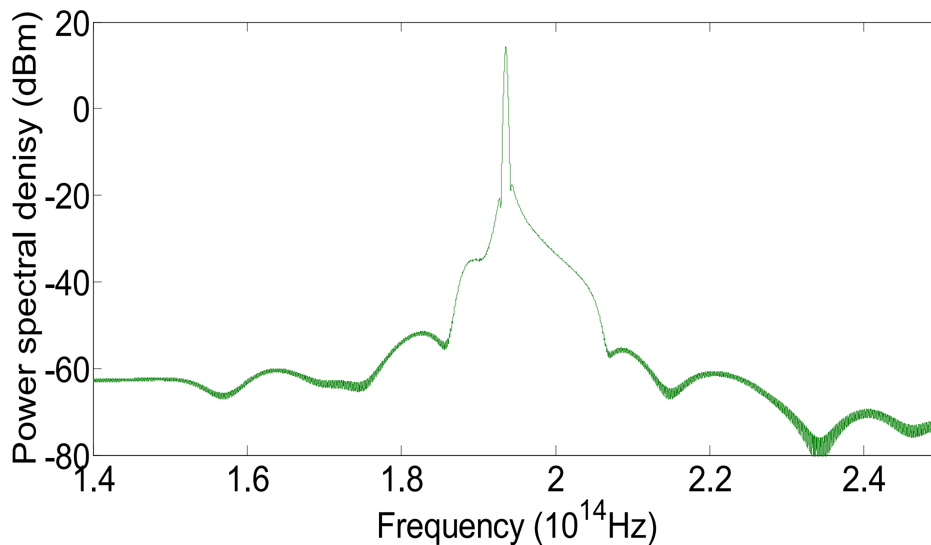

(b)

Fig. 8.3 Amplified output waveform of a Gaussian input pulse with the peak power of $0.1mw$ (a) temporal waveform (b) power spectral density.

Figures 8.4a and b show the temporal and power spectral density of the amplified output when the peak power of the input Gaussian pulse (Fig.8.1a) is $1mw$. The output peak time, pulse width and peak power are, respectively, $0.712ps$, $1.116ps$ and $0.1006W$ and the output power spectral density central frequency and bandwidth are $193.533THz$ and $377.12GHz$, respectively. Comparison of the two output temporal waveforms of Fig. 8.3a and Fig.8.4a shows that by increasing the the input pulse power from $0.1mW$ to $1mW$, the peak time decreases from $1.33ps$ to $0.712ps$, the pulse width increases from $1.116ps$ to $1.374ps$ and the peak power increases from $0.05W$ to $0.1W$ which implies the corresponding amplified output pulse gain decreases from about $27dB$ to $20dB$ due to the amplifier gain saturation. Also comparison of Fig.8.3b and Fig. 8.4b indicates for this increase in the input pulse power the center frequency of the output spectra decreases from $193.539THz$ to $193.533THz$ and the spectra bandwidth the input power increases from $283.84GHz$ to $377.12GHz$. These features, such as the spectral broadening and the pulse

duration narrowing of the amplified output pulse are qualitative agreement with experimental results reported in the reference [139].

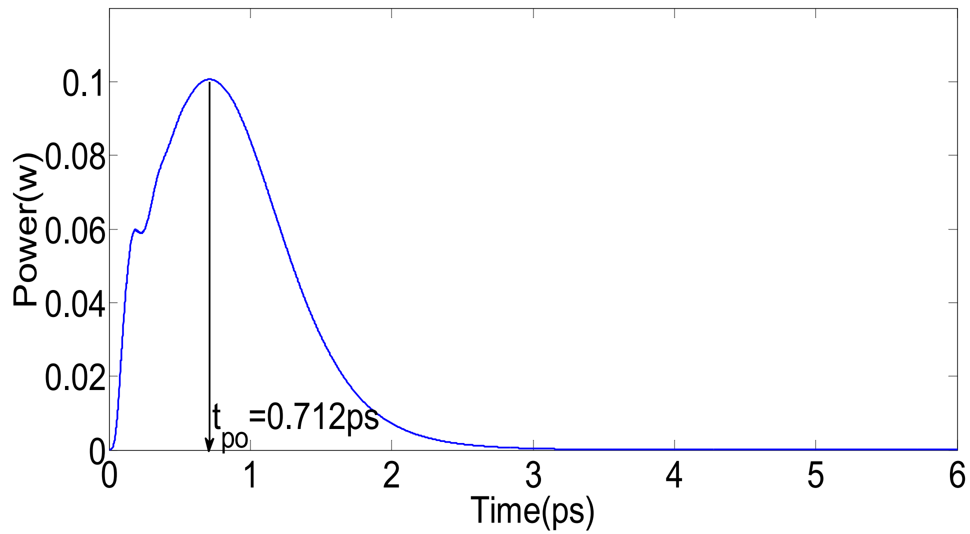

(a)

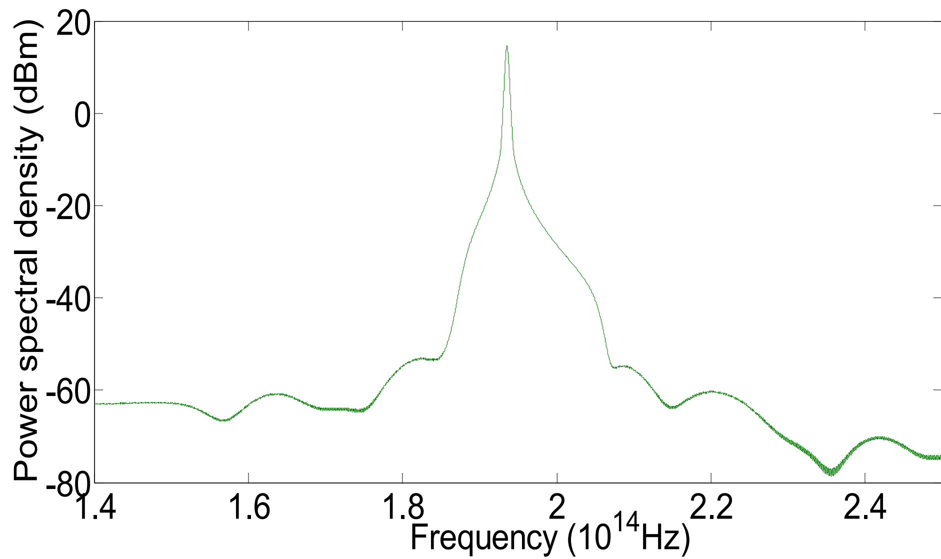

(b)

Fig. 8.4 Amplified outputs of a Gaussian pulse with the peak power value $1mw$ (a) temporal waveform (b) power spectral density.

8.3 Q-TLM Method for Quantum Dot Amplifiers

8.3.1 Model for Quantum Dot Semiconductor Optical Amplifiers (QD-SOAs)

The structure of the QD-SOA model based on Q-TLM is the same as that of quantum well amplifiers (Fig.8.1). That is, it consists of stimulated emission module, transmission line, transmission coefficient and spontaneous emission module. The internal structure of stimulated and spontaneous emissions' modules for the QD-SOA model are presented in section 4 of Chapter 7.

8.3.2 Carrier Density Distribution Model

The variations of carrier density distribution in QD-SOA are described by the following rate equations [140]:

$$\frac{dN_s}{dt} = \frac{\eta I}{qV_s} - \frac{N_s}{\tau_s} - \frac{N_s}{\tau_n(N_s)} + \frac{V_a}{V_s}\frac{N_w}{\tau_e} \tag{8.6}$$

$$\frac{dN_w}{dt} = \frac{V_s}{V_a}\frac{N_s}{\tau_s} + \frac{N_d}{\tau_{eq}} - \frac{N_w}{\tau_n(N_w)} - \frac{N_w}{\tau_e} - \frac{N_w}{\tau_d} \tag{8.7}$$

$$\frac{dN_d}{dt} = \frac{N_w}{\tau_d} - \frac{N_d}{\tau_n(N_d)} - \frac{N_d}{\tau_{eq}} - \frac{\Gamma}{q\Delta V}\frac{V_{in}}{Z_p} \tag{8.8}$$

where, q is the electron charge, Γ is the optical confinement factor, ΔV is the volume of each section, Z_p is the transverse wave impedance, τ_n is the carrier recommendation lifetime, which is given by Eq. 8.5, V_{in} is the input voltage of the stimulated emission module in each section, N_s , N_w and N_d are the carrier density in the separate confinement heterostructure (SCH) region, wetting layer and quantum dots, respectively, I is the injected current, η is the injection efficiency, V_s and V_a are the volumes of the SCH and the active region, respectively, τ_s is the carrier transport time in the SCH region, τ_e is the

carrier re-excitation time from the quantum well to the SCH, τ_{eq} is the carrier re-excitation time from the quantum dot to the wetting layer, τ_d is the carrier relaxation time of the quantum dot.

8.3.3 Modelling of Femtosecond Pulse Propagation in QD-SOAs

In this section amplification of a femtosecond Gaussian pulse in quantum dot amplifiers is investigated based on the proposed Q-TLM method. The envelope of the input femtosecond pulse is Gaussian with the peak power of $1mW$, pulse width of $60fs$ centered at $90fs$. The central wavelength of the pulse is $t_{po} = 1.1\mu m$. The quantum dot amplifier has $750\mu m$ long cavity which is divided into 10000 small sections along the cavity. Fig. 8.5 shows the schematic diagram of the simulated object-quantum dot amplifier, in which a six-layer quantum dot active region is sandwiched between two cladding layers. The $InAs$ quantum dots are taken as micro-disk; the well and barrier are $InGaAs$ and $GaAs$, respectively. Tab.8.2 shows the parameters used in the simulation.

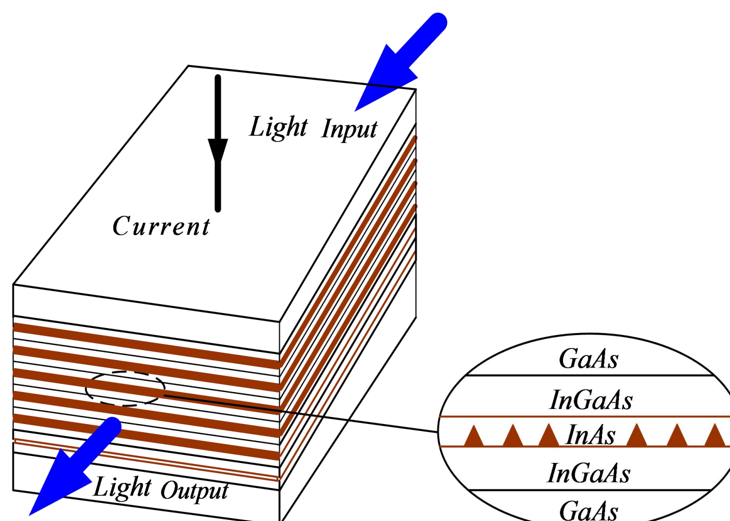

Fig. 8.5 Scheme diagram of QD amplifiers. The quantum dot amplifier consists of a six-layer

quantum dot active region and two cladding layers. The materials for the quantum dots, wells and the material for the quantum dot is $InAs$ while the materials for the wells and barriers are $InGaAs$ and $GaAs$, respectively.

Tab. 8.2 Parameters used in the analysis of femtosecond pulse amplification in QD-SOAs [126]

Symbol	Description	Value
n	Background refractive index	3.51
f_{sam}	Sampling frequency	$1.0\times10^{15}Hz$
Q	$Q-factor$	22
A	Linear recombination	$2\times10^{8}s^{-1}$
B	Bi-molecular recombination	$6\times10^{-16}m^{3}s^{-1}$
C	Auger recombination	$8\times10^{-41}m^{6}s^{-1}$
γ	Linewidth of QW-SOA	$2\times10^{13}rad/s$
Γ	Confinement factor	0.025
N_{dot}	QD density of states	$5\times10^{10}cm^{-2}$
η	Injection efficiency	0.6
I	Injected current	$300mA$
τ_s	Carrier transport time in the SCH region	$500ps$
τ_e	Carrier reexcitation time from quantum well to SCH	$400ps$
τ_{eq}	Carrier reexcitation time from the quantum dot to the wetting layer	$200ps$
τ_d	carrier relaxation time into the quantum dot	$50ps$
W_s	Width of the SCH region	$1\mu m$
W_a	Width of the active region	$1\mu m$
D_s	Thickness of the SCH region	$0.2\mu m$

D_a	Thickness of the active region	$0.12\mu m$
L	Length of active region	$750\mu m$

Figure 8.6 shows the temporal evolution of the above input Gaussian pulse in the quantum dot amplifier cavity at different distances (i.e. $525\mu m$ to $750\mu m$) along the amplifier. The peak power of the amplified output pulse increases from $0.394\,W$ at distance of $525\mu m$ along the amplifier cavity to $5.03\,W$ at distance of $750\mu m$ (i.e. amplifier output facet) and the pulse width increases from $70\,fs$ to $77\,fs$ which are due to the gain saturation caused by the decrease in the carrier density. The corresponding spectral evolution of the amplified femtosecond pulse is also shown in Fig. 8.7. The central wavelengths of the power spectral densities at these different distances are $1097.14nm$, $1097.02nm$, $1096.92nm$ and $1096.84nm$. This is because, the quantum dot amplifier gain spectra peak wavelength is $1096.10nm$ (see Fig. 7.14(a) of Chapter 7), which is shorter than the input pulse wavelength. The $3dB$ bandwidth of the power spectral density decreases from $19.27nm$ to $16.09nm$ as the pulse propagates from the distance of $525\mu m$ along the amplifier cavity to $750\mu m$ (i.e. the amplifier output facet) which is due to the narrowing of the gain spectrum caused by the decrease of the carrier density.

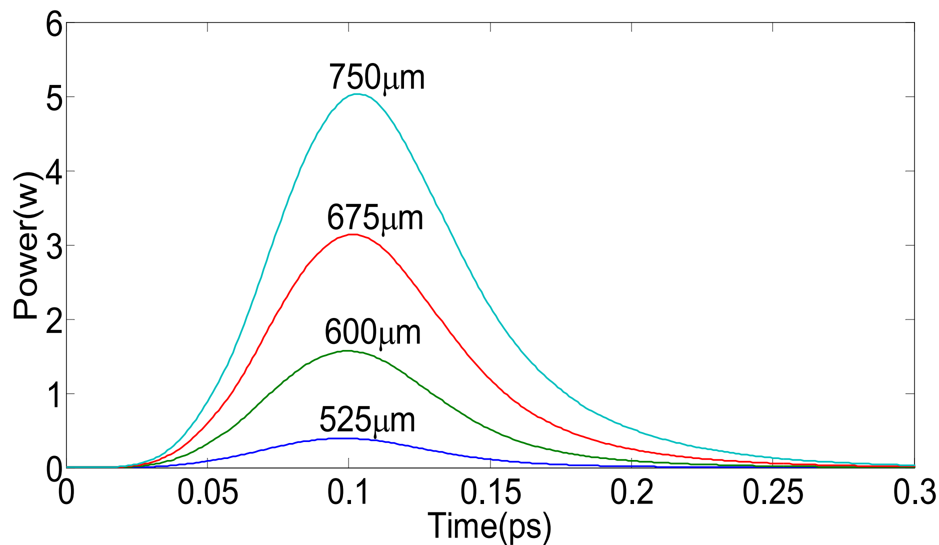

Fig. 8.6 Temporal evolution of an input femtosecond pulse along the amplifier cavity obtained by the proposed Q-TLM method.

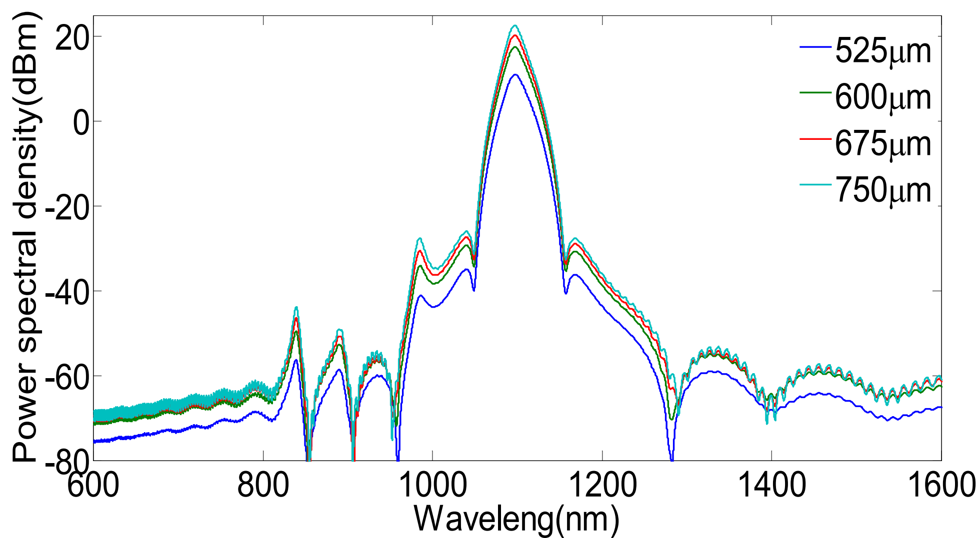

Fig. 8.7 Spectra evolution of an input femtosecond pulse along the amplifier cavity obtained by the Q-TLM method.

Figure 8.8 shows the carrier density distribution as a function of the distance Z along the amplifier cavity when the peak power of the input femtosecond pulse is $1mW$. It was found when $98\mu m \leq Z \leq 750\mu m$, the carrier density in the amplifier cavity apparently decreases. This is because as the distance increases, the power of the amplified pulse signal increases

(shown in Fig. 8.6) and more carrier densities will be depleted. At the higher input power the input signal amplification depletes more carrier densities than that depleted by amplified spontaneous emission (ASE). When $0\mu m < Z < 98\mu m$, there is a slight increase of carrier density, which is because the backward propagating ASE in the distance that is near the input facet has a larger power and thus depletes more carrier densities. The carrier density distribution along the distance explains the temporal broadening and spectral narrowing of the amplified pulse along the amplifier cavity (shown in Fig. 8.6 and Fig. 8.7). The above simulation results confirm that the proposed Q-TLM method can effectively model the temporal and spectral behaviors of femtosecond pulse amplification in the quantum dot amplifier.

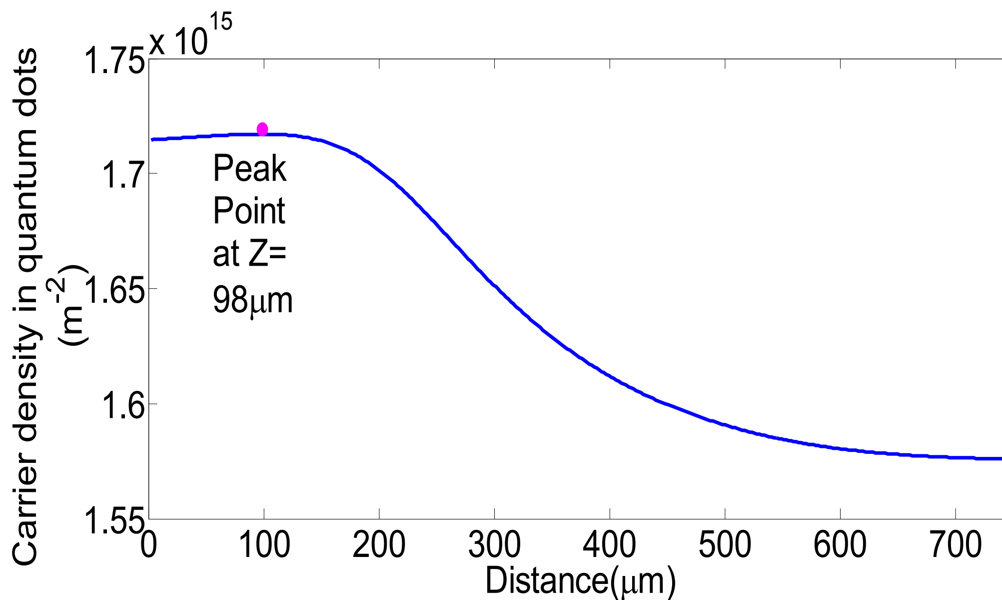

Fig. 8.8 Carrier density distribution along the amplifier cavity when the peak power of the input femtosecond pulse is $1mW$

8.4 Q-TLM Model of Quantum Well Lasers

8.4.1 Description of the Model

In the following, the Q-TLM method is applied to model QW semiconductor laser diodes

and study both the temporal and spectral properties of them.

Figure 8.9 shows the proposed model for the QW laser based on Q-TLM method. In this model, the laser cavity is also divided into m sections, each of which consists of scattering module, spontaneous emission module, transmission line and transmission efficient α . The facet model S_f is used to describe the facet reflection.

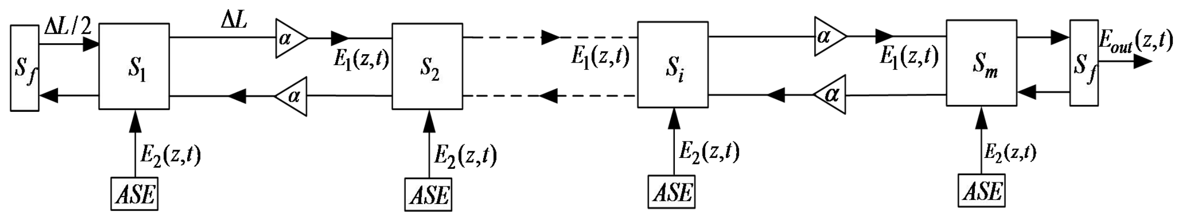

Fig. 8.9 The proposed Q-TLM model for quantum well laser.

Both the stimulated and spontaneous emission modules are employed to model the photon stimulated and spontaneous emissions processes in the laser cavity. The electric fields propagate along the transmission line and stimulate the photon emission in the stimulated emission module. Both the stimulated emission and the spontaneous emission modules consist of parallel QW-TLM units (see Chapter 7). The length of the transmission line between two adjacent stimulated emission modules is ΔL while the length of the transmission line linking the facet model and the closest stimulated emission module is $\Delta L/2$. The structure of the stimulated emission module S_i and the spontaneous emission module ASE in the laser model are the same as the structures shown in Figs. 7.6 and 7.8 of Chapter 7. Figure 8.10 shows the electric fields flow at the end facets of the QW laser model.

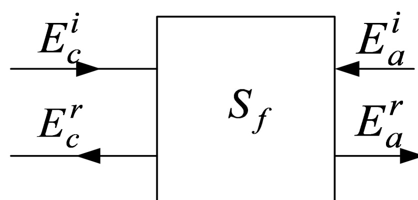

Fig. 8.10 Electric field flow for a laser facet model.

In the facet model, the Fresnel reflection and transmission at the facet can be expressed as [123]:

$$\begin{bmatrix} E_c^r \\ E_a^r \end{bmatrix} = \begin{bmatrix} \rho_{cc} & \rho_{ac} \\ \rho_{ca} & \rho_{aa} \end{bmatrix} \begin{bmatrix} E_c^i \\ E_a^i \end{bmatrix} \tag{8.9}$$

where, E_c^i and E_a^i are the input electric fields of the facet from the adjacent stimulated emission module and the air, E_c^r and E_a^r are the reflected electric fields, ρ_{cc} is the electric field reflection coefficient (EFRC) from the cavity to cavity, ρ_{aa} is the EFRC from air to air, ρ_{ca} is the electric field transmission coefficient (EFTC) from cavity to air and ρ_{ac} is the EFTC coefficient from air to cavity.

8.4.2 Carrier Transport effects in the Q-TLM Laser Model

Carrier transport across the separate confinement heterostructure (SCH) affects the gain bandwidth of quantum well lasers, which further results in the variation of the output of quantum well lasers in the time-frequency domains[141]. In this section, the effects of carrier transport on the output of quantum well lasers are investigated based on the Q-TLM method. Under the assumption that the current is injected from the left side of the separate confinement heterostructure (SCH) laser, the rate of change of carrier densities N_1 and N_2 at the left and right sides of SCH laser can be expressed, respectively, as [141]:

$$\frac{dN_1}{dt} = \frac{\eta I}{qV_1} - \frac{N_1}{\tau_s} - \frac{N_1}{\tau_n(N_1)} + \frac{V_{well}}{V_1}\frac{N_{well}}{\tau_e} + \xi\frac{N_2}{\tau_s} \tag{8.10}$$

$$\frac{dN_2}{dt} = -\frac{N_2}{\tau_s} - \frac{N_2}{\tau_n(N_2)} + \frac{V_{well}}{V_2}\frac{N_{well}}{\tau_e} + \xi\frac{N_1}{\tau_s} \tag{8.11}$$

In the well region, the carrier rate equation which includes the transport effects can be written as:

$$\frac{dN_{well}}{dt} = (1-\xi)\frac{V_1}{V_{well}}\frac{N_1}{\tau_s} + (1-\xi)\frac{V_2}{\tau_s} - \frac{2N_{well}}{\tau_n(N_{well})} - \frac{2N_{well}}{\tau_e} - \frac{\Gamma}{qDW\Delta L}\frac{V_{in}}{Z_p} \quad (8.12)$$

where, I is the injected current, η is the internal quantum efficiency, V_1 and V_2 are the volumes of the left and right sides of the SCH layers, τ_s is the carrier transport time in the SCH region, τ_e is the carrier thermionic emission time, ξ is the leak factor, V_{well} is the volume of the well, V_{in} is the input voltage of each scattering module, D and W are the thickness and width of the well, N_{well} is the carrier density in the well region and ΔL is the length of the transmission line between two adjacent scattering modules. Both $\tau_n(N_1)$ and $\tau_n(N_{well})$ which are carrier recombination lifetimes in the SCH and in the quantum well regions, respectively. They can be obtained by using the well- known formula $1/(A + BN + CN^2)$, where, A , B and C are linear recombination constant, Bi-molecular recombination constant and Auger recombination constant, respectively.

8.4.3 Analysis of Quantum Well Lasers based on the Q-TLM method

In this section, effects of carrier transport and bias current spike on the output properties of the strained $In_{0.64}Ga_{0.36}As - InGaAsP$ quantum well lasers are studied using the above proposed model. The well and barrier widths are $4.5nm$ and $10nm$, respectively, and the other parameters used in the simulations are provided in the following Tab. 8.3.

Tab. 8.3 Simulation parameters for quantum well lasers [140, 142-144]

Symbol	Description	Value
n	Background refractive index	3.67
m	Number of sections	10000
Q	Stub filter Q-factor	60.8
f_{sam}	Sampling frequency	$1.0\times10^{15}\,Hz$

A	Linear recombination	$2\times10^{8}s^{-1}$
B	Bi-molecular recombination	$6\times10^{-16}m^{3}s^{-1}$
C	Auger recombination	$8\times10^{-41}m^{6}s^{-1}$
η	Internal quantum efficiency	0.86
β	Spontaneous emission factor	5×10^{-3}
ρ_{cc}	Cavity-cavity reflection coefficient	0.32
ρ_{ca}	Cavity-air transmission coefficient	0.68
ρ_{ac}	Air-cavity transmission coefficient	0
ρ_{aa}	Air-air reflection coefficient	0
γ	Linewidth of QW-SOA	$2\times10^{13}rad/s$
α_0	Transmission efficient	0.9976
Γ	Confinement factor	0.025
N_0	Transparent carrier density	$1.2\times10^{24}m^{-3}$
W	laser width	$1\mu m$
D	laser thickness	$24.5nm$
L	Laser length	$340\mu m$

Variations of the output power versus the bias current for the above quantum well laser is shown in Fig. 8.11, which indicates the linear relationship between the laser output power and the injected current. The laser threshold current and current density are $47mA$ and $13.82KA/cm^2$, respectively.

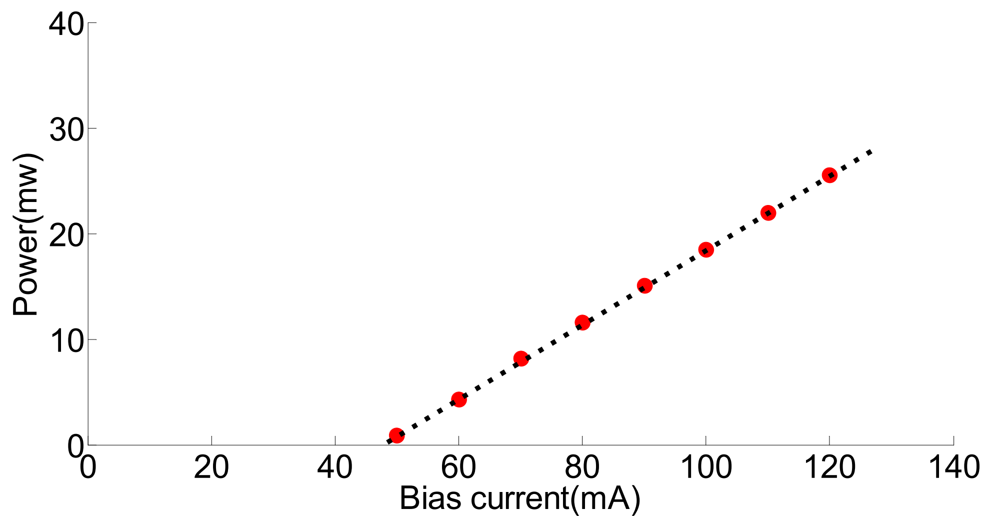

Fig. 8.11 Power-current characteristics of a $340\mu m$ long quantum well laser.

8.4.3.1 Effects of Carrier Transport

Figure 8.12 shows the simulation results of turning-on transients (ToT) of the strained QW laser both with (green) and without (blue) the carrier transport effect (CTE). In the simulation it is assumed the initial bias current is $i(0) = 50mA$ (corresponding to the current density of $14.71KA/cm^2$). As the figure shows, the turning-on response can be divided into four stages hereby referred to as $T1$, $T2$, $T3$ and $T4$ where $T1$ is the time period during which the output power varies from zero to the first peak, $T2$ is the time interval between the first peak and the first valley, $T3$ is the stage during which the output power arrives at the second peak from the first valley and $T4$ is the time interval from the second peak to the end. Tab. 8.4 compares these four time intervals both in the presence and absence of the carrier transport effect.

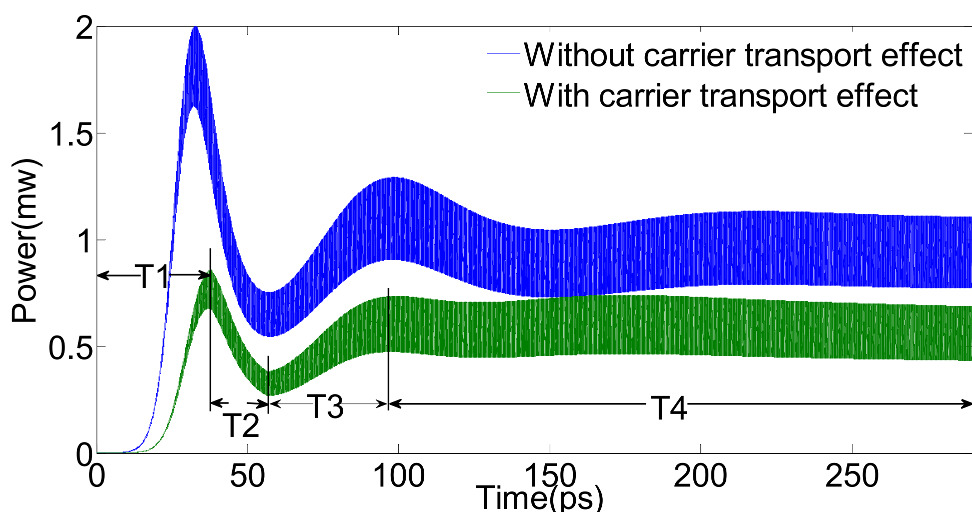

Fig. 8.12 Turning-on transients of strained QW lasers without (blue) and with (green) carrier transport effect.

Tab. 8.4 Four stages in the ToT with and without carrier transport effect

Items	$T1$ (ps)	$T2$ (ps)	$T3$ (ps)	$T4$ (ps)
ToT without CTE	$0 \sim 32.67$	$32.67 \sim 57.51$	$57.51 \sim 98.46$	$98.46 \sim 290$
ToT with CTE	$0 \sim 37.92$	$37.92 \sim 56.62$	$56.62 \sim 99.36$	$99.36 \sim 290$

Table 8.4 shows that the time intervals $T1$ and $T3$ of the turning-on transient with the carrier transport effect are larger than those without it. This is because carriers transporting across the SCH region without being captured by the well region will not take part in the stimulated process, which delays the response speed of the output power. In the stage $T2$, the output power suffers from the gain saturation and decreases. The magnitudes of the first peak ($2mW$) and the second peak ($1.292mW$) in the absence of carrier transport are higher than those in the presence of carrier transport which are $0.857mW$ and $0.735mW$. Also, carrier transport causes a decrease in output power shown in stage T_4 which is due to lower average carrier density level in the well.

Figure 8.13 shows the output power spectral densities both in the presence (green) and

absence (blue)of the carrier transport at the steady stage (after $250ps$ see Fig.8.12). The peak values of the output power spectral densities are $-22.72dBm$ (blue) and $-16.35dBm$ (green). As figure shows the carrier transport has caused a red shift in the laser output power spectral density that is, the central frequency has shifted from $195.318THz$ to $195.315THz$ (the difference is $2.563GHz$). Also, carrier transport has decreased the $3dB$ bandwidth of the laser output spectra from $180.78THz$ to $178.75THz$. This is because the carrier transport reduces the carrier density level in the well region which leads to the red shift and bandwidth narrowing of the gain spectrum.

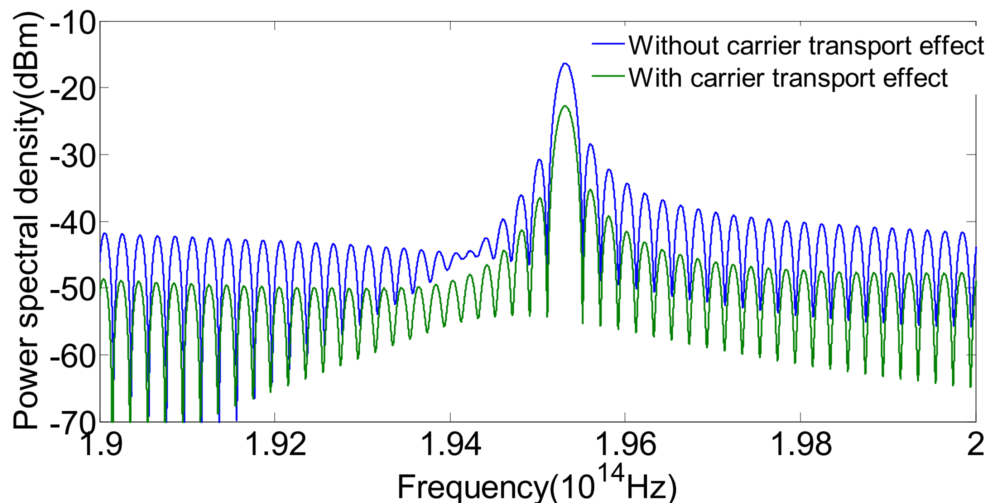

Fig. 8.13 Output power spectral density at the steady state both in the presence (green) and absence (blue) of the carrier transport.

Figure 8.14 compares the output power spectral densities during the initial oscillation process (i.e. at the first peak where $t = 37.9ps$) and that of steady state (i.e. for $t > 100ps$). Comparison of the two output spectra reveals that during the oscillation process both the central frequency and $3dB$ bandwidth are higher. In the initial oscillation process, the central frequency and the bandwidth of the power spectral density (blue curve in Fig. 8.13) are $195.317THz$ and $183.34THz$, respectively. Also, at $t = 37.9ps$ the peak value of the

output power spectral density is $-19.43dBm$.

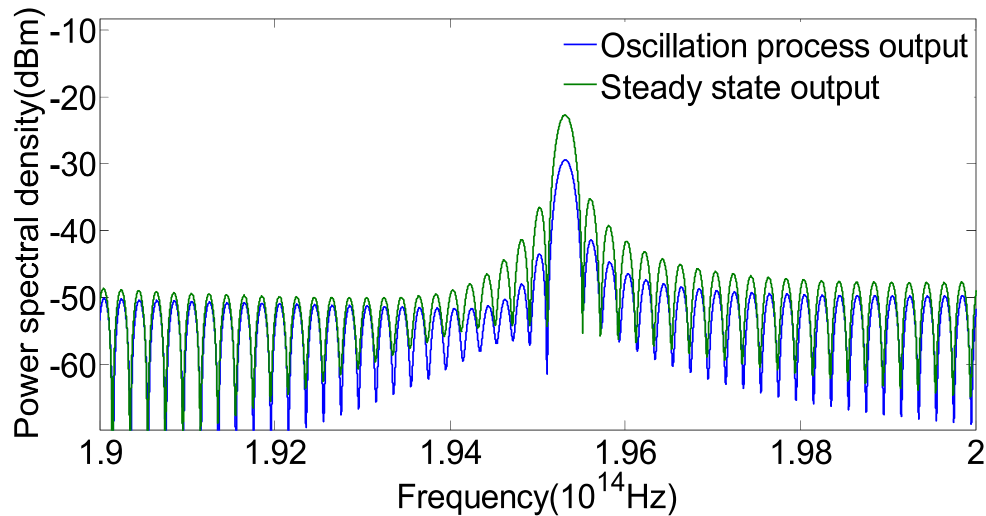

Fig. 8.14 Output power spectral density in the presence of the carrier transport. at the oscillation process (blue, around $37.9ps$) and the steady state (green , i.e. $t > 100ps$) .

The effects of carrier transport on the turn-off transients of QW lasers are shown in Fig. 8.15. At $t = 0$, the input current of QW laser is set to be zero. The time taken for the output power to decrease 20% of its initial value is $33.47ps$ in the presence of carrier transport and $2.15ps$ in the absence of the carrier transport. Carrier transport causes an apparent turn-off delay due to the large transport time across the SCH region [141].

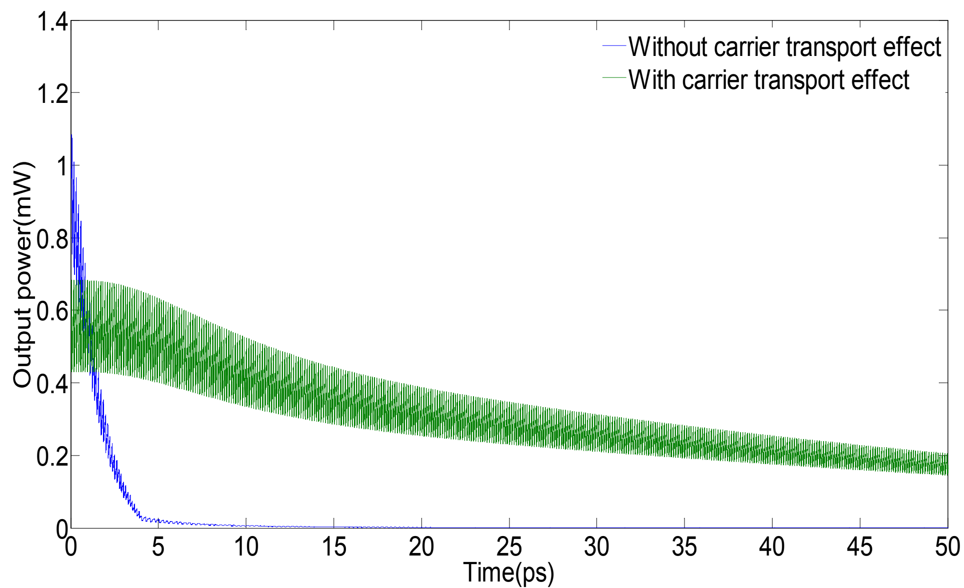

Fig. 8.15 Turning-off transients of QW lasers both in the presence (green) and absence of the transport effect.

8.4.4.2 Effect of Impulse Bias Current

In the following, the above Q-TLM laser model is used to perform small signal analysis of the laser output spectra when an impulse bias current is applied to the laser after the laser output has reached its steady state. The impulse bias current is shown in Fig.8.16 which has a peak and width values of $100mA$ and $0.5ps$, respectively. Fig. 8.17 shows the laser output spectra Tab. 8.5 compares important parameters of the laser output spectra before and after the impulse bias current (IBC) is applied.

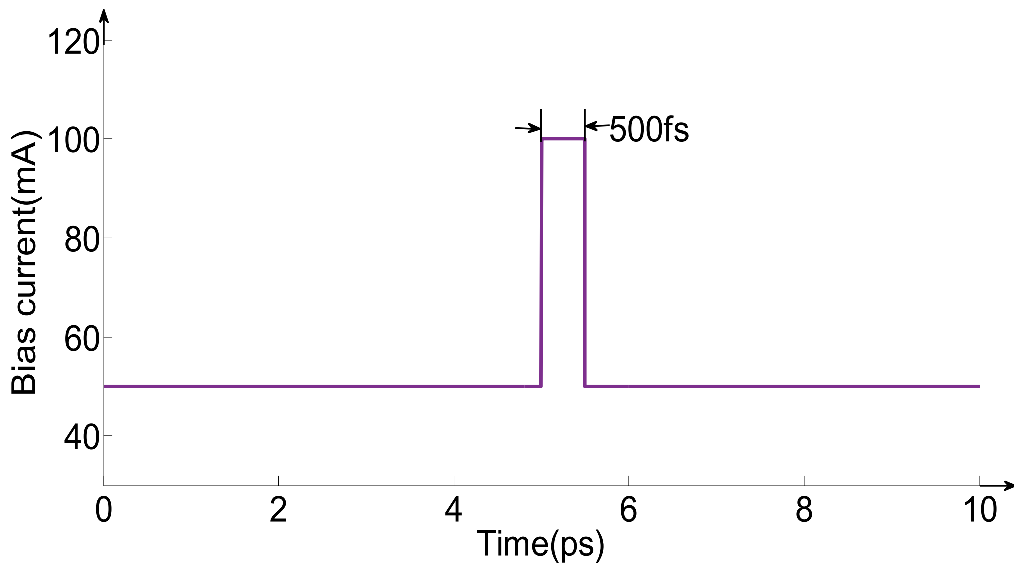

Fig. 8.16 Impulse bias current.

Tab. 8.5 Laser output spectral parameters before and after impulse bias is applied

Parameter	Peak value	$3-dB$ bandwidth	Central frequency	SLSR
Before IBC	$-22.72dBm$	$178.75THz$	$195.315THz$	$12.624dB$
After IBC	$-23.44dBm$	$180.54THz$	$195.317THz$	$12.155dB$

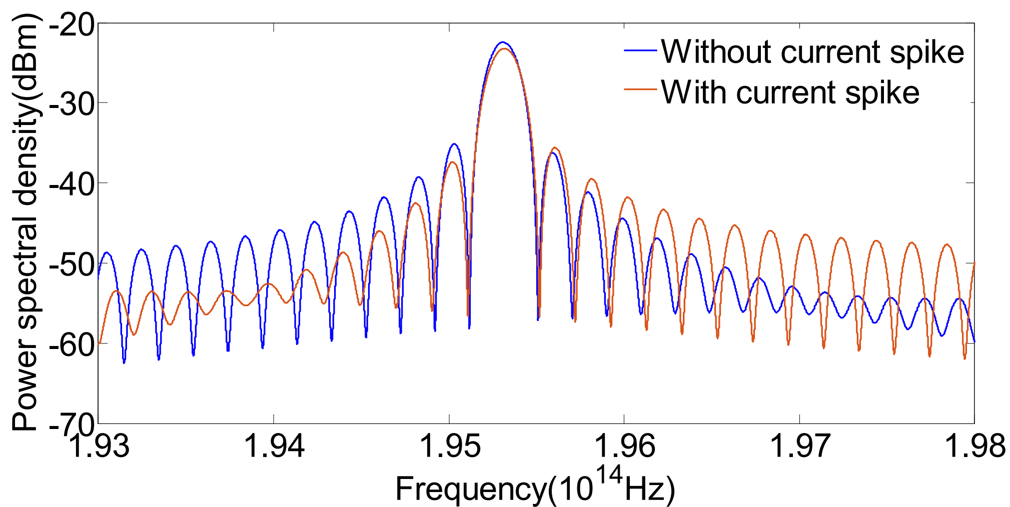

Fig. 8.17 Effect of impulse bias current on the laser output spectra.

Table 8.5 clearly indicates that the impulse bias current has broadened the laser output spectra bandwidth and shifted the central frequency from $195.315THz$ to $195.317THz$ (i.e. red

shift). The peak values of the output spectra before and after applying the impulse bias current are $-22.72dBm$ and $-23.44dBm$, respectively, which indicates that although the bias current spike can increase the output power in the time domain, it lowers the peak value in the frequency domain. Also, the side lobe suppression ratios (SLSR) before and after applying the impulse bias current are $12.624dB$ and $12.155dB$, respectively, This shows that the impulse bias current has reduced the SLSR of the laser output spectrum.

8.5 Conclusions

In this Chapter, the newly proposed Q-TLM modelling method is used to establish the theoretical model for quantum well/dot amplifiers and quantum well lasers. Ultrashort optical pulse amplification in quantum well and quantum dot amplifiers are analyzed using the proposed new model. As for picosecond pulse amplification in quantum well amplifiers, it was found that the temporal waveform of the amplified output pulse is distorted due to the gain saturation that is, the temporal peak shift and pulse width narrowing were observed while in the output spectrum an apparent bandwidth broadening and red shift were observed as the peak power value of the input signal was increased. For the femtosecond pulse amplification in quantum dot amplifiers, the pulse evolution process is studied in both time and frequency domains. Finally, based on the proposed Q-TLM method, effects of carrier transport and impulse bias current on the output properties of strained QW lasers were studied. All simulation results were in good agreement with the existing reported experimental results, which confirms that the new proposed Q-TLM method can accurately study the temporal and spectral behaviors of QW amplifiers and lasers.

Chapter 9

Analysis of Femtosecond Pulse Propagation in QW-SOAs Based on Quantum Transmission Line Modelling Method

9.1 Introduction

The amplification of femtosecond optical pulse in QW-SOAs provides an attractive method to obtain high-power ultrashort optical pulses [145-146]. However, this amplification suffers from the amplifier gain saturation which is due to slow carrier recovery. Tapered-waveguide (TW) structures for semiconductor optical amplifiers are proposed to increase the saturation output power by providing a larger cross-sectional area in the active region [100, 139]. Theoretical and experimental studies of the bulk semiconductor optical amplifier have shown that a tapered waveguide structure provides higher gain saturation and suppresses the backward amplified spontaneous emission as compared with a conventional semiconductor optical amplifier having rectangular active region waveguide [37, 147-150]. However, these theoretical analyses have focused on the temporal output by assuming that the input signal is monochromatic. There is no detailed study of the spectral characteristics of amplified output signal and the multi-channel wavelength-dependent amplification in the tapered-waveguide quantum well amplifiers,

which are significantly important in the wavelength division multiplexing systems. Strain in a quantum well device introduces additional coupling between the heavy hole, light hole and spin-orbit spilt-off bands in the energy structure of quantum well, which leads to the change of electron-photon interaction in the optical amplification process and change the output properties of quantum well devices. Strain can be used to adjust the gain characteristics of quantum well structures. It has been reported [126] that, in the present of stain, quantum well amplifiers show superior characteristics as compared with those of unstrained amplifiers. However, no detailed work is done to analyze the effects of strain on the spectrum of amplified femtosecond pulse. In this chapter, the Q-TLM modelling method is adopted to analyze the wavelength-dependent femtosecond pulse propagation in conventional waveguide (CW), exponentially tapered waveguide (ETW) and linearly tapered waveguide (LTW) quantum well amplifiers (QWAs) (shown in Fig. 9.1) and the strain effects on the dynamic spectra of femtosecond pulse amplification in QWAs.

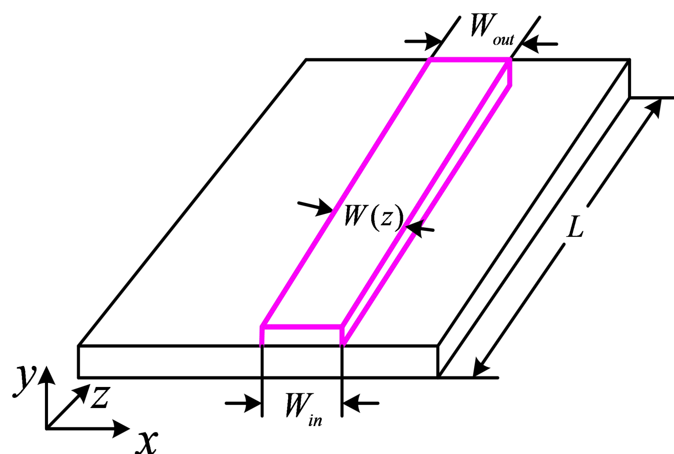

(a)

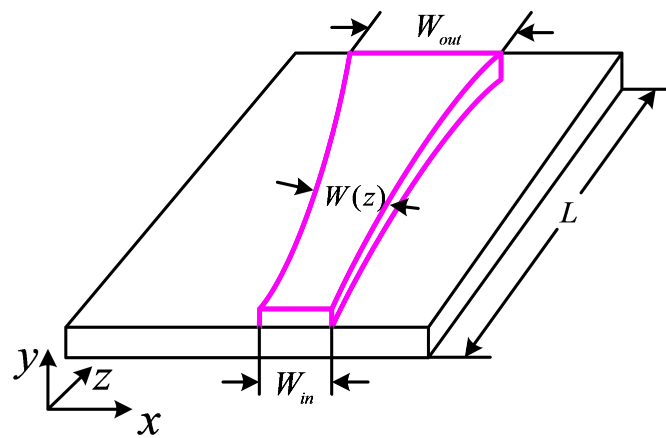

(b)

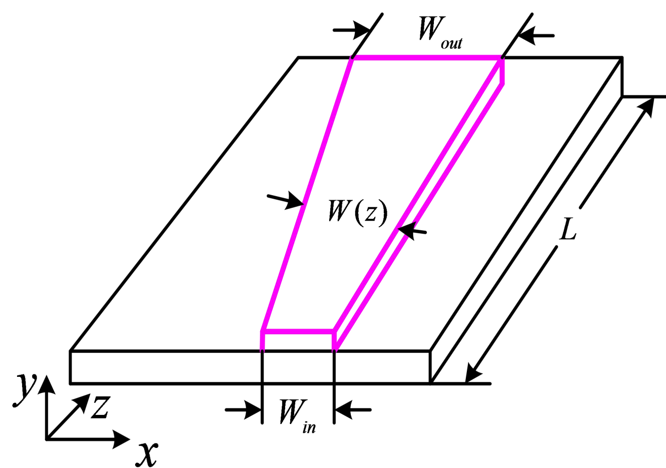

(c)

Fig. 9.1 Schematic diagram of the active regions of different tapered QW-SOAs (a) rectangular (b) exponential (c) linear.

9.2 Wavelength-dependent Femtosecond Pulse Amplification in Tapered QW-SOAs

9.2.1 The Q-TLM Model for Tapered QW-SOAs

Figure 9.2 shows the structure of the Q-TLM model for tapered waveguide QW-SOAs. It consists of stimulated emission modules (S_i), amplified spontaneous emission (ASE)

modules, transmission line and transmission coefficient α . S_i and ASE modules describe the stimulated and spontaneous emission processes in the amplifier, respectively.

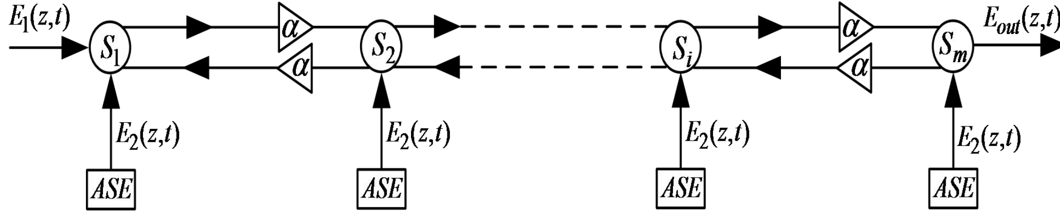

Fig. 9.2 The proposed Q-TLM model for a tapered waveguide QW-SOA.

The electric fields $E_1(z,t)$ and $E_2(z,t)$ from the input signal and spontaneous emission module propagate along the transmission line which links the adjacent scattering modules. The transmission coefficient α is used to describe the waveguide loss in the propagation process, which can be expressed as:

$$\alpha = \alpha_0 - \alpha_{tap} \tag{9.1}$$

where, α_0 is the transmission coefficient for the rectangular shape of the waveguide, α_{tap} accounts for the variation of the transmission coefficient due to the taper shape of the waveguide and can be expressed as [148]:

$$\alpha_{tap} = -\Delta L W(z) \frac{d}{dz}\left(\frac{1}{W(z)}\right) \tag{9.2}$$

In Eq.(9.2), ΔL is the length of the link transmission line between two adjacent scattering modules, $W(z)$ is the width of the tapered active region. As discussed in the previous chapters, both the stimulated and the spontaneous emission modules consist of parallel QW-TLM units, each of which consists of two parallel RLC stub filters and the corresponding weight coefficients [151]. The internal structures of the stimulated- and the spontaneous-emission modules have already been described in Chapter 7.3.

In a tapered waveguide QW-SOAs, the carrier density $N(x,z)$ can be expressed as [148]:

$$N(x,z) = N_{ave}(z) - N_1(z)\cos\left(\frac{2\pi x}{W(z)}\right) \tag{9.3}$$

where, $N_{ave}(z)$ is the average carrier density, $N_1(z)$ is the amplitude of the spatial carrier density distribution along the x direction. The carrier density rate equation for a tapered waveguide QW-SOA is given by [150-151]:

$$\frac{\partial N}{\partial t} = \rho\frac{\partial^2 N}{\partial x^2} + \frac{J}{qD} - \frac{N}{\tau_s} - \frac{\Gamma}{qDW(z)\Delta L}\frac{V_{in}}{Z_P} \tag{9.4}$$

where,

$$\tau_s = \frac{1}{A + BN + CN^2} \tag{9.5}$$

q is the electron charge, Γ is the optical confinement factor, N is the carrier density, ρ is the diffusion coefficient, J is the input current density, D is the thickness of the active region, V_{in} is the input voltage of the parallel QW-TLM units in the stimulated emission module, Z_P is the transverse wave impedance, A, B and C are linear recombination, Bi-molecular recombination and Auger recombination, respectively. The rate equation of the average carrier density N_{ave} can be obtained by substituting Eq. (9.4) into (9.3) and integrating the result over the cross sectional area of the active region, that is [150]:

$$\frac{\partial N_{ave}}{\partial t} = \frac{J}{qD} - AN_{ave} - B(N_{ave}^2 + \frac{N_1^2}{2})$$

$$- C(N_{ave}^3 + 1.5N_{ave}N_1^2) - \frac{\Gamma}{qDW(z)\Delta L}\frac{V_{in}}{Z_P} \tag{9.6}$$

The rate equation for N_1 can be obtained using the same method, but multiplying the result by $\cos(2\pi x / W)$ before integrating over the cross sectional area of the active region, that is [151]:

$$\frac{\partial N_1}{\partial t} = -\rho(\frac{2\pi}{W(z)})^2 N_1 - AN_1 - 2BN_{ave}N_1$$

$$- C(3N_{ave}^2 N_1 + 0.75N_1^3) + \frac{2\Gamma}{qDW(z)\Delta L}\frac{V_{in}}{Z_P} \quad (9.\ 7)$$

9.2.2 Analysis of Femtosecond Pulse Amplification in Straight, Exponential and Linear Tapered QW-SOAs

In the following, the wavelength-dependent amplification of femtosecond pulse in QW-SOAs having conventional, exponential and linear tapered active regions are studied using the Q-TLM method. An optical signal is applied at the input of a compressively strained $In_{0.67}Ga_{0.33}As/InGaAsP$ QW-SOAs. The well and barrier widths are $4.5nm$ and $10nm$, respectively with the barrier bandgap wavelength $\lambda = 1.15\mu m$ which is lattice-matched to the InP substrate. The structures of the exponential and linear tapered waveguide QWAs considered in this study are shown in Figs.9.1b and c. The z-dependent width $W(z)$ of the exponential and linear tapered waveguides can be expressed as:

$$W(z) = W_{in} \exp\left[\frac{z}{L}\ln\left(\frac{W_{out}}{W_{in}}\right)\right], \quad 0 \le z \le L \quad (9.8)$$

$$W(z) = W_{in} + \left(\frac{W_{out} - W_{in}}{L}\right)z, \quad 0 \le z \le L \quad (9.9)$$

where, W_{in} and W_{out} are the input and output widths of the tapered waveguide. Other parameters used in the simulation are given in Tab. 9.1 and Ref. [151].

Tab. 9.1 Simulation parameters for three kinds of QW-SOAs [129]

Symbol	Description	Value
Q	Stub filter Q-factor	60.8
f_{sam}	Sampling frequency	$1.0\times10^{15}\,Hz$

J	Input current density	$16KA/cm^2$
Γ	Confinement factor	0.025
A	Linear recombination	$2\times10^{8}s^{-1}$
B	Bi-molecular recombination	$6\times10^{-16}m^3s^{-1}$
C	Auger recombination	$8\times10^{-41}m^6s^{-1}$
γ	Linewidth of QW-SOA	$2\times10^{13}rad/s$
α_0	Transmission coefficient	0.9979
L	Length of QW-SOA	$750\mu m$
D	Thickness of QW-SOA	$24.5nm$
W	Width of straight waveguide	$1\mu m$
W_{in}	Input width of tapered waveguide	$1\mu m$
W_{out}	Output width of tapered waveguide	$10\mu m$

9.2.2.1 Single Femtosecond Pulse Amplification

The input is a single Gaussian femtosecond pulse centered at $120fs$, with FWHM pulse width of $80fs$ and peak power of $1mW$. The corresponding central frequency and spectral bandwidth of the input signal are $153.55THz$ and $5.703THz$, respectively. Fig. 9.3 shows the temporal waveforms of the amplified output pulses in three different quantum well amplifiers (QWAs) having conventional, exponential and linear tapered active regions.

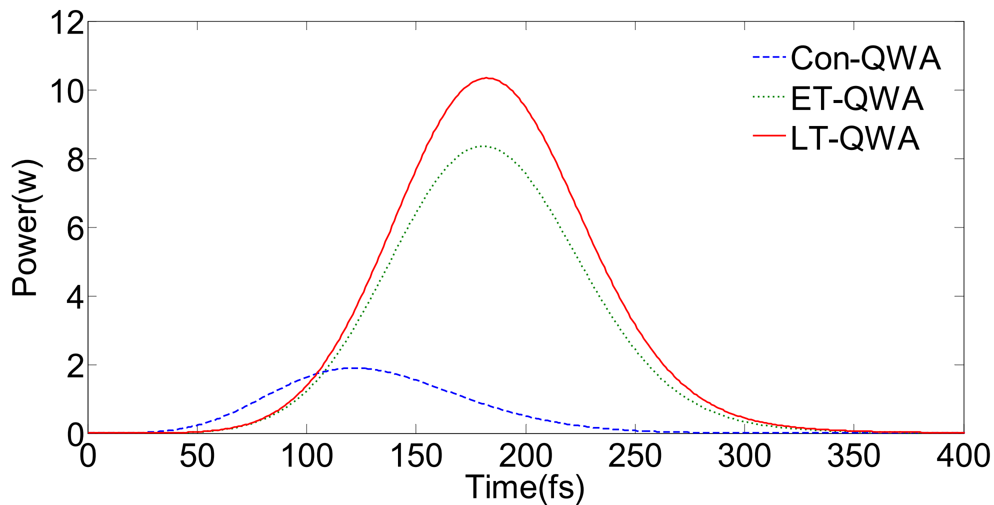

Fig. 9.3 Temporal waveforms of the amplified output pulse in the Con, ET and LT QWAs.

The above results clearly show that the applied input signal gains more amplification in the tapered QWAs. The peak power, pulse width and the peak time values in conventional, exponential and linear tapered QWAs are $(1.9W, 100fs, 123fs)$, $(8.36W, 102fs, 182fs)$ and $(10.34W, 101fs, 183fs)$, respectively. This is because the broader cross-section area of the tapered waveguide improves the saturation performance of QWAs and hence makes the pulse amplification gain larger. Fig. 9.4 shows the power spectral density of the amplified output pulse in all three types of QWAs. In each of the above mentioned three structures, the peak central frequency and 3-dB bandwidth values of the output power spectral density are, respectively, $(31.7dBm, 193THz, 4.78THz)$, $(38.2dBm, 192.76THz, 4.95THz)$ and $(39.1dBm, 192.75THz, 4.96THz)$, which indicates that the 3-dB bandwidth of the amplified output spectrum in both tapered QWAs are almost the same and wider than the conventional QWA. This is because the reduction rate of the carrier density in the TW structure is smaller than that in conventional QWA. The lower carrier density level leads to the narrower bandwidth of the gain spectrum.

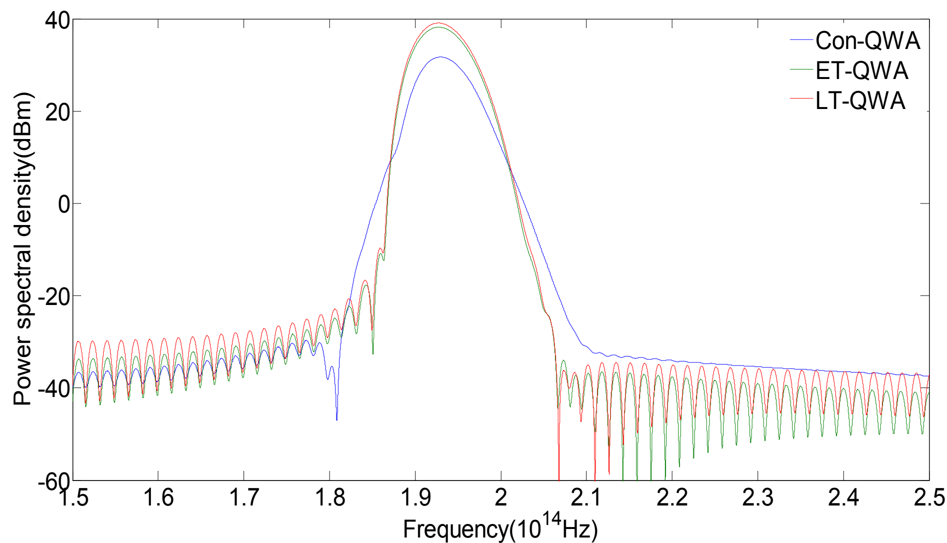

Fig.9.4 Power spectral density of the amplified output pulse in the conventional, exponential and linear tapered QWAs.

Figure 9.5 shows the power temporal evolution of the input pulse along the cavity within the QWAs having conventional (Fig.9.5a), exponential (Fig.9.5b) and linear (Fig.9.5c) tapered active regions. The results show that conventional QWA has suffered from the gain saturation at distances above $600\mu m$ whereas no gain saturation effect has observed in the power temporal responses of the two tapered QWAs. However, at distances less than $600\mu m$ along the amplifier cavity amplification of the input signal, at a given distance, the output power is less in both tapered structures as compared with the conventional amplifier structure. This is due to higher waveguide loss in the tapered structure which reduces the amplification gain at the initial stage of pulse propagation.

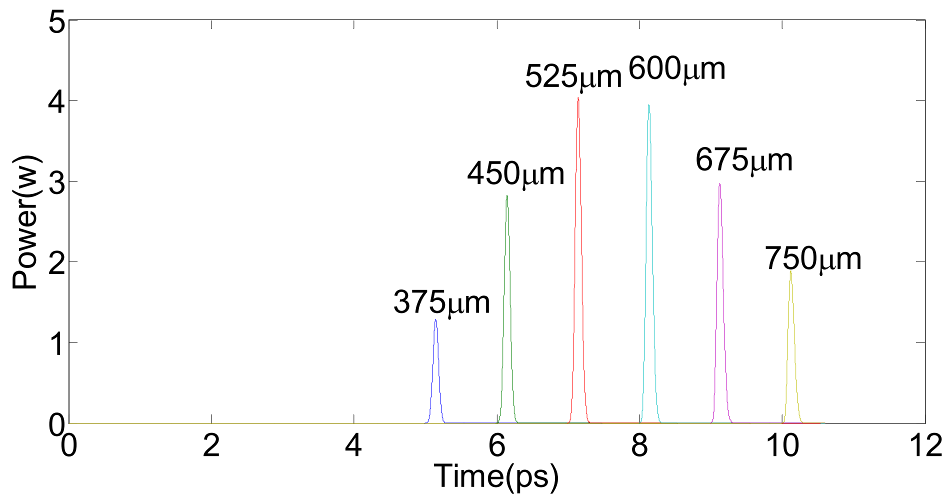

(a)

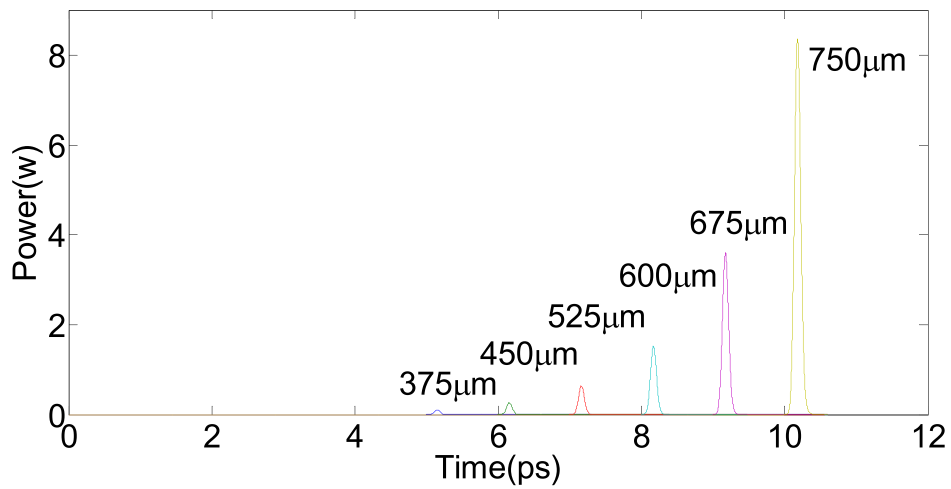

(b)

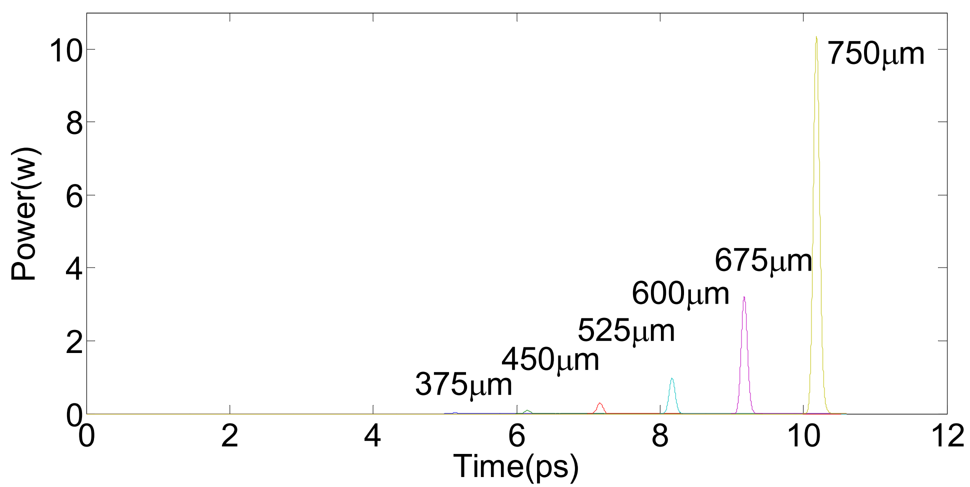

(c)

Fig.9.5 Amplification of femtosecond pulse propagation along the QWA cavity (a) conventional (b) exponential taper and (c) linear taper.

Furthermore, the spectral evolution of the input pulse along the QWA cavity for both conventional and tapered structures is shown in Fig. 9.6. The characteristic parameters of amplified pulse spectra (magnitude, $3dB$ bandwidth and central frequency) at different distances for three amplifier structures are listed in Tab. 9.2. In all cases at the amplifier output (i.e. $Z = L$, where L is the amplifier cavity length) a red shift (i.e. higher wavelength) and bandwidth narrowing in the spectra are observed. However, in the conventional QWA when $Z \geq 600\mu m$, the peak value of the spectra density decreases whereas in both tapered amplifiers as Z increases the peak value of the spectra density increases too. Fig. 9.6 also indicates that the power spectral density in each tapered amplifier is less distorted as compared with that in conventional QWA.

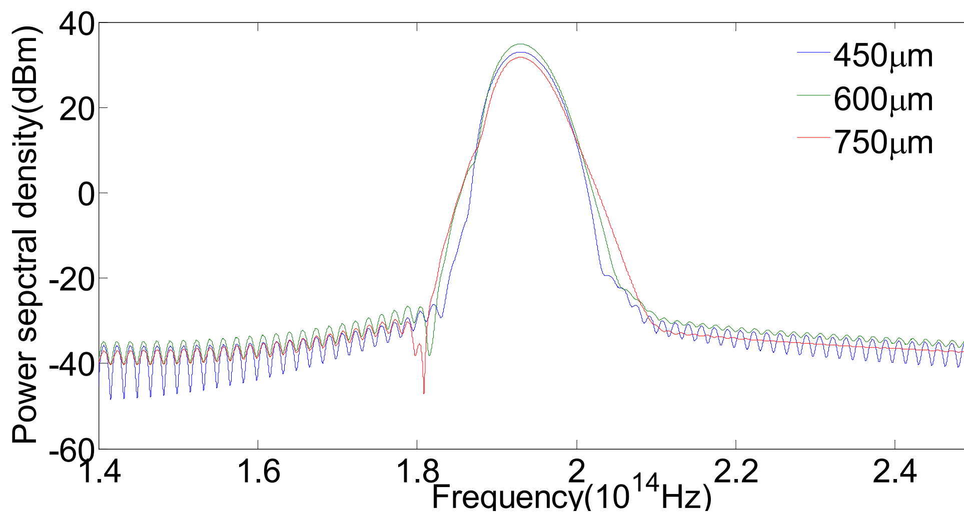

(a)

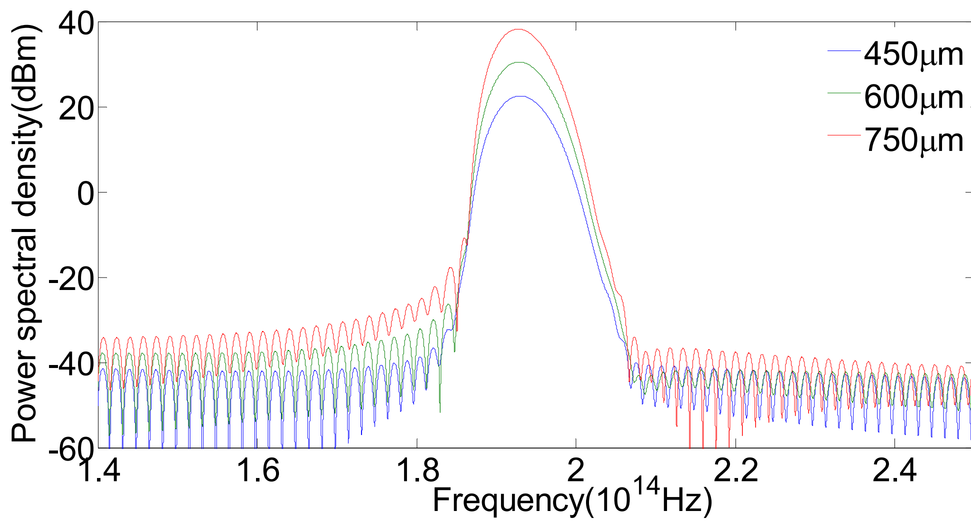

(b)

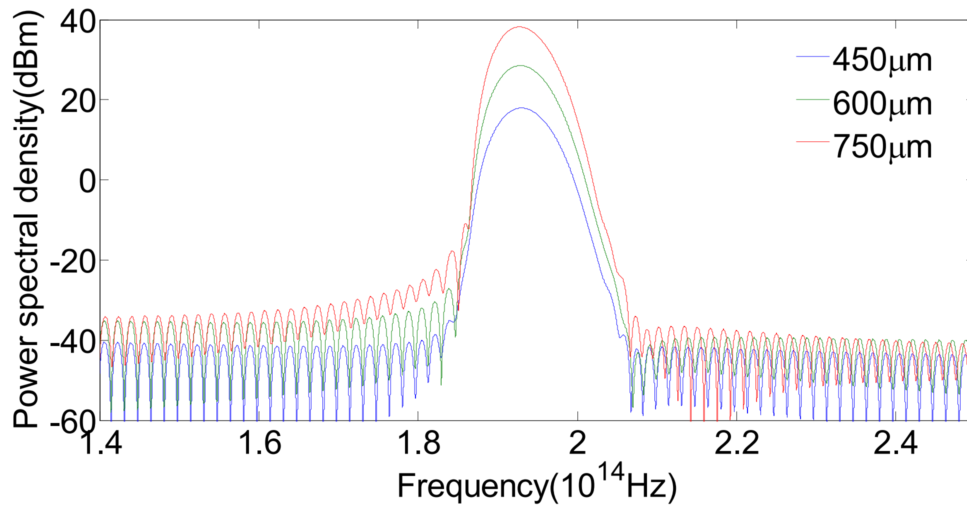

(c)

Fig. 9.6 Power spectral density evolution of a femtosecond pulse propagation along the QWA cavity (a) conventional (b) exponential taper and (c) linear taper.

Tab. 9.2 Characteristic parameters of dynamic spectra

Type	Distance (μm)	Magnitude (dBm)	$3-dB$ Bandwidth (THz)	Central Frequency (THz)
Con-QWA	450	33.01	5.138	193.09

	600	34.87	4.910	193.04
	750	31.72	4.78	193.00
ET-QWA	450	22.52	5.240	193.04
	600	30.47	5.098	192.90
	750	38.19	4.95	192.76
LT-QWA	450	17.94	5.253	193.04
	600	28.52	5.116	192.89
	750	39.08	4.96	192.75

The distribution of carrier density in the lateral direction (x direction in Fig. 9.1) can affect the gain spectrum of QW-SOAs and change the output properties of QW-SOAs [150]. Figure 9.7 compares the temporal outputs of the amplified femtosecond pulse in the tapered QWAs both with and without taking into account variations of the lateral carrier density. The results show that in the absence of the lateral carrier density (i.e. the green curve), the peak arriving time and the peak power of the amplified output pulse are $161fs$ and $7.237w$ while they are $182fs$ and $10.34w$ in the presence of the lateral carrier density. This shows that the lateral carrier density affects the amplified output the peak arriving time and peak power of the amplified output pulse.

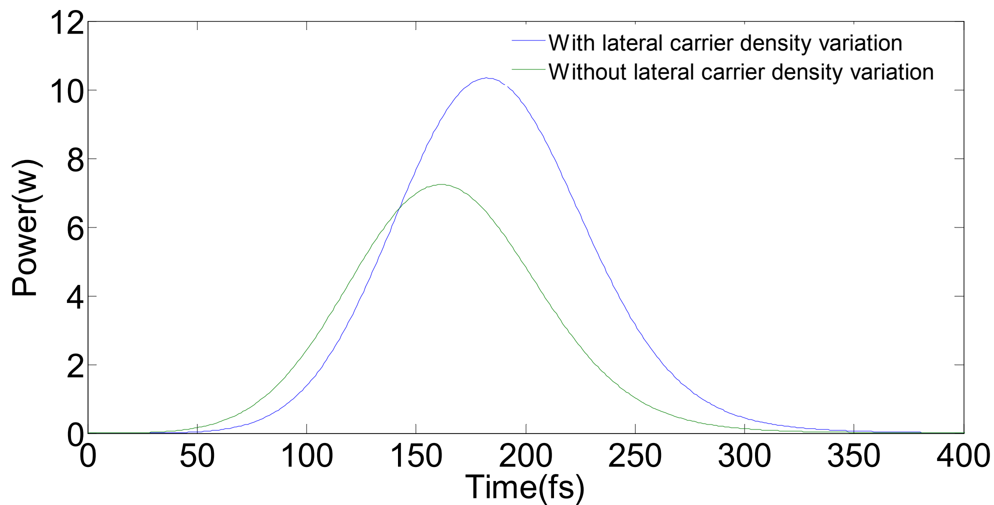

Fig.9.7 Temporal outputs of the amplified femtosecond pulse in the tapered QW amplifiers with and without taking into account the effects of lateral carrier density.

9.2.2.2 Simultaneous Amplification of Two Femtosecond Pulses with Different Central Frequencies

Two femtosecond pulses with the electric fields $E_a(z,t) = I(t)e^{i2\pi f_1 t}$ and $E_b(z,t) = I(t)e^{i2\pi f_2 t}$ are simultaneously applied to the input of the QWA. The envelope function, $I(t)$, is a Gaussian pulse centered at $120 fs$ with pulse width of $80 fs$. The central frequencies f_1 and f_2 of the two femtosecond pulses are $193.55 THz$ and $198.55 THz$, respectively, while their $3dB$ bandwidths are $5.703 THz$ and $5.603 THz$, respectively.

Figures 9.8(a), (b) and (c) show the output power spectral densities of two simultaneously amplified femtosecond pulses in all three QWA structures having different input peak powers of 0.5mW, 2mW and 8mW. In all cases, the pulse with the central frequency f_1 amplifies more than the pulse with the frequency f_2 since the amplifier gain is higher at the lower frequency. Values of two peaks labeled as 1 and 2 in the output spectra of the conventional, exponentially and linearly tapered QWAs shown in Fig. 9.8(a) are

$(25.93\,dBm, 20.91\,dBm)$, $(29.33\,dBm, 23.49\,dBm)$ and $(30.00\,dBm, 24.18\,dBm)$, respectively. Also, the 3-dB bandwidths of the output spectra at f_1 for the three QWA structures are $3.816THz$, $4.194THz$ and $4.230THz$, respectively, which clearly indicates that tapered structures offer larger bandwidth. The values of minimum points between the two peaks observed in the output power spectral density (labeled as 3 in Fig.9.8) for all three amplifier structures shown in Figs.8(a) are $10.89dBm$, $22.11dBm$ and $21.13dBm$, respectively, which indicate that when the peak power values of the two input pulses are small, the spectrum alias in both tapered structures is more serious. Comparison of the results shown in Figs. 9.8(a), (b) and (c) reveals that by increasing the input pulse power the spectrum alias also occurs in the conventional QWA whereas there are only small changes in spectrum alias of the tapered structures. Tab. 9.3 shows the output peak power values (P_1, P_2 and P_3) at points 1, 2 and 3, respectively, at three different input powers for all structures. Also shown in Tab. 9.3 are the aliasing values (P_1-P_3) and (P_2-P_3) which clearly indicates that, as the input power increases from 0.5mw to 8mw the value of P_1-P_3 deceases from $15.04dB$ to $5.56dB$ in the Con-QWA whereas it increases from $8.87dB$ to $8.96dB$ in the LT-QWA.

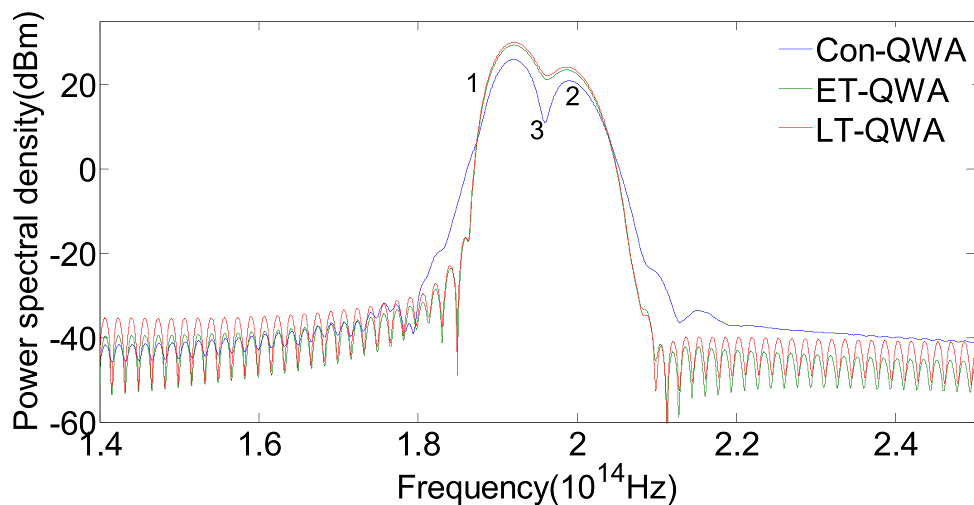

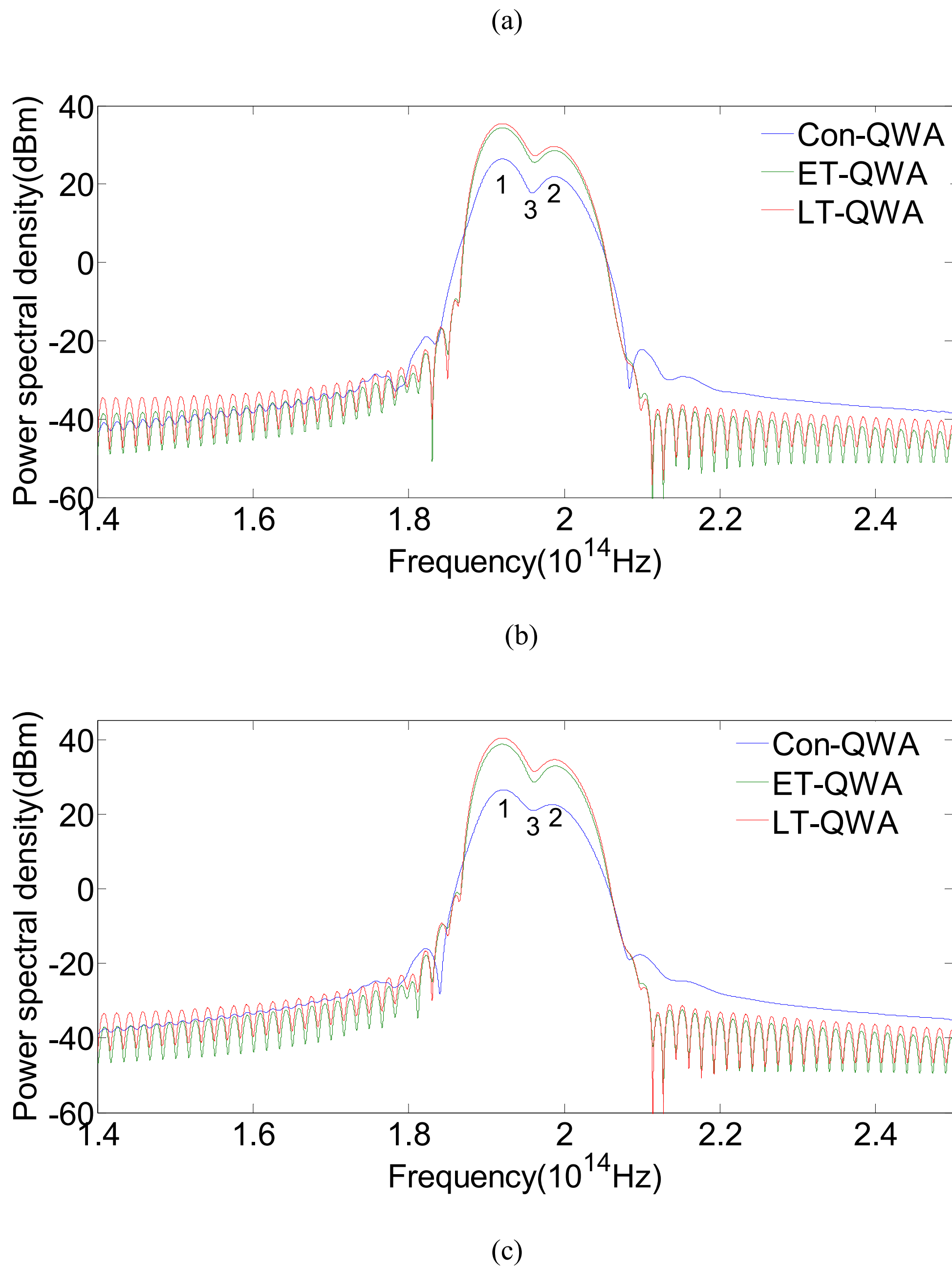

Fig.9.8 Output power spectral density waveforms of two simultaneously amplified femtosecond pulses in the three different QWA structures for three different input peak powers of (a) 0.5mW, (b) 2mW and (c) 8mW.

Tab. 9.3 Output peak powers for different waveguides and input powers

Peak input power (mW)	Waveguide type	P_1 (dBm)	P_2 (dBm)	P_3 (dBm)	P_1-P_3 (dBm)	P_2-P_3 (dBm)

0.5*mw*	Con-QWA	25.93	20.91	10.89	15.04	10.02
	ET-QWA	29.33	23.49	22.11	7.22	1.38
	LT-QWA	30.00	24.18	21.13	8.87	3.05
2*mw*	Con-QWA	26.40	21.91	17.71	8.69	4.2
	ET-QWA	34.39	28.55	25.54	8.85	3.01
	LT-QWA	35.45	29.63	27.21	8.24	2.42
8*mw*	Con-QWA	26.52	22.57	20.96	5.56	1.61
	ET-QWA	38.74	32.92	28.52	8.69	4.4
	LT-QWA	40.42	34.61	31.46	8.96	3.15

9.2.2.3 Femtosecond Pulse Train Amplification

The amplification of a $50Gb/s$ femtosecond pulse train shown in Fig.9.9 in the conventional, exponential and linear tapered QWAs is studied using the Q-TLM method. Each pulse in the train has 1mW peak power.

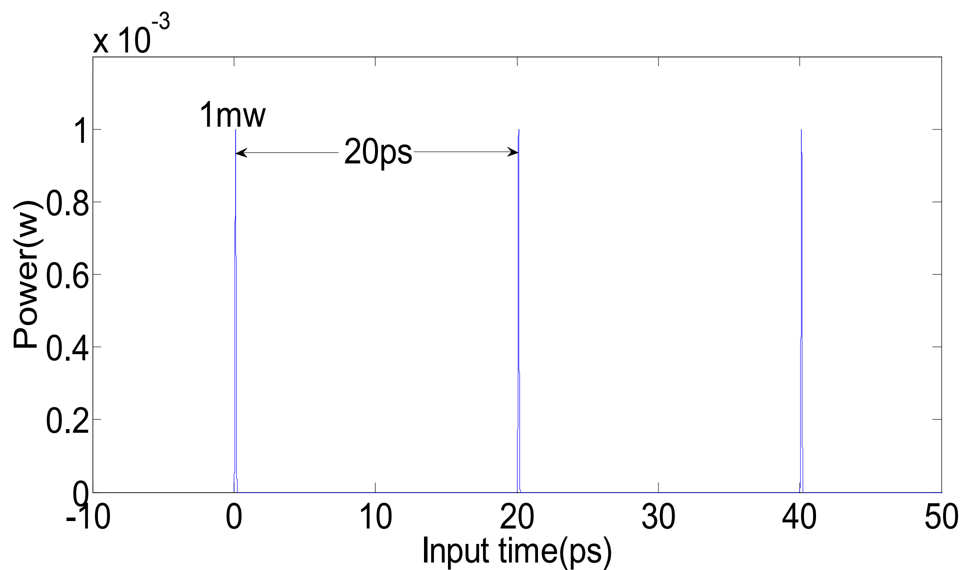

Fig. 9.9 Temporal waveform of the input pulse train.

Figure 9.10 shows the amplified temporal output waveforms in the three QWA structures. The output powers of the first three amplified pulses in the train are (1.9W, 0.4W, 0.12W), (8.36W, 3.22W, 1.5W) and (10.34W, 5.34W, 3.07W) in the conventional, exponential and linear tapered QWA structures, respectively. The results indicate that the peak power values of each amplified pulse in the linear tapered QWA are larger than those in the other two QWAs. This is because the gain saturation in the linear tapered QWA is higher than the other two structures. The peak power ratios between the 2nd and the 1st as well as between 3rd and 1st in the amplified output pulses are (0.212 and 0.063), (0.385 and 0.179) and (0.517, 0.279), respectively, in the conventional, exponential and linear tapered QWA structures. The results show that the linear tapered QWA structure has the highest power ratios between the 2nd and 1st as well as between the 3rd and 1st in the amplified output waveforms, which shows it has the highest carrier density level and hence, the fastest gain recovery among the other two QWA structures.

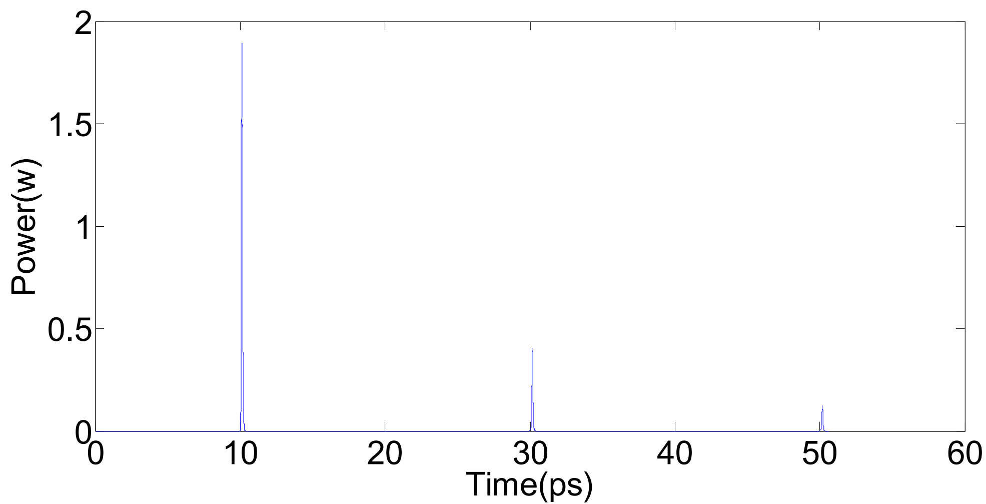

(a)

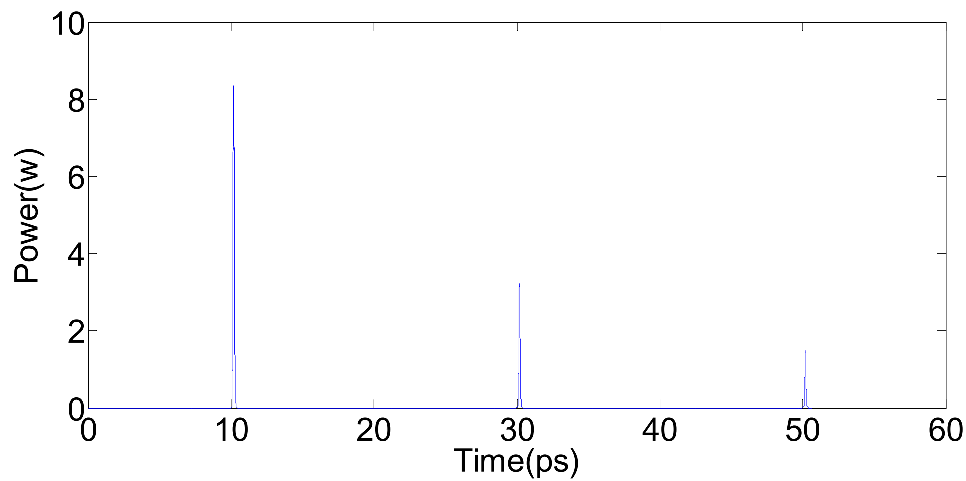

(b)

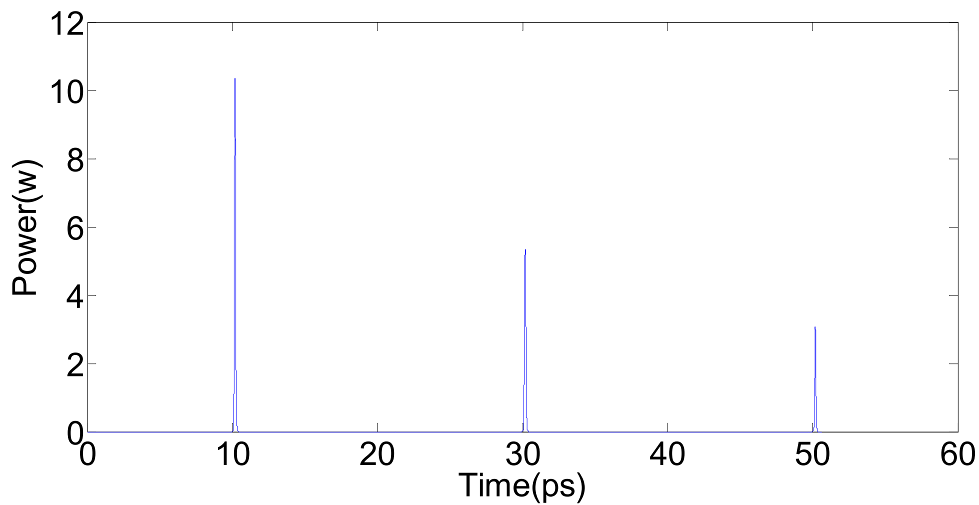

(c)

Fig. 9.10 Temporal output waveforms of the amplified femtosecond pulse train in the QWA (a) conventional (b) exponential taper and (c) linear taper.

9.3 Effects of Strain on the Dynamic Spectra of Femtosecond Pulse Amplification in QW-SOAs

In the following, based on Q-TLM method effects of strain on the gain and spontaneous emission spectra as well as the dynamic spectra of the amplified femtosecond pulse of an $InGaAs-InGaAsP$ quantum well amplifier operating at $1550nm$ are investigated. Tab.

9.4 lists values of different parameters used in the simulations.

Tab. 9.4 Parameters used in the analysis of strain effects [129]

Symbol	Description	Value
n	Background refractive index	3.67
f_{sam}	Sampling frequency	$1.0\times10^{15}\,Hz$
A	Linear recombination	$2\times10^{8}\,s^{-1}$
B	Bi-molecular recombination	$6\times10^{-16}\,m^{3}s^{-1}$
C	Auger recombination	$8\times10^{-41}\,m^{6}s^{-1}$
γ	Linewidth of QW-SOA	$2\times10^{13}\,rad/s$
Γ	Confinement factor	0.025
N_0	Transparent carrier density	$1.2\times10^{24}\,m^{-3}$
W	SOA width	$1\mu m$
D	SOA thickness	$24.5nm$

9.3.1 Strain Effects on the Gain and Spontaneous Emission Spectra

Figure 9.11 shows the normalized gain spectra of the strained QWA. The FWHMs of the normalized gain spectra are 39.06 , 36.13 and 30.52 THz, respectively, for compressively strained (CS, blue), unstrained (US, green) and tensile strained (TS, red) while their central wavelengths are 188.72 , 203.86 and 218.26 THz, respectively, which indicates a decrease in the gain bandwidth and a blue shift in gain central wavelength as the strain changes from compressive to tensile. This is because as the molar fraction of Gallium x increases from 0.3 which is for CS , to 0.47 for US and to 0.65 for TS , the first heavy hole is moved to the lower energy level while the first light hole is moved to the higher energy level which causes a decrease in the gain magnitude. Also, the magnitudes of the normalized gain spectra in the three strained cases, are 1 (CS), 0.6175(US) and 0.2799(TS), respectively.

Fig.9.12 shows the normalized spontaneous emission spectra of the QW amplifier under different strained. The central frequencies of the spontaneous emission spectra for QW-SOAs in different strain cases are $207.76(CS)$, $213.87(US)$ and $220.95(TS)$ THz, respectively, while the FWHMs of the spontaneous emission spectra are 62.01, 54.93 and 49.56 THz. In contrast with the gain spectra, the magnitude of the spontaneous emission spectra in all three cases are almost the same (0.93344, 1 and 0.9328). Further comparisons of the gain and spontaneous emission spectra show that the compressively strained QW amplifier has the highest ratio between the gain and the spontaneous emission spectra magnitudes.

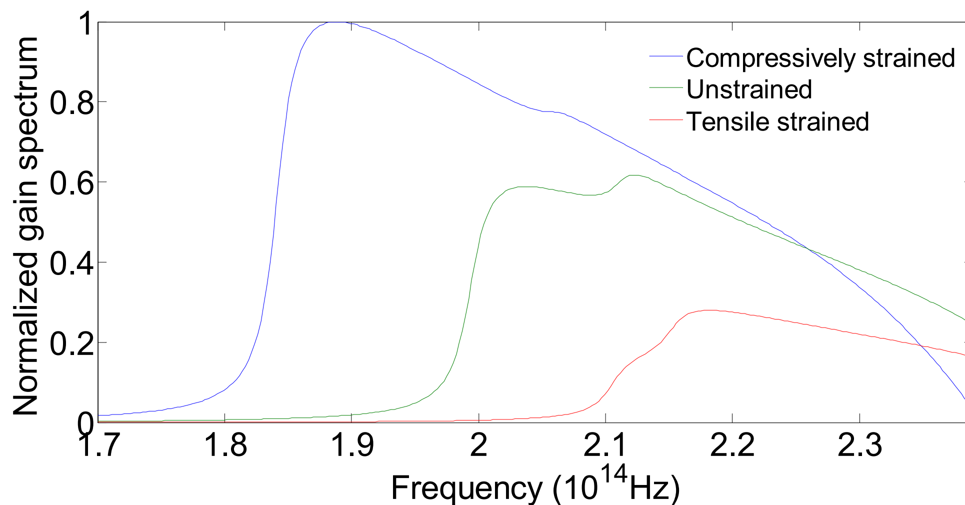

Fig. 9.11 Normalized gain spectra of QW amplifiers for three strain cases at carrier density of $8\times10^{24}\,m^{-3}$ obtained by the scattering module in the Q-TLM model.

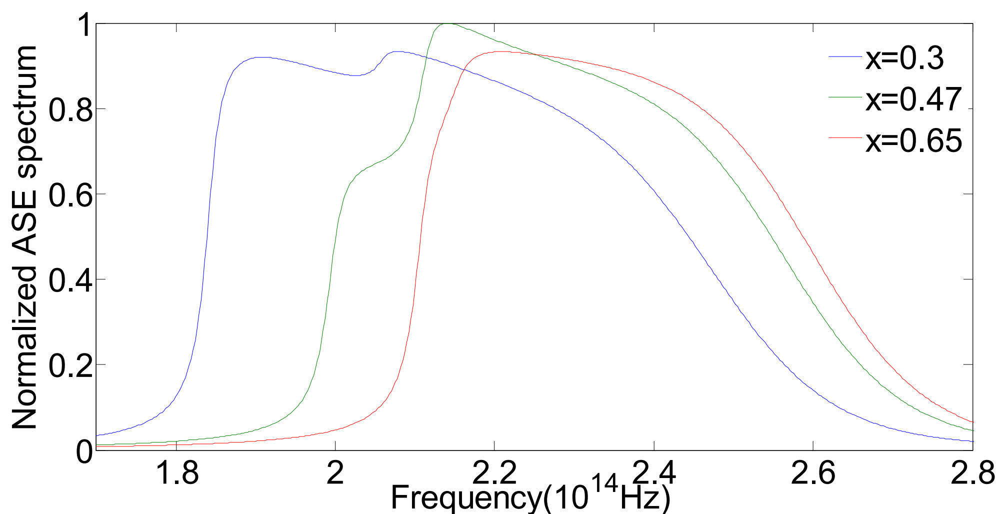

Fig. 9.12 Normalized spontaneous emission spectra of QW amplifiers for three strain cases at the carrier density of $8\times10^{24}m^{-3}$ obtained by the spontaneous emission source in the Q-TLM model.

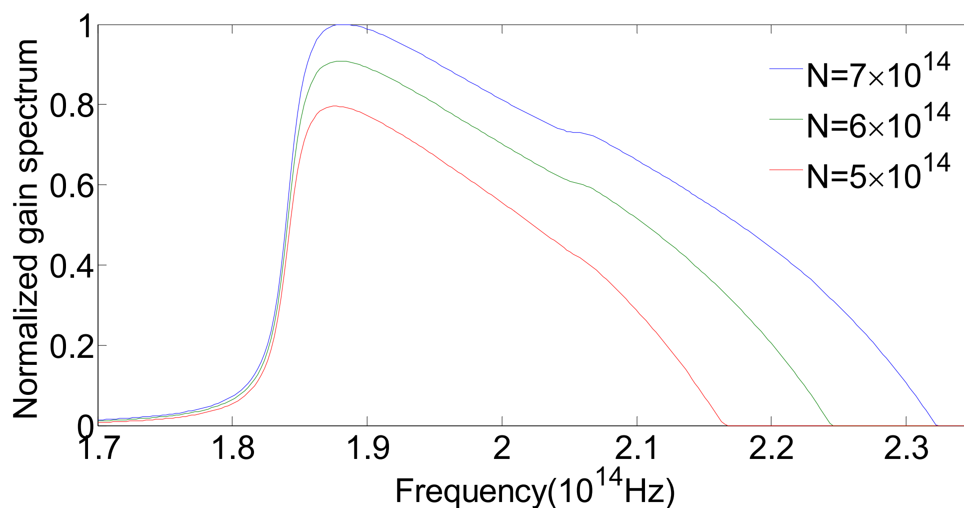

Fig. 9.13 Normalized gain spectra of the compressively strained(CS) QW amplifier at three different carrier densities obtained by the scattering module in the QW-TLM model

Figure 9.13 shows the normalized gain spectra of a CS QW amplifier at different carrier densities. The results show that as the carrier density decreases from $7\times10^{24}m^{-3}$ to $5\times10^{24}m^{-3}$ the peak value of the normalized gain reduces from 1 to 0.8 and also the bandwidth of the gain spectrum reduces from 34.18 to 22.95 THz and the central frequency shifts from 188.23 to 187.74 THz.

9.3.2 Dynamic Spectral Analysis in the Femtosecond Pulse Amplification

The temporal envelope function of the input optical electric field is a Gaussian pulse centered at $90\,fs$ with the peak power $1mW$ and FWHM values $60\,fs$, respectively. The corresponding input pulse frequency response has its central frequency and bandwidth at 193.48 and 7.6 THz, respectively. This femtosecond pulse is applied in the input of a compressively strained $In_{0.7}Ga_{0.3}AsP$/InGaAsP QW-SOA.

Figure 9.14 shows the evolution of the amplified pulse spectra waveforms along four different positions (lengths) of the amplifier cavity. The results show that the peak value of the power spectra density increases (i.e. from $17.29dBm$ at $300\mu m$ to $27.04dBm$ at $750\mu m$) as the pulse propagates towards the output facet of the amplifier while the central frequencies decreases from 193 to 192.72 THz (i.e. red shift). Also, the $3\,dB$ bandwidth of the power spectral densities decreases from 7.404 to 7.001 THz. This is because as the distance increases, the input signal gets more amplifications which results in an increase in the magnitude of the power spectral density and the reduction of carrier density in the amplifier cavity (shown in Fig. 9.15).

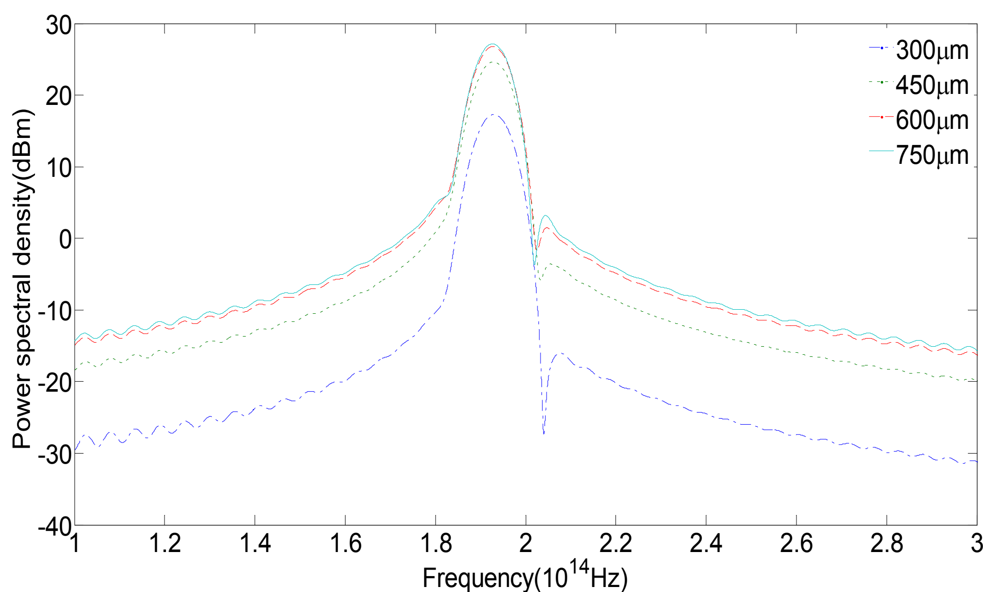

Fig. 9.14 Evolution of the amplified pulse spectra waveforms along 4 different positions of a compressively strained QW amplifier cavity.

Figure 9.15 shows the variations of the carrier density during femtosecond pulse amplification in a CS QW amplifier at different distances along the amplifier cavity. As the figure shows the carrier density decreases as the amplified pulse approaches the output facet of the amplifier.

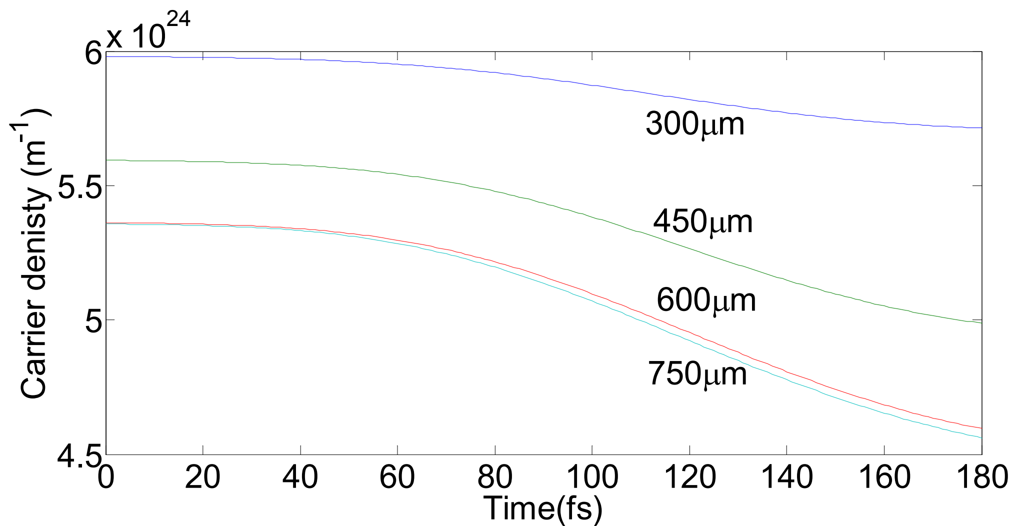

Fig. 9.15 Variations of carrier densities in a compressively strained QW amplifier at different distances along the amplifier cavity.

Figure 9.16 shows the effect of strain (compressive and tensile) on the output power spectral density of the amplified femtosecond pulse. In order to compare the effect of strain on the dispersion of the amplified output pulse we have set the center frequencies of the input signals at 188.72 , 203.86 and 218.26 THz for CS, US and TS, respectively, which correspond to the center frequencies of their gain spectra. It was found in all cases the amplified output pulse has a narrower bandwidth as compared with that of the input pulse and also in each case a red-shift in the center frequency is observed. In the CS, US and TS QW amplifiers, the center frequency shifts of the amplified output spectra with respect to the input spectra are 1.231, 0.790 and 0.113 THz, respectively. This is due to the fact that in

the CS QW amplifier the gain value around the center frequency is the largest (see Fig. 9.11) which implies that the input signal is highly amplified during its propagation within the amplifier cavity and hence, the average carrier density level is lower, which causes a larger red shift. The magnitudes of the output power spectral density in the CS, US and TS cases are 27.11 , 14.94 and 4.93 dbm, respectively. In the CS case, the variations of the $3dB$ spectral bandwidths is 0.638 THz while in the US and TS cases, they are 0.529 and 0.424 THz, respectively. This is because in the CS case, the highest optical filed in the amplifier cavity leads to the lowest carrier density level, which suppresses the bandwidth of the gain spectrum. Also, the output spectral shape of the amplified femtosecond pulse in the CS QWA shows the smallest fluctuation. This is because the CS QWA has the largest magnitude ratio between the gain spectrum and the spontaneous emission spectrum in the three QW amplifier structures as shown Figs. 9.13 and 9.14.

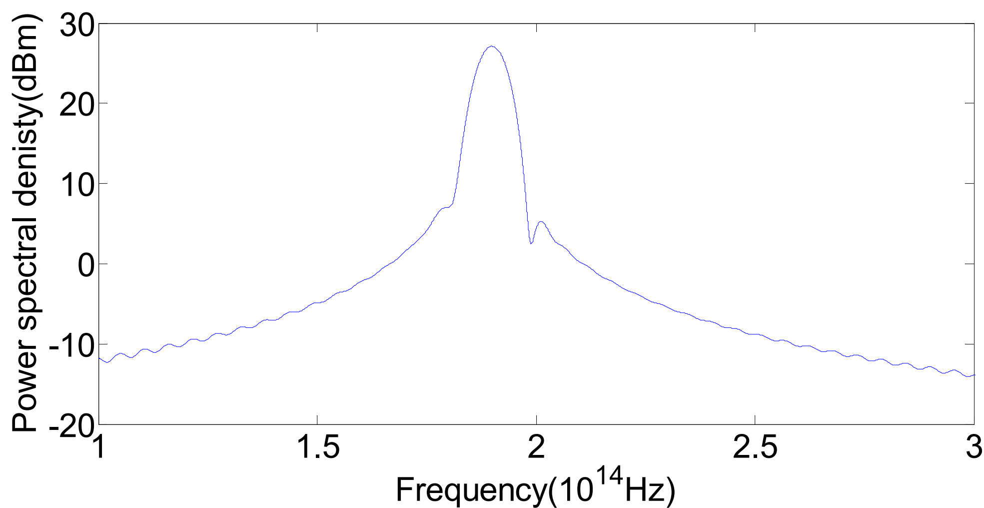

(a)

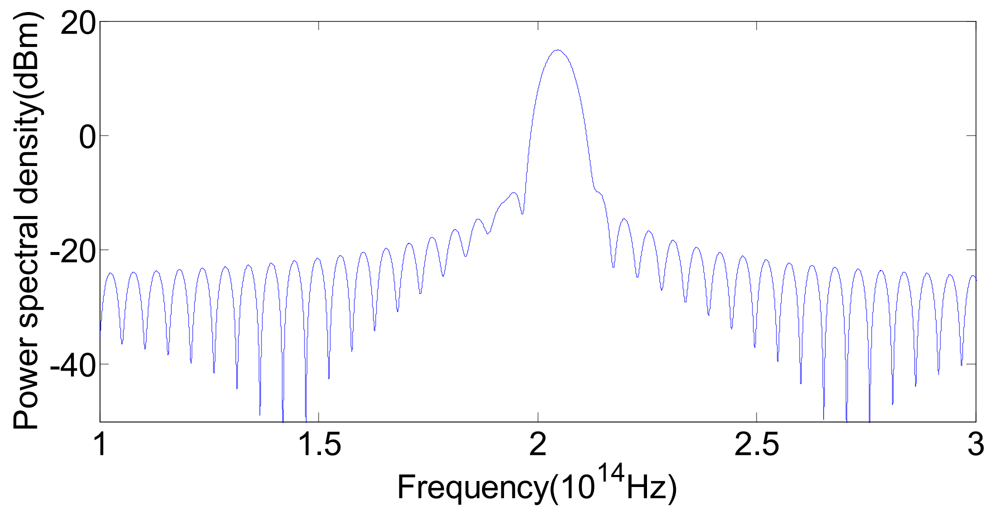

(b)

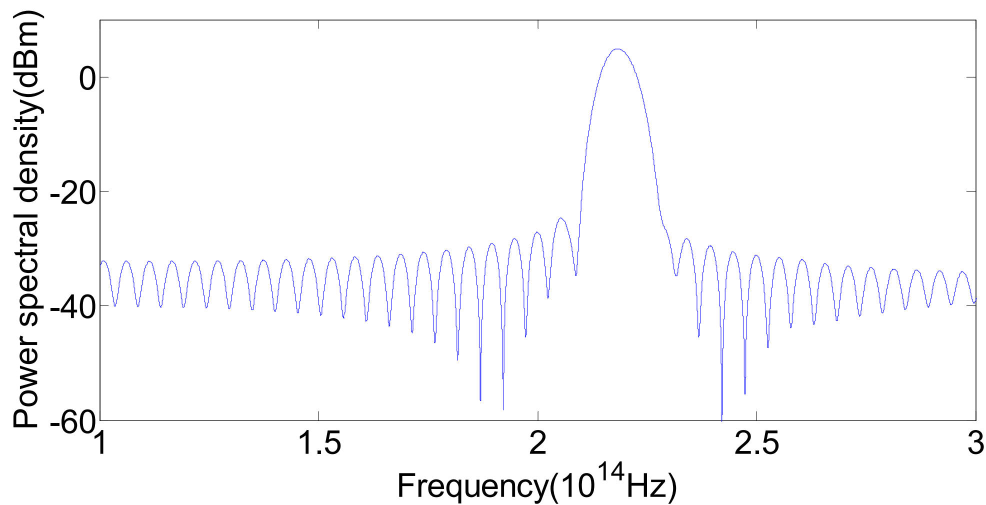

(c)

Fig. 9.16 Output spectra of the amplified femtosecond pulse (a) CS, (b) US and (c) TS.

9.4 Conclusions

In this Chapter, the wavelength-dependent femtosecond pulse propagation in QW-SOAs is analyzed. First, a new theoretical model for the tapered QW-SOAs based on the quantum transmission line modelling method is presented which takes into account both the effect of lateral carrier density distribution and the strain effect on the band structure. The

femtosecond pulse amplification in the conventional, exponential and linear tapered waveguide QWAs are compared using Q-TLM models. Simulation results show that for the amplification of a single femtosecond pulse, the tapered waveguide structure provides higher saturation gain and minimal distortion in the temporal and spectral waveforms of the amplified output pulse. For the simultaneous amplification of two femtosecond pulses with different central frequencies, it has been found that at low input pulse power, the spectrum alias in tapered QWAs is more serious as compared with the conventional QWA. However, as the input peak power increases the spectrum alias in tapered QWAs becomes smaller than that in conventional QWA. In the amplification of femtosecond pulse train the linear tapered QWA exhibits the fastest gain recovery as compared with the other two amplifier structures.

Secondly, based on the quantum transmission line modelling method (i) the effect of strain on the gain and spontaneous spectra of QWs and (ii) the dynamic spectral behavior of strained QW amplifiers during the femtosecond pulse amplification are analysed. Simulation results show that the CS QWA offers a bigger ratio between the gain and the spontaneous emission spectra magnitudes as compared with US and TS QWA. Also, it was found that as the distance approaches to the amplifier length, both the center frequency and bandwidth of the amplified pulse spectra decrease and that the compressively strained QW amplifier exhibits the optimum output spectral properties (i.e. the highest magnitude and the lowest spectra fluctuations).

These studies provide important basis for optimization of the QW-SOAs for femtosecond pulse amplification. Also, the results further verified that the newly proposed quantum transmission line modelling method is an effective tool for analysis of the QW amplifier performance both in time-frequency domains.

Chapter 10

Conclusions and Future Work

10.1 Conclusions and Contributions

In this thesis, the ultrashort optical pulse propagation in semiconductor optical amplifiers has been theoretically and experimentally investigated through analysis, optimization and quantum transmission line modelling.

The thesis begins with the fundamentals, including electronic and optical properties as well as the optical processes in semiconductor optical amplifiers. The band structure of quantum well is calculated using the finite difference method and the effect of strain on the quantum well band structure distribution is discussed. The stimulated and spontaneous emissions' processes in SOAs as well as some important optical properties including momentum matrix, differential gain and linewidth enhancement factor are analysed and discussed. These physics of semiconductor optical amplifiers are significantly important to understand the dynamic process of optical pulse propagation in SOAs.

Chapter 3 investigates the carrier temperature dynamics in bulk and quantum well semiconductor optical amplifiers. A new analytical method for the analysis of carrier heating effects in bulk SOAs is proposed based on Fermi-Dirac integrals of 3/2 and 1/2 orders. The relation between Fermi-Dirac integral of 3/2 order and Fermi-Dirac integral of 1/2 order is used to remove the derivates of Fermi-Dirac integral in the analysis of

carrier heating effects in amplifiers. The method allows to use the global approximations of Fermi Dirac integral of 3/2 order and 1/2 order to obtain the analytical expression for the carrier temperature dynamics in bulk SOAs. As for a QW-SOA, an accurate method to describe carrier heating effects is presented taking into account the discontinuous distribution of energy band structure and the coupling among heavy hole band, light hole band and spin-orbit spilt-off band. Effects of carrier heating on the picosecond pulse amplification in both bulk and quantum well SOAs are studied based on the proposed theoretical methods.

In Chapters 4 and 5 theoretical and experimental investigations were performed on the amplifier bias current optimization in order to obtain high gain distortionless ultra-short pulse amplification. A new formula which relates the amplifier bias current with the maximum distance along the amplifier cavity where the amplified pulse is distortionless is presented in Chapter 4. This formula can be used to obtain the amplifier optimized bias current and to find relationship between the optimized current and input pulse peak power. This theoretical method provides an effective guidance for choosing a suitable bias current in the practical application of semiconductor optical amplifiers. Chapter 5 experimentally investigates the optimized bias current for high-speed pulse train amplification with low distortion and high gain. The relationship between the optimized bias current and the parameters of the input pulse (i.e. peak power, pulse duration and repetition rate) are experimentally investigated. The effect of assist light injection and carrier temperature on the optimized bias current are also discussed.

Chapter 6 reviewed the transmission line matrix (TLM) method and its application in the analysis of TEM wave propagation. The TEM wave propagation in the bounded and unbounded space is described based on TLM. Also, TLM is adopted to obtain the wave

impedance in a rectangular waveguide which is then compared with that obtained by the analytical expression where the two results were in a good agreement. The basics of applying the one-dimension TLM to high-frequency circuits and the previous transmission line laser modelling (TLLM) method are reviewed. It was found that although TLLM was used to provide an explanation for the time-frequency behavior of the bulk laser diodes, it has the following disadvantages (i) it only considers the wave properties of light but ignores the light's particle properties (ii) it uses only one RLC filter to approximate the whole gain spectrum of laser diode and ignores the interaction between the light and semiconductor materials and also lacks the necessary theoretical basis.

Chapter 7 presents a new modelling technique referred to as quantum transmission line modelling (Q-TLM) method, which can be taken as the basic theory to apply TLM to model the semiconductor optical devices. Q-TLM method is proposed for modelling the photon emission by combining the time-dependent perturbation theory and the transmission line modelling method. New models for quantum well and quantum dot structures are established based on Q-TLM method which are denoted by QW-TLM and QD-TLM, respectively. In the quantum well structure model, three parallel RLC filters together with their associated weight coefficients constitute one QW-TLM unit, which represents the photon emission processes during which electrons transit from the conduction band to the heavy hole band, the light hole band and the spin-orbit split-off band at a specific wave vector. Parallel QW-TLM units are employed to describe the electron transitions in the wave vector space. Also, Q-TLM is used to establish models for quantum dot structure. The gain and spontaneous emission spectra of quantum well and quantum dot structures are simulated based on Q-TLM. The simulation results showed a very good agreement with those obtained by the analytical model. Q-TLM technique

becomes a promising method to study the temporal and spectral behavior of semiconductor optical devices.

The proposed Q-TLM method is adopted to establish models for quantum well amplifiers, quantum dot amplifiers as well as quantum well lasers in Chapter 8. Ultrashort pulse propagation in semiconductor optical amplifiers is analysed using the proposed new model. For the picosecond pulse amplification in quantum well amplifiers, it was found that gain saturation causes the temporal distortion of the amplified output pulse, including the temporal peak shift and pulse width narrowing which in frequency domain results in bandwidth broadening and red shift in the spectrum of the amplified output pulse. Also, as the peak power value of the input signal increases, the temporal and spectral distortions are aggravated. For the femtosecond pulse amplification in quantum dot amplifiers, the pulse evolution process in the amplifier cavity is studied in the time-frequency domain. The effects of carrier transport and bias current impulse on the output properties of strained QW lasers are studied based on Q-TLM laser model. These simulation results are in good agreement with the existing experimental results, which verifies that the new proposed Q-TLM method can accurately study the temporal and spectral behavior of QW amplifiers and lasers.

In Chapter 9, the proposed Q-TLM method is adopted to study the wavelength-dependent femtosecond pulse amplification in tapered quantum well amplifiers and the effect of strain on the dynamic spectrum of femtosecond pulse amplification in quantum well amplifiers. First, a new theoretical model for the tapered QW-SOAs is established based on Q-TLM method, which takes into account effects of both lateral carrier density distribution and the strain on the band structure. The new models are employed to compare the femtosecond pulse amplifications (single femtosecond pulse, two femtosecond pulses with different

central frequencies and femtosecond pulse train) in the conventional, exponential and linear tapered waveguide QWAs. The distortion of the amplified output pulse in the tapered QWAs becomes smaller than that in conventional QWA. Morover, based on Q-TLM method the effect of strain on the dynamic spectra of a strained QW amplifier during the femtosecond pulse amplification is analysed. It was found that the compressively strained QWA offers a larger ratio between the magnitudes of gain and the spontaneous emission spectra as compared with that in unstrained and tensile strained QWAs. Also, the compressively strained QW amplifier exhibits the best output spectral properties for femtosecond pulse amplification, including the highest magnitude and the lowest spectra fluctuations.

In short, the major contributions of this thesis are as the following:

1. An accurate and simple analytical method to study carrier heating effect in bulk semiconductor optical amplifiers is presented by using Fermi–Dirac integrals of 3/2 and 1/2 orders. Effects of carrier heating on the amplified picosecond Gaussian pulse propagation in a quantum well semiconductor optical amplifier (QW-SOA) are studied taking into account the holes' non-parabolic density of states.
2. A novel method to optimize the quantum well semiconductor optical amplifier bias current for distortionless pulse amplification is developed and an analytical formula which relate the optimised current with amplifier parameters is introduced. Detailed experimental studies are performed to investigate the relationship between the optimised bias current and the parameters of the SOA input pulse train.

3. A novel modelling method-quantum transmission line modelling (Q-TLM) method is first presented by combining quantum statistic description and photon-electron dynamic interaction process description. The modelling method can be taken as the basic theory to establish models for semiconductor optical devices. Q-TLM is used to establish models for quantum dot and quantum well structures, quantum well/dot amplifiers, quantum well lasers and it is verified that the new modelling method can be used to accurately predict the temporal and spectral behaviors of the amplified output signal in active semiconductor optical devices.

4. Q-TLM is adopted to analyse the wavelength-dependent femtosecond pulse amplification in tapered quantum well amplifiers. Also, the strain (compressive strain and tensile stain) effects on the dynamic spectra of amplified femtosecond pulses in a quantum well semiconductor optical amplifier (QW-SOA) are studied using the Q-TLM method.

10.2 Future Work

The thesis focuses on the optimization, analysis and quantum transmission line modelling of ultrashort pulse amplification in semiconductor optical amplifiers. Great progress has been made in this topic and future research work will be recommended to be performed in the following specific topic:

Semiconductor optical amplifiers have been widely used in the high-speed optical communications and optical signal processing due to their advantages, such as low-power cost, small footprint and monolithic integration. However, compared with fiber amplifiers, the noise generated by the spontaneous emission process has a bad influence on the output performance of ultrashort pulse amplification in semiconductor optical amplifiers. Future

work needs to focus on exploring new methods to minimize or suppress the amplified spontaneous emission in SOAs.

Semiconductor optical amplifiers are widely used in optical communications networks as a means to boost signal strength and thus maintain an adequate signal to noise ratio. However, the use of optical amplifiers requires careful consideration of the network dynamics to avoid generating errors during the optical single amplification. When SOAs are operated in a packet switched or burst mode environment, gain-clamping is required to reduce the undesirable gain transients. Gain clamping enables SOAs to stable the amplification gain over a wide dynamic range. Gain regulation can be implemented by varying the bias current of SOAs however, changes in bias current influences the maximum linear operating power of the amplifier which is undesirable. Hence, another future work can be focused on the design of a high-performance gain-clamped semiconductor optical amplifiers.

The thesis has discussed how to apply the proposed quantum transmission line modelling (Q-TLM) method to the active semiconductor optical devices. However, Q-TLM is also a promising modelling tool for the integrated optical system and silicon circuits. Hence, it can be modified and applied to model the electro-photonic integration systems and investigate their dynamic performances both in the time and frequency domains. Furthermore, Q-TLM can be used to study the optical data stream propagation in the optical network, such as analyzing the bit error rate (BER) and pseudorandom binary sequence (PRBS), which are important in the optical communication system.

References

1. R. N. Hall, G. E. Fenner, J. D. Kingsley, T. J. Soltys, and R. O. Carlson, "Coherent light emission from GaAs emission," *Phys. Rev. Lett.*, vol. 9, no. 9, pp. 366-368, Nov. 1962.

2. I. Nathan, W. P. Dumke, G. Burns, F. H. Dill, Jr. and G. Lasher, "Stimulated emission of radiation from GaAs p-n junctions," *Appl. Phys. Letts.*, vol. 1, no 62, pp. 62–64, Nov.1962.

3. Y. Yamamoto, "Characteristics of AlGaAs Fabry-Perot cavity type laser amplifiers," *IEEE J. Quantum Electron.*, vol. 16, no. 10, pp.1047-1052, Oct. 1980.

4. T. Mukai, Y. Yamamoto, and T. Kimura, "S/N and Error rate performance in AlGaAs semiconductor laser preamplifier and linear repeater systems," *IEEE Transactions on Microwave Theory and Techniques.*, vol. 30, no. 10, pp. 1548-1556, Oct. 1982.

5. I. Hayashi, M. B. Panish, P. W. Foy, and S. Sumski, "Junction lasers which operate continuously at room temperature," *Appl. Phys. Lett.* vol. 17, no. 3, pp. 109-111, Aug. 1970.

6. Z. I. Alferov, V. M. Andreev, E. L. Portnoy, and M. K. Trukan, "AlAs-GaAs heterojunction injection lasers with a low room-temperature threshold," *Sov. Phys. Semicond.* , vol. 4, no. 9, pp. 1573-1575, May 1970.

7. N. A. Olsson et al., "Polarisation-independent dependent optical amplifier with buried facet," *Electron. Lett.*, vol. 25, no. 16, pp. 1048-1049, Jun. 1989.

8. J. Simon, "GaInAsP semiconductor laser amplifiers for single-mode fibre communications," *J. Lightw. Technol.*, vol. 5, no.9, pp.1286-1295, Sept. 1987.

9. M. J. Connelly, Semiconductor optical amplifiers. New York, Kluwer Academic Publishers, 2001.

10. P. Petroff and S. DenBaars, "MBE and MOCVD growth and properties of self-assembling quantum dot arrays in III-V semiconductor structures," *Superlattices and Microstructures*, vol. 15, no. 1, pp. 15-21, Jan. 1994.

11. M. Aoki, H. Sano, M. Suzuki, M. Takahashi, K. Uomi, and A. Takai, "Novel structure MQW electroabsorption modulator/DFB-laser integrated device fabricated by selective area MOCVD growth," *Electron. Lett.*, vol. 27, no.23, pp. 2138-2140, Nov. 1991.

12. Y. Ding, et al., "High peak-power picosecond pulse generation at 1.26 μm using a quantum-dot-based external-cavity mode-locked laser and tapered optical amplifier," *Opt. Express*, vol. 20, no. 13 pp.14308-14320, June 2012.

13. M. Kolarczik, et al., "Picosecond pulses from wavelength-swept continuous-wave Fourier domain mode-locked lasers," *Nat. Commun.*, vol. 4, Art. no. 2953, Dec. 2013

14. C. Weber et al., “Picosecond pulse amplification up to a peak power of 42 W by a quantum-dot tapered optical amplifier and a mode-locked laser emitting at 1.26 µm,” *Opt. Lett.*, vol. 40, no. 3, pp. 395–398, Feb. 2015.

15. R. W. Hellwarth, Advances in Quantum Electronics. New York, Columbia Press, 1961.

16. A. J. DeMaria, D. A. Stetser, and H. Heinan, "Self mode-locking of lasers with saturable absorbers," *Appl. Phys. Lett.* , vol. 8, no. 7, pp.174-176, Apr. 1966.

17. C.V. Shank and E.P. Ippen, “Sub-picosecond kilowatt pulses from a mode-locked cw dye laser,”*Appl. Phys. Lett.* vol. 24, no. 8, pp. 373-375, Apr. 1974.

18. K. J. Blow and D. Wood, “Mode-locked lasers with nonlinear external cavities,” *J. Opt. Soc. Am. B* , vol. 5, no. 3, pp. 629-632, Mar. 1988.

19. D. E. Spence, P. N. Kean, and W. Sibbett, “60-fsec pulse generation from a self-mode-locked Ti:Sapphire laser,” *Opt. Lett.* , vol. 16, no.1 , pp. 42-44, Jan. 1991.

20. R. Kawakami et al., “Visualizing hippocampal neurons with in vivo two-photon microscopy using a 1030 nm picosecond pulse laser,” *Scientific Report*, vol. 3, Art. no. 1014, Jan. 2013.

21. A. Pyatenko, H. Wang, Naoto Koshizaki, and Takeshi Tsuji, “Mechanism of pulse laser interaction with colloidal nanoparticles,” *Laser Photonics Rev.*,vol. 7, no. 4, pp. 596–604, July 2013.

22. R. I. Woodward, et al., “Few-layer MoS2 saturable absorbers for short-pulse laser technology: current status and future perspectives,” *Photon. Res.*,vol. 3, no. 2, pp. A30-A42, Apr. 2015

23. Z. Li, A. M. Heidt, J. M. O. Daniel, Y. Jung, S. U. Alam, and D. J. Richardson, “Thulium-doped fiber amplifier for optical communications at 2 µm,” *Opt. Express*, vol. 21, no. 8, pp.9289-9297, Apr. 2013.

24. M. Xia and H. Ghafouri-Shiraz, “Theoretical analysis of carrier heating effect in semiconductor optical amplifiers,” *J. Optical and Quantum Electronics*, vol. 47, no.7, pp.2141-2153, Dec. 2014

25. X. Sun, N. Vogiatzis, and J. M. Rorison, “Theoretical study on dilute nitride 1.3µm quantum well semiconductor optical amplifiers: incorporation of N compositional fluctuations,” *IEEE J. Quantum Electron.*, vol. 49, no. 10, pp. 811-819, Oct. 2013.

26. M. Xia and H. Ghafouri-Shiraz, “High-performance quantum well amplifiers for the WDM system,” *the 36th IEEE Sarnoff Symposium*, New Jersey, pp.62-65, Sept.2015.

27. N. Ishii, K. Kaneshima, K. Kitano, T. Kanai, S. Watanabe, and J. Itatani, “Carrier-envelope phase-dependent high harmonic generation in the water window using few-cycle infrared pulses,” *Nat. Commun.*, vol. 5, Art. no. 3331, Feb. 2014.

28. B. Y. Chang, S. Shin, A. Palacios, F. Martín, and I. R. Sola, "Ultrafast coherent control of giant oscillating molecular dipoles in the presence of static electric fields," *J. Chem. Phys.* ,vol. 139, Art. no. 084306, 2013

29. M. Th. Hassan et al., "Optical attosecond pulses and tracking the nonlinear response of bound electrons," *Nature*, vol. 530, pp. 66-70, Feb. 2016.

30. A. Capua, O. Karni1, G. Eisenstein1, V. Sichkovskyi, V. Ivanov, and J.P. Reithmaier, "Coherent control in a semiconductor optical amplifier operating at room temperature," *Nat. Commun.*, vol. 5, Art. no. 5025, Sept. 2014.

31. G. Sobon, K. Krzempek, P. Kaczmarek, and K. M Abramski, "An eye-safe, high-repetition rate single-mode femtosecond chirped pulse amplification system at 1560 nm," Laser Phys., vol. 23, no. 7, Art. no. 075104, May 2013.

32. V. Ataie, E. Myslivets, B. P.-P. Kuo, N. Alic, and S. Radic, "Spectrally equalized frequency comb generation in multistage parametric mixer with nonlinear pulse shaping," *J. Lightw. Technol.*, vol. 32, no. 4, pp. 840-846, Feb. 2014.

33. V. I. Tolstikhin and M. Willander, "Theory of hot carrier effects on nonlinear gain in GaAs-GaAlAs lasers and amplifiers," *IEEE. Quantum Electron.*, vol. 26, no. 10, pp.1989-1704, Aug. 1990.

34. J. Mørk, J. Mark, and C. P. Seltzer, "Carrier heating in InGaAsP laser amplifiers due to two-photon absorption," *Appl. Phys. Lett.*, vol. 64, no. 17, pp. 2206-2208, Apr. 1994.

35. N. Majer1, K. Ludge1, J. Gomis-Bresco, S. Dommers-Volkel, U. Woggon, and E. Schöll1, "Impact of carrier-carrier scattering and carrier heating on pulse train dynamics of quantum dot semiconductor optical amplifiers," *Appl. Phys. Lett.*,vol. 99, 131102, pp. 1-3, Sept. 2011.

36. F. Tao, L. Zhan, X. Yang, Z. Gu, J. Peng, and S. Luo, "Group velocity manipulation of 10 Gb/s signal by mutually-modulated cross-gain modulation in semiconductor optical amplifiers," *IEEE Photon. Technol. Lett.*, vol. 26, no. 6, pp. 606-608, Mar. 2014.

37. H. Ghafouri-Shiraz, Peh Wei Tan, and T. Aruga, "Picosecond Pulse Amplification in Tapered-Waveguide Laser-Diode Amplifiers," *IEEE. Selected Topics in Quantum Electron.*, vol. 3, no. 2, pp. 210-217, Dec. 1997.

38. E. Zhou et al., "Reduction of patterning effects in SOA-based wavelength converters by combining cross-gain and cross-absorption modulation," *Opt. Exp.*, vol. 16, no. 26, pp. 21522-21528, Dec. 2008.

39. A. Knorr, R. Binder, E. M. Wright, and S. W. Koch, "Amplification, absorption, and lossless propagation of femtosecond pulses in semiconductor amplifiers," *Opt. Lett.* vol. 18, no. 18, 1538-1540, Sept.1993.

40. A.V. Uskov, J. R. Karin, J. E. Bowers, J. G. McInerney and J. Le Bihan, "Effects of carrier cooling and carrier heating in saturation dynamics and pulse propagation through bulk semiconductor absorbers," *IEEE J. Quantum Electron.*, vol. 34, no. 11, pp. 2162–2171, 1998.

41. J. M. Dailey and T.L. Koch, "Impact of carrier heating on SOA dynamics for wavelength conversion," Lasers and Electro-Optics Society, 19th Annual Meeting of the IEEE, 2006.

42. J. M. Dailey and T.L. Koch, "Impact of carrier heating on SOA transmission dynamics for wavelength conversion," *IEEE Photon. Technol. Lett.*, vol. 19, no. 14, pp. 1078-1080, 2007.

43. J. Pleumeekers, et al., "Acceleration of gain recovery in semiconductor optical amplifiers by optical injection near transparency wavelength," *IEEE Photon. Technol. Lett.*, vol. 14, no. 1, pp. 12-14, Jan. 2002.

44. Y. Lai, K. L. Hall, E. P. Ippen, and G. EIsenstein, "Short pulse gain saturation in InGaAsP laser diode amplifier," *IEEE Photon. Technol. Lett.*, vol. 2, no. 10, pp. 711-713, Oct. 1990.

45. M. Xia and H. Ghafouri-Shiraz, "Analysis of carrier heating effects in Quantum Well semiconductor optical amplifiers considering holes' non-parabolic density of states," *Opt. Quantum Electron.*, vol. 47, no. 7, pp. 1847-1858, Jul. 2016.

46. A. V. Uskov, J. Mørk, B. Tromborg, T. W. Berg, I. Magnusdottir, and E. P. O'Reilly, "On high-speed cross-gain modulation without pattern effects in quantum dot semiconductor optical amplifiers," *Opt. Commun.*,vol. 227, no. 4-6, pp. 363-369, Sept. 2003.

47. V. V. Lysak, H. Kawaguchi, I. A. Sukhoivanov, T. Katayama, and A. V. Shulika, "Ultrafast gain dynamics in asymmetrical multiple quantumwell semiconductor optical amplifiers," *IEEE J. Quantum Electron.*, vol. 41, no. 6, pp. 797-807, Jun. 2005.

48. H. Wang, J. Wu, and J.T. Lin, "Spectral characteristics of optical pulse amplification in SOA under assist light injection," *J. Lightwave Technol.* Vol. 23, no. 9, pp.2761-2771, Sept. 2005.

49. L. Zhang, et al., "Reduced recovery time semiconductor optical amplifier using p-type-doped multiple quantum wells," *IEEE Photon. Technol. Lett.*, vol. 18, no. 22, pp. 2323-2325, Nov. 2006.

50. A. H. Gnauck, P. J. Winzer, S. Chandrasekhar, X. Liu, B. Zhu, and D. W. Peckham, "Spectrally efficient longhaul WDM transmission using 224-Gb/s polarization-multiplexed 16-QAM," *J. Lightwave Technol.* , vol. 29, no.4, pp. 373-377 , Feb. 2011.

51. G. Contestabile, Y. Yoshida, A. Maruta, and K. Kitayama, "Coherent wavelength conversion in a quantum dot SOA," *IEEE Photon. Technol. Lett.* vol. 25, no. 9, pp. 791-794 , May 2013.

52. M. Xia and H. Ghafouri-Shiraz, "Pump current optimization for pulse distortionless amplification in quantum well amplifiers," *IEEE J. Lightw. Technol.*, vol. 33, no. 18, pp. 3907-3913, Sept. 2015.

53. L. Hou, M. Haji, J.H. Marsh, "Monolithic mode-locked laser with an integrated optical amplifier for low-noise and high-power operation," *IEEE. Selected Topics in Quantum Electron.*, vol. 19,no. 4, pp. 1100808, Jul. 2013.

54. L. M. Frantz and J. S. Nodvik, “Theory of pulse propagation in a laser amplifier,” *J. Appl. Phys.*, vol. 34, no. 8, pp. 2346-2349, Jun. 1963.

55. M. Premaratne, D. Nesic, and G. P. Agrawal, “Pulse amplification and gain recovery in semiconductor optical amplifiers: a systematic analytical approach,” *J. Lightwave Technol.*, vol. 26, no. 12, pp. 1653-1660, Jun. 2008.

56. M. J. Connelly, “Wideband semiconductor optical amplifier steady-state numerical model,” *IEEE J. Quantum Electron*, vol. 37, no. 3, pp. 439-447, Mar. 2001.

57. L. Gillner, “Comparative study of some traveling-wave semiconductor laser amplifier models,” *IEE Proc. J. Optoelectron.*, vol. 139, no. 5, pp. 339-347, Oct. 1991.

58. R. Brosson, “Analytic model of a semiconductor optical amplifier,” *J. Lightwave Technol.*, vol. 12, no. 1, pp. 49-54, Jan. 1994.

59. S. Ruiz-Moreno and J. Guitart, “Practical method for modeling the nonlinear behavior of a traveling-wave semiconductor optical amplifier,” *IEE Proc. J. Optoelectron.*, vol. 140, no. 1, pp. 39-43, Feb. 1993.

60. P.B. Johns and R.L. Beurle, “Numerical solution of 2-dimensional scattering problems using a transmission-line matrix,” *IEE Proc. J. Optoelectron.*,vol. 188, no. 9, pp. 1203-1208, Sept.1971.

61. A.J. Lowery, “New dynamic semiconductor laser model based on the transmission line modelling method,” *IEE Proc. J. Optoelectron.*, vol. 134, no. 5, pp.281-290, Oct.1987.

62. L. V. T. Nguyen, A. J. Lowery, P. C. R. Gurney, and D. Novak, “A time-domain model for high-speed quantum-well lasers including carrier transport effects,” *IEEE J. Select. Topics Quantum Electron.*, vol. 1, no. 2, pp.494-504, Jun.1995.

63. W. M. Wong and H. Ghafouri-Shiraz, “Dynamic model of tapered semiconductor lasers and amplifiers based on transmission line laser modelling,” *IEEE J. Select. Topics. Quant. Electron.*, vol. 6, no. 4, pp. 585-593, Jul. 2000.

64. W. M. Wong and H. Ghafouri-Shiraz, “Integrated semiconductor laser transmitter model for microwave-optoelectronic simulation based on transmission-line modelling,” *IEE Proc. J. Optoelectron.*, vol. 146, no. 4, pp. 181-188, Aug. 1999.

65. M. Xia and H. Ghafouri-Shiraz, “Quantum transmission line modelling method and its application to quantum dot amplifiers,” *IEEE J. Quantum Electron.*, vol. 52, no. 5, pp. 5100107, Mar. 2016.

66. H. Ghafouri-Shiraz, The theory of semiconductor laser diodes and amplifiers: analysis and transmission line laser modelling. London, Imperial College Press, 2004.

67. M. Planck, The Theory of Heat Radiation. Masius, M. (transl.) (2nd ed.). P. Blakiston's Son & Co. OL 7154661M, 1914.

68. P. J. A. Thijs, L. F. Tiemijer, P. I. Kuindersma, J. J. M. Binsma, and T. van Dongen, "High-performance of 1.5 pm wavelength InGaAs-InGaAsP strained quantum-well lasers and amplifiers," *IEEE J. Quantum Electron.*, vol. 27, no.6, pp.1426-1438, Jun. 1991.

69. P. J. A. Thijs, L. F. Tiemijer, J. J. M. Binsma, and T. van Dongen, "Progress in long-wavelength strained-layer InGaAs(P) quantum-well semiconductor lasers and amplifiers," *IEEE J. Quantum Electron.* , vol.30, no. 2, pp.477-499, Feb. 1994.

70. C. Chang and S. Chuang, "Modeling of strained quantum-well lasers with spin-orbit coupling," *IEEE J. Sel. Topics Quantum Electron.* ,vol.1, no. 2, pp.218–229, Jun. 1995.

71. M. Sugawara, N. Okazalu, T. Fujii, and S. Yamazalu, "Conduction-band and valence-band structures in strained $In_{1-x}Ga_xAs/InP$ quantum wells on (001) InP substrates,'' *Phys. Rev B*, vol. 48, no. 11, pp. 8102-8118, Sept.1993.

72. C. Y -P. Chao and S L Chuang, "Spin-orbit-coupling effects on the valence-hand structure of strained semiconductor quantum wells," *Phys Rev B*., vol. 46, no. 7, pp. 4110-4122, Aug.1992

73. C. G. Van de Walle, "Band lineups and deformation potentials in the model-solid theory," *Phys. Rev. B*, vol. 39, no.3, pp. 1871-1883, Jan. 1989.

74. S. L. Chuang, Physics of Optoelectronic Devices. New York, Wiley, 1995.

75. Shun Lien Chuang, "Efficient band-structure calculations of strained quantum wells," Phys. Rev. B, vol. 43, no. 12, pp.9649-9661, Apr. 1991

76. C. Qin, X. Huang, and X. Zhang, "Gain recovery acceleration by enhancing differential gain in quantum well semiconductor optical amplifiers," *IEEE. Quantum Electron.*, vol. 47, no.11, pp. 1443-1450, Nov. 2011.

77. X. Huang, Study on nonlinearities in quantum well semiconductor optical amplifiers, PhD thesis, 2012

78. A. Kendall, An introduction to numerical analysis, 2nd edn. New York, Wiley, 1989.

79. M. Osinski and J. Buus, "Linewidth broadening factor in semiconductor lasers-An overview," *IEEE J. Quantum Electron.*, vol. 23, no. 1, pp. 9-29, Jan. 1987.

80. M. Xia and H. Ghafouri-Shiraz, "Analysis of strain effects on the dynamic spectra of a quantum well semiconductor optical amplifier using quantum well transmission line modelling method," J. Opt. Communications., vol. 364 pp. 60-66, Apr. 2016

81. P. P. Vasilev, "Ultrashort pulse generation in diode-lasers," *Opt. Quantum Electron.* , vol. 24, no. 8, pp. 801-824, Aug. 1992.

82. K. Kim, S. Lee, and P. J. Delfyett, "Extreme chirped pulse amplification - beyond the fundamental energy storage limit of semiconductor optical amplifiers," *IEEE J. Sel. Top. Quantum Electron.* , vol.12, no.12, pp.245-254, Mar. 2006.

83. U. Keller, “Recent developments in compact ultrafast lasers,” *Nature*, vol. 424, pp. 831-838 , Aug. 2003.

84. H. Wenzel et al., “High peak power optical pulses generated with a monolithic master-oscillator power amplifier,” *Opt. Lett.* vol. 37, no. 11, pp. 1826-1828, May. 2012.

85. A. V. Uskov, C. Meuer, H. Schmeckebier, and D. Bimberg, “Auger capture induced carrier heating in quantum dot lasers and amplifiers,” *Appl. Phys. Express* ,vol. 4, no. 2, Art. no. 022202, Feb. 2011.

86. K.L.Hall, G. Lenz, A.M. Darwish and E. P. Ippen, “subpicosecond gain and index nonlinearities in InGaAsP diode laser,” Opt. Comm. , vol. 111, pp. 589-612,1994.

87. A. Mecozzi and J. Mørk, “Saturation induced by picosecond pulses in semiconductor optical amplifiers,” *J. Opt. Soc.Am. B*, vol. 14, no. 4, pp.761-770, Apr. 1997.

88. K. Hussain and P. K. Datta, “Effect of including intraband phenomena in the semiconductor optical amplifier model for propagation of short pulses,” *Applied Optics*, vol. 52, no. 29 , pp.7171-7177, Oct. 2013.

89. P. Runge, R. Elschner, and K. Petermann, “Chromatic dispersion in InGaAsP semiconductor optical amplifiers,” *IEEE J. Quantum Electron.* vol. 46, no. 5,pp. 644-649, May 2010.

90. H. Ghafouri-Shiraz and P. W. Tan, “Study of a novel laser diode amplifier structure,” *Semicond. Sci. Technol.*, vol. 11, no. 10, pp. 1443-1449, Oct. 1996.

91. J. Dailey and T. Koch, “Simple rules for optimizing asymmetries in SOA-based Mach-Zehnder wavelength converters,” *Lightw. Technol.*, vol. 27, no. 11, pp. 1480–1488, 2009.

92. L. A. Coldren and S. W. Corzine, Diode Lasers and Photonic Integrated Circuits. New York, Wiley, 1995.

93. X. Aymerich-Humet. F. Serra-Mestres, and J. Millan, “An analytical approximation for the Fermi-Dirac integral $F_{3/2}(\eta)$,” *Solid-State Electronics*, vol. 24, no. 10, pp. 981-982, Oct. 1981.

94. N. G. Nilsson, “Empirical approximations for the Fermi energy of a semiconductor with parabolic bands,” *Appl. Phys. Lett.*, vol. 33, no. 7, pp. 653–654, Oct. 1978.

95. D. Bednarczyk and J. Bednarczyk, “The approximation of the Fermi-Dirac integral $F_{1/2}(\eta)$,” *Phys. Lett.*, vol. 64A, no. 4, pp. 409-410, Jan. 1978.

97. A. Yariv , Opt. Electron. , New York, HWR International, 1985.

96. S. Adachi , GaAs and related materials, Singapore, World Scientific, 1994.

98. G. P. Agrawal and N. A. Olsson, “Amplification and compression of weak picosecond optical pulses by using semiconductor laser amplifiers,” *Opt. Lett.*, vol. 14, no. 10, pp. 500-502, May 1989.

99. J. Mørk, A. Mecozzi, and C. Hultgren, “Spectral effects in short pulse pump–probe measurements,” *Appl. Phys. Lett.*, vol. 68, no. 4, pp. 449-451, Jan. 1996.

100. A. H. Quarterman, et al. “A passively mode-locked external-cavity semiconductor laser emitting 60-fs pulses,” *Nat. Photon.*, vol. 3, pp.729-731, Dec. 2009.

101. X. Huang, Z. Zhang, C. Qin, Y. Yu, and X. L. Zhang, “Optimized quantum-well semiconductor optical amplifier for RZ-DPSK signal regeneration”, *IEEE J. Quantum Electron.* , vol. 47, no. 6, pp. 819-826, Jun. 2011.

102. P. W. Juodawlkis, J. J. Plant, W. Loh, L. J. Missaggia, K. E. Jensen, and F. J. O’Donnell, “Packaged 1.5- μm Quantum-Well SOA with 0.8-w output power and 5.5-dB noise figure,” *IEEE Photon. Technol. Lett.*, vol. 21, no. 17, pp. 1208–1210, Sep. 2009

103. M. L. Nielsen, J. Mørk, R. Suzuki, J. Sakaguchi, and Y. Ueno, “Experimental and theoretical investigation of the impact of ultrafast carrier dynamics on high-speed SOA-based all-optical switches,” *Opt. Exp.*, vol. 14, no. 1, pp. 331–347, Jan. 2006.

104. V. V. Lysak, I. A. Sukhoivanov, O. V. Shulika, I. M. Safonov, and Y. T. Lee “Carrier tunneling in complex asymmetrical multiple-quantum-well semiconductor optical amplifiers,” *IEEE Photon. Technol. Lett.*, vol. 18, no. 12, pp. 1362-1364, June. 2006

105. V. V. Lysak, H. Kawaguchi, I. A. Sukhoivanov, Y. T. Lee, T. Katayama, and A. V. Shulika, “Ultrafast dynamics in asymmetrical multiple quantum well SOAs,” *Proc. SPIE Phys. Applicat. Optoelectron. Devices*, vol. 5594, pp. 21-32, 2004.

106. P. P. Baveja, D. N. Maywar, A. M. Kaplan, and G. P. Agrawal, “Self-phase modulation in semiconductor optical amplifiers: Impact of amplified spontaneous emission,” *IEEE J. Quantum Electron.*, vol. 46, no. 9, pp. 1396-1403, Sept. 2010.

107. W. Mathlouthi, F. Vacondio, P. Lemieux, and L. A. Rusch, “SOA gain recovery wavelength dependence: simulation and measurement using a single-color pump-probe technique,” *Opt. Exp.*, vol. 16, no. 25, pp.20656-20665, Oct. 2008.

108. R. J. Manning, D. A. O. Davies, and J. K. Lucek, “Recovery rate in semiconductor laser amplifiers: optical and electrical bias dependencies,” *Electron. Lett.* vol. 30, no. 15, pp. 1233-1235, Jul. 1994.

109. J. Mandon, G. Guelachvili, and N. Picque, “Fourier transform spectroscopy with a laser frequency comb,” *Nature Photon.*, vol. 3, pp. 99-102, Feb. 2009.

110. L. Daniault, et. al, “Passive coherent beam combining of two femtosecond fiber chirped-pulse amplifiers,” *Opt. Lett.*, vol. 36, no.5, pp. 4023-4025, Mar. 2011.

111. M. Kienel, et. al, “Analysis of passively combined divided-pulse amplification as an energy-scaling concept,” *Opt. Exp.*, vol. 21, no. 23, pp. 29031-29042, Nov. 2013.

112. J. R. Whinnery and S. Ramo, “A new approach to the solution of high-frequency field problems,” *Proc. IRE.*, vol. 32, pp. 284-288, May 1944

113. G. Kron, “Equivalent circuit of the field equations of Maxwell-I,” *Proc. IRE*, vol. 32, pp. 289-299, May 1944.

114. J. R. Whinnery, C. Concordia, W. Ridgway, and G. Kron, “Network analyzer studies of electromagnetic cavity resonators,” *Proc. IRE*, vol. 32, pp. 360-367, June 1944.

115. P. B. Johns, “The solution of inhomogeneous waveguide problems using a transmission-line matrix,” *IEEE Trans. Microwave Theory Tech.*, vol. MIT-22, no. 3, pp. 209-215, Mar. 1974.

116. S. Akhtarzad and P.B. Johns, “Three-dimensional transmission-line matrix computer analysis of microstrip resonators,” *IEEE Trans. Microwave Theory Tech.*, vol. MTT-23, no. 12, pp. 990-997, Dec. 1975.

117. C, Huygens, “Traite de la Lumiere,” Lelden, 1690.

118. S. Akhtarzad, “Analysis of lossy microwave structures and microstrip resonators by the TLM method,” PhD dissertation, University of Nottingham, England, July 1975.

119. N. Yoshida and I. Fnkai, “Transient analysis of a stripline having a corner in three-dimensional space,” *IEEE Tran. Microwave Theory Tech.*, vol. MTT-32, no. 5, pp. 491-498, May 1984.

120. J. W. Bandler, P.B.Johns and M.R.M. Rizk, “Transmission-line modelling and sensitivity evaluation for lumped network simulation and design in the time domain,” *Jour. Frank. Inst.*, vol. 304, no.1, pp. 15-32, July 1977.

121. S. Kobayashi, “Injection-locked semiconductor laser amplifiers,” in *Coherence, Amplification, and Quantum Effects in Semiconductor Lasers*, Y. Yamamoto (Ed), John Wiley and Sons, Inc., New York, 1991.

122. R. E. Collins, Foundations of Microwave Engineering. New York: McGraw-Hill, 1966.

123. A.J. Lowery, “New inline wideband dynamic semiconductor laser amplifier model,” *IEE Proc. J.*, vol. 135, no. 3, pp. 242-250, Jun. 1988.

124. W. M. Wong and H. Ghafouri-Shiraz, “Dynamic model of tapered semiconductor lasers and amplifiers based on transmission line laser modelling,” *IEEE Jour. Select. Top. Quant. Elec.*, vol. 6, no. 4, pp. 585-593, Jul. 2000.

125. A. Yariv, Quantum Electronics, 3d ed, Wiley, New York, 1989

126. S. L. Chuang, Physics of Optoelectronic Devices, Wiley, New York, 2009

127. M. Kira and S. Koch, Semiconductor Quantum Optics, Cambridge University Press, 2012.

128. Hans R. Griem, Principles of Plasmas Spectroscopy, Cambridge University Press, 1997.

129. M. Xia and H. Ghafouri-Shiraz, "A novel transmission line model of quantum well semiconductor optical amplifiers," *J. Optical and Quantum Electronics*, vol. 48, no. 52, pp. 51-64, Jan. 2016.

130. P.B. Johns and M. O'Brien, "Use of the transmission-line modelling (TLM) method to solve non-linear lumped networks," *Radio & Electron. Eng.*, vol. 50, pp. 59-70, 1980.

131. A. Capua, O. Karni and G. Eisenstein, "A finite-difference time-domain model for quantum-dot lasers and amplifiers in the Maxwell–Schrödinger framework," *IEEE J. Select. Topic. Quantum Electron.* , vol. 19, no. 5, pp. 1900410, Sept. 2013.

132. Z. Vujicic, R. P. Dionisio, A. Shahpari, N. B. Pavlovic, and A. Teixeira, "Efficient dynamic modelling of the reflective semiconductor optical amplifier," *IEEE J. Select. Topics Quantum Electron.*, vol. 19, no. 5, pp. 3000310, Sept. 2013.

133. W. Mathlouthi, P. Lemieux, M. Salsi, A. Vannucci, A. Bononi and L. A. Rusch, "Fast and efficient dynamic WDM semiconductor optical amplifier model," *IEEE J. Lightw. Technol.*, vol. 24, no. 11, pp. 4353-4365, Nov. 2006.

134. K. L¨udge, E. Sch¨oll, E. Viktorov, and T. Erneux, "Analytical approach to modulation properties of quantum dot lasers," *J. Appl. Phys.*, vol. 109, pp. 103112, May 2011.

135. J. Mørk and A. Mecozzi. "Theory of the ultrafast optical response of active semiconductor Waveguides," *Opt. Soc. Am. B.*, vol. 13, no. 8, pp. 1803-1816, Aug. 1996

136. S. Bennett and C. M. Snowden, "Nonlinear dynamics in directly modulated multiple-quantum-well laser diodes," *IEEE J. Quantum Electron.*, vol.33, no.11, pp.2076-2083, Nov.1997.

137. A.J. Lowery, "Efficient material-gain models for the transmission-line laser model," *International Journal of Numerical Modelling*, vol. 8, no. 5, pp.315-330, Sept. 1995.

138. C. Cohen-Tannoudji, G. Grynberg, Atom-Photon Interaction, Wiley, 1992.

139. G. P. Agrawal and N. A. Olsson, "Self-phase modulation and spectral broadening of optical pulses in semiconductor laser amplifiers," *IEEE J. Quantum Electron.*, vol. 25, no. 11, pp. 2297-2306, Nov. 1989.

140. M. Sugawara, K. Mukai, Y. Nakata, H. Ishikawa, and A. Sakamoto, "Effect of homogeneous broadening of optical gain on lasing spectra in self-assembled $In_xGa_{1-x}As\,/\,GaAs$ quantum dot lasers," *Phys. Rev. B*, vol. 61, no. 11, pp. 7595-7603, Mar. 2000.

141. R. Nagarajan, M. Ishikawa, T. Fukushima, R. S. Geels, and J. E. Bowers, "High speed quantum-well lasers and carrier transport effects," *IEEE J. Quantum Electron.*, vol. 28, no. 10, pp. 1990-2008, Oct. 1992.

142. E. P. O'Reilly and A. R. Adams, "Band-structure engineering in strained semiconductor lasers," *IEEE. Quantum Electron.*, vol. 30, no. 2, pp.366-379, Feb.1994.

143. M. Xia and H. Ghafouri-Shiraz, "Transmission line model for strained quantum well lasers including carrier transport and carrier heating effects," *Applied Optics*, vol. 55, no. 7, pp.1518-1524, Mar. 2016

144. M. Xia and H. Ghafouri-Shiraz, "Wavelength-dependent femtosecond pulse amplification in wide band tapered-waveguide quantum well semiconductor optical amplifiers," *Applied Optics*, vol. 55, no. 3, pp.10524-10531, Dec. 2015

145. K. G. Wilcox et al., "4.35 kW peak power femtosecond pulse modelocked VECSEL for supercontinuum generation," *Opt. Exp.*, vol. 21, no. 2, pp. 1599-1605, Jan. 2013.

146. G. Obara, H. Shimizu, T. Enami, E. Mazur, M. Terakawa and M. Obara, "Growth of high spatial frequency periodic ripple structures on SiC crystal surfaces irradiated with successive femtosecond laser pulses," *Opt. Exp.* vol. 21.no.22, pp.26323-26334, Nov.2013.

147. G. Bendeli, K. Komori, S. Arai, and Y. Suematsu, "A new structure for high power TW-SLA (Travelling wave semiconductor laser amplifier)," *IEEE Photon. Technol. Lett.*, vol. 3, no. 1, pp.42-45, 1991.

148. G. Bendelli, K. Komori, and S. Arai, "Gain saturation and propagation characteristics of index-guided tapered-waveguide travelling-wave semiconductor laser amplifiers (TTW-SLA's)," *IEEE J. Quantum Electron.*, vol.28, no.2, pp.447-458, Mar.1992.

149. F. Koyama, K. Y. Liou, A. G. Dentai, T. Tanbun-Ek, and C. A. Burrus, "Multiple-quantum-well GaInAs/GaInAsP tapered broad-area amplifiers with monolithically integrated waveguide lens for high-power applications," *IEEE Photon. Technol. Lett.*, vol. 5, no. 8, pp.916-919 , Sept.1993.

150. B. Zhu, I. H. White, K. A. Williams, F. R. Laughton and R. V. Penty, "High-peak power optical pulse generation from Q-switched bow-tie laser with a tapered travelling-wave amplifier," *IEEE Photon. Technol. Lett.*, vol.8, no. 4, pp.503-505, May 1996.

151. M. Xia and H. Ghafouri-Shiraz, "A new optical gain model for quantum wells based on quantum well transmission line modelling method," *IEEE J. Quantum Electron.*, vol. 51, no. 3, pp.1-8, Mar. 2015.